



Universidade de Aveiro
Ano 2016

Departamento de Eletrónica, Telecomunicações e
Informática

**Alírio de Jesus
Soares Boaventura**

**Sistemas Eficientes de Transmissão de Energia
Sem-Fios e Identificação por Radiofrequência**

**Efficient Wireless Power Transfer and Radio
Frequency Identification Systems**



**Alírio de Jesus
Soares Boaventura**

**Sistemas Eficientes de Transmissão de Energia
Sem-Fios e Identificação por Radiofrequência**

**Efficient Wireless Power Transfer and Radio
Frequency Identification Systems**

Tese apresentada à Universidade de Aveiro para cumprimento dos requisitos necessários à obtenção do grau de Doutor em Engenharia Eletrotécnica, realizada sob a orientação científica do Doutor Nuno Borges de Carvalho, Professor Catedrático do Departamento de Eletrónica, Telecomunicações e Informática da Universidade de Aveiro

Apoio financeiro da Fundação para a
Ciência e a Tecnologia (FCT) através
da bolsa de doutoramento com a
referência SFRH/BD/80615/2011.

Aos meus pais Alfredo e Maria Boaventura.

o júri

presidente

Prof. Doutora Ana Isabel Miranda
professora Catedrática do Departamento de Ambiente e Ordenamento da Universidade de Aveiro

Prof. Doutora Mónica Fernádes Barciela
professora titular da Escola de Engenharia e Telecomunicações da Universidade de Vigo

Prof. Doutor Nuno Miguel Gonçalves Borges de Carvalho
professor catedrático do Departamento de Eletrónica Telecomunicações e Informática da Universidade de Aveiro

Prof. Doutor João Nuno Pimentel da Silva Matos
professor associado do Departamento de Eletrónica Telecomunicações e Informática da Universidade de Aveiro

Prof. Doutor Vitor Manuel Grade Tavares
professor auxiliar da Faculdade de Engenharia da Universidade do Porto

Prof. Doutor Jorge Ribeiro Fernandes
professor auxiliar do Departamento de Engenharia Eletrotécnica e de Computadores do Instituto Superior Técnico de Lisboa

Agradecimentos

Obrigado, acima de tudo, a Deus, por esta conquista apesar dos obstáculos!

A etapa que agora culmina com a escrita desta dissertação tem sido uma jornada extraordinária, sem dúvida de muito trabalho, mas também de muita diversão, satisfação e conquistas, e estou certo de que assim não seria se não fosse pelo apoio, amizade e colaboração de muitas pessoas e suporte de algumas instituições. Algumas destas pessoas e instituições, pela sua intervenção de forma mais direta e continuada merecem aqui uma palavra de agradecimento e apreço. Para as muitas outras, que de uma forma ou de outra contribuíram, fica também um obrigado.

Em primeiro lugar, um imenso obrigado à toda a minha família pelo acreditar em mim, pelo respeito, carinho e admiração mútua. Em especial aos meus pais, Maria e Alfredo Boaventura, meus irmãos José, Luísa e Rosa Boaventura, sobrinha Goreth Boaventura e primo Fernando Monteiro. Apesar da distância, o vosso apoio e conforto tem estado sempre à distância de uma chamada telefónica.

Um grande obrigado ao meu orientador, professor Nuno Borges Carvalho, pela confiança que sempre depositou em mim, desde o mestrado até agora, pela sua mentoria como professor e como grande profissional da área das comunicações sem fios, e também pela amizade ao longo destes anos. Considero-me afortunado por ter tido a oportunidade de colaborar com o professor Nuno Borges e de ter tido as excelentes condições oferecidas pela Universidade de Aveiro e pelo Instituto de Telecomunicações.

Um muitíssimo obrigado aos amigos e colegas, sem esquecer os de longa data, que das mais diversas formas contribuíram para a chegada a bom porto, Odracir Almeida, Elizangela Fonseca, João Ramos Rocha, Widson Monteiro, Narciso Gomes, Manuel Rocha, Celestino Martins, Luís Oliveira, Ludimar Guenda, Irina Carvalho, Igor Fonseca, ...

Uma palavra de agradecimento ao engenheiro João de Deus da Luz pela amizade e por me ter ensinado o ABC da eletrónica quando ainda estava eu no liceu. Também a alguns dos mentores que tiveram um papel importante no meu percurso académico desde o pré-universitário, nomeadamente os professores Tomás Cruz, Angelita, Albertino Mota, Rafael Oliveira, entre outros. Não poderia esquecer a minha terra natal, em especial os amigos de Fajã de Matos, pelo carinho, suporte e amizade que sempre demonstraram.

Gostaria ainda de agradecer a todos os colegas e amigos do Instituto de Telecomunicações, que de uma forma ou de outra deram o seu contributo, Ricardo Gonçalves, Wonhoon Jang, Ricardo Correia, Ricardo Fernandes, Daniel Belo, Hugo Mostardinha, Paulo Gonçalves, Sérgio Lopes, João Santos. Também aos professores Arnaldo Oliveira e José Vieira, ambos do DETI.

Um agradecimento especial aos colaboradores externos pelo trabalho desenvolvido em colaboração com os respetivos grupos, nomeadamente, os professores Apostolos Georgiadis e Ana Collado do CTTC em Barcelona, Espanha, Alejandro Rodrigues e a professora Mónica Barciela da universidade de Vigo, Espanha, Ning Pan e as professoras Dominique Schreurs e Sofie Pollin da universidade de Leuven, Bélgica.

Uma palavra de agradecimento vai também para o engenheiro Jorge Renato Graça e para a empresa Acronym Lda, pela contínua colaboração desde o mestrado até agora.

Os agradecimentos estendem-se à Fundação para a Ciência e a Tecnologia (FCT) pela bolsa de doutoramento, sem a qual este projeto não teria sido possível.

Gostaria também de endereçar um agradecimento aos elementos do júri que dispensaram o seu precioso tempo e se disponibilizaram a discutir este trabalho, e finalmente, a todos os autores anónimos cujos trabalhos serviram de referência a esta tese.

palavras-chave

Identificação por Radiofrequência, Transmissão de Energia Sem Fios, Colheita de Energia Electromagnética, Eficiência de Conversão RF-DC, Optimização de Formas de Onda, Sinais Multi-seno.

resumo

No contexto da internet das coisas (IoT), onde são esperados bilhões de objetos conectados espalhados pelo planeta de forma ubíqua, torna-se impraticável uma frequente manutenção e troca de baterias dos dispositivos sem fios ubíquos. Nestes cenários, os sistemas radio backscatter passivos terão um papel preponderante dado o seu baixo custo, baixa complexidade e não necessidade de baterias nos nós móveis. Uma vez que a transmissão de energia sem fios é o principal aspeto limitativo nestes sistemas, a sua otimização tem sido um tema central de investigação, ganhando ainda mais ênfase no contexto IoT.

Tradicionalmente, a transferência de energia sem-fios é feita através de sinais CW e a maximização da eficiência é conseguida através da otimização dos circuitos recetores. Neste trabalho explora-se uma abordagem fundamentalmente diferente, em que a otimização foca-se nas formas de onda em vez dos circuitos. Demonstra-se, teoricamente e através de simulações e medidas que, devido à sua maior capacidade em superar a barreira de potencial intrínseca dos dispositivos retificadores, os sinais multi-seno (MS) de elevado PAPR são capazes de excitar os circuitos de colheita de energia de forma mais eficiente quando comparados com o sinal CW tradicional. Usando sinais MS ótimos em circuitos retificadores, foram verificadas experimentalmente melhorias de eficiência de conversão RF-DC notáveis de até 15 dB relativamente ao sinal CW.

A fim de mostrar a eficácia desta abordagem na melhoria da distância de comunicação de sistemas backscatter passivos, integrou-se um front-end MS num leitor RFID comercial e observou-se um aumento significativo de 25% na distância de leitura. Além disso, desenvolveu-se de raiz um leitor RFID baseado em software rádio, compatível com o protocolo ISO18000-6C e capaz de gerar sinais MS, com os quais interrogou-se transponders passivos, obtendo-se ganhos de sensibilidade dos transponders maiores que 3 dB. Uma vez que a amplificação de sinais de elevado PAPR é uma operação crítica, propôs-se também novas arquiteturas eficientes de transmissão baseadas na combinação de sinais em espaço livre.

Esta tese aborda também outros aspetos não menos importantes, como o self-jamming em leitores RFID passivos, tido como o segundo fator limitativo neste tipo de sistemas. Estudou-se técnicas de cancelamento de self-jamming CW e estendeu-se o conceito a sinais MS, tendo-se obtido isolamentos entre o transmissor e o recetor de até 50 dB no primeiro caso e de até 60 dB no segundo.

Finalmente, com o objetivo de demonstrar uma aplicação prática dos conceitos de transmissão de energia sem fios e comunicação backscatter, desenvolveu-se um sistema de controlo remoto sem pilhas, cujo protótipo foi integrado num televisor comercial a fim de controlar quatro funcionalidades básicas (CH+,CH-,VOL+,VOL-).

keywords

Wireless Identification, Wireless Power Transfer, Radio-Frequency Identification, Passive-Backscatter Radios, Energy Harvesting Circuits, RF-DC Conversion Efficiency, Waveform Design Optimization, Multi-sines.

abstract

In the IoT context, where billions of connected objects are expected to be ubiquitously deployed worldwide, the frequent battery maintenance of ubiquitous wireless nodes is undesirable or even impossible. In these scenarios, passive-backscatter radios will certainly play a crucial role due to their low cost, low complexity and battery-free operation. However, as passive-backscatter devices are chiefly limited by the WPT link, its efficiency optimization has been a major research concern over the years, gaining even more emphasis in the IoT context.

Wireless power transfer has traditionally been carried out using CW signals, and the efficiency improvement has commonly been achieved through circuit design optimization. This thesis explores a fundamentally different approach, in which the optimization is focused on the powering waveforms, rather than the circuits. It is demonstrated through theoretical analysis, simulations and measurements that, given their greater ability to overcome the built-in voltage of rectifying devices, high PAPR multi-sine (MS) signals are capable of more efficiently exciting energy harvesting circuits when compared to CWs. By using optimal MS signals to excite rectifying devices, remarkable RF-DC conversion efficiency gains of up to 15 dB with respect to CW signals were obtained.

In order to show the effectiveness of this approach to improve the communication range of passive-backscatter systems, a MS front-end was integrated in a commercial RFID reader and a significant range extension of 25% was observed. Furthermore, a software-defined radio RFID reader, compliant with ISO18000-6C standard and with MS capability, was constructed from scratch. By interrogating passive RFID transponders with MS waveforms, a transponder sensitivity improvement higher than 3 dB was obtained for optimal MS signals. Since the amplification and transmission of high PAPR signals is critical, this work also proposes efficient MS transmitting architectures based on space power combining techniques.

This thesis also addresses other not less important issues, namely self-jamming in passive RFID readers, which is the second limiting factor of passive-backscatter systems. A suitable self-jamming suppression scheme was first used for CW signals and then extended to MS signals, yielding a CW isolation up to 50 dB and a MS isolation up to 60 dB.

Finally, a battery-less remote control system was developed and integrated in a commercial TV device with the purpose of demonstrating a practical application of wireless power transfer and passive-backscatter concepts. This allowed battery-free control of four basic functionalities of the TV (CH+,CH-,VOL+,VOL-).

List of figures

Fig. 1.1	The history of radio transmission and wireless power transfer (recreated from [33])	13
Fig. 1.2	The listening device inside the <i>Great Seal Bug</i> – a very sophisticated passive-backscattering system developed by Soviets during the cold war for espionage [source: Wikimedia Foundation]	14
Fig. 1.3	First patented passive RFID transponder with readable and rewritable memory [56]	15
Fig. 1.4	RFID technology milestones	15
Fig. 2.1	Active, semi-passive and passive RFID systems	24
Fig. 2.2	Illustration of Near-field and far-field operating regions	26
Fig. 2.3	Near-field passive RFID system. The magnetic field lines (B) are in actuality closed ones	27
Fig. 2.4	Inductively-coupled 1-bit RFID system [After Walton, US Patent 3,752,960]	28
Fig. 2.5	1-bit microwave system based on harmonic generation of an RF diode	28
Fig. 2.6	Passive-backscatter RFID system	30
Fig. 2.7	Passive RFID tag/RFID-enabled sensor. The advanced functionality blocks of RFID-enabled sensors are filled with yellow.	32
Fig. 2.8	Basic RFID reader configuration based on a commercial ASIC	33
Fig. 2.9	Typical SDR RFID reader implementation	34
Fig. 2.10	Passive-backscatter RFID system using binary RCS modulation	36
Fig. 2.11	(a) Example of PSK modulation states at the tag, (b) Received baseband constellation. (c) Constellation rotation after change in distance and consequent propagation phase shift. (d) Received signal after change in self-jamming and scattering components, and distance change. (e) DC-offset rejection by using a HPF. (f) Constellation phase rotation to the real axis	39
Fig. 2.12	Typical curves of power harvested by tag and power level reflected by tag and received by reader	42
Fig. 3.1	Wireless power transfer subsystem	47
Fig. 3.2	Multiple antenna receiver	49
Fig. 3.3	Solar-assisted RFID tag concept (after [51])	51
Fig. 3.4	State-of-the-art efficiencies for different frequency bands as a function of input power (data from [56][78][79])	52
Fig. 3.5	CMOS threshold-compensation schemes. (a) Self- V_{th} cancellation. (b) Photovoltaic-assisted rectifier. Both circuits are voltage doublers using diode-connected nMOS and pMOS transistors. [92]	56
Fig. 4.1	Basic blocks of an RF-DC conversion circuit	64
Fig. 4.2	Typical energy harvesting circuit topologies. (a) Shunt diode rectifier. (b) Series diode rectifier. (c) Shunt diode rectifier using microstrip $\lambda/4$ stubs. (d) N-stage Dickson voltage multiplier	65
Fig. 4.3	Typical efficiency curves of different rectifying circuits	65

Fig. 4.4	Physical model of a Schottky diode	66
Fig. 4.5	Typical DC I-V curve of a Schottky diode and respective operating regions	67
Fig. 4.6	Typical RF-DC characteristic of a detector circuit, illustrating the operation in square-law, linear and compression regions	68
Fig. 4.7	(a) Illustration of single-carrier rectification in a series diode detector. (b) Breakdown effect	69
Fig. 4.8	(a) Time-domain waveform of a 4-tone MS with random phase arrangement. (b) 4-tone MS with 0° phase arrangement (blue signal) overlapped with a CW with same average power (green signal). (c) frequency spectrum of a CW and MS signal	72
Fig. 4.9	CW (green signal) versus MS (blue signal) rectification	72
Fig. 4.10	(a) Simple series diode rectifier used in ADS HB simulations. (b) Frequency mapping of the input signals used in the HB simulations	77
Fig. 4.11	Time-domain waveforms obtained in the HB simulations. (a) Input 2-tone MS signal overlapped with a CW signal with the same average power, and (b) respective output waveform. (c) Input 4-tone MS signal overlapped with a CW signal with the same average power, and (d) respective output waveform. In (b) and (d), the constant curve (blue) corresponds to the CW signal and the rippled waveforms (red and green) corresponds to the MS signals	78
Fig. 4.12	(a) Simulated DC voltage as a function of average input power for several input excitation signals. (b) Efficiency gain as a function of average input power	79
Fig. 4.13	(a) Rectifier circuit matched to the source impedance at 2.4 GHz. (b) Efficiencies under CW and MS excitations as a function of the average input power and number of tones. In this case, the actual average input power level is calculated based on the voltage and current at the input of the circuit as in (4.23)	80
Fig. 4.14	Rectifying circuits used in the cabled measurements and respective input return loss (simulated and measured). (a) Single diode detector operating at 2.3 GHz band. (b) Charge pump rectifier with 866 MHz center frequency	81
Fig. 4.15	(a) Measured DC output voltage of the single diode detector, as a function of average input power. (b) Efficiency gain of the single diode detector, as a function of average input power. Except for the 64-tone MS, as the number of tones and the PAPR increase, the gain also increases. (c) Output DC voltage as a function of the input signal bandwidth. It is visible that there is an optimal MS bandwidth that produces a maximum output DC	82
Fig. 4.16	(a) Measured DC output voltage of the charge pump, as a function of average input power. (b) Efficiency gain of the charge pump, as a function of average input power. (c) Output DC voltage as a function of the input signal bandwidth	83
Fig. 4.17	Probability density functions of noise and synthesized MS signals. (a) Normal distribution. (b) Uniform distribution	84
Fig. 4.18	Measured DC output voltage of the charge pump, for a CW signal, and a 16-tone MS with uniform and normal amplitude distributions, and with 0° phase arrangement	84
Fig. 5.1	(a) Externally-synchronized multi-sine transmitter. (b) Mode-locked coupled-oscillator array with coupling through the antennas	92
Fig. 5.2	Measurement setup to evaluate rectifier performance under two-tone and CW signal ($r = 35\text{cm}$)	92

Fig. 5.3	(a) Diagram of the multi-sine measurement setup. (b) Multi-sine transmitter. (c) Receiver. $d = 9\text{cm}$, $r = 70\text{cm}$	94
Fig. 5.4	Time-domain waveform of the received signals. (a) Single-carrier. (b) Three-tone signal with synchronized subcarriers. (c) Three-tone signal with unsynchronized subcarriers .	96
Fig. 5.5	RF-DC efficiency gain G_η of synchronized and unsynchronized three-tone signals	96
Fig. 5.6	4x1 array of active antenna oscillators. (a) Implemented array. (b) Layer scheme of the 4x1 array. [built in CTTC, Spain]	97
Fig. 5.7	Measured mode-locked synchronization phenomena. (a) Two oscillators. (b) Three oscillators. (c) Four oscillators. Subcarrier frequency spacing is initially set to 50 MHz	98
Fig. 5.8	Measured mode-locked multi-tone signal with frequency spacing 75 MHz. (a) Frequency spectrum. (b) Time-domain waveform	99
Fig. 5.9	Measured mode-locked multi-tone signal with frequency spacing 45 MHz. (a) Frequency spectrum. (b) Time-domain waveform	99
Fig. 5.10	Measured single-carrier signal. (a) frequency spectrum (b) time-domain waveform	100
Fig. 5.11	Measurement setup used for the performance evaluation of the rectifier circuit when using the mode-locked active antenna array as transmitting source	101
Fig. 5.12	Measured RF-DC efficiency gain (G_η) versus available input power at the rectifier ...	102
Fig. 6.1	Fig. 6.1 Architecture of an RFID reader plus external multi-sine front-end. Using a proper MS design, the transponder response can be directly forward to the reader receiver. The attenuator in the forward path is used to find the minimum activation power level of the transponder	106
Fig. 6.2	Spectrum of a modulated multi-sine signal. The tone separation in the multi-sine must be higher than the bandwidth of the reader-to-transponder baseband signal in order to avoid spectrum overlapping that prevent the transponder to recover the reader's baseband information	108
Fig. 6.3	(a) Even number of tones scheme. (b) Odd number of tones scheme. Dashed line represents the low-pass filter. In the first case (even MS), a conventional reader is not able to recover the transponder baseband information, while in the second case (odd MS), a common reader is allowed to access and process the transponder response	111
Fig. 6.4	Laboratory setup used to measure tag sensitivity gain	113
Fig. 6.5	RFID reader and multi-sine front-end setup: 1-RFID reader, 2-power splitter, 3-variable attenuator, 4-mixer, 5-signal generator, 6-power amplifier, 7-power splitter, 8-power meter, 9-cable to the transmitting antenna, 10-cable from the receiving antenna, 11-mixer, 12-oscilloscope, 13-spectrum analyzer	113
Fig. 6.6	Baseband signal visualized in the oscilloscope: RFID reader commands followed by tag responses	114
Fig. 6.7	Transmitter configurations. (a) Setup used in the experiments, where a DC component is added to the baseband multi-sine in order to create a central component in the bandpass multi-sine. (b) alternative setup configuration, where a sample of the reader signal is directly transmitted to provide a central component in the multi-sine	116
Fig. 6.8	Modulated 8+1 tones multi-sine signal. (a) Frequency spectrum: the 866.6 MHz RF carrier is modulated by an arbitrary ASK signal at 100 kbps and the resultant signal is then mixed with the baseband multi-sine. In this example the baseband multi-sine is a 4-	

	tone (centred at 5 MHz, with 2 MHz tone separation) plus a DC component externally imposed by a function generator. (b) Normalized time-domain waveform	116
Fig. 6.9	Tone separation effect illustrated in the time-domain. (a) Higher average DC voltage obtained with a lower envelope period (higher tone separation). (b) Lower average DC voltage for higher envelope period. The pulsed signal is the envelope of the high PAPR signal after being rectified , maximum ripple value depends both on tone separation and on the output filter of the RF-DC converter	118
Fig. 7.1	(a) Bank of matched filters. (b) MS matched filter. On the left is the hardware implementation and on the right is the corresponding software version. LPF1 is utilized to remove the RF components and LPF2 is a narrower filter which is part of the matched filter	123
Fig. 7.2	(a) Simplified block diagram of the developed MS SDR RFID Reader platform. The dashed blocks in the digital part are proposed functionalities or CPU allocations that are still to be implemented. (b) Photograph of the developed reader hardware. Main blocks: A – RF/analog part, B – digital signal processing part, C – power amplifier, D – MS DAC, E – MS reconstruction filter. With exception of block B (DSP development board) and block D (DAC evaluation board) all the hardware has been designed from scratch. (c) Multi-polarization antenna concept. (d) The designed multi-polarization antenna with three feeding points and respective RF switch	127
Fig. 7.3	(a) Inventory round after EPC Global Gen2/ISO18000-6C with a single tag reply [14]. (b) Gen2 protocol stack. Dashed blocks in the Tx path are either to be implemented (e.g. the Hilbert transform) or are not implemented in real time; PIE encoding, ASK modulation, interpolation and raised-cosine filtering are applied to the individual Tx binary pulses, which are then stored in the DSP memory to be used in a look-up table approach. The same approach is used for MS signal generation	129
Fig. 7.4	Simplified flowchart of the implemented firmware showing dual-core CPU operation. The EPC protocol handling module (in grey) is detailed in the next figure	130
Fig. 7.5	Flowchart of implemented firmware, EPC protocol handling module (grey block in previous figure)	131
Fig. 7.6	Measurement setup	134
Fig. 7.7	Waveforms in the transmitting path of the MS RFID reader. (a) 4-tone baseband MS plus a DC component at the output of the MS DAC. (b) Pulses of the resulting bandpass MS with 8+1 tones which results from the mixture of the baseband MS and the LO RF carrier. (c) RFID PIE-encoded, ASK-modulated symbols using a CW carrier (black signal) and a MS carrier (blue signal) with the same average power. Notice the higher peaks in the MS case	135
Fig. 7.8	(a) RN16 tag response after down-conversion. (b) Tag baseband on top of the central subcarrier, recovered after a simple low-pass filtering. (c) Amplitude of In-phase tag response as a function of the distance. (d) Tag baseband recovered by using a MS matched filter (Bottom) in a tag position where the information on the central subcarrier is null (Top)	137
Fig. 7.9	(a) Received average power level in a lab environment as a function of distance from the reader, for a CW and a 9-tone MS with same average power. (b) Received PAPR as a function of the distance, when transmitting a 9-tone MS signal. In both cases, a 7 dBi Tx antenna and a dipole Rx antenna were used. A power meter was used in the first case, and an RF oscilloscope was used in the second measurement	138
Fig. 7.10	Screenshot of Termite RS232 application showing several tag readings	139

Fig. 8.1	(a) Sources of self-jamming in a bistatic antenna configuration. (b) Self-jamming sources in a monostatic configuration, c) illustration of external interference, LO jammer and phase noise leakage	145
Fig. 8.2	(a) Monostatic reader front-end incorporating a self-jamming cancellation unit. (b) Vector modulator used to control amplitude and phase of the canceller signal	147
Fig. 8.3	Passive self-jamming cancellation using a coupler terminated with a reflective load ...	148
Fig. 8.4	Measurement setup to evaluate the reflective load method. (a) Block diagram. (b) Lab setup using an impedance load tuner, a bi-directional coupler and an RFID reader	149
Fig. 8.5	Coupler characterization and evaluation of the cancellation method by using a VNA. Coupling (circles): 12 dB @ 860 MHz, Isolation without carrier suppression (triangles): 19 dB @ 860 MHz, and Isolation with carrier suppression (squares): 46 dB @ 860 MHz	149
Fig. 8.6	$S(\alpha_c, \phi_c)$ - theoretical RSSI of the residual signal after self-jamming cancellation depending on the attenuation and phase shift of the canceller signal. In this example, the jamming signal has a 0° phase shift and 20 dB attenuation w.r.t. the sample of the Tx signal used for cancellation	151
Fig. 8.7	Amplitude-phase constellation: the blue points correspond to the coarse search grid and the red ones correspond to the fine search grid. Note: although the same number of points (N) is considered for both control parameters, different values can be used as convenient	153
Fig. 8.8	Adaptive cancellation based on gradient descent algorithm. (a) Direct implementation of gradient descent. (b) Alternative implementation	155
Fig. 8.9	(a) Block diagram of the SDR RFID reader. Notice the use of a non-linear switched HPF. (b) Photography of the implemented hardware where the following blocks are visible: 1 – EPC tag mounted in a stand, 2 – Tx antenna, 3 – Rx antenna, 4 – a computer power supply used to supply the reader, 5 – Baseband receiving PGA including filters, 6 – DSP/MCU development board, 7 –RF part including up-converter and down-converter mixers and amplifiers up, 8 – VCO/PLL/frequency synthesizer	157
Fig. 8.10	Receiver using a simple high-pass filter capacitor to remove DC-offset before LPF and amplification. This simple HPF imposes a transient effect that corrupts the received signal	158
Fig. 8.11	(a) Reader command followed by tag RN16 response. (b) Zoomed tag response. The transient effect imposed by the high-pass filter is visible. The tag data rate used is 320 kbps	158
Fig. 8.12	Tag RN16 response with transient effect (blue) and the respective (negative) moving average (red): a) $w = 31$ samples, b) $w = 101$ samples	159
Fig. 8.13	Corrected signal, centered at DC. Additional low-pass filter should be used to remove noise	159
Fig. 8.14	Down-conversion mixer followed by a non-linear switched high-pass filter, with pre-charged initial condition, followed by low-pass filter, signal conditioning and baseband amplification. The output of the PGA is centered at proper DC level for ADC conversion (1.5V provides optimal ADC dynamic range)	160
Fig. 8.15	Principle of operation of the non-linear filter and respective waveforms	161

Fig. 8.16 (a) Reader command followed by tag RN16 response after passing through the non-linear high-pass filter. (b) Zoom around tag response. Using the two switches, the pulses of the down-converted reader command are also suppressed	161
Fig. 8.17 Received tag response (RN16) sampled at 61.440 MSPS. Captured by the FPGA	162
Fig. 8.18 RN16 signals at the different stages of the FIR filter chain implemented in Matlab. (a) Signal spectrum before FIR filter chain. (b) Signal spectrum after low-pass FIR filter to remove noise and decimator by 20 to reduce sampling rate. (c) Spectrum after high-pass FIR filter to remove DC component. (d) Time-domain signal before low-pass filter (bottom) and after high-pass filter (top). These results were obtained in Matlab while the ones in the next figure were obtained using the FPGA test bed.	162
Fig. 8.19 Filtered RN16 signal without DC component obtained in FPGA. (a) Frequency spectrum, b) Time-domain waveform centered at 0V	163
Fig. 9.1 (a) Diagram of the proposed multi-RFID <i>ReC</i> . (b) alternative passive sensor-alike configuration	168
Fig. 9.2 (a) Port termination composed of a switch-controlled series resonant circuit in parallel with a matched RFID chip. (b) Model of the multi-port microstrip network with $N+1$ ports. Port Z_{in} is the shared antenna port and ports Z_i are the N key ports. (c) Illustration of a 4-key <i>ReC</i> in which chip RFID4 is active and all other are inactive. The active chip is routed to the antenna port	171
Fig. 9.3 Custom calibration standards and DUTs mounted on the SMA fixtures	173
Fig. 9.4 Measured input impedance of the RFID chip. A simple L-matching circuit is used to match the chip to 50Ω	173
Fig. 9.5 Measurements of the stand-alone switch (points A and B), and measurements of the switch-controlled resonant circuit in parallel with the matched RFID chip. When the switch is closed the series circuit resonates at 866.6 MHz imposing an approximate short circuit (point C). When the switch is open the input impedance is approximately equal to the matched chip impedance (point D)	173
Fig. 9.6 (a) Four-port network in which the antenna port (P1) and one of the key ports (P2) are probed using the VSA in order to evaluate return loss and insertion loss performance. (b) Simulations (solid line) and measurement (crosses) of the four-port network	175
Fig. 9.7 (a) Evaluated multi-port network, fabricated in low-cost FR4 substrate in a 50Ω environment. (b) Measured return loss of the antenna port as a function of n (number of the active port). (c) Measured insertion loss between the antenna port and the active port. (d) Measured isolation between the antenna and an inactive port adjacent to the active one. The isolation between the active port and an adjacent inactive port, not shown here, presents similar values	175
Fig. 9.8 (a) Simple dipole antenna fabricated in FR4 substrate and respective return loss at 50Ω . (b) A three-key remote control prototype using a star configuration. (c) A four-key remote control prototype that implement the four basic TV control functions (CH +, CH – , Vol +, Vol –)	176
Fig. 9.9 (a) Diagram of the system using an external RFID-IR adapter to interact with the TV. (b) Demonstration prototype: 1 – RFID reader, 2 – reader antennas, 3 – external RFID-IR interface and universal IR remote control	181
Fig. 9.10 Demo application software that controls the RFID reader. In this case the channel up icon is red indicating that the corresponding key is being pressed in the remote controller .	181
Fig. 9.11 Simplified flowchart of the developed JAVA application software	182

List of Abbreviations

AAR	Association of American railroads
ADC	Analog-to-digital converter
ADS	Agilent's advanced design system
AEI	Automatic equipment identification
API	Application programming interface
ASIC	Application-specific integrated circuit
ASK	Amplitude shift keying
AWG	Arbitrary waveform generator
BLF	Backscatter link frequency
CPU	Central processing unit
CLA	Control law accelerator
CMOS	Complementary metal-oxide-semiconductor
CPL	Coupler
CPLD	Complex Programmable Logic Device
CW	Continuous wave
DAC	Digital-to-analog converter
DC	Direct current
DCR	Direct conversion receiver
DeC	Device to control
DMA	Direct memory access
DSB-ASK	Double side band ASK
DSP	Digital signal processor
DUT	Device under test
EAS	Electronic article surveillance
EEPROM	Electrically erasable programmable read only memory

EH	Energy harvesting
EIRP	Equivalent isotropically radiated power
EM	Electromagnetic
EPC	Electronic product code
FHSS	Frequency-hopping spread spectrum
FIR	Finite impulse response
FOM	Figure of merit
FPGA	Field-programmable gate array
FPU	Floating point unit
HF	High frequency
IFF	Identify friend or foe
IoT	Internet-of-things
IR	Infrared
ISR	Interrupt service routine
kbps	Kilobits per second
LF	Low frequency
MAC	Multiply-accumulate operation
MCU	Microcontroller Unit
MIPS	Millions of instructions per second
MMACS	Million multiply-accumulate operations per second
MPT	Microwave power transmission
MS	Multi-sine
MSPS	Mega-samples per second
PAPR	Peak-to-average power ratio
PGA	Programmable gain amplifier
PIE	Pulse-interval encoding
PLL	Phase-locked loop

PR-ASK	Phase-reversed ASK
PWM	Pulse width modulation
PWS	Passive wireless sensors
PWSN	Passive wireless sensor network
QAM	Quadrature amplitude modulation
RADAR	Radio detection and ranging
RCS	Radar cross section
ReC	Remote control device
RISC	Reduced instruction set computer
RF	Radio-frequency
RF4CE	RF for consumer electronics
RFID	Radio-frequency identification
RMS	Root-mean square
RN16	16 bits random number
RTF	Reader-talks-first
SDR	Software-defined radio
SMPA	Switching mode power amplifier
SNR	Signal-to-noise ratio
SOL	Short, open and thru calibration kit
SPI	Serial peripheral interface
SPNT	Single-pole N-throw
SPS	Solar power satellite
SSB-ASK	Single side band ASK
UHF	Ultra high frequency
UPC	Universal product code
uPP	Universal parallel port
UWB	Ultra-wide band

VCO	Voltage-controlled oscillator
VSA	Vector signal analyzer
VSG	Vector signal generator
WISP	Wireless identification and sensing platform
Word	8 bits
WPC	Wireless power consortium
WPT	Wireless power transfer or wireless power transmission
WSN	Wireless sensor networks
ZC	Zero-cross detection

Table of Contents

Agradecimientos	i
abstract.....	v
List of figures	vii
List of Abbreviations.....	xiii
1. INTRODUCTION.....	1
1.1. Background and motivation	1
1.2. Objectives and methodology	2
1.3. Thesis outline	4
1.4. Original contributions of the thesis.....	7
1.5. List of publications	8
1.5.1. Main publications in conferences and journals	8
1.5.2. Other related publications and communications	9
1.6. History of wireless power transfer and radio-frequency identification	11
1.6.1. Early radio transmission in the 19 th century	11
1.6.2. Transmitting power via radio waves	12
1.6.3. Wireless power and wave backscatter for RF-identification	13
References.....	17
2. FUNDAMENTALS OF RFID SYSTEMS	21
2.1. Introduction to RFID systems.....	21
2.1.1. Basic concepts and definitions	21
2.1.2. Frequency bands, power levels, read ranges and standards	22
2.1.3. EPC-Global Class 1 Generation 2 and ISO18000-6C standards	23
2.1.4. Passive versus active RFID systems.....	23
2.2. Operating principles of passive RFID systems.....	24
2.2.1. Defining near-field and far-field operating regions	25
2.2.2. Near-field inductively-coupled systems	26
2.2.3. Inductively-coupled 1-bit systems	27
2.2.4. 1-bit microwave systems based on non-linear effects	28
2.2.5. Far-field passive-backscatter systems.....	29
2.3. Passive RFID transponders and RFID-enabled sensors	30
2.4. RFID Reader architectures.....	32

2.4.1.	Software Defined Radio-based reader architectures.....	34
2.5.	Backscatter communication in passive RFID	35
2.5.1.	Analysis of the backscatter link	35
2.5.2.	Forward and backscatter power budgets	39
2.5.3.	A power budget example	42
2.5.4.	Remarks.....	42
References.....		45
3.	LITERATURE REVIEW	47
3.1.	Current research topics in passive RFID	47
3.2.	Improving wireless power transfer in passive-backscatter RFID	47
3.2.1.	Beam efficiency improvement	48
3.2.2.	Enhancement of RF-DC conversion efficiency.....	51
3.3.	Closely-related work: waveform design for improved efficiency	56
References.....		57
4.	UNCONVENTIONAL WAVEFORM DESIGN FOR WIRELESS POWER TRANSFER	63
4.1.	Introduction.....	63
4.2.	RF-DC power conversion basics.....	64
4.3.	Typical RF-DC converter topologies	64
4.4.	Rectifying device characterization and modeling	66
4.5.	CW envelope detection	68
4.5.1.	Self-biasing and breakdown effects	69
4.6.	High PAPR signal rectification	70
4.7.	Using multi-sines for wireless power transfer	71
4.7.1.	MS signal definition	71
4.7.2.	Multi-sine rectification	72
4.7.3.	Memoryless model to describe MS RF-DC conversion	73
4.7.4.	Waveform optimization: MS phase arrangement optimization	75
4.8.	Defining a FOM to evaluate the efficiency gain	75
4.9.	Simulations	76
4.10.	Measurements	80
4.11.	Conclusions.....	85
References.....		87
5.	SPATIAL POWER COMBINING OF MULTI-SINE SIGNALS FOR WPT APPLICATIONS	89

5.1.	Introduction	89
5.2.	Spatial power combining: spatially-combined MS signals	90
5.3.	Externally-synchronized spatially-combined MS transmitters	91
5.3.1.	Spatially-combined two-tone signal.....	91
5.3.2.	Spatially-combined three-tone signal	93
5.3.3.	The effect of phase synchronization	94
5.4.	Mode-locked coupled-oscillator arrays.....	95
5.4.1.	Mode-locked multi-sine signal synthesis	97
5.4.2.	Single-carrier signal synthesis	100
5.4.3.	Performance evaluation.....	100
5.5.	Conclusions	102
	References.....	103
6.	JOINT WIRELESS POWER TRANSFER AND BACKSCATTER COMMUNICATION USING MS SIGNALS.....	105
6.1.	Introduction: extending the reading range of commercial RFID readers	105
6.2.	The radio link using multi-sine signals	106
6.1.1.	Multi-sine data downlink	106
6.1.2.	Multi-sine data uplink	108
6.3.	Laboratorial setup and measurements	111
6.1.3.	Measurement setup 1	112
6.1.4.	Measurement setup 2	114
6.4.	Results discussion and conclusions	117
	References.....	119
7.	SOFTWARE-DEFINED RADIO RFID READER DESIGN WITH IMPROVED POWERING WAVEFORMS.....	121
7.1.	Introduction: prior work.....	121
7.2.	Theoretical analysis.....	122
7.3.	The software-defined radio design	125
7.3.1.	SDR RFID hardware implementation.....	125
7.3.2.	A multi-polarization antenna scheme	126
7.3.3.	Gen2 RFID protocol and software implementation	128
7.3.4.	Baseband waveform generation	132
7.3.5.	Self-jamming Cancellation.....	133
7.4.	Measurements	133
7.4.1.	The measurement setup	133

7.4.2.	Measurement of RFID Chip sensitivity improvement	135
7.4.3.	MS demodulation	136
7.4.4.	Field measurements	137
7.4.5.	RFID reader – PC interface	138
7.5.	Conclusions.....	139
References.....		141
8.	SELF-JAMMING IN PASSIVE-BACKSCATTER RFID SYSTEMS.....	143
8.1.	Introduction.....	143
8.2.	Self-jamming and interference in passive RFID.....	144
8.3.	Basic isolation between transmitter and receiver	145
8.4.	RF self-jamming cancellation.....	146
8.4.1.	Classical self-jamming suppression scheme	146
8.4.2.	Passive self-jamming cancellation using reflective loads.....	148
8.4.3.	MS self-jamming suppression	150
8.4.4.	Adaptive self-jamming cancellation	150
8.5.	Baseband DC-offset removal techniques	156
8.5.1.	Experimental hardware	156
8.5.2.	DC-offset elimination and transient issues	156
8.5.3.	Analog DC-offset removal using a non-linear HPF	159
8.5.4.	Software DC-offset removal using a FIR HPF.....	161
8.6.	Conclusions.....	163
References.....		165
9.	A BATTERY-LESS RFID REMOTE CONTROL SYSTEM.....	167
9.1.	Introduction.....	167
9.2.	The proposed system	168
9.2.1.	A multi-port switched network	168
9.3.	Simulation and measurement results	172
9.3.1.	RFID chip and switch characterization and matching	172
9.3.2.	Multi-port simulation and measurement.....	174
9.3.3.	Reading range measurements.....	177
9.4.	Battery-free demonstration prototype	179
9.5.	Conclusions.....	180
References.....		183

10.	CONCLUSIONS	185
10.1.	Concluding remarks.....	186
10.2.	Main achievements in the scope of this thesis	186
10.3.	Future work	187
APPENDIX A – DERIVATION OF AN AC-DC TRANSFER FUNCTION FOR RECTIFIER CIRCUITS UNDER HIGH PAPR SIGNALS		189
A.	RF-DC model derivation	190
B.	Preliminary model validation	193
C.	Output DC voltage, RF-DC efficiency and efficiency gain.....	195
D.	Conclusions and future improvements.....	197
APPENDIX B – PHYSICAL LAYER ASPECTS OF THE EPC GEN2 PROTOCOL.....		199
APPENDIX C –ALTERNATIVE CONFIGURATIONS FOR THE BATTERY-LESS REMOTE CONTROL		201

1. INTRODUCTION

1.1. Background and motivation

The third internet generation or the Internet of Things (IoT) is rapidly moving beyond the traditionally-connected devices (e.g. personal computers, tablets or smartphones) to the quotidian objects. The future internet grid is expected to link computers/phones/people, household appliances, buildings, industrial plants, transportation, clothing, wearables, groceries and many other quotidian things. More than 50 Billions of connected objects are expected worldwide by 2020 [1][2], and eventually, beyond a trillion in a not so distant future [3]. The ideal IoT vision is to ubiquitously provide connectivity to everything, anywhere, anytime. Thus, in addition to the conventional power-consuming and high-complexity wireless technologies devoted to bandwidth-demanding applications [4-6], low profile technologies featuring low-power consumption, ideally battery-free, low-cost and low complexity, are imperative to allow ubiquitous applications. Moreover, as billions of IoT devices are expected to be deployed across the planet or even into space, the (frequent) replacement of batteries is not a viable option. Therefore, low power wireless sensors, passive-backscatter radios such as passive RFIDs, RFID-enabled sensors and passive wireless sensors [7-11] are seen as key-enabling technologies to realize the future ubiquitous IoT. The latter make use of Wireless Power Transfer (WPT) and energy harvesting technologies to operate in a battery-free manner.

The theoretical analysis of radio path shows that, unlike conventional wireless communication systems, which are mainly limited by noise and receiver sensitivity, passive-backscatter systems are primarily limited by the forward power link, i.e. the energy transfer from the reader or interrogator device to the transponder [12][13]. A closer look reveals that this limitation lies on the reduced RF-DC conversion efficiency of existing RF power harvesting circuits at low power level regime. Because Schottky diode and CMOS devices commonly used in rectifier circuits exhibit a non-zero turn-on voltage, the RF-DC conversion efficiency at low input power levels is limited [14-16]. Therefore, improving the overall energy transfer efficiency is crucial to achieve longer coverage range and expand the computation capabilities of wirelessly-powered devices.

Traditionally, WPT efficiency has been maximized through circuit and system level design optimization, and a variety of approaches to enhance the overall WPT efficiency and extend the coverage distance have been attempted, including the use of threshold-compensated CMOS rectifiers [17][18], custom-built schottky diodes, harmonically-terminated rectennas [19], antenna beamforming [20] and auxiliary transmitters [21]. As opposed to the majority of conventional approaches, which focus exclusively on circuit optimizations, this thesis addresses waveform design optimization as an alternative to improve WPT efficiency. By using properly formatted high

Peak-to-Average Power Ratio (PAPR) waveforms such as in-phase Multi-Sine (MS) signals, the RF-DC conversion efficiency of existing rectifier circuits can be improved in comparison to traditional Continuous Wave (CW) signals. This is owed to the higher peak voltage swings that allow to efficiently overcome the turn-on voltage of rectifying devices at low average power levels. Although another research group had already looked to a similar approach [60][61], our findings were done independently when our group was focused on the study [22][23] and modeling [I-III] of diode power probes for RF and microwave measurements. During that study it was found that, at certain output load conditions, a CW-calibrated diode power probe can provide erroneous power measurement values when measuring wideband and high PAPR signals. For instance, a two-tone signal can provide a rectified DC output different than that obtained with a CW signal with the same average power, which gives a wrong indication of average power if the probe is calibrated with a CW signal. Because at that time we were also focused on WPT, the following questions were formulated: 1) “*Can the same effect that leads to errors in power probe measurements of high PAPR signals be used to boost the efficiency of similar RF-DC converter circuits used in WPT?*”; 2) “*How can we efficiently generate and transmit such high PAPR waveforms?*”; and 3) “*Can properly designed waveforms improve the coverage range of passive-backscatter systems such as passive RFID?*”. This thesis sought an answer to the first question by evaluating the efficiency of rectifying circuits under high PAPR MS signals. Afterward, efficient transmitter schemes were proposed to address the second challenge. Finally, the concept was applied to passive-backscatter radios, both through the integration of MS signals in commercial RFID readers and through the design of Software-Defined Radio (SDR) RFID readers with waveform design capability.

1.2. Objectives and methodology

The central objective of this thesis is the evaluation of waveform design optimization as an alternative to circuit optimization to maximize the efficiency of rectifying circuits and consequently enhance the coverage range of passive-backscatter systems such as passive RFID. For this purpose, non-CW signals featuring high PAPR such as in-phase MS signals will be tested. First, cabled experiments will be conducted, where a Vector Signal Generator (VSG) will directly feed the rectifying circuits with a CW and several MS signals, and the RF-DC conversion efficiency will be evaluated. Rectifying circuits under test include single diode detector and charge pump circuits both based on discrete Si-Schottky devices. As these circuits behave in a similar way as diode-connected CMOS rectifiers typically used in passive RFID transponders, the cabled measurements will first assess the potential of this approach to increase the communication range of passive transponders. In order to optimize the MS waveforms, the frequencies, amplitudes and phases of the individual subcarriers must be properly selected. Additionally, the MS bandwidth should fit the

rectifier input bandwidth, and the frequency separation of the MS subcarriers should match to the output filter of the rectifier circuits.

Having completed the cabled measurements, field experiments will be performed to validate the proposed approach in multipath faded wireless channels. A study of joint WPT and backscatter data communication and an evaluation of the reading range improvements using MS signals will be conducted. First, the MS scheme will be integrated in a commercial RFID reader, and then a MS-capable RFID reader based on software-defined radio will be constructed. The latter approach gives the possibility of creating software-defined waveforms to satisfy the initial waveform design goal. From the view-point of the WPT receiver, high PAPR is a desired feature, however, it challenges the power amplification stage of the transmitter. Thus, the evaluation of enhanced transmitting architectures to efficiently deliver high PAPR waveforms is also an important goal.

Other not less important objectives, which somehow complement the previous ones, include non-linear analysis, characterization and modelling of RF-DC converter circuits, evaluation of self-jamming in passive-backscatter systems and design of prototypes and demonstrators. 1) Non-linear analysis, characterization and modelling are essential to understand and predict the behaviour of rectifying circuits and to assist in waveform design optimization; 2) Since self-jamming is an important limiting factor (actually the second most limiting one) in passive-backscatter systems, both CW and MS self-jamming cancellation will deserve attention in this thesis; 3) The thesis aims also at the design of prototypes and demonstrators including RF-DC converter circuits for the previously described cabled experiments, hardware for the SDR RFID readers, and complete battery-free prototypes capable of demonstrating real application of passive RFID and WPT concepts.

The objectives of this thesis can be summarized as follows:

- Waveform design optimization for improved RF-DC conversion efficiency.
- Evaluation of rectifying circuits under optimal MS signals.
- Proposal and demonstration of improved architectures for high PAPR transmission.
- Evaluation of joint WPT and backscatter data communication using MS signals.
- Integration of MS schemes into existing backscatter radio systems.
- Design of SDR RFID Readers with waveform design capabilities.
- Evaluation of self-jamming and DC-offset generation in DCR receivers
- Non-linear analysis, characterization and modeling of RF-DC converter circuits.
- Design of prototypes and demonstrators.

1.3. Thesis outline

Chapter 1 first presents the motivations, objectives and original contributions of this work. Afterward, a history overview of WPT and RFID is presented, showing the common roots of these technologies, highlighting the main events and contributors to their evolution and showing how they are intimately related, namely concerning the role of WPT as the enabler of passive-backscatter RFID.

Chapter 2 introduces basic definitions, concepts and operating principles of near-field and far-field RFID systems and presents the fundamentals of passive-backscatter RFID. An analysis of the backscatter communication link is conducted to support later design. In order to evaluate which of the forward or reverse link imposes the most stringent limitation in passive-backscatter systems, a power budget analysis is performed. This chapter also introduces advanced concepts such as RFID-enabled sensors and software-defined radio-based RFID readers. The latter concept is applied in chapter 7.

Chapter 3 starts by listing the main research topics of current RFID technology. Then, RFID-related literature and state-of-the-art industry implementations are reviewed with focus on strategies that use WPT efficiency optimization to maximize the coverage range and improve the performance of passive systems. The first part of this chapter covers system and circuit approaches, while the second part addresses approaches closely related to the work presented in this thesis, namely involving waveform design.

Chapter 4 evaluates waveform design optimization for efficient WPT. It is demonstrated through theoretical analysis, simulations and measurements that properly-designed high PAPR MS signals are capable of enhancing the RF-DC conversion efficiency of rectifying circuits, especially at low power levels. Such circuits including envelope detectors and charge pumps are tested under several MS signals and a figure of merit is introduced to evaluate the efficiency gains relative to CW signals. This chapter also suggests optimal conditions for maximum gains.

Chapter 5 proposes architectures to efficiently deliver high PAPR MS signals by using spatial power combining, where the individual tones are generated, amplified and radiated separately, and the MS signal is passively combined in free space. Hence, the problem of amplifying large PAPR signals is overcome. Two different architectures are unveiled, one of them using an external reference signal to phase-lock several frequency synthesizers and another one based on mode-locked oscillator arrays that avoid the use of an external phase reference.

Chapter 6 evaluates joint WPT and backscatter communication through MS signals and reports on the integration of a MS scheme in a commercial RFID reader. 1) a description is provided for downlink and uplink using MS signals; 2) guidelines are presented for the MS design including subcarrier separation, MS bandwidth and central subcarrier positioning; 3) by following these guidelines, the reading range can be improved and a traditional reader receiver architecture is still able to demodulate/decode the backscattered MS signal without requiring any change.

Chapter 7 reports on the design of a SDR-based RFID reader with MS capability. The chapter discusses aspects of hardware, software, EPC Gen2 protocol implementation and MS generation. In order to show the effectiveness of the MS reader in enhancing the operation of the transponders, the sensitivity of a commercial transponder is measured using several software-defined waveforms. The chapter ends with a performance assessment of MS signals in multipath faded channels.

Chapter 8 addresses the second limiting factor of passive RFID systems, namely RF self-jamming and the consequent generation of DC-offsets. Several approaches to deal with these issues are evaluated and new proposals are presented namely a method for transient correction in software and an improved non-linear HPF to simultaneously cancel the DC-offset and the transient effect. Self-jamming suppression of MS signals is also investigated. The study in this chapter is accompanied by lab experiments and measurements conducted on two SDR reader platforms based on DSP and FPGA.

Chapter 9 describes the implementation of a battery-less remote control system. First, the design and measurements of the remote control unit (*ReC*) are presented. An off-the-shelf reader is used to assemble an RFID-to-infrared interface which is then incorporated in a commercial TV device to form a complete demonstration prototype. This allows a four-key *ReC* prototype to control four basic functionalities of the TV (CH+, CH-, VOL+, VOL-).

Chapter 10 presents the final conclusions, the main accomplishments of this thesis, the proposals for future work and the list of publications.

Appendix A derives an AC-DC transfer function for envelope detectors under high PAPR signals.

Appendix B presents some aspects of the Gen2/ISO18000-6C protocol used in chapters 6-9.

Appendix C showcases alternative configurations for the battery-less remote control unit.

1.4. Original contributions of the thesis

The original contributions of this thesis are:

- First assessment of the behavior of rectifying circuits under high PAPR MS signals. This triggered the interest of some groups in the wireless power transfer community to look to alternative waveforms (other than CW) for energy transfer.
- Transmitting architectures based on space power combining for efficient generation and radiation of high PAPR MS signals.
- Survey on the use of unconventional waveforms for wireless power transfer.
- Evaluation of joint wireless power transfer and backscattering through non-CW signals (e.g. MS signals)
- Reading range extension of commercial UHF RFID readers by using a MS front-end, and guidelines to design a MS waveform that allows a conventional RFID receiver to demodulate a backscattered MS signal without requiring any change in the receiving path.
- First design from scratch of a software-defined radio RFID reader with arbitrary waveform design capability (e.g. MS waveforms). Given its flexibility, this platform is also a powerful tool for RFID measurement, characterization and research.
- Development of a battery-less remote control system and its integration in a commercial TV device to provide a functional demonstration prototype. This system proved to be a very effective didactic tool to demonstrate wireless power transfer and battery-less concepts to the general public through social media.
- An X-parameter RF-DC model for energy harvesting circuits. Useful to encapsulate circuit behavior, which can be gathered directly from measurements, and also useful to protect intellectual properties.

1.5. List of publications

1.5.1. Main publications in conferences and journals

- [I] Boaventura, A.J.S. and Nuno Borges Carvalho, "*Using X-parameters to Model RFID Energy Harvesting Circuits*", European Conference on Antennas and Propagation, EuCap 2011, Rome April 2011.
- [II] Boaventura, A.J.S., Alerandro R. Testera, Nuno Borges Carvalho and Mónica F. Barciela, "*Using X-parameters to Model Diode-based RF Power Probes*", IEEE International Microwave Symposium, Baltimore, June 2011.
- [III] A. Rodriguez-Testera, O. Mojón, Boaventura, A.J.S., M. Fernandez-Barciela, N. Borges Carvalho, M. Vanden Bossche and G. Pailloncy, "*Diode power detector X-parameter model extraction using an LSNA-based measurement system*", IET Electronics Letters, vol. 49, pp. 196-8, January 2013.
- [IV] Boaventura, A.J.S. and Nuno Borges Carvalho "*Maximizing DC Power in Energy Harvesting Circuits Using Multisine Excitation*", IMS2011 - International Microwave Symposium, June, 2011, Baltimore, USA.
- [V] Boaventura, A.J.S.; Belo, D.; Fernandes, R.; Collado, A.; Georgiadis, A.; Borges Carvalho, N., "*Boosting the Efficiency: Unconventional Waveform Design for Efficient Wireless Power Transfer*," in Microwave Magazine, IEEE , vol.16, no.3, pp.87-96, April 2015.
- [VI] Boaventura, A.J.S.; Collado, A.; Georgiadis, A.; Borges Carvalho, N., "*Spatial Power Combining of Multi-Sine Signals for Wireless Power Transmission Applications*," in Microwave Theory and Techniques, IEEE Transactions on , vol.62, no.4, pp.1022-1030, April 2014.
- [VII] Boaventura, A.J.S., Carvalho, Nuno Borges, Georgiadis Apostolos, "*The impact of multi-sine tone separation on RF-DC efficiency*," in Microwave Conference (APMC), 2014 Asia-Pacific , vol., no., pp.606-609, 4-7 Nov. 2014.
- [VIII] Boaventura, A.J.S., N.B. Carvalho, "*Spatially-Combined Multisine Transmitter for Wireless Power Transmission*", IEEE Wireless Power Transmission Conference 2013, Perugia, Italy, May 201.
- [IX] Boaventura, A.J.S.; Carvalho, N.B., "*Enhanced front-end to extend reading range of commercial RFID readers using efficient multisine signals*," in Microwave Symposium Digest (MTT), 2012 IEEE MTT-S International , vol., no., pp.1-3, 17-22 June 2012.
- [X] Boaventura, A.J.S.; Carvalho, N.B., "*Extending Reading Range of Commercial RFID Readers*," in Microwave Theory and Techniques, IEEE Transactions on , vol.61, no.1, pp.633-640, Jan. 2013.
- [XI] Boaventura, A.J.S.; Borges Carvalho, N.B., "*Evaluation of simultaneous wireless power transfer and backscattering data communication through multisine signals*," in Wireless Power Transfer Conference (WPTC), 2015 IEEE , vol., no., pp.1-3, 13-15 May 2015.
- [XII] Boaventura, A.J.S., and N.B. Carvalho "*A Software-Defined Radio RFID Reader with Multi-sine Capability for Improved Wireless Power Transfer*", Submitted for publication in IEEE Transactions On Microwave Theory and Techniques.
- [XIII] Boaventura, A.S.; Borges Carvalho, N., "*Investigation on self-jamming suppression in passive RFID when using multisines to enhance wireless power transfer*," in Wireless Power Transfer Conference (WPTC), 2015 IEEE , vol., no., pp.1-3, 13-15 May 2015.
- [XIV] Boaventura, A.J.S., João Santos, Arnaldo Oliveira, Nuno Borges Carvalho, "*Highly Isolated: Dealing with Self-jamming in Passive RFID Systems*", Accepted for publication in IEEE Microwave Magazine.
- [XV] Boaventura, A.J.S., Carvalho, N.B., "*A Batteryless RFID Remote Control System*", in Microwave Theory and Techniques, IEEE Transactions on , vol.61, no.7, pp.2727-2736, July 2013.
- [XVI] Boaventura, A.J.S.; Borges Carvalho, N., "*A battery-less remote control based on a novel multi-RFID scheme*," in Microwave Conference (EuMC), 2013 European , vol., no., pp.995-998, Oct. 2013.
- [XVII] Boaventura, A.J.S.; Borges Carvalho, N., "*Feasibility of a battery-less wirelessly-powered RFID remote control system*," in Wireless Power Transfer (WPT), 2013 IEEE , vol., no., pp.139-142, 15-16 May 2013
- [XVIII] Boaventura, A.J.S., Gonçalves R., Belo D. and Borges Carvalho N. "*A Software-Defined Radio RFID Reader Design with Improved Wireless Power Transfer Capabilities*", Submitted for presentation in Wireless Power Transfer Conference 2016, Aveiro, Portugal.

1.5.2. Other related publications and communications

Patent:

- [XIX] PT-106920-2013 "SISTEMA DE CONTROLO REMOTO SEM PILHAS (Battery-less Remote Control System)", Alirio Boaventura and Nuno Borges Carvalho, UNIVERSIDADE DE AVEIRO e INSTITUTO DE TELECOMUNICAÇÕES.

Book chapter:

- [XX] In the Book: "Green RFID Systems" edited by Luca Roselli, published by Cambridge University Press, Chapter: "*Unconventional RFID Systems*" by Alírio Soares Boaventura, Ricardo Dias Fernandes, João Nuno Matos and Nuno Borges Carvalho.

Publications:

- [XXI] N. B. Carvalho, Boaventura, A.J.S, et al "*Wireless Power Transmission: R&D Activities within Europe*", Trans. Microwave Theory and Techniques, Trans. Microwave Theory and Techniques, p.p.: 1031 - 1045, Vol. 62, Issue 4, April 2014.
- [XXII] Boaventura, A.J.S, Ana Collado, Nuno Borges Carvalho, and Apostolos Georgiadis, "*Optimum Behavior: Wireless power transmission system design through behavioral models and efficient synthesis techniques*", IEEE Microwave Magazine, Vol. 14, Issue 2, p.p.: 26-35, March 2013.
- [XXIII] Boaventura, A.J.S and Nuno Borges Carvalho, "*Low Power Wakeup Radios for Application in Indoor Location-Systems*", International Journal of Wireless Information Networks: Volume 20, Issue 1 (2013), p.p. 67-73
- [XXIV] Diogo Ribeiro, Boaventura, A.J.S, Pedro Cruz and Nuno Borges Carvalho, "*Mixed-signal and Mixed-domain Instrumentation for Emerging Technology Device Characterization*" to be presented in 8^o Congresso do Comité Português da URSI, Lisboa, Portugal, Nov. 2014.
- [XXV] Luis Filipe Ribeiro Dias, Boaventura, A.J.S and Nuno Borges de Carvalho, "*RF-DC Converter Efficiency Optimization Using Source-Pull Techniques*", International Workshop on Integrated Nonlinear Microwave and Millimetre-wave Circuits (INMMiC), Leuven, April 2014.
- [XXVI] Boaventura, A.J.S, and Nuno Borges Carvalho, "*A Measurement Strategy for Test and Characterization of UHF RFID Systems*", 79th ARFTG Conference, Montréal, Canada, June 2012
- [XXVII] Boaventura, A.J.S, and Nuno Borges Carvalho, "*A Proposal for Dynamic Power Control in RFID and Passive Sensor Systems Based on RSSI*", EuCAP2012 - European Conference on Antennas and Propagation 2012, Prague, Czech Republic, March 2012
- [XXVIII] Boaventura, A.J.S, and Nuno Borges Carvalho, "*Power Measurement of Modern Wireless Signals: The Impact of PAPR in Diode Power Measurements*", URSI Cong., Lisboa, Portugal, Nov. 2011
- [XXIX] Boaventura, A.J.S, and Nuno Borges Carvalho, "*Efficient Excitation Signals for Microwave Power Transmission: From theory to system integration in commercial RFID readers*", 5^o Congresso do Comité Português da URSI, Lisboa, Portugal, Nov. 2011.
- [XXX] Ricardo Dias Fernandes, Boaventura, A.J.S, Nuno Borges Carvalho, João N. Matos "*Increasing the Range of Wireless Passive Sensor Nodes using Multisines*", IEEE International Conference on RFID Technology and Applications (RFID-TA 2011), Spain, September 2011.

Workshops:

- [XXXI] Boaventura, A.J.S, "*Energy Without Wires and Battery-less Systems: Battery-less Remote Controls*", The Science and Technology Week at University of Aveiro, Nov. 2012.
- [XXXII] Boaventura, A.J.S, Ana Collado, Apostolos Georgiadis and Nuno B. Carvalho, "*Improving Wireless Power Transmission Efficiency Using Signal Optimization*", European Microwave Conference, Nuremberg, Germany, Oct. 2013.
- [XXXIII] Boaventura, A.J.S, "*Supporting Technologies for Ubiquitous Internet-of-Things*", Departamento de Ciência e Tecnologia - University of Cape Verde, Praia – Cape Verde, Oct. 2014.
- [XXXIV] Boaventura, A.J.S, "*Wireless Power Transfer*", Departamento de Ciência e Tecnologia - University of Cape Verde, Praia – Cape Verde, Oct. 2014.

- [XXXV] Boaventura, A.J.S, "*WPT: theory and applications*", Departamento de Engenharias e Ciências do Mar - University of Cape Verde, Mindelo Cape Verde, Oct. 2014.
- [XXXVI] N. Carvalho, Boaventura, A.J.S, D. Belo, "*Special Designed Waveforms for Wireless Power Transmission*", IMS 2015, USA
- [XXXVII] N. Carvalho, Boaventura, A.J.S, H. Gomes, "*The use of Non-linear Generation for Passive RFID Tag design*", IMS2015, USA.
- [XXXVIII] Nuno Borges Carvalho, Boaventura, A.J.S, Ana Collado, Apostolos Georgiadis, "*Specially Designed Waveforms for Wireless Power Transmission Improvement*", RFIC 2014, Tampa Bay, June 2014.
- [XXXIX] N. Pan, Boaventura, A.J.S, D. Schreurs, N. Carvalho, "Optimal Multi-sine Signal Selection for Rectifiers: Amplitude and frequency analysis of the efficiency of multi-sine based wireless power transfer", 4th Meeting and Workshop, COST -WIPE, March 2015.

1.6. History of wireless power transfer and radio-frequency identification

1.6.1. Early radio transmission in the 19th century

As we know it today, wireless technology is the result of many contributions in electricity and electromagnetism (EM) fields. Modern electromagnetism started with Michael Faraday (1791-1867), a self-educated British scientist, who discovered, in 1831, that the movement of a magnet in the vicinity of a conductor circuit generates an electric current in the circuit, establishing the law of electromagnetic induction [24]. Later, Faraday envisaged the existence of lines of force around electric charges and magnetic poles and he predicted the existence of EM waves [25]. Faraday was, however, unable to theoretically demonstrate the existence of such electromagnetic waves to the scientific community. A couple of decades later (in 1864), James Clerk Maxwell (1831–1879), a Scottish physicist who believed in Faraday's ideas, provided a mathematical support for the Faraday's hypothesis on the existence of EM waves. In the volume entitled "*A Dynamical Theory of the Electromagnetic Field*", Maxwell not only summarized the concepts of electricity known at that time, but also considerably extended the theory, converging the electrical, magnetic and optic concepts [26]. According to Maxwell's theory, EM waves are of the same nature as light, having the same characteristics as propagation speed, polarization, reflection and refraction, and the light itself is an electromagnetic phenomenon.

After a contest of the Academy of Science in Berlin to experimentally validate some aspects of the Faraday-Maxwell theory, Heinrich Hertz (1857-1894), the first scientist to successfully generate, transmit and receive EM waves [25], provided the ultimate proof of the existence of EM waves and their similarities with light. Hertz's experimental setup consisted of a tuned spark gap transmitter and a tuned spark gap receiver [27]. The transmitting oscillator was formed of an induction coil, a Leyden jar (used as a "condenser" or capacitor), and several accumulators (batteries). Oscillations were achieved by discharging an electric "condenser" through an air gap, which produced a spark over the air gap and originated an oscillatory phenomenon. The oscillatory wave was then radiated using metal plates and detected some meters away from the transmitter by another coil with a spark air gap, in which small sparks were induced whenever the transmitter circuit was operated. The very small sparks at the receiver were visually detected in a dark room. Hertz also used metal reflectors in parabolic shape as mirrors to focus the electromagnetic beam. Despite his great findings, as a pure scientist, Hertz did not get interested for practical applications of EM waves.

The first reportedly experiments with EM waves were conducted by Nikola Tesla (1856-1943) in the United States in 1889 [25], who dedicated to the transmission of energy wirelessly [28][29]. At the same time, Guglielmo Marconi (1874-1937) invented radio/wireless telegraphy and was able to make it a commercial success (Fig.1.1).

1.6.2. Transmitting power via radio waves

Nikola Tesla was the first to experiment with EM waves for the transference of energy wirelessly in the late 1800's and early 1900's [30][31]. Among other experiments, Tesla demonstrated wireless lamps at the World Columbian Exposition in Chicago in 1893, by illuminating lamps without using wires for powering [32]. Tesla also worked on high frequency and high voltage transformers and started the construction of a radiation station (the Wardenclyffe tower) intended for wireless transfer of electricity [25]. However, his large scale experiments for electricity transportation failed mainly due to very high power requirements, inappropriate (low) frequency band, power diffusion, limitations on the radiating structures and low power densities [33]. After that, Tesla projects on wireless electricity were stopped, the Wardenclyffe tower was demolished some years later, and WPT activities were interrupted for several decades. However, Tesla's pioneer work in WPT and many other fields [34] fostered many of the great technological advances of the twenty century.

Benefiting from the technological advances occurred during the second world war, namely on high power devices (e.g. magnetron microwave tubes), WPT experiments were successfully resumed in the 1960's, mainly with the work of William C. Brown. He first proposed the use of microwaves to transfer energy – Microwave Power Transmission (MPT) [30][35]. Brown introduced the concept of rectifying antenna, the rectenna, for receiving and rectifying microwaves [35], and also carried out many experiments at 2.45 GHz band [31]. In 1964, he demonstrated the concept of MPT by powering a subscale helicopter from ground using a microwave beam at 2.45 GHz [36]. Several academic and research activities followed Brown experiments on MPT. The concept of Solar Power Satellite (SPS) systems was proposed in 1968 to efficiently explore out-of-space solar energy by harvesting solar energy outside the Earth's atmosphere and sending it to the Earth through microwave beams [37-39]. The SPS studies and experiments greatly helped to advance the MPT technology even further. In 1987, the world's first fuel free airplane powered from ground by microwaves was reported in Canada [40]; in 2004, Japan proposed the wireless charging of electric motor vehicles by using MPT; in 2007, high power WPT through inductive resonant coupling was demonstrated by MIT researchers who wirelessly powered a 60W light bulb with 40% efficiency at 2m [41]; one year later Intel reproduced the same experiment with an increased efficiency of 75% [42]. With the growth of the consumer electronics, portable devices and wireless communications markets, WPT has become attractive also for the industry. In 2008, several large companies created the Wireless Power Consortium (WPC), dedicated to inductive WPT [43]. WPC later introduced Qi [44], one of the first inductive WPT standards. Several companies employed WPT in portable applications, and new companies devoted to WPT emerged (e.g. sCoupled, WiPower, Powermat, Powercast, WiTricity, EVWireless, Momentum Dynamics [45-48]).

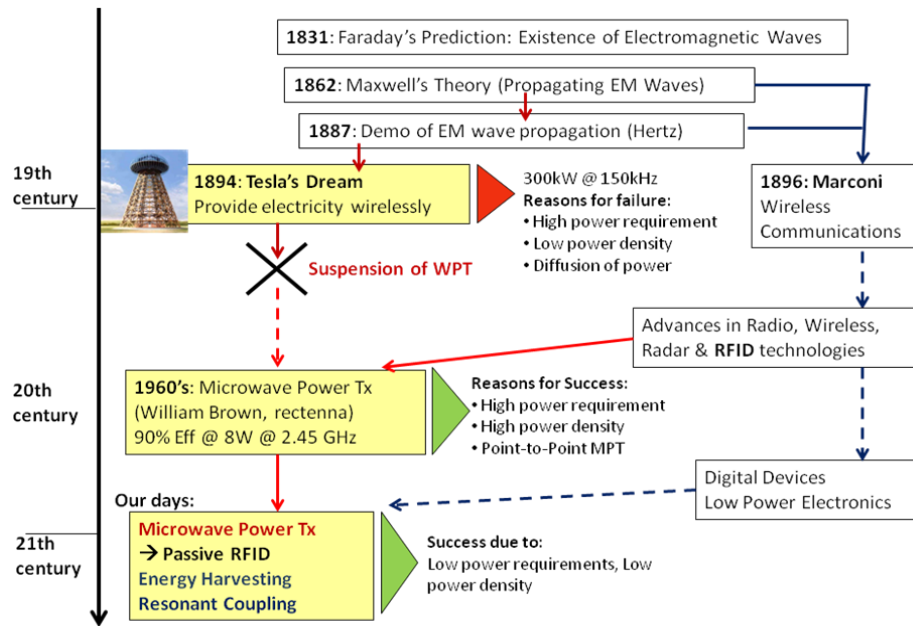


Fig. 1.1 The history of radio transmission and wireless power transfer (recreated from [33])

1.6.3. Wireless power and wave backscatter for RF-identification

One of the first use of radio waves for remote sensing is attributed John L. Baird, who received one of the earliest patents on radio object detection in 1926 [50]. Baird's system remotely illuminated an object with a directional beam of radio waves and the reflected signals were captured and processed to obtain a picture of the scanned object. In 1935, Robert Watson-Whatt developed the first practical RADAR (Radio Detection and Ranging) system, which played a decisive role in the second world war [51]. By sending pulses of radio waves and by measuring the reflected signals, the system was able to detect the presence of distant objects such as aircrafts and ships. However, the first radar system had an important limitation as it was unable to distinguish the aircrafts. One of the first methods of true identification by means of radio frequency is the IFF (Identify Friend or Foe) system, also developed during the second world war. As opposed to the first radar systems, the IFF system was able to distinguish between allied and enemy by providing allied aircrafts with a transponder or responder system which replied to the ground interrogation station with a "friend" identification.

During the cold war, a very advanced modulated-backscatter device was used by the Soviet Union to spy on the US embassy in Moscow. In 1945, Soviet scout children presented to the US ambassador a wooden replica of the Great Seal of the United States with a hidden listening device engineered by Leon Theremin [52], which was composed of a monopole antenna attached to a resonant cavity with a sound-sensitive membrane (see Fig.1.2). The membrane deformations due to sound waves caused the cavity resonant frequency and antenna load to change. Hence, when

illuminated from outside with an RF CW signal the antenna re-transmitted a version of this signal modulated by the voice sound from the ambassador's office. This very elaborated backscattering system was well in advance compared to the first counter-theft 1-bit EAS RFID systems developed later in the 1960's, or even some N-bit transponder systems developed in the next decade.

In the paper entitled "*Communications by means of Reflected Power*" published in 1948 [53], Henry Stockman theorized on the use of radio, light and sound wave reflections for passive transference of information. This theory is essentially the same used in modern backscatter RFID systems.

Since very early, attention was given to the battery handicaps in mobile devices, namely the increased size and weight, need for periodical replacement and maintenance expenses. Thus, efforts were also put on the development of battery-free devices. In 1960, Donald B. Harris proposed a battery-free backscattering system for voice communication [54]. This was one of the first attempts to combine WPT and backscattering, which contributed to the conception of modern passive RFID. In the 1960's the RFID technology advanced significantly and RFID was first considered as a commercial solution. The first large scale commercial use of the RFID concept took place in this decade with 1-bit Electronic Article Surveillance (EAS) systems used for counter-theft [55]. In 1966, the first RFID companies were born, namely Sensormatic and Checkpoint.

In 1973, Mario W. Cardullo received the first patent on RFID [56]. Cardullo's system (Fig.1.3) referred to a passive RFID transponder with rewritable memory, logic circuitry and processing capability, which was initially thought for car electronic toll collection systems. For the first time, RFID transponders were proposed as data carriers that could be remotely accessed by an interrogator or reader. Following this, several other patents in similar RFID concepts were conceded and the technology was on the path to industry adoption.

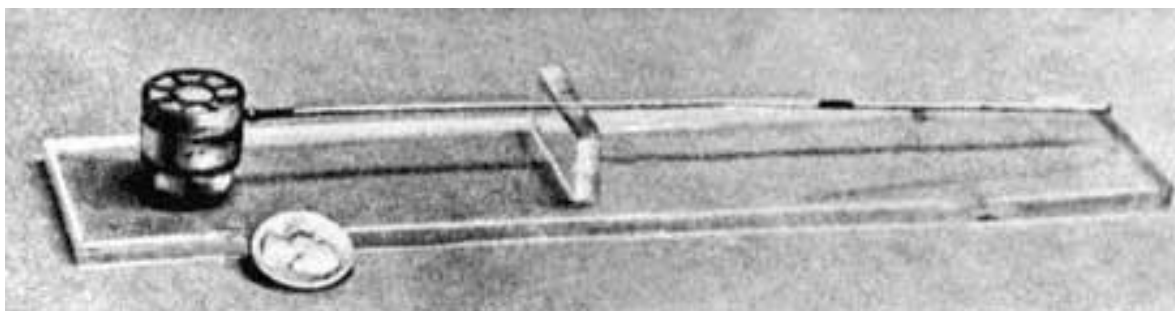


Fig. 1.2 The listening device inside the *Great Seal Bug* – a very sophisticated passive-backscattering system developed by Soviets during the cold war for espionage [source: Wikimedia Foundation]

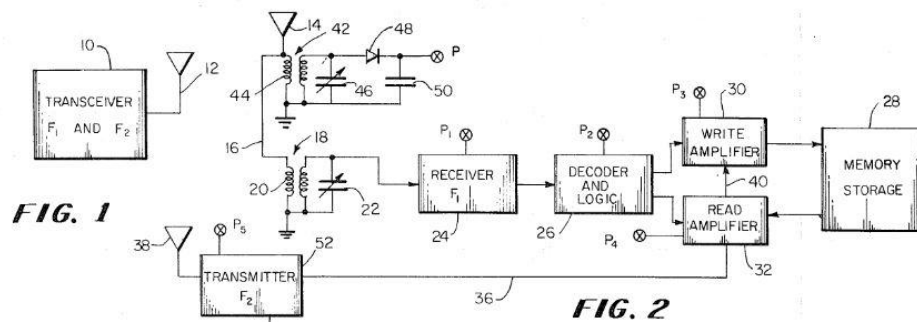


Fig. 1.3 First patented passive RFID transponder with readable and rewritable memory [56]

The 1990's was a period of affirmation of the RFID tag concept, mainly driven by the large scale deployment of toll collection systems in several countries. Although the first RFID implementations were based on proprietary infrastructures, during this decade there was a great effort on standardization in order to provide interoperability. One of the first standards to emerge was the Automatic Equipment Identification (AEI) in 1991, approved by the Association of American Railroads (AAR) to substitute a previous (unsuccessful) optical barcode identification system [57]. In the following years, AAS mandated the adoption of RFID tags under AEI standard to identify and track railcars. In 1999, the MIT Audio-ID center, a consortium of several global consumer products manufacturers, was founded to develop the EPC (Electronic Product Code), a global RFID-based identification system intended to replace bar codes. The first version of EPC was released by 2003. Several versions of the EPC standard followed the 2003 version, and by today, most of the deployed passive RFID systems in the UHF band are under the EPC Class 1 Generation 2 specification [58]. Figure 1.4 summarizes the main milestones in the evolution of RFID technology.

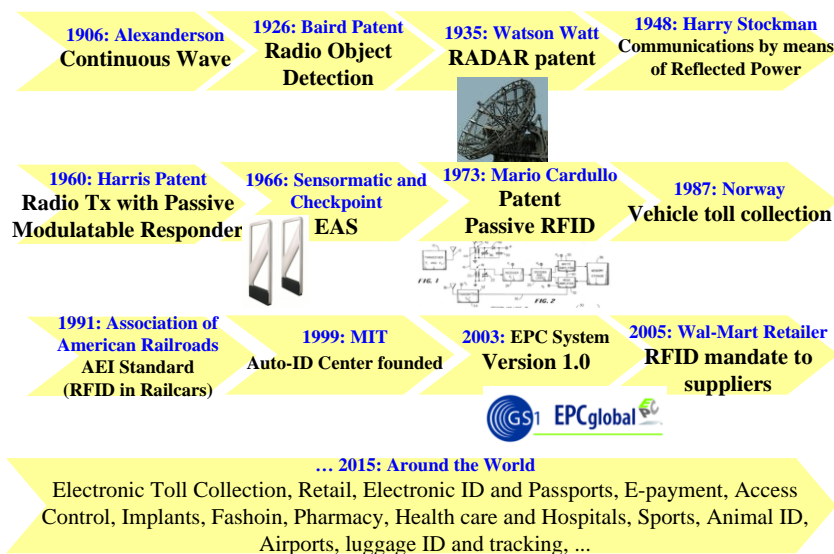


Fig. 1.4 RFID technology milestones

References

- [1] Hao Yue et al “DataClouds: Enabling Community-Based Data-Centric Services Over the Internet of Things”, IEEE INTERNET OF THINGS JOURNAL, VOL. 1, NO. 5, OCTOBER 2014
- [2] Ericsson, “More than 50 billion connected devices”, Ericsson White Paper 284 23-3149 Uen, Feb. 2011.
- [3] John A. Stankovic, “Research Directions for the Internet of Things”, IEEE INTERNET OF THINGS JOURNAL, VOL. 1, NO. 1, FEBRUARY 2014.
- [4] IEEE Standard for Telecommunications and Information Exchange Between Systems—lan/man—Specific Requirements—Part 15: Wireless Medium Access Control (mac) and Physical Layer (phy) Specifications for Wireless Personal Area Networks (wpans), IEEE 802.15.1-2002 [Online].
- [5] Wireless lan Medium Access Control (mac) and Physical Layer (phy Specification, IEEE 802.11 [Online]. Available: <http://standards.ieee.org/getieee802/download/802.11-2012.pdf>
- [6] L. Li, X. Hu, K. Chen, and K. He, “The applications of wifi-based wireless sensor network in internet of things and smart grid,” in Proc. IEEE Conf. Ind. Electron. Appl. (ICIEA), 2011, pp. 789–793.
- [7] Sara Amendola et al, “RFID Technology for IoT-Based Personal Healthcare in Smart Spaces”, IEEE INTERNET OF THINGS JOURNAL, VOL. 1, NO. 2, APRIL 2014,
- [8] Muhammad S. Khan et al, “Design of a Reconfigurable RFID Sensing Tag as a Generic Sensing Platform Toward the Future Internet of Things”, IEEE INTERNET OF THINGS JOURNAL, VOL. 1, NO. 4, AUGUST 2014.
- [9] D. Yeager, P. Powledge, R. Prasad, D. Wetherall, and J. Smith, “Wirelessly-charged uhf tags for sensor data collection,” Apr. 2008, pp.320–327.
- [10] Cesare Alippi, Giuseppe Anastasi, Mario Di Francesco, and Manuel Roveri, “Energy Management in Wireless Sensor Networks with Energy-Hungry Sensors”, IEEE Instrumentation & Measurement Magazine April 2009.
- [11] C. Gomez and J. Paradells, “Wireless home automation networks: A survey of architectures and technologies,” IEEE Commun. Mag., vol. 48, no. 6, pp. 92–101, Jun. 2010.
- [12] Pavel V. Nikitin and K. V. S. Rao, “Performance Limitations of Passive UHF RFID Systems”, IEEE Antenna and Propagation International Symposium 2006, p.p.: 1011-1014, July 2006.
- [13] Pekka Pursula, “Analysis and Design of UHF and Millimetre Wave Radio Frequency Identification”, PhD Thesis, VTT Technical Research Centre of Finland, Dec. 2008.
- [14] Huichu Liu et. al. “Tunnel FET RF Rectifier Design for Energy Harvesting Applications”, IEEE Journal on Emerging and Selected Topics in Circuits and Systems, Vol.: 4, Issue: 4, p.p.: 400-411, Oct. 2014.
- [15] D. Liu, F. Li, X. Zou, Y. Liu, X. Hui, and X. Tao, “New analysis and design of a RF rectifier for RFID and implantable devices,” Sensors, vol. 11, pp. 6494–6508, June 2011.
- [16] Hucheng Sun, Zheng Zhong, and Yong-Xin Guo, “An Adaptive Reconfigurable Rectifier for Wireless Power Transmission”, IEEE Microwave and Wireless Components Letters, Vol.:23, No.: 9, September 2013.
- [17] T. Feldengut, R. Kokozinski, and S. Kolnsberg, “A UHF Voltage Multiplier Circuit Using a Threshold-Voltage Cancellation Technique,” in Research in Microelectronics and Electronics, July 2009, pp. 288 – 291.
- [18] Koji Kotami, “Highly Efficient CMOS Rectifier Assisted by Symmetric and Voltage-Boost PV-Cell Structures for Synergistic Ambient Energy Harvesting”, IEEE Custom Integrated Circuits Conference, p.p.: 1-4, San Jose, CA, Sept. 2013.
- [19] Ken Hatano, Naoki Shinohara, Tomohiko Mitani, Kenjiro Nishikawa, Tomohiro Seki, Ken Hiraga, “Development of Class-F Load Rectennas”, International Microwave Workshop Series on Innovative Wireless Power Transmission: Technologies, Systems, and Applications (IMWS), 2011
- [20] Mehmet Abbak and Ibrahim Tekin, “RFID Coverage Extension Using Microstrip Patch Antenna Array”, IEEE Antennas and Propagation Magazine, Feb. 2009.

- [21] Jun-Seok Park, Jin-Woo Jung, Si-Young Ahn, Hyoung-Hwan Roh, Ha-Ryoung Oh, Yeung-Rak Seong, Yoon-Deock Lee and Kyoung Choi, “*Extending the Interrogation Range of a Passive UHF RFID System With an External Continuous Wave Transmitter*”, IEEE Transactions on Instrumentation and Measurement, p.p.: 2191-1297, Vol. 58, Issue 8, Aug 2010.
- [22] H. Gomes, A. R. Testera, N. B. Carvalho, M. F. Barciela, and K. A. Remley, “*The impact of long-term memory effects on diode power probes*,” in IEEE MTT-S Int. Microw. Symp. Dig, Anaheim, CA, May 2010, pp. 596–599.
- [23] H. Gomes, A. R. Testera, N. B. Carvalho, M. F. Barciela, and K. A. Remley, “*Diode Power Probe Measurements of Wireless Signals*”, IEEE Transactions on Microwave Theory and Techniques, Vol. 59, Issue. 4, p.p.: 987-997, Jan. 2011.
- [24] Richard G. Carter, *Electromagnetism for Electric Engineers*, Richard G. Carter & Ventus Publishing ApS, 2010.
- [25] Anton A. Huurdeman, *The worldwide history of Telecommunications*, John Wiley & Sons, Inc., Hoboken, New Jersey, 2003.
- [26] J. C. Maxwell, “*A Dynamical Theory of the Electromagnetic Field*”, Philosophical Transactions of the Royal Society of London, 1865.
- [27] Ewan Fenn (GEC-Marconi Communications), *The transmitter*, EBU Technical Review, 1995.
- [28] N. Tesla, *The Transmission of Electric Energy Without Wires* (The Thirteenth Anniversary Number of the Electrical World and Engineer). New York: McGraw-Hill, Mar. 5, 1904.
- [29] N. Tesla, Apparatus for transmitting electrical energy, US patent number 1,119,732, issued in December 1914.
- [30] W. C. Brown, “*The history of power transmission by radio waves*,” IEEE Trans. Microwave Theory Tech., vol. MTT-32, pp. 1230–1242, 1984.
- [31] Zoya Popovic, David R. Beckett, Scott R. Anderson, Diana Mann, Stuart Walker, Sheldon Fried, “*Lunar Wireless Power Transfer Feasibility Study*”, March 2008.
- [32] S. Sheik Mohammed, K. Ramasamy, T. Shanmuganantham, “*Wireless Power Transmission – A Next Generation Power Transmission System*”, 2010 International Journal of Computer Applications.
- [33] Naoki Shinohara, “*Power without wires*,” IEEE Microwave Magazine, Vol. 12, Issue 7, pp.S64-S73, Dec. 2011.
- [34] J. Glenn, Ed., *The Complete Patents of Nikola Tesla*, Barnes and Noble Books, New York, 1994, pp. 346–360.
- [35] W. C. Brown, “*The history of the development of the rectenna*,” in Proc. SPS Microwave Systems Workshop at JSC-NASA, 1980, pp.271–280.
- [36] W.C. Brown, J.R. Mims and N.I. Heenan, “*An Experimental Microwave-Powered Helicopter*”, 1965 IEEE International Convention Record, Vol. 13, Part 5, pp.225-235.
- [37] P. E. Glaser, “*Power from the sun; its future*,” Science, vol. 162, no.3856, pp. 857–886, 1968.
- [38] US Department of Energy. Doe/nasa reference system report for satellite power system (sps). Technical Report DOE/ER-0023, US DoE, Oct. 1979.
- [39] H. Matsumoto, “*Research on solar power station and microwave power transmission in Japan: Review and perspectives*,” IEEE Microwave Mag., pp. 36–45, Dec. 2002.
- [40] J.J. Schelesak, A. Alden and T. Ohno, “*A microwave powered high altitude platform*” , IEEE MTT-S Int. Symp. Digest, pp - 283- 286, 1988.
- [41] André Kurs, Aristeidis Karalis, Robert Moffatt, J. D. Joannopoulos, Peter Fisher, Marin Soljacic, “*Wireless Power Transfer via Strongly Coupled Magnetic Resonances*”, Science 317, 83 (2007), DOI: 10.1126/science.1143254.

- [42] Chun-Chih Lo, Yu-Lin Yang, Chi-Lin Tsai, Chieh-Sen Lee, and Chin-Lung, Yang, “*Novel Wireless Impulsive Power Transmission to Enhance the Conversion Efficiency for Low Input Power*”, Microwave Workshop Series on Innovative Wireless Power Transmission, p.p.: 55-58, May 2011.
- [43] Bill Johns, “*An introduction to the Wireless Power Consortium standard and TI’s compliant solutions*”, Texas Instruments, 2011. Available online 13-07-2015: <http://www.ti.com/lit/an/slyt401/slyt401.pdf>
- [44] Qi WPT Standard: System Description Wireless Power Transfer, Volume I: Low Power, Part 1: Interface Definition, Version 1.1.2, June 2013. Available online 13-07-2015:
<http://www.wirelesspowerconsortium.com/downloads/wireless-power-specification-part-1.html>
- [45] Powercast - Powerharvester modules <http://www.powercastco.com/>.
- [46] eCoupled. Available from: <http://www.ecoupled.com/>. Online 25/07/2015
- [47] WiPower. Available from: <http://wipower.com/>. Online 25/07/2015
- [48] Powermat. Available from: <http://powermat.com/>. Online 25/07/2015
- [49] The Biography of Ernst F. W. Alexanderson, IEEE Global History Network. http://www.ieeeahn.org/wiki/index.php/Ernst_F._W._Alexanderson
- [50] J.L. Baird, “*Improvements in or relating to apparatus for transmitting views or images to a distance*”. Patent number GB292,185, 1928.
- [51] Stephen A. Weis, “*RFID (Radio Frequency Identification): Principles and Applications*”, MIT - Computer Science and Artificial Intelligence Laboratory.
- [52] P. V. Nikitin, “*Leon Theremin (Lev Termen)*”, IEEE Antennas and Propagation Magazine, vol. 54, no. 5, pp. 252-257, October 2012
- [53] Stockman, H. “*Communication by Means of Reflected Power*”. Proceedings of the Institute of Radio Engineers. N.10, Vol. 36, p.p.:1196-1204, October 1948.
- [54] D.B. Harris, “*Radio transmission systems with modulatable passive responder*,” U.S. Patent 2 927 321, Mar. 1, 1960.
- [55] Finkenzeller, Klaus, “*RFID Handbook*”, 2nd Edition ed. Wiley
- [56] Mário W. Cardullo, “*Transponder apparatus and system*”, U.S. Patent 3713148 A, Jan 1973.
- [57] Juan Ignacio Aguirre, “*EPCglobal: A Universal Standard*”, Academic thesis, Massachusetts Institute of Technology, June 2007.
- [58] EPC Class-1 Generation-2 UHF RFID, Protocol for Communications at 860 MHz – 960 MHz, Version 1.2.0.
- [59] Daniel M. Dobkin, *The RF in RFID: Passive UHF in Practice*, 2nd Edition, Newness, Dec. 2012.
- [60] M. S. Trotter, J. D. Griffin and G. D. Durgin, “*Power-Optimized Waveforms for Improving the Range and Reliability of RFID Systems*”, 2009 IEEE International Conference on RFID.
- [61] M.S. Trotter, G.D. Durgin, “*Survey of Range Improvement of Commercial RFID Tags With Power Optimized Waveforms*”, IEEE International Conference on RFID, 2010.

2. FUNDAMENTALS OF RFID SYSTEMS

2.1. Introduction to RFID systems

2.1.1. Basic concepts and definitions

Radio-Frequency Identification is an automatic identification method in which a fixed RF interrogator or reader wirelessly access the memory of a mobile data carrier named transponder or tag [1][2]. The very attractive features of RFID, namely non-line-of-sight operation and very fast inventory capability over large tag populations, make this technology preferable over other automatic identification methods (e.g. bar-codes). Although mass adoption of RFID initially encountered obstacles mainly related to per-unit tag price and infrastructure deployment costs, recent advances in semiconductors specially in CMOS tag technology have made the technology affordable. RFID systems are currently used for a variety of purposes including supply chain logistics, personnel identification and access control to buildings, animal tagging, ticketing, anti-theft systems, indoor localization, airline baggage handling, vehicle identification and intelligent transportation systems, passive keyless entry, electronic passports, product authentication, pharmaceutical and health care industry, etc [3][4].

Passive RFID concept is intimately-related to WPT technology, and in fact, passive RFID is the most spread commercial application of WPT so far. Being free of batteries and signal generators, passive RFID transponders offer very interesting possibilities, and there has been a great research effort to expand the functionalities of passive tags beyond simple identification. The integration of passive RF identification, passive sensing and increased computation capabilities has enabled the concept of RFID-enabled sensors and Passive Wireless Sensors (PWS) [5], that are not only able to perform RF identification but also sensing, data logging and advanced computation. It is expected that these technologies will play a fundamental role within the IoT eco-system, allowing the interaction with quotidian objects in a low-cost and ubiquitous manner.

RFID systems can be categorized according to tag power-supply mechanism, reader-tag coupling method, tag memory capacity, system architecture, etc. Regarding the memory capacity, RFIDs can be divided into 1-bit tag systems and N-bit tag systems. The first systems allow to distinguish only between the presence or absence of tags in the field of the reader, and are typically used in counter-theft applications. N-bit transponders have higher memory capacity, being able to store unique N-bit identification numbers or user data. With respect to the coupling mechanism, RFID systems are divided in three groups according to the component of the EM field that is used to transfer data/energy between reader and tags: electrical, inductive and electromagnetic systems. The latter is the object of this thesis.

2.1.2. Frequency bands, power levels, read ranges and standards

Table 2.1 presents the allocated frequency bands for RFID applications along with the respective allowed power levels, maximum achievable range, target applications and main standards for each frequency band. Also, some of the main RFID manufactures are listed.

TABLE 2.1
FREQUENCY BANDS, ALLOWED POWER LEVELS AND READ RANGES

Frequency band	Allowed Power	Max. Range	Standards	Comments, applications, manufactures
9 - 135 kHz		Up to 20cm	ISO11784/5, ISO14223, ISO/IEC 18000-2, HiTag	Low Frequency, inductive systems. EM Microelectronics SA
3.155 - 3.4 MHz				EAS Systems, Anti-theft
13.55 - 13.567 MHz		Up to 1m	ISO14443-A & B, Mifare, EPC HF Class 1, ISO15693, Tag-It, I-Code, ISO18000-3, ISO/IEC-18047, TIRIS	ISM Medium Frequency (13.56 MHz), inductive systems, smart cards and smart labels, NFC, contactless, proximity and vicinity systems. LEGIC, NXP, 3ALogics, AMS, TI
26.957 - 27.283 MHz				ISM Medium Frequency, Industry an hospital applications
402-405 MHz	25uW ERP			Medical Implants
433 MHz	10 - 100 mW	Up to 100m (active)	ISO/IEC 18000-7, ANSI 371.2, RFCODE	ISM UHF, active systems
860 - 960 MHz EU: 866-868 MHz US: 902-928 MHz Japan: 950-956 MHz China: 920-924.5 MHz	EU: 2W ERP ¹ US: 4W EIRP Japan: 4W EIRP China: 2W ERP	Up to 10m	EPCGlobal, Class 0, Class 1, Gen2, ISO18000-6A e 6B, ISO1037, Ucode	UHF, ISM, US-915 MHz, EU-968 MHz, backscatter modulation. NXP, Creative Systems, AMS, Mojix, Allien Technology, Impinj, Gao RFID, ThinkMagic, Motorola
2.4 - 2.483 GHz	4 W US, 500 mW EIRP EU	Up to 10m		ISM Microwaves, backscatter modulation
2.446 - 2.454 GHz	0.5 W outdoor, 4 W indoor		ISO/IEC-18047, ISO1037, ISO/IEC 18000-4, Intellitag, μ -chip, Alien BAP	ISM Microwaves, AVI (Automatic Vehicle Identification)
5.725 - 5.875 GHz	4W US, 500 mW EU			ISM Microwaves, backscatter modulation,
24,05 - 24,5GHz				For future use

¹ EIRP = Equivalent Isotropic Radiated Power; $EIRP = P_{TX} + G_{TX}$; ERP = Equivalent Radiated Power; $ERP = EIRP - 2.15dB$.

TABLE 2.2
PARAMETERS OF THE ISO18000-6C AND EPC GENERATION 2 STANDARD

Frequency	R→T coding	R→T bit rate	R→T Mod	T→R coding	T→R bit rate	T→R Mod	Anti-Collision Algorithm
860-960 MHz	PIE	Max. 128 kbps	ASK or PR-ASK	FM0 or Miller	Max. 640 kbps	ASK or PSQ	Random Slotted (Q-Algorithm)

2.1.3. EPC-Global Class 1 Generation 2 and ISO18000-6C standards

Standardization is an important aspect for the global adoption of RFID. In particular, the standardization on spectrum usage is fundamental to avoid interference to other systems sharing the spectrum as well as to guarantee an efficient spectrum usage. In 1999, the MIT Audio-ID center was founded to develop an RFID-based identification system to replace bar-codes (UPC). Accordingly, the first version of the EPC system, EPC Gen 1, was launched in 2003. In the same year, the MIT Auto-ID center formally became Auto-ID Labs (the research-oriented group) and EPC-Global (the network and standard-oriented group).

Due to several mandates of international retailers and also governmental bodies (e.g. US DoD), EPC systems have been largely adopted worldwide, and currently, EPC-Global C1 Gen2 [6] as well as its counterpart ISO18000-6C stand as the dominant standards for passive-backscattering RFID systems operating in the UHF band. EPC C1 Gen2 version attempted to put together the best of its predecessors (Gen 1) and previous ISO protocols in order to provide improved modulation and codification schemes, improved anti-collision algorithm, operation for dense reader environments, increased security and higher tag read rates (up to 1500tags/s [4]). The current EPC version (Gen2) defines the requirements for the physical and logical layers for passive-backscatter, Reader Talks First (RTF), RFID systems operating in the 860-960 MHz band (902-928 MHz for US and 866-868 MHz for EU). Table 2.2 presents the physical parameters of EPC Gen 2 standard. Some aspects of Gen2 physical layer protocol are presented in Appendix B, and a detailed explanation of the *Q*-slotted anti-collision algorithm is given in chapter 7.

2.1.4. Passive versus active RFID systems

Depending on the power supply method, tags can be categorized as passive, semi-passive or active. An active tag [Fig. 2.1(a)] is similar to a traditional radio transceiver, employing a transmitter, receiver and battery, and generating its own RF signal. This allows long coverage range, only limited by transmitted power and receiver sensitivity. Active tags usually have larger memory capacity and are able to perform complex computation tasks. They can also operate offline (without

communicating with the reader), for instance, to sample a temperature sensor and store the data, and communicate the data to the reader only when it is turned on. Drawbacks of active tags include increased complexity, cost and size, and the need for battery maintenance.

Passive tags [Fig. 2.1(b)] harvest their supply power from the magnetic or electromagnetic field generated by the reader. Additionally, they use power backscattering to communicate data to the reader. In general, passive tags are smaller and cheaper than active transponders, and do not require maintenance. However, a shorter coverage range is possible and tag functionalities are limited in comparison with active transponders.

Semi-passive or semi-active systems stand in between passive and active systems [Fig. 2.1(c)]. Semi-passive transponders employ a battery only for the digital section, while the tag-to-reader communication is realized by power backscattering as in passive systems. Semi-active systems present a trade-off solution, permitting longer ranges than passive systems and increased battery life time in comparison with active systems.

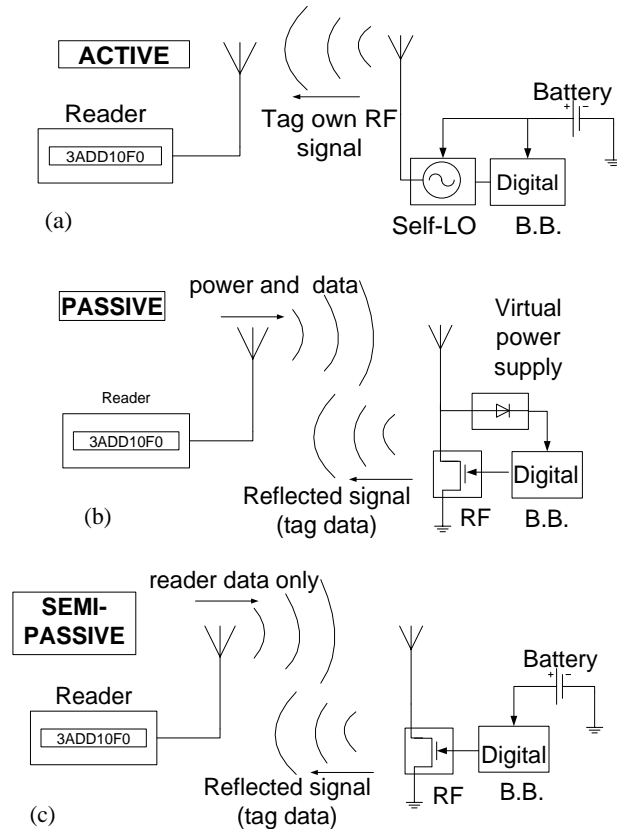


Fig. 2.1 Active, semi-passive and passive RFID systems

2.2. Operating principles of passive RFID systems

Most RFID systems on the market today rely on near-field magnetic induction and far-field electromagnetic propagation. The first method is typically used for short range LF and HF systems, while the second is generally applied to UHF, microwave, and more recently Millimeter-wave

RFID systems with higher data rates and potentially longer coverage range. These are essentially the same methods used for general purpose WPT applications. The main difference is that in passive RFID applications WPT (used for tag power-supply) is combined with an additional mechanism for tag-to-reader data communication. Load-modulation is used for this purpose in inductive systems and backscatter modulation is used in far-field systems.

2.2.1. Defining near-field and far-field operating regions

Whether or not a system is operating in the near-field or far-field depends on how close the receiver is from the radiating antenna, on the largest antenna dimension and on the wavelength or operating frequency. As illustrated in Fig. 2.2, the space surrounding the antenna can be classified into reactive near-field region ($r < r_1$), radiating near-field or Fresnel region ($r_1 < r < r_2$) and far-field region ($r > r_2$), where r_1 and r_2 are given by (2.1) and (2.2) respectively [7] and r_3 extends to infinity. In the reactive near-field region, the reactive fields predominate, the electric (E) and magnetic (H) fields are not in phase and the angular field distribution is strongly dependent on the distance and direction from the radiating source. In this region the fields strength decay rapidly with the distance according to $1/r^2$ or $1/r^3$. Beyond r_2 , we are in the far-field region where the electromagnetic field separates from the antenna and propagates into free-space in TEM mode. Here, the electric and magnetic fields are related via the free-space impedance ($E/H = 377\Omega$) and decay according to $1/r$. As the distance increases toward infinity, the spherical wave front emanated from the antenna approximates to the ideal planar phase front of a plane wave. Since the change from near to far field is not abrupt, there exist a transition region defined by $r_1 < r < r_2$, where the electric field and magnetic fields are not completely orthogonal to each other (non-TEM mode) and any structure inside this region will couple with the antenna distorting its radiating pattern. As a result, antenna gain measurement inside this region varies with distance and it is not a meaningful parameter.

For electrically small antennas ($D \ll \lambda$) used in LF/HF RFID (e.g. at 13.56 MHz), r_1 may be larger than r_2 which means that there is no radiating near-field region and the near-far-field boundary is given by (2.1). For antennas used in UHF RFID, with size comparable to the wavelength, the approximate boundary between the near field and the far field regions is given by the sphere with radius r_2 (2.2).

$$r_1 = 0.62 \sqrt{\frac{D^3}{\lambda}} \quad (2.1)$$

$$r_2 = \frac{2D^2}{\lambda}$$

(2.2)

where D is the largest dimension of the antenna, r is the distance from the antenna, and λ is the wavelength. For instance, the far-field region of a UHF antenna, with $D=0.25\text{m}$ operating at 866 MHz ($\lambda \approx 0.35\text{m}$), starts at approximately 0.36m.

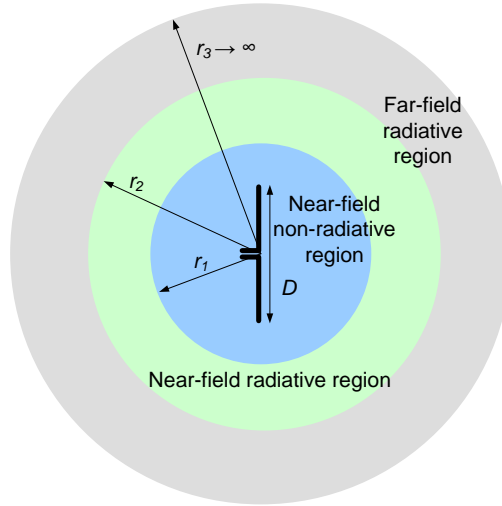


Fig. 2.2 Illustration of near-field and far-field operating regions.

2.2.2. Near-field inductively-coupled systems

Near-field inductively-coupled RFID systems (Fig. 2.3) rely on magnetic induction to transfer energy from the reader to the tag, and load-modulation to transfer data from the tag to the reader. Similar to a voltage transformer, the energy is wirelessly transferred from the primary coil at the reader side to the secondary coil at the tag side. By applying an alternating current to its coil, the reader creates an alternating magnetic field (B) according to Ampere's law. An alternating electromotive force (EMF) or AC voltage proportional to the rate of change of the generated magnetic flux is developed on the tag coil, which is coupled to the primary via a mutual coupling factor M , according to Faraday's law of induction. By using an RF-DC converter circuit, the AC energy induced in the tag's coil is converted to DC power to supply the digital electronics. Additionally, circuits for over-voltage protection, voltage regulation and power management are used to deliver a stable DC supply to the tag. A capacitor ($C1$ in Fig 2.3) is often used in parallel with the coil to form a resonant LC circuit tuned to the operating frequency, and thereby improve the energy transfer efficiency [1]. In order to transfer its data to the reader, the tag load-modulates its coil according to the data bits to be sent, by using a MOSFET transistor connected across the coil. By switching the gate of the transistor ON and OFF, the tag changes the load impedance of the secondary coil, and thereby modulates the voltage and current across the primary coil. These small current/voltage perturbations on the reader coil are used to decode the tag data.

Inductively-coupled RFID systems include contactless IC cards, proximity cards [8] and NFC systems [9], with coverage distance of several centimeters, and vicinity cards [10] covering up to 1 meter. Typical operating frequencies are at the LF band (100-135kHz) and HF band (10-15 MHz).

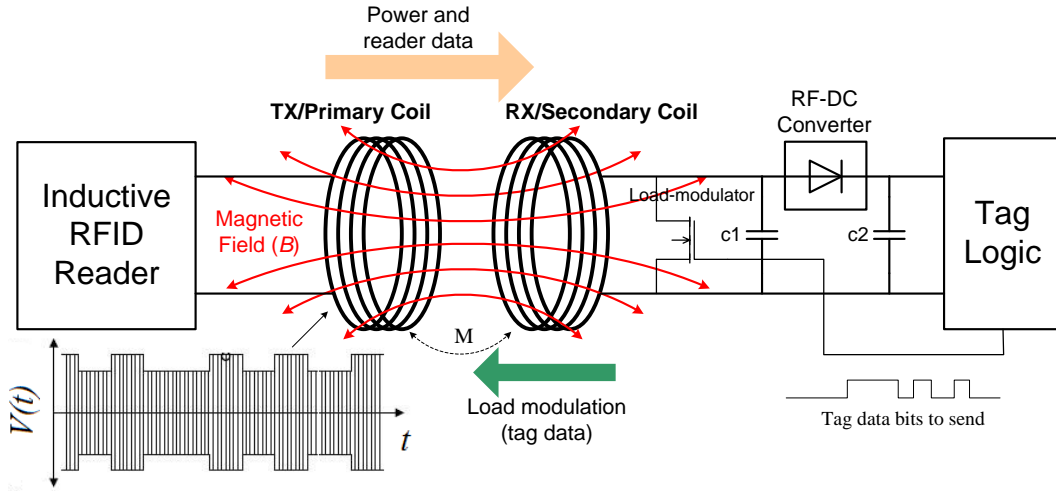


Fig. 2.3 Near-field passive RFID system. The magnetic field lines (B) are in actuality closed ones.

2.2.3. Inductively-coupled 1-bit systems

Inductively-coupled 1-bit systems are the simplest RFID systems, which detect only the presence or absence of a tag in the vicinity of the reader. The reader coil and tag coil are coupled via magnetic induction. A simple 1-bit transponder [Fig. 2.4(a)] consists of a tuned LC circuit resonating at a given frequency f_c , where the inductance is commonly that of the coil antenna. At the resonance frequency, a large current flows through the LC circuit and therefore when the tag is brought to the proximity of the reader, it produces a load effect, extracting energy from the reader's field and causing a drop in the voltage across the reader coil antenna [see Fig. 2.4(b)][2]. By sweeping its operating frequency, the reader can detect the abrupt voltage drop on its coil whenever the tag is in the field. By using multiple resonances in the same tag and by coding each resonance with a binary weight, it is possible to create a very low-cost and low complexity N-bit chipless system.

Alternatively to the LC circuit, a resonant 1-bit tag can also be constructed by using a strip of magnetically sensitive metal mechanically resonant at the operating frequency of the reader [2]. Tags of this type were first introduced in the 1960's for use in anti-theft applications, and are still in use today. Similarly to the LC tags, this system presents several benefits: the tag is quite simple, practical, compact and inexpensive; the reader is also practical and inexpensive; moreover, the low operating frequency used (from tens of kHz to 10 MHz) simplifies the design of both reader and tag.

2.2.4. 1-bit microwave systems based on non-linear effects

Figure 2.5 depicts another 1-bit system, based on EM propagation, devoted to EAS applications. This system explores the non-linear generation mechanism of an RF diode, and uses a very simple transponder design consisting of a single diode attached to a $\lambda/4$ dipole antenna. When the tag is illuminated by a microwave signal (with a fundamental frequency f_c), harmonics of the fundamental (at $2f_c, 3f_c, \dots, nf_c$) are generated in the diode and re-radiates to the medium. Typically, a fundamental frequency of 2.45 GHz is used, which generates harmonics at 4.9 GHz, 7.35 GHz, 9.8 GHz, etc. The reader detects the presence of transponders in the field by analyzing one of the harmonics (typically the second one): if the reader receives/detects incoming energy at that harmonic it learns that there is a tag in the field. In order to make the receiver immune to noise and external interference, the fundamental carrier is modulated by a known baseband pattern (e.g. a 1kHz square wave) before being transmitted [1]. A suitable detection technique consists of passing the received down-converted base-band signal through a bandpass filter centred at the frequency of the modulating signal. Other ideas have been proposed to explore the nonlinear effects of a single RF diode, such as the one proposed in [11] which uses intermodulation for localization purposes.

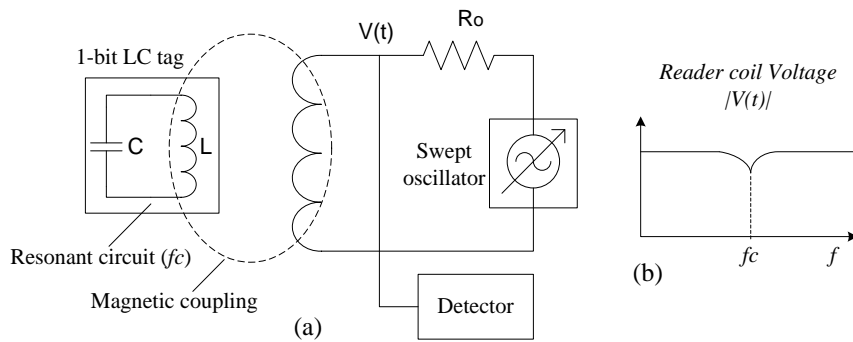


Fig. 2.4 Inductively-coupled 1-bit RFID system [After Walton, US Patent 3,752,960]

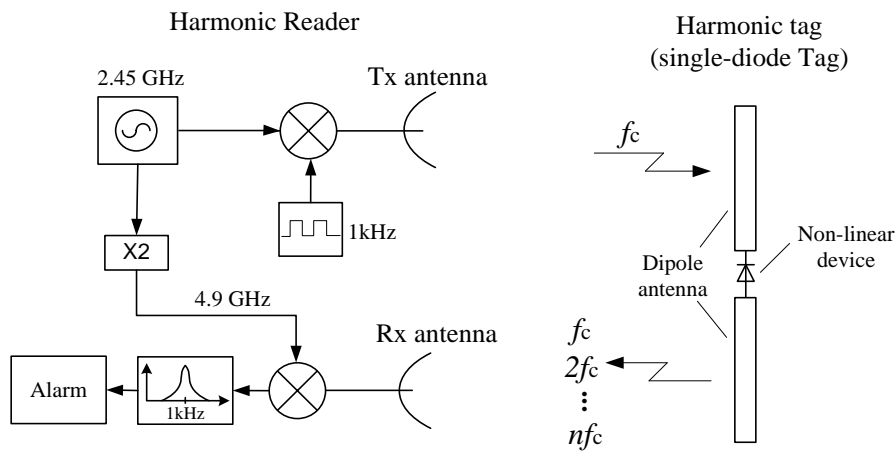


Fig. 2.5 1-bit microwave system based on harmonic generation of an RF diode.

2.2.5. Far-field passive-backscatter systems

In a far-field passive-backscatter system (see Fig. 2.6), wireless energy and data are conveyed through EM wave propagation. The backscatter mechanism used in passive RFID systems, consists of three steps: first, the reader radiates an un-modulated CW signal; second, the tag harvests DC power from the incoming RF signal, and once it collects enough energy it activates its electronics; third, the tag reflects part of the received RF power according to the data bit stream to be sent to the reader. By controlling the gate of a backscatter-modulator transistor connected across the antenna, the tag is able to vary its antenna reflection coefficient and thereby modulate its antenna Radar Cross Section (RCS). Communication by means of RCS modulation is described in section 2.5.

A possible binary modulation scheme utilizes a matched and an unmatched state: when the transistor is OFF (i.e. the gate is open), the tag antenna is matched to the RFID chip impedance and there is only a (minimal) structural reflection due to the tag antenna itself. This state is coded with a logical value “0”. On the other hand, when the transistor is ON, it short-circuits the tag antenna causing its complete mismatch and increasing significantly the reflected power. This is coded with a logical value “1”. Switching between a matched state, that maximizes the power delivered to the RFID chip, and a load resistance that introduces a mismatch to generate a backscatter signal, is a very common way to implement an ASK modulator (commonly used in commercial chips). Other strategies using arbitrary impedance states are also implemented in practice; For instance, binary PSK modulation can be implemented by switching a capacitor across the terminals of the antenna to introduce a phase shift [12].

Regardless of whether the tag locally generates ASK or PSK modulation, most readers perform an *IQ* demodulation followed by a rotation of the constellation to the real axis, allowing the constellation to be demodulated as if it was ASK-modulated. This is done because the constellation suffers arbitrary phase rotations along the propagation channel, which makes it unpredictable at the reader location. Moreover, a given change in the tag antenna is altered by reader self-jamming and other un-wanted environment scattering. For these reasons, existing codification schemes are based on state transitions rather than amplitude or phase. For instance, the FM0 coding scheme used in ISO18000-6c and EPCGlobal for uplink communication is based on the time interval between transitions [6].

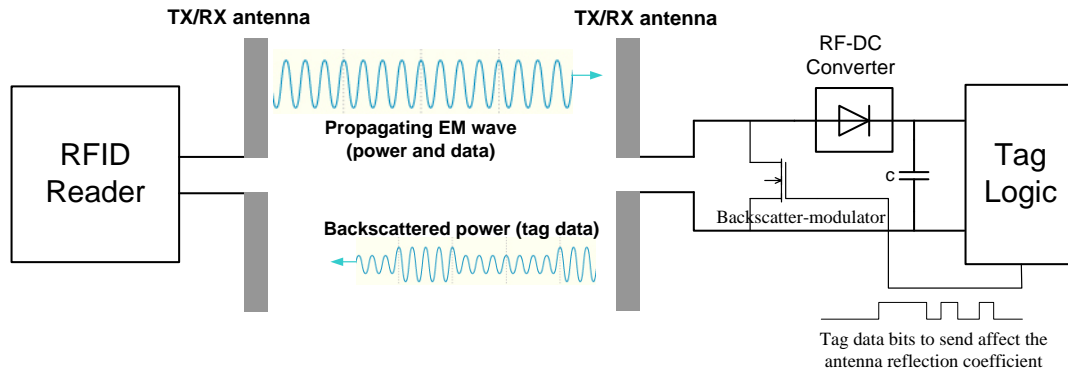


Fig. 2.6 Passive-backscatter RFID system.

2.3. Passive RFID transponders and RFID-enabled sensors

Passive RFID tags are unique compared to other wireless systems, as they do not require batteries, self-oscillator, mixers, amplifiers or other complex blocks. This allows to drastically reduce the power consumption, complexity, size and cost of passive tags, making them ideal for ubiquitous applications. The architecture of a passive RFID transponder/RFID-enabled sensor is depicted in Fig. 2.7. A typical RFID transponder incorporates the following basic blocks:

- 1) *Energy Harvesting Circuit*: is one of the most important blocks of a passive RFID tag, responsible for collecting energy from the incoming RF signal to power up the tag electronics. Typically, charge pump circuits are used to boost the output DC magnitude to a level that complies with the digital electronics of the transponder. This block is detailed in chapter 4.
- 2) *Power Management Unit*: is composed of a voltage regulator, a voltage supervisor and an over-voltage protection circuit [13]. The voltage regulator circuit at the output of the harvesting circuit provides the tag with a stable DC power independently of the RF power at the antenna. Additionally, the voltage supervisor monitors the DC output, and when the DC reaches a predefined level, an interrupt signal is issued to wake up the digital circuitry.
- 3) *Clock oscillator*: is used for clocking the baseband logic and for timing the data communications. Passive tags usually employ oscillators with relatively low frequency in order to reduce the overall power consumption. In some implementations, the required clock is remotely sent by the reader embedded in the data encoding [14], which considerably reduces the tag complexity and consumption.
- 4) *Demodulator*: receives the data from the reader. Modulation and codification schemes are carefully selected in order to reduce the complexity while maintaining an acceptable performance and a stable power delivery to the tag. For simplicity, ASK modulation is used in most passive systems for reader-to-tag data link and therefore a low complexity envelope detector is sufficient to demodulate the reader data. On the other hand, reader-to-tag codification schemes must avoid long periods of absence of signal. For this reason, NRZ coding may not

suitable the most appropriate, instead pulse interval encoding (PIE) techniques with very short dead periods are utilized, as in Gen2 standard. Other standards (e.g. ISO14443-B) utilize modulation indexes different than 1 to improve energy transference.

- 5) *Backscatter-Modulator*: is most of times based on a simple MOSFET transistor operating as a switch, which is used to modulate the antenna load impedance and thereby modulate the RCS.
- 6) *Memory*: is usually based on a EEPROM (Electrically Erasable Programmable Read Only Memory), which contains the tag ID and eventually user data. Some user memory fields (including the transponder ID) can be programmed online by the reader.
- 7) *Baseband Digital Logic*: is typically based on a finite state-machine processor which performs vital tasks including data encoding/decoding, reader command processing and protocol handling, memory access and power management. In passive sensors, the control unit is also responsible for handling sensors and data logging. While commercial tags employ low-cost, low complexity ASIC state-machine processors, other solutions dedicated to research may use microcontrollers (WISP platform [5]) or more sophisticated resources such as FPGAs/CPLDs (Complex Programmable Logic Devices)[15]. Note that a tradeoff between flexibility and power consumption exists: while ASICs and CPLDs consume significantly less power than microcontrollers, the latter allows superior flexibility and arbitrary instruction execution [15].

Over the years, RFID has become an umbrella term that covers a panoply of related technologies such as RFID-enabled sensors, Passive Wireless Sensors (PWS), Internet of Things, autonomous wireless sensors and much more. Although the traditional function of passive RFID is associated to mere identification, the current research and industry trend is to expand the functionalities of passive RFID in order to include sensing and other advanced functionalities. This emerging concept named passive wireless sensor or RFID-enabled sensor has been applied to several situations including passive sensor networks and biomedical implants [5][16-19]. A well known passive sensor platform for research is Wireless Identification and Sensing Platform (WISP) [5], which consists of a custom-built passive UHF RFID with a programmable microcontroller that can communicate with commercial RFID readers running EPCGlobal C1 Gen2 protocol.

The industry has also released passive RFID devices with expanded functionalities. An example is the SL900A RFID sensor [20], which incorporates an internal temperature sensor and interfaces for external sensors, an integrated Analog-to-Digital Converter (ADC) to sample the internal and external sensors and a digital serial data interface (SPI) for communication with external digital devices. Some passive tags also provide auxiliary DC ports for external power sources [21]; Other incorporate multiple antenna ports in order to allow improved antennas arrangements [22].

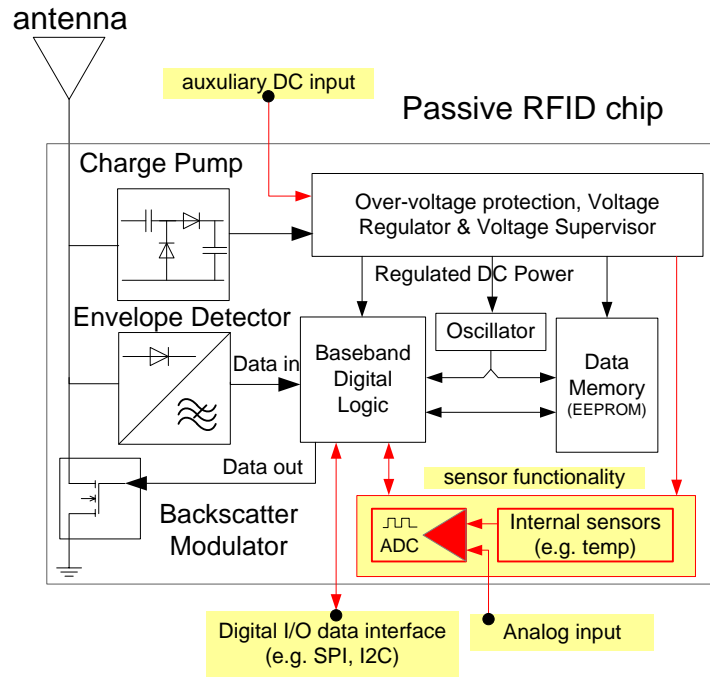


Fig. 2.7 Passive RFID tag/RFID-enabled sensor. The advanced functionality blocks of RFID-enabled sensors are filled with yellow.

Because passive RFID design is generally ruled by low power consumption, low complexity, small size and low-cost requirements, the integration of new functions significantly augments the design challenges, especially in terms of energy demand, because new features like sensors also need to be powered wirelessly. Hopefully, the continuous reduction in power consumption of modern semiconductor technologies allied with efficient wireless power delivery will enable the efficient realization of passive wireless sensors. Furthermore, synergistic energy harvesting from multiple sources including electromagnetic, solar, thermal and vibration has been explored to energy-assist passive wireless devices.

2.4. RFID Reader architectures

Current RFID reader implementations are either based on commercial ASICs (Application Specific Integrated Circuits) [23-25] and custom-designed ICs [26-27] or on SDR design [28-31]. The SDR approach fundamentally diverges from the other approaches, as it utilizes software to implement functions that are conventionally implemented in hardware. In terms of architecture, most of today RFID readers use direct conversion, in which the received RF signal is directly down-converted to baseband, and the transmit baseband data is directly translated to the desired RF frequency. Although simple ASK modulation is commonly used for downlink and uplink, readers employ in-phase and quadrature (*IQ*) modems. Since the reader-to-tag distance is variable and unknown and

so it is the channel phase shift, an IQ modulator is essential to receive the tag constellation affected by arbitrary phase rotations. Transmitting IQ modulator is needed to implement advanced modulation schemes, such as Single-Side Band (SSB) ASK, that provides increased spectral efficiency compared to Double-Side Band (DSB) ASK.

Since passive RFID requires full-duplex operation, readers need to separate the transmitter and receiver paths by using either a bistatic (separate transmitter and receiver antenna) or a monostatic (single antenna) configuration. The RFID front-end design is challenging because the transmitted power and noise may couple into the receiver and overpower the faint backscatter signal from the transponder, preventing the reader to decode the tag information; Therefore, readers quite often employ self-jamming cancellation schemes, which are implemented externally to the main RFID reader [30] or incorporated in the reader IC design [24][26].

Hand-held or portable RFID reader is a class of readers used in logistics to complement fixed RFID reader infrastructures. Attempts also have been made to integrate RFID readers into mobile devices (e.g. smart phones). In these application scenarios, the compactness of reader and antennas, and the power consumption are the primary design constraints.

Figure 2.8 depicts the basic block diagram of an ASIC-based RFID reader implementation. Typical UHF ASIC chips incorporate an analog RF front-end and a digital part. The analog front-end is composed of frequency synthesizer, IQ modem, filters and amplifiers; the digital part includes data converters, built-in processor for baseband and RFID protocol handling, and digital interface to communicate with an external microcontroller. Commercially available UHF reader chips are capable of implementing the complete physical and data link layers of RFID protocols. Some ICs also incorporate advanced functions such as self-jamming suppression.

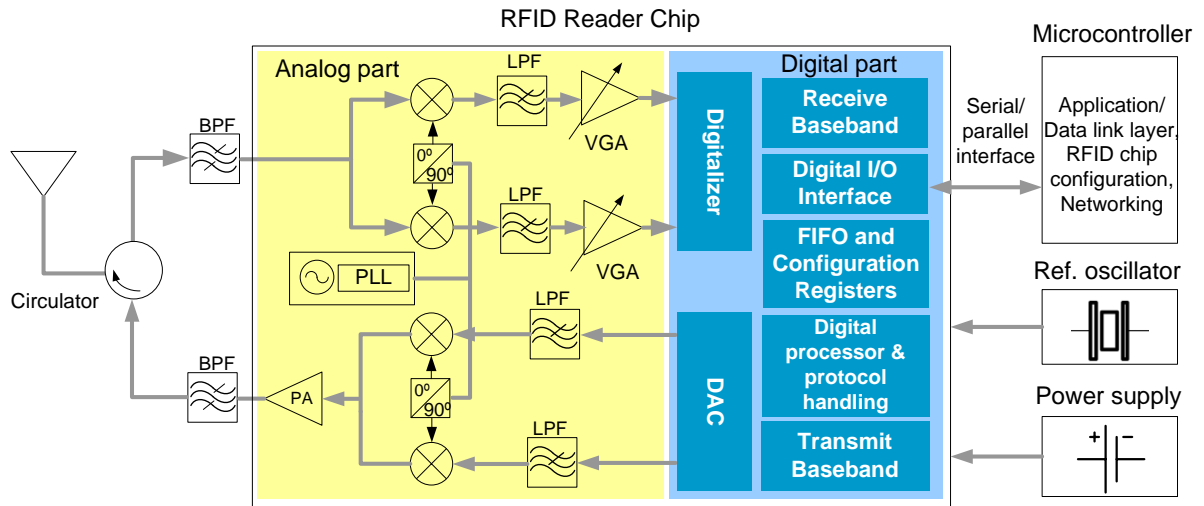


Fig. 2.8 Basic RFID reader configuration based on a commercial ASIC.

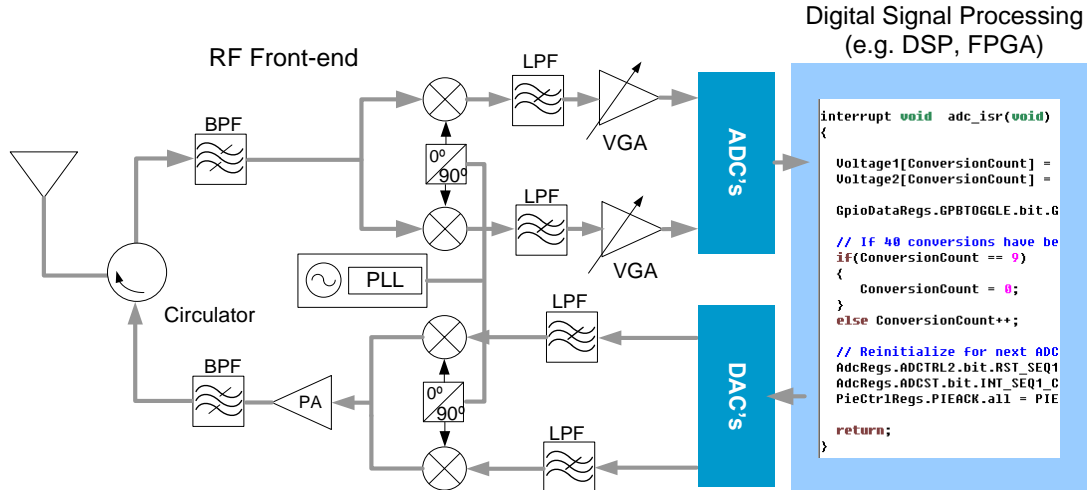


Fig. 2.9 Typical SDR RFID reader implementation.

2.4.1. Software Defined Radio-based reader architectures

Since its inception, RFID technology has been in constant evolution, and consequently, the standards have been suffering mutations in order to achieve improved performance (e.g. higher data rates, improved anti-collision schemes, better reader operation in dense reader environments, etc). However, since ASIC solutions are typically tied to a given standard, they have to be replaced/re-designed whenever it is necessary to operate a new standard. Moreover, even for current standards, ASIC-based solutions are often inflexible, not allowing for parameter tuning (e.g. power level, frequency, etc), which is sometimes useful for RFID measurements and protocol evaluation. In contrast to that, SDR is a flexible radio implementation approach in which some or all of the physical-layer functions (e.g. modulation, codification, tuning, etc.) are implemented in or defined by software. SDR was first used in the military to allow backward compatibility and equipment interoperability, and in recent years, this technology has moved to general wireless and mobile applications, providing radios with the ability to accommodate different communication standards by using adaptable software along with reconfigurable hardware.

Similarly, an SDR reader provides increased flexibility and is able to interoperate with different standards and upgrade to new ones by simply upgrading its software. Therefore, the SDR approach has been used in commercial RFID readers [32] as well as in research [28], RFID characterization and measurements [29], protocol exploration [30] and localization [31]. In this thesis, SDR is used to implement an RFID reader that is able to generate efficient software-defined waveforms for improved communication range.

Figure 2.9 presents the SDR architecture typically used in RFID applications. In this implementation, a direct conversion *IQ* modem is used to down-convert the incoming signal to baseband, and up-convert the outgoing baseband to the desired RF frequency. A digital signal

processor unit (typically based on DSP or FPGA) processes the complex data that are received from *IQ* ADC and sent via *IQ* DAC.

2.5. Backscatter communication in passive RFID

The use of reflected radio waves from an object was first explored in the early radar systems developed during the second world war, and the use of radio wave backscattering for communication purposes has been studied since the work of Harry Stockman in 1949. In radar theory, any reflective object can be characterized by a RCS, σ_{RCS} , that is a measure of how reflective the object is to RF signals. The greater the RCS is, the larger the amount of scattered power. A passive-backscatter transponder utilizes the concept of cooperative radar to convey information to the reader by modulating the RCS of its antenna and thereby modulate the power being scattered.

2.5.1. Analysis of the backscatter link

This section presents an analysis of the backscatter link in passive RFID systems. The analysis consider the effects of the communication channel, namely, arbitrary propagation phase shift due to variable distance between reader and tag, self-jamming provoked by imperfect reader transmitter-to-receiver isolation and scattering from surrounding objects. Figure 2.10 shows a passive-backscatter radio system including a tag with two modulation states (binary ASK or PSK) and an *IQ* demodulator. In the forthcoming analysis, the following assumptions are made: all link gain/loss factors are neglected; the effective length of each antenna is assumed to be unitary such that the electric field and voltage at the antenna interface are interchangeable and simply referred to as signal [$S(t)$]; the un-modulated structural scattering from the tag antenna is not considered; noise is disregarded; the wireless channel is considered to be stationary with respect to the data signal backscattered from the tag, in other words, the tag data rate is much higher than the rate of change of the un-wanted signals (self-jamming and reflections) and the tag moving speed relative to the reader. Consider that the reader radiates an un-modulated carrier given by:

$$S_{tx}(t) = |S_{tx}(t)|e^{j\omega t} \quad (2.1)$$

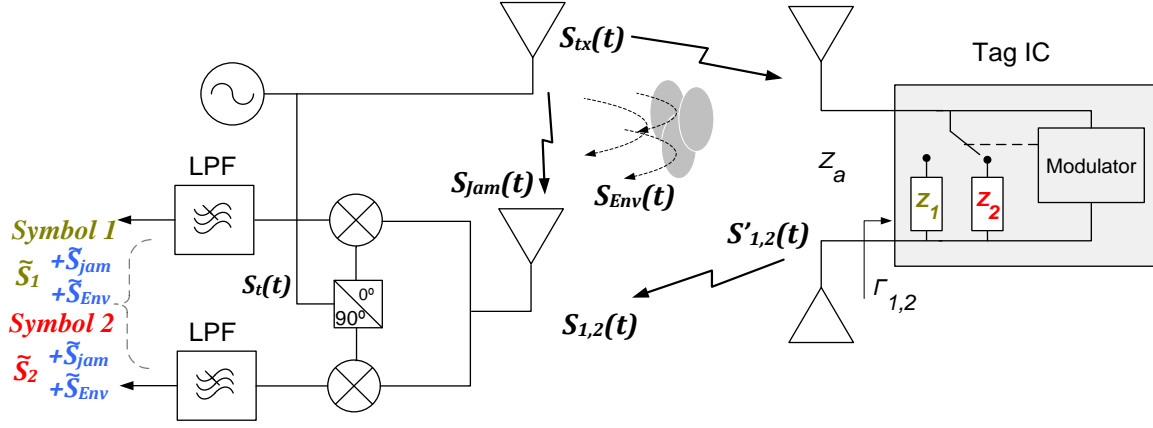


Fig. 2.10 Passive-backscatter RFID system using binary RCS modulation.

The modulated signal backscattered by the tag is related to the reflection coefficient in each modulation state, represented by the complex phasor $|\Gamma_{1,2}|e^{j\Phi_{1,2}}$. This yields the signal at the tag site (2.2) and its corresponding phase-shifted version at the reader site (2.3). Amplitude scaling due to path loss is not considered and the contributions of jammer and environment reflections are added later in (2.13) and (2.14).

$$S'_{1,2}(t) = k|\Gamma_{1,2}||S_{tx}(t)|e^{j(\omega t + \Phi_{1,2})} \quad (2.2)$$

$$S_{1,2}(t) = k|\Gamma_{1,2}||S_{tx}(t)|e^{j(\omega t + \Phi_{1,2} + \Phi_{path})} \quad (2.3)$$

where Φ_{path} is the modulation-independent round trip phase shift due to the propagation channel, Φ_1 and Φ_2 are the phases of the two modulation states and k is a real-valued scaling constant. Assuming a PSK modulation ($\Phi_2 = \Phi_1 + 180^\circ$), the signals at the receiver site for the two modulation states come as,

$$\text{Modulation state 1: } S_1(t) = k|\Gamma_1||S_{tx}(t)|e^{j(\omega t + \Phi_1 + \Phi_{path})} \quad (2.4)$$

$$\text{Modulation state 2: } S_2(t) = k|\Gamma_2||S_{tx}(t)|e^{j(\omega t + \Phi_1 + \pi + \Phi_{path})} \quad (2.5)$$

The contribution of reader self-jammer signal and scattered signals from surrounding environment at the reader receiver antenna are given respectively by (2.6) and (2.7).

$$S_{jam}(t) = |S_{jam}(t)|e^{j(\omega t + \Phi_{jam})} \quad (2.6)$$

$$S_{Env}(t) = \sum_{n=1}^N |\Gamma_n| |S_{tx}(t)| e^{j(\omega t + \Phi_n)} \quad (2.7)$$

where $|S_{jam}|$ and Φ_{jam} are respectively the amplitude and phase shift of the jammer signal, N is the total number of reflections, $|\Gamma_n|$ and Φ_n are respectively the amplitude and phase with respect to the LO of the n -th reflection coefficient of the n -th reflecting object. The received signals (2.4), (2.5), (2.6) and (2.7) can be processed separately by the IQ demodulator (which performs a correlation product with the LO signal), then the resulting complex baseband signals can be combined. Accordingly, the complex output solely due to modulation state 1 is given by:

$$\begin{aligned} \tilde{S}_1 &= \tilde{S}_1^I + j\tilde{S}_1^Q = \frac{1}{T_{bit}} \int_0^{T_{bit}} \text{Re} \left\{ k|\Gamma_1| |S_{tx}(t)| e^{j(\omega t + \Phi_1 + \Phi_{path})} \right\} \text{Re} \left\{ |S_{tx}(t)| e^{j\omega t} \right\} dt \\ &\quad + j \frac{1}{T_{bit}} \int_0^{T_{bit}} \text{Re} \left\{ k|\Gamma_1| |S_{tx}(t)| e^{j(\omega t + \Phi_1 + \Phi_{path})} \right\} \text{Re} \left\{ |S_{tx}(t)| e^{j(\omega t + \frac{\pi}{2})} \right\} dt \\ &= \frac{k|\Gamma_1| |S_{tx}(t)|^2}{2} \cos(\Phi_1 + \Phi_{path}) + j \frac{k|\Gamma_1| |S_{tx}(t)|^2}{2} \sin(\Phi_1 + \Phi_{path}) \end{aligned} \quad (2.8)$$

which can be written using the complex baseband notation as:

$$\tilde{S}_1 = \frac{k|\Gamma_1| |S_{tx}(t)|^2}{2} e^{j(\Phi_1 + \Phi_{path})} \quad (2.9)$$

Similarly, the complex-baseband signals of modulation state 2, jammer and reflections come as follows:

$$\tilde{S}_2 = \frac{k|\Gamma_2| |S_{tx}(t)|^2}{2} e^{j(\Phi_1 + \pi + \Phi_{path})} \quad (2.10)$$

$$\tilde{S}_{jam} = \frac{|S_{jam}| |S_{tx}|}{2} e^{j\Phi_{jam}} \quad (2.11)$$

$$\tilde{S}_{Env} = \sum_{n=1}^N |\Gamma_n| |S_{tx}| e^{j\Phi_n} \quad (2.12)$$

Finally, the total signal received for each symbol comes as the sum of the respective modulation state signal, $S_{1,2}$, and the arbitrary jamming (2.11) and reflection (2.12) components:

$$\begin{aligned}
\widetilde{S}_1^T &= \widetilde{S}_1 + \widetilde{S}_{jam} + \widetilde{S}_{Env} \\
&= \frac{k|\Gamma_1||S_{tx}(t)|^2}{2} e^{j(\Phi_1 + \Phi_{path})} + \frac{|S_{jam}(t)||S_{tx}(t)|}{2} e^{j\Phi_{jam}} + \sum_{n=1}^N |\Gamma_n||S_{tx}(t)| e^{j\Phi_n}
\end{aligned} \tag{2.13}$$

$$\begin{aligned}
\widetilde{S}_2^T &= \widetilde{S}_2 + \widetilde{S}_{jam} + \widetilde{S}_{Env} \\
&= \frac{k|\Gamma_2||S_{tx}(t)|^2}{2} e^{j(\Phi_1 + \pi + \Phi_{path})} + \frac{|S_{jam}(t)||S_{tx}(t)|}{2} e^{j\Phi_{jam}} + \sum_{n=1}^N |\Gamma_n||S_{tx}(t)| e^{j\Phi_n}
\end{aligned} \tag{2.14}$$

Figure 2.11(b) depicts the complex baseband vectors, (2.13) and (2.14), which result from the demodulation of a PSK constellation similar to that shown in Fig. 2.11(a).

In the RFID reader design carried out in chapter 7, the High-Pass Filter (HPF) illustrated in Fig. 2.11(e) is implemented in the analog domain by using a switched non-linear HPF similar to the one described in [XIV], which not only removes the DC-offset component but also eliminates transient effects. A straightforward implementation of the phase rotation operation described in Fig. 2.11(f) consists of finding the absolute value of the complex IQ signal ($|\widetilde{S}| = \sqrt{S_I^2 + S_Q^2}$), dropping the phase information which is not relevant for ASK demodulation. An alternative implementation consists of first processing the data in one of the branches (I or Q) and only process the second branch if the first data demodulation attempt is unsuccessful. This approach was followed in the design presented in chapter 7. This method can be further improved by first pre-processing the two branches in order to access their signal strength/quality, and accordingly, decide which branch to fully process first for data demodulation.

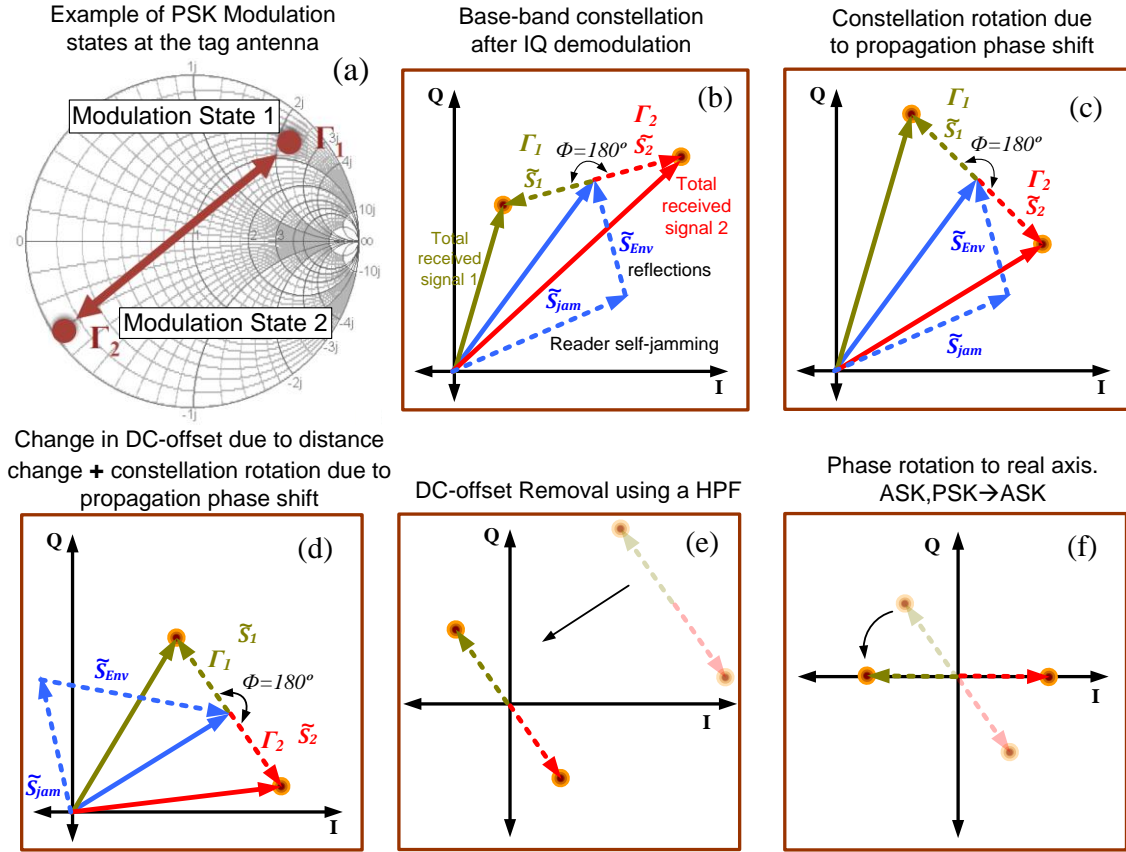


Fig. 2.11 (a) Example of PSK modulation states at the tag, (b) Received baseband constellation. (c) Constellation rotation after change in distance and consequent propagation phase shift. (d) Received signal after change in self-jamming and scattering components, and distance change. (e) DC-offset rejection by using a HPF. (f) Constellation phase rotation to the real axis.

2.5.2. Forward and backscatter power budgets

The power transferred to the transponder chip and the power reflected by the transponder antenna and received by the reader receiving antenna are given respectively by the Friis equation, as the power density at the transponder location times its effective antenna aperture area (2.15) and by the radar equation (2.16)[12]:

$$P_{tag} = A_e \frac{P_{TX} G_{TX}}{4\pi d^2} \quad (2.15)$$

$$P_{RX} = \sigma_{RCS} \frac{P_{TX} G_{TX} G_{RX} \lambda^2}{(4\pi)^3 d^4} \quad (2.16)$$

where P_{TX} is the power radiated by the reader, G_{TX} and G_{RX} are respectively the gain of the reader transmitting and receiving antennas, λ is the radiation wavelength, d is the distance between reader

and transponder, A_e is the effective aperture of the transponder antenna, which determines the power transferred to the chip and σ_{RCS} is the RCS of the transponder antenna, which determines the amount of power being scattered. The effective aperture and the RCS of an antenna loaded by an impedance Z_L are given respectively by [32][35]:

$$A_e = \frac{G_{tag}\lambda^2}{4\pi} (1 - |\Gamma_L|^2) \text{ [m}^2\text{]} \quad (2.17)$$

$$\sigma_{RCS} = \frac{G_{tag}^2\lambda^2}{4\pi} |A_s - \Gamma_L|^2 \text{ [m}^2\text{]} \quad (2.18)$$

where Γ_L is reflection coefficient of the load as defined by (2.19) and A_s is a complex vector that represents the load-independent RCS component due to the antenna structural mode. The term $(1 - |\Gamma_L|^2)$ is the power transmission coefficient, accounting for the mismatch between the antenna Z_a and the load Z_L . When the load is matched ($\Gamma_L=0$), A_e assumes the usual form of effective aperture described by Friis ($A_e=G_{tag}\lambda^2/4\pi$).

Although (2.17) and (2.18) suggest that minimizing the mismatch between the antenna and the load ($\Gamma_L = 0$) gives the best results, backscatter modulation for data transfer requires two (or more) distinct load impedance states, thereby in terms of RCS, more important than the RCS of each individual state is the differential RCS as given by (2.22).

$$\Gamma_L = \frac{Z_L - Z_a^*}{Z_L + Z_a} \quad (2.19)$$

Equation (2.19) is the Kurokawa power wave reflection coefficient [38] valid when the source and load impedances are complex and there is no transmission line in between, as is the case for a passive RFID chip directly connected to an antenna. Note that Kurokawa's definition reduces to the usual form of transmission-line reflection coefficient when Z_a is purely real.

By varying Z_L between two load impedances, Z_1 and Z_2 , it is possible to modulate the antenna reflection coefficient between two modulation states, Γ_1 and Γ_2 , and thereby modulate its RCS:

$$\Gamma_{1,2} = \frac{Z_{1,2} - Z_a^*}{Z_{1,2} + Z_a} \quad (2.20)$$

After Pursula [34], assuming a 50% duty-cycle square wave modulation between two impedance states, the effect of load modulation on (2.17) and (2.18) leads to the averaged effective aperture (A_e^m) and differential modulated RCS (σ_{RCS}^m):

$$A_e^m = \frac{G_{tag}\lambda^2}{4\pi} (1 - \frac{1}{2}(|\Gamma_1|^2 + |\Gamma_2|^2)) \text{ [m}^2\text{]}$$

(2.21)

$$\sigma_{RCS}^m = \frac{G_{tag}^2 \lambda^2}{16\pi} |\Gamma_1 - \Gamma_2|^2 [\text{m}^2]$$

(2.22)

where the superscript m indicates modulation, the one-half weighting term in equation (2.21) is due to the modulation between two states which causes the power available to the tag to be an average of the power in the individual states [34]. Substituting (2.21) in (2.15), and (2.22) in (2.16), one ends up respectively with the average power delivered to the transponder chip and the modulated power backscattered by the transponder and received by the reader receiving antenna:

$$P_{tag}^m = G_{TX} P_{TX} G_{tag} \left(\frac{\lambda}{4\pi d} \right)^2 \left(1 - \frac{1}{2} (|\Gamma_1|^2 + |\Gamma_2|^2) \right) [\text{W}]$$

(2.23)

$$P_{RX}^m = G_{TX} P_{TX} G_{RX} G_{tag}^2 \left(\frac{\lambda}{4\pi d} \right)^4 \frac{1}{4} |\Gamma_1 - \Gamma_2|^2 [\text{W}]$$

(2.24)

The power reflected from the tag depends on the differential reflection coefficient $|\Gamma_1 - \Gamma_2|$, and a load modulation index or modulation loss (between 0 and 1) is usually defined as $\frac{1}{4} |\Gamma_1 - \Gamma_2|^2$. The power reflection is maximized when extreme reflection coefficient values (-1 and 1) are used for the two states, however such choice would cause all the power to be backscattered and no power would be available to supply the transponder electronics. A tradeoff is, thus, necessary in the design.

By including the polarization mismatch loss and the multipath fading margin, and by writing (2.23) and (2.24) in a more convenient form, one ends up with the following:

$$P_{tag}^m = P_{TX} + G_{TX} + G_{tag} + 20 \log_{10} \left(\frac{\lambda}{4\pi d} \right) + 10 \log_{10} \left(1 - \frac{1}{2} (|\Gamma_1|^2 + |\Gamma_2|^2) \right) + \Theta_f - F_f [\text{dBm}]$$

(2.25)

$$P_{RX}^m = P_{TX} + G_{TX} + G_{RX} + 2G_{tag} + 40 \log_{10} \left(\frac{\lambda}{4\pi d} \right) + 10 \log_{10} \left(\frac{1}{4} |\Gamma_1 - \Gamma_2|^2 \right) + \Theta_f + \Theta_b - F_f [\text{dBm}]$$

(2.26)

where Θ_f is the polarization mismatch loss between the reader transmitter antenna and the tag antenna, Θ_b is the polarization mismatch loss between the tag antenna and the reader receiver antenna; F_f is the forward fade margin, which is defined as the additional transmitted power needed in a faded channel to keep the same read rate achieved in a non-faded channel [35]. Note that, other aspects affect the power budget, e.g., tag gain penalty due to attachment in objects or blockage loss due to the obstruction of the line-of-sight [35], etc. Some of these aspects are discussed in chapter 3.

2.5.3. A power budget example

In order to evaluate which of (2.25) or (2.26) primarily limits the range of passive-backscatter RFID, consider the following typical parameters and conditions: $P_{TX} = 30$ dBm; $G_{TX} = G_{RX} = 6$ dBi ($EIRP = 36$ dBm); $G_{tag} = 2$ dBi; $\Theta_f = \Theta_b = -3$ dB (circular reader versus linear tag polarization); $F_f = F_b = 0$ dB (a dominant direct line-of-sight link is considered); $\lambda \sim 35$ cm ($f_c = 866$ MHz); the transponder switches between a matched state ($\Gamma_1 = 0$, obtained by using a conjugate match, $Z_l = R_a - jX_a$) and an unmatched state ($\Gamma_2 = -1$), yielding a modulation index of $M = 0.25$; Finally, two receiver sensibility values and tag activation power values are considered $S_i = -80$ dBm (typical value) and $S_i = -90$ dBm (state-of-art value), $P_{tag_min} = -15$ dBm (typical value) and $P_{tag_min} = -20$ dBm (state-of-art value). Accordingly, (2.25) and (2.26) are plotted in Fig. 2.12.

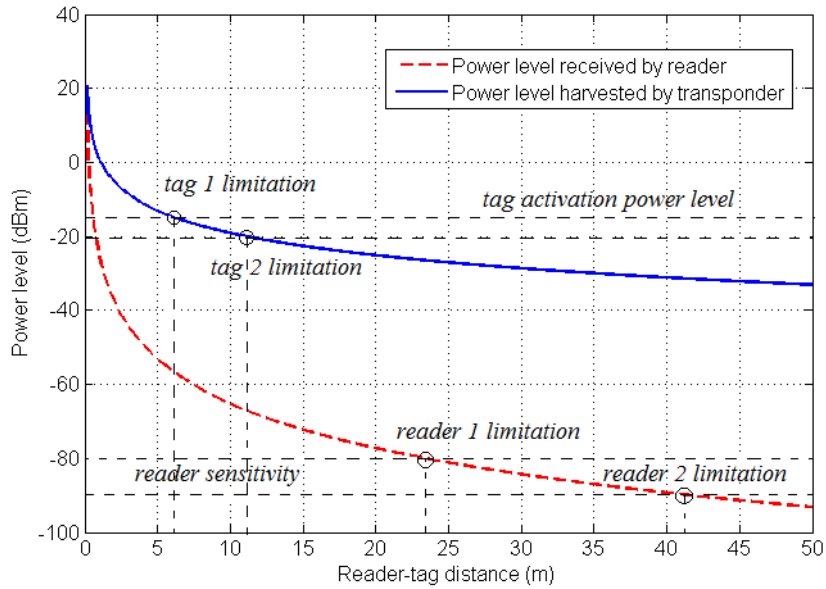


Fig. 2.12 Typical curves of power harvested by tag and power level reflected by tag and received by reader.

2.5.4. Remarks

- Due to variable distance between the reader and tag, and the consequent change in the propagation phase shift (ϕ_{path}), the transponder constellation suffers unpredictable rotations before it reaches the reader [refer to Fig. 2.11(c)]. On the other hand, self-jamming and environment scattering generate a variable baseband DC-offset component [see Fig. 2.11(d)]. While this DC-offset must be eliminated during the demodulation procedure, strong self-jamming can saturate the RF stage of the receiver and degrade its sensitivity. These issues are addressed with more details in [XIV] and chapter 8. A pre-processing of the down-converted baseband signal is needed, including DC-offset removal and constellation rotation to the real axis [see Fig. 2.11(e)-(f)].

- Tag modulation states must be properly chosen in order to maximize power transfer to the tag while providing a backscatter power sufficiently strong. For instance, reflection coefficient of 1 or -1 maximizes the power reflection but penalizes the available power to the chip. A matched/unmatched scheme must be properly designed such that enough power can be received during the matched state for operation while in the unmatched state.
- Although virtually all current passive-backscatter transponders available commercially employ binary modulation schemes (ASK or PSK), some works have recently explored multi-state M-ary QAM modulation schemes to achieve increased data rates [12][36-37].
- From Fig. 2.12, it can be concluded that the operating range of passive-backscatter systems is primarily limited by the forward link (tag limitation). The stated example shows that, although reader sensitivities of -80 dBm/-90 dBm would allow to reach ranges of 23m/42m, the coverage distance is limited by the transponder activation power level (-20 dBm/10 μ W) which only permits a maximum range of 11m.

References

- [1] K. Finkenzeller, *RFID Handbook: Fundamentals and Applications in Contactless Smart Cards and Identification*. John Wiley and Sons, 2003.
- [2] D. M. Dobkin, *The RF in RFID: Passive UHF in Practice*. Elsevier, Burlington, MA, 2008
- [3] Steven Shepard, "Radio Frequency Identification" McGraw-Hill, New York, 2005.
- [4] Harvey Lehpamer, *RFID Design Principles*, Artech House, London, 2008.
- [5] J. Smith, A. Sample, P. Powledge, A. Mamishev, and S. Roy, "A wirelessly powered platform for sensing and computation," in 8th International Conference on Ubiquitous Computing (Ubicomp), September 2006, pp. 495-506.
- [6] EPC Class-1 Generation-2 UHF RFID, Protocol for Communications at 860 MHz – 960 MHz, Version 1.2.0.
- [7] C. A. Balanis, *Antenna Theory: Analysis Design – Chapter 2*, 3rd Edition, John Wiley & Sons, 2005.
- [8] ISO/IEC 14443-2:2010, Identification cards — Contactless integrated circuit cards — Proximity cards — Part 2: Radio frequency power and signal interface. Available online 28-07-2015: <http://www.nhzzj.com/asp/admin/editor/newsfile/2010318175217930.pdf>
- [9] Standard ECMA-352, Near Field Communication (NFC) Interface and Protocol -2 (NFCIP-2), 3th edition, June 2013. Available online 28-07-2015: <http://www.ecma-international.org/publications/files/ECMA-ST/ECMA-352.pdf>
- [10] ISO/IEC 15693-2:2006, Identification cards — Contactless integrated circuit cards — Vicinity cards — Part 2: Air interface and initialization.
- [11] Hugo Cravo Gomes and Nuno Borges Carvalho, "The use of Intermodulation Distortion for the Design of Passive RFID", Proceedings of the 37th European Microwave Conference, p.p.: 377-380, Munich, Oct. 2007.
- [12] Stewart J. Thomas, Eric Wheeler, Jochen Teizer, and Matthew S. Reynolds, "Quadrature Amplitude Modulated Backscatter in Passive and Semi-Passive UHF RFID Systems", *Microwave Theory and Techniques*, Vol. 60, Issue 4, April 2012.
- [13] Wang Yao, Wen Guangjun, Mao Wei, He Yanli, and Zhu Xueyong, "Design of a passive UHF RFID tag for the ISO18000-6C protocol", *Journal of Semiconductors*, Vol. 32, No. 5, May 2011.
- [14] P. Pursula, J. Marjonen, H. Ronkainen and K. Jaakkola, "Wirelessly Powered Sensor Transponder for UHF RFID" Proceedings of Transducers & Eurosensors'07 Conference. Lyon, France, June 10–14, 2007, pp. 73–76.
- [15] S. Roy, V. Jandhyala, J. Smith, D. Wetherall, B. Otis, R. Chakraborty, M. Buettner, D. Yeager, Y.-C. Ko, and A. Sample, "RFID: From Supply Chains to Sensor Nets," Proceedings of the IEEE, vol. 98, no. 9, pp. 1583 { 1592, September 2010.
- [16] P. Pursula, J. Marjonen, H. Ronkainen and K. Jaakkola, "Wirelessly Powered Sensor Transponder for UHF RFID" Proceedings of Transducers & Eurosensors'07 Conference. Lyon, France, June 10–14, 2007, pp. 73–76.
- [17] Yeager, D.J.; Holleman, J.; Prasad, R.; Smith, J.R.; Otis, B.P. "Neural WISP: A Wirelessly Powered Neural Interface with 1-m Range. *IEEE Trans. Biomed. Circ. Syst.* 2009, 3, 379-387.
- [18] Toshiyuki Umeda, Hiroshi Yoshida, Shuichi Sekine, Yumi Fujita, Takuji Suzuki, and Shoji Otaka, "A 950-MHz Rectifier Circuit for Sensor Network Tags With 10-m Distance", *IEEE JOURNAL OF SOLID-STATE CIRCUITS*, VOL. 41, NO. 1, JANUARY 2006.
- [19] D. J. Young, "An RF-powered wireless multi-channel implantable biosensing microsystem," in Proc. Annu. Int. Conf. IEEE Eng. Med. Biol.Soc., Sep. 2010, pp. 6413–6416.
- [20] RFID with Senses, SL900A – EPC Gen2 Sensor Tag IC, www.ams.com/SL900A.

- [21] NXP RFID Tag, UCODE G2iL and G2iL+ Product datasheet, Ver. 4.4, 17 March 2014. Available online, 15-08-2015: http://www.nxp.com/documents/data_sheet/SL3S1203_1213.pdf
- [22] Impinj Monza X-2K Dura Datasheet Rev 1.51 March 24th , 2014. Available 14-08-2015: <https://support.impinj.com/hc/en-us/articles/202756848-Monza-X-2K-Dura-Datasheet>
- [23] AMS RFID products: <http://www.ams.com>, online 12/02/2015
- [24] Impinj Indy UHF RFID reader chips: <http://www.impinj.com>, online 12/02/2015
- [25] PR9000/PR9200 UHF RFID Reader SoC. Datasheet available online, 10-09-2015:
- [26] J Lee, j Choi, KH Lee, B Kim, M Jeong, Y Cho, H Yoo, K Yang, S Kim, SM Moon, JY Lee, S Park, W Kong, J Kim, TJ Lee, BE Kim, BK Ko. "A UHF mobile RFID reader IC with self-leakage canceller." IEEE Radio Frequency Integrated Circuits RFIC Symposium, Honolulu, June 2007 (IEEE,Piscataway, 2007), pp. 273–276.
- [27] Le Ye; Huailin Liao; Fei Song; Jiang Chen; Chen Li; Jinshu Zhao; Ruiqiang Liu; Chuan Wang; Congyin Shi; Junhua Liu; Ru Huang; Yangyuan Wang, "A Single-Chip CMOS UHF RFID Reader Transceiver for Chinese Mobile Applications," in Solid-State Circuits, IEEE Journal of , vol.45, no.7, pp.1316-1329, July 2010.
- [28] Ettus Research: www.ettus.com, online 12/02/2015
- [29] L. Catarinucci, D. De Donno, et.al., "A cost-effective SDR platform for performance characterization of RFID tags," IEEE Transactions on Instrumentation and Measurement, vol. 1, no. 4, pp. 903-911, April 2012.
- [30] M. Buettner and D. Wetherall, "A software radio-based UHF RFID reader for PHY/MAC experimentation," IEEE International RFID Conference, pp.: 134-141, Orlando, April 2011.
- [31] Ales Povalac, "Spatial Identification Methods and Systems for RFID Tags", Ph.D. Thesis, Brno Univerisity of Technology, Brno 2012.
- [32] Alien RFID Reader - Hardware Setup Guide ALR-9800, Feb. 2008. Available online 14-08-2015 <ftp://ftp.alientechnology.com/pub/readers/alr9800/docs/Guide,%20Hardware%20Setup,%20ALR-9800.pdf>
- [33] Pursula, P.; Vaha-Heikkila, T.; Muller, A.; Neculoiu, D.; Konstantinidis, George; Oja, A.; Tuovinen, J., "Millimeter-Wave Identification—A New Short-Range Radio System for Low-Power High Data-Rate Applications," in Microwave Theory and Techniques, IEEE Transactions on , vol.56, no.10, pp.2221-2228, Oct. 2008
- [34] Pursula, P. "Analysis and Design of UHF and Millimetre Wave Radio Frequency Identification", Ph.D. Thesis, Faculty of Information and Natural Sciences, Helsinki University of Technology, Finland, January, 2009.
- [35] J. D. Gri_n and G. D. Durgin, "Complete link budgets for backscatter radio and RFID systems," IEEE Antennas and Propagation Magazine, April 2009.
- [36] Stewart J. Thomas and Matthew S. Reynolds, "A 96 Mbit/sec, 15.5 pJ/bit 16-QAM Modulator for UHF Backscatter Communication", IEEE International Conference on RFID, p.p.: 185-190, Orlando, FL, April 2012.
- [37] M. Winkler, T. Faseth, H. Arthaber, and G. Magerl, "An UHF RFID tag emulator for precise emulation of the physical layer," in 2010 European Wireless Technology Conference (EuWIT) , Sept. 2010, pp. 273–276.
- [38] Nikitin, P.V.; Rao, K.V.S.; Lam, S.F.; Pillai, V.; Martinez, R.; Heinrich, H., "Power reflection coefficient analysis for complex impedances in RFID tag design," in Microwave Theory and Techniques, IEEE Transactions on , vol.53, no.9, pp.2721-2725, Sept. 2005

3. LITERATURE REVIEW

3.1. Current research topics in passive RFID

As demonstrated in the previous chapter, the reader-to-transponder power link imposes the more stringent limitation in passive RFID systems in terms of coverage range and transponder functionalities. Therefore, considerable research is dedicated to improve WPT in passive RFID systems (a literature/industry review is presented in the next section). Self-jamming caused by imperfect isolation between transmitter and receiver is the second limiting aspect of passive-backscatter systems. Since passive RFID systems operate in full-duplex mode, power and noise from the transmitter can leak into the receiver degrading its sensitivity. A number of research works address CW self-jamming cancellation techniques for passive RFID systems [1-7]. In chapter 8 and [XIV] self-jamming cancellation is treated for CW signals and extended to MS signals. Other relevant research topics include Integrated Circuit (IC) design [8-10], antenna design for tags and readers [11], RFID-based localization techniques [12][13], non-conventional substrates and inject-printed electronics for tag design [14-17], anti-collision algorithms [18][19], basic principles of backscattering propagation [20], low-power and low-cost design, higher order modulation schemes (QAM) for increased data rates [21], and RFID-enabled sensors and passive wireless sensors. A number of other issues make the design of passive RFID challenging, including polarization mismatch loss, tag orientation sensitivity, degradation of tag performance, namely antenna gain reduction and impedance mismatch, due to tag attachment in objects, small-scale multipath fading loss, etc. Also, SDR-based RFID reader design has been devoted to research [22], RFID characterization and measurement [23], protocol exploration [24] and localization [13].

3.2. Improving wireless power transfer in passive-backscatter RFID

Figure 3.1 depicts the WPT subsystem of a far-field passive RFID system. The DC-to-DC efficiency is given by the ratio between the DC power collected at the transponder and the DC power injected at the reader transmitter (3.1). The maximization of DC-to-DC efficiency is achieved by improving the DC-RF efficiency, the beam efficiency and the RF-DC efficiency. In order to enhance the first, switching mode power amplification (SMPA) [25][26] along with SMPA-based transmitter architectures [27][28] have been used. State-of-art approaches to enhance the beam efficiency and RF-DC efficiency are reviewed in the next sections.

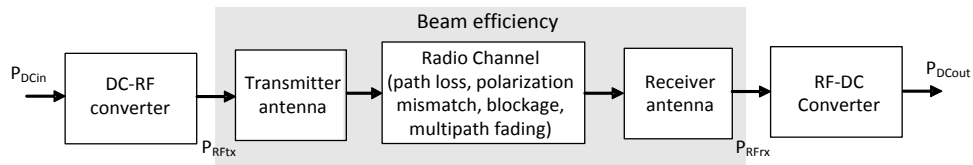


Fig.3.1 The wireless power transfer subsystem

$$\eta_{Total} = \frac{P_{DCout}}{P_{DCin}} = \eta_{DC-RF} \cdot \eta_{Beam} \cdot \eta_{RF-DC} = \frac{P_{RFtx}}{P_{DCin}} \frac{P_{RFrx}}{P_{RFtx}} \frac{P_{DCout}}{P_{RFrx}} \quad (3.1)$$

3.2.1. Beam efficiency improvement

Considering the free-space model of the forward power link presented in chapter 2, equation 2.25, we can infer several ways of improving the beam efficiency, e.g., by increasing the gains of the antennas, by selecting proper backscatter modulation loads, by using polarization insensitive antenna schemes and by mitigating multipath fading. Some of these approaches are reviewed next.

A. Antenna beamforming:

An effective way to increase the beam efficiency in a point-to-point MPT system is by increasing the gain of the antennas [29]. Parabolic antennas, horn antennas and large antenna arrays with very high gains (20 dBi or higher) and very narrow 3 dB beamwidth (of less than 10°) are used to achieve very high beam efficiencies [30]. However, in most passive RFID applications, low gain antennas (around 5 to 7 dBi) are traditionally used in the reader. In order to simultaneously achieve high gain while maintaining wide coverage area, antenna beamforming have been proposed. In [31], a steerable beam antenna array featuring 12.1 dBi directivity in two different directions was proposed. Also, RFID manufacture companies as Mojix Inc. currently use steerable phased-array antennas to improve RFID reader performance and provide additional functionalities (e.g. object location) [32][33]. It is worth mentioning that the improved gain performance is obtained at the expense of an increased equipment cost, size and weight (especially at UHF band), and a trade-off is necessary. Nevertheless, this technique is very effective at microwave frequency bands (e.g. 5.8 GHz) where the electrical length is substantially smaller, allowing the design of very high gain antenna arrays at reduced size, weight and cost.

B. Circular polarization

The polarization mismatch between the transmitter and receiver antenna affects the energy transfer efficiency between reader and transponder. Passive RFID tags typically employ simple linearly-polarized antennas while readers are often equipped with circularly-polarized antennas to reduce polarization sensitivity. In a circular-to-linear antenna polarization scheme, the polarization loss is equal to ½ (3 dB) regardless of the relative orientation between the antennas. In a linear-to-linear antenna configuration, the polarization loss is a function of the angle between the two antennas, being zero (i.e. no loss) when the antennas are fully aligned (0°), and infinity (i.e. no link) if the antennas are orthogonally-oriented (90°). Because RFID tags are often attached to objects that can

appear in the field of the reader with arbitrary orientations, in spite of the 3 dB power loss, circular-to-linear arrangement is preferred in the majority of RFID applications, providing improved orientation insensitivity. Besides, circular polarization presents improved performance in vehicular applications [34][35].

C. Multiple polarizations

In order to take advantage of the increased efficiency of linear polarization while maintaining the desired orientation insensitivity of circular polarization, the use of multi-polarized antennas is a viable option for RFID readers. This technique can also increase the immunity to multi-path fading. A commercial application of this concept is claimed in Impinj Inc. RFID reader portal. The Speedway reader portal is claimed to be able to continuously switch between a pair of linearly-polarized antennas to obtain an alternating vertical-horizontal polarization pattern [36]. Nevertheless, we have not found detailed information in the literature about this approach. In chapter 7, we designed a multi-polarization antenna to work in conjunction with our SDR RFID reader.

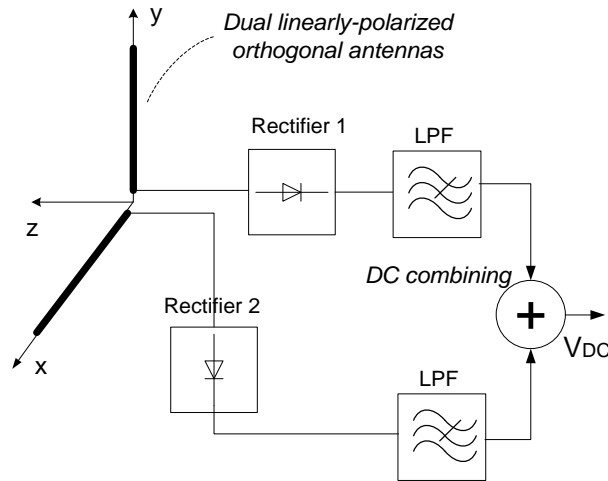


Fig. 3.2 Multiple antenna receiver.

D. Multi-antenna receivers

A strategy to improve the insensitivity to polarization misalignment between transmitter and receiver consists of providing the receiver with multiple antennas. For instance, by using two linearly-polarized orthogonal antennas, the receiver is able to collect energy from vertical and horizontal E-field components regardless of the polarization angle. By combining signals from various antennas after envelope detection as in Fig. 3.2, the orientation insensitivity and coverage range can be improved. Dual linearly-polarized antenna approaches have been proposed for energy harvesting, MPT and Passive Wireless Sensor Networks (PWSN) applications [37][38]. Multi-

antenna RFID tags have also been proposed [39][40], and RFID manufactures currently provide multi antenna port chips [41], giving the possibility to use dual-polarization schemes as in [42].

E. Diversity schemes to combat multipath fading

In a multipath faded channel, radio signals reach the receiving antenna by several paths with different amplitudes, phases and angles of arrival, causing the signal to combine constructively or destructively at different locations or time instants. In passive RFID, multipath fading is caused by waves scattered from walls and surrounding objects located in the vicinity of the RFID system, which causes the power received by the tag to vary as a function of position – *small-scale multipath fading*. This phenomenon can render the transponder powerless in some locations and significantly reduce the communication range and reliability. In order to combat the effects of multipath fading, techniques as frequency diversity, spatial/antenna diversity or polarization diversity are often employed. These techniques are based on the observation that a relatively subtle change in frequency, transmitter/receiver antenna position or polarization can completely change the multipath fading pattern. Thereby, a field null (*fade*) can be dislocated by slightly changing the frequency, antenna position or polarization. Modern RFID readers utilize Frequency Hopping as a frequency diversity mechanism [43][44]. The use of multiple antennas in the reader and transponder has been proposed to provide space diversity [45][46]. Also, polarization diversity has been investigated [47].

F. Auxiliary power sources

Other techniques that can improve the overall performance include the use of extra power sources in RFID tags in addition to the power of the main RFID reader. Park et. al. were able to double the read range of passive tags by using an auxiliary CW transmitter in addition to the main RFID reader [48]. A similar strategy is used by Mojix Inc. RFID manufacturing company, which deploys auxiliary excitation nodes in addition to the main RFID reader [49][50], which greatly increases the overall coverage. With the same purpose of providing RFID tags with extra energy, A. Georgiadis et. al. proposed an ingenious scheme that uses a solar-to-RF converter to assist a passive RFID tag [51]. This concept, illustrated in Fig. 3.3, uses a solar cell to convert solar energy into DC power, which is used to power up an RF oscillator that feeds the transponder with extra RF power. By taking advantage of recent industry releases, the same concept can also be implemented with new RFID chips either supporting multiple antenna ports [41], or providing auxiliary DC input ports [52]. The use of exposed DC ports in passive RFID transponders, first proposed in [53], also allows the realization of semi-passive configurations with improved sensitivity. For instance, the read and

write sensitivity of NXP UCODE G2iL chip can be improved up to -27 dBm when assisted by a 1.85V external power supply [52].

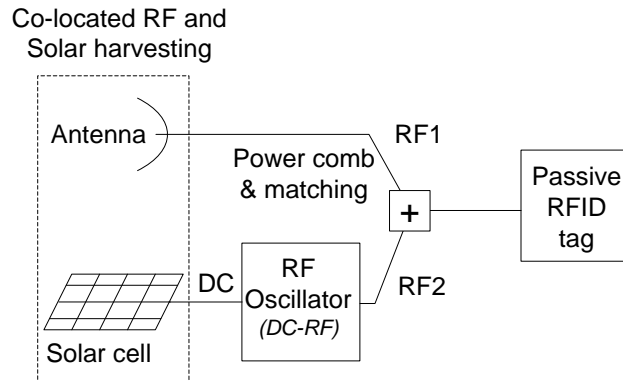


Fig. 3.3 Solar-assisted RFID tag concept (after [51])

3.2.2. Enhancement of RF-DC conversion efficiency

In passive RFID and passive sensors devices, voltage multipliers or charge pumps are commonly employed. As the maximum power level radiated by RF interrogators is limited by regulations, and the RF energy received by passive devices is usually very small, especially in multipath faded environments and far away from the interrogator, these devices must be able to operate at very low power levels (from few mW down to μW [54-56]). In order to obtain a DC level that complies with digital electronics, N-stage CMOS-based Dickson charge pumps are commonly used to boost the small amplitude of the incoming RF signal [57-62]. Although low barrier Schottky diodes can achieve higher RF-DC conversion efficiency (specially at low power levels), diode-connected MOSFET transistors are currently preferred for UHF RFID applications because they are process-compatible with CMOS, which is a well matured and very low-cost technology, and CMOS performs quite well at UHF frequencies. On the other hand, Schottky diodes are incompatible with low-cost standard CMOS processes, which prevents them to enter into mainstream UHF RFID applications. In fact, the widespread adoption of passive UHF RFID technology is greatly attributed to the possibility of integrating all the tag electronics (including N-stage charge pumps) into the same CMOS chip, allowing to dramatically reduce the cost of tags. However, a weakness of CMOS is the increase of threshold voltage due to the transistor body effect [62], which leads to efficiency degradation at low power levels. Some strategies to deal with this issue are overviewed later in this section.

However, while performing well at the UHF band, CMOS technology has not yet been satisfactorily scaled to microwave bands in terms of cost, power and efficiency. For this reason, most rectifiers/rectennas for SPS and MPT applications at high microwave frequencies employ discrete, low potential barrier, Schottky diodes [63-69]. The increased efficiency of single and

double diode rectifiers, at low power levels, also justifies their use in low power ambient energy harvesting applications.

Since the RF-DC conversion efficiency ultimately limits the range of MPT, energy harvesting, passive RFID and passive wireless sensor systems, a great research effort is put on the optimization of the RF-DC efficiency. One of the highest efficiencies ever reported was achieved in 1977 by W. Brown at Raytheon Company [70]. Using a GaAs – Pt Schottky barrier diode and an aluminum bar dipole, a conversion efficiency of 90.6% was achieved at 8W microwave input power level. Later, Brown reported a printed thin-film rectenna version at 2.45 GHz with 85% RF-DC conversion efficiency [71]. In 1991, ARCO power Technologies Inc. company, built a rectenna at 35 GHz with 72% RF-DC conversion efficiency [72].

Figure 3.4 presents typical RF-DC conversion efficiencies reported in the literature [54-79], including a recent survey conducted by Valenta et. al. on state-of-the-art far-field energy harvesting circuits and efficiencies [79].

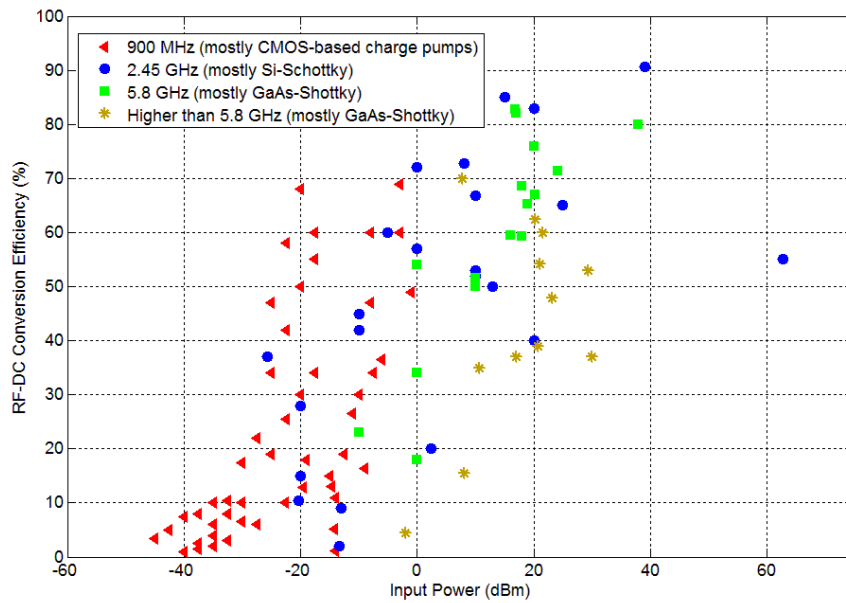


Fig. 3.4 State-of-the-art efficiencies for different frequency bands as a function of input power (data from [56][78][79]).

According to the literature review and Fig. 3.4, the following conclusions can be drawn:

- The RF-DC conversion efficiency decreases with the decrease in power level and with the increase in frequency. The first behavior is because of the need to overcome the threshold barrier and the second effect is due to the increase of parasitic losses at higher frequencies.
- Harvesting circuits for UHF RFID applications are mostly based on CMOS technology and operate at lower power levels (typically below 0 dBm).

- Circuits for SPS, MPT and WPT-oriented applications, working at microwave range (2.4 GHz, 5.8 GHz and beyond), are based on discrete Schottky diodes, work at significantly higher input power levels and present increased efficiencies (e.g. 90.6% @39 dBm~8W [77]).
- The efficiency of ambient EM energy harvesting at very low power levels (below -30 dBm) is reduced (e.g. lower than 20% in UHF band [56]).

In general, the conversion efficiency of rectifier circuits is affected by diode-device parameters, RF input signal frequency and amplitude, circuit topology, input filter and output load conditions. In the following we review some approaches attempted to enhance the RF-DC conversion efficiency.

A. Selecting rectifying devices

Most of rectenna designs found in the literature are based on off-the-shelf discrete silicon (Si) Schottky diodes, mainly because these devices are commercially available at low-cost. The main parameters to take into account in the choice of a rectifying diode are: the series resistance, which is a major source of losses; the parasitic junction capacitance, which limits the efficiency at higher frequencies; the threshold or turn-on voltage and the breakdown voltage. The last two parameters determine the power handling capability or dynamic range of the device. The lower the threshold voltage is, the more suitable and efficient the device is for low power levels. Zero-bias Schottky diode exhibit very low threshold voltages (around 150-300mV) and are suitable for applications below -20 dBm [80]. On the other hand, the higher the breakdown voltage is, the higher the power handling capability of the device. Conventional rectifiers utilizing Si-based Schottky diodes typically operate at power levels below 30 dBm [81].

B. Alternative rectifying devices

Although existing rectifier circuits are predominantly based on Schottky diodes and diode-connected CMOS transistors, alternative devices have also been used. An example is Gallium Arsenide (GaAs) Schottky technology. In spite of being similar to Si Schottky diodes in most aspects, GaAs present higher carrier mobility and very low junction capacitance, which permit them to operate at much higher frequencies (commercially available beyond 100 GHz). E-pHEMT transistors have also been tested for rectifying purposes, showing good efficiency performance at medium power levels [82]. In order to take advantage of high switching speed and low turn-on voltage of Schottky diodes and also to benefit from modern CMOS processes, attempts have been made to integrate Schottky junctions into CMOS [83]. Heterojunction tunnel field-effect transistors (HTFET) featuring very low turn-on voltage were used to achieve an improved performance at very low UHF ambient power levels (over 50% conversion efficiency at -40 dBm to -25 dBm input

power) [56]. Some works have also investigated custom-built Schottky diodes using non-conventional material in order to reduce the parasitic losses [84].

C. Harmonic filters:

The optimization of the overall rectenna design is necessary to maximize the RF-DC conversion efficiency. In order to prevent higher harmonics generated in the non-linear device to be re-radiated, harmonic filters/terminations are often used at the input of the rectifier circuit [85][86].

In order to suppress the higher frequency components at the output load resistance, a capacitor is typically used for relatively low frequencies. Alternatively, a quarter wavelength open stub, which acts as short-circuit at the operating frequency, is often used in the microwave range. Nevertheless, these load impedance terminations allow the current and voltage waveforms across the diode to overlap in time, which results in power dissipation in the series resistance, and consequently in degradation of the efficiency. The use of improved harmonic terminations, such as Class-F loads, have been investigated to improve the efficiency of rectifying circuits [87]. Similarly to switching mode power amplifier design [88], multi-resonant load networks are used to impose non-overlapping voltage and current waveforms, and reduce the dissipation loss in the diode. The condition for class-F operation is that the impedance of the rectifier output filter is zero at even harmonics and infinity at odd harmonics. By using a class-F-terminated rectenna, a conversion efficiency of 65.6% was obtained at 24 GHz in contrast with 52.1% efficiency obtained with a conventional capacitor-terminated rectenna.

D. Improved rectifier topologies

Achieving high RF-DC conversion efficiency is challenging at extreme conditions of very low power level (limited by the turn-on voltage) and very high power level (limited by the breakdown voltage). High power RF-DC conversion using Si-based Schottky diodes is challenging not only because the rectification of signal amplitudes in excess to the diode breakdown voltage becomes inefficient, but also because excessively high input power levels can permanently damage the semiconductor junction. Some approaches have been proposed to overcome the breakdown voltage limitation and achieve efficient rectification at high input power levels. The simplest way to increase the power handling capability of a rectifier is by putting N diodes in series to form a N-diode structure with a higher voltage breakdown and improved efficiency at higher power levels [89]. Another approach consists of splitting the input power before rectifying. In [81], a transformer-based power-dividing network is used to split a high power signal into four signals with lower power level that are separately rectified using regular Si-based Schottky diodes, and then the resulting DC voltages are combined at the load. By using this scheme an input power level as high as 41 dBm was handled without reaching the breakdown limit of the diodes.

Rectifiers are commonly designed to work either in a low or high narrow power range, in which the RF-DC conversion efficiency is satisfactory. However, some applications may require extended dynamic range to cover both low and high input power levels. In [89], an adaptive rectifier circuit is proposed, that automatically adapts to the input power level and provides high efficiency over a wide input power range. With that arrangement, an efficiency of more than 50% was kept from -14 dBm to 21 dBm.

Conversely to the serialization of diodes to optimize high power operation, several diodes are often used in parallel, in order to reduce the overall series resistance and consequently reduce their resistive loss at low power levels [87]. However, this approach is not recommended for very high frequencies, as the parallelization of diodes increases the total parasitic capacitance.

Half-wave (Dickson topology) voltage multipliers are widely utilized in passive UHF RFID tags. These rectifiers consist of diodes, pumping capacitors and stage voltage storage capacitors. The pumping capacitors are pre-charged in parallel in the negative half cycle of the RF signal, and in the next positive half cycle, the pumping capacitors feed the current to the grounded storage capacitors. Because the current from the RF signal enters the diodes only half cycle, this topology presents a limited current capability, which drops significantly with increased output load current. Hence, full-wave charge pump circuits were proposed in [90] to overcome the limitations in current driving capability, and thereby improve the efficiency in comparison to half-wave voltage multipliers. The main drawback of the full-wave charge pump is the larger layout area required, since twice the number of diodes are needed.

E. Threshold-compensated CMOS

A major limitation of diode-connected CMOS transistors is the increased threshold voltage, which penalizes the conversion efficiency at very low power levels (this is the case in passive RFID). Therefore, researches have attempted strategies to either reduce the intrinsic threshold voltage of devices by adjusting the physical parameters of the transistors, or compensate the turn-on voltage internally or externally. Several threshold compensation schemes have been proposed. One of them used an external voltage from a battery or a second energy harvester to bias the main high efficiency charge pump circuit [91]. While this is effective to reduce the turn-on voltage of the main rectifier circuit, the requirement of having a battery may be a problem in passive scenarios where a local power source is not desired or available. Other schemes employ self-compensation methods, by using the own DC output generated by the rectifier itself to bias the gate of the transistors [see Fig. 3.5 (a)]. In another approach, rather than using the output voltage of the rectifier, K. Kotani et. al. inserted photovoltaic cells into the gate bias paths to compensate the turn-on voltage of MOSFETs with the photo-generated voltages [92]. Similarly to A. Georgiadis et. al.

who used a solar-assisted RFID tag [51], this is an example of synergistic energy harvesting, combining multiple energy harvesting sources to improve the overall efficiency.

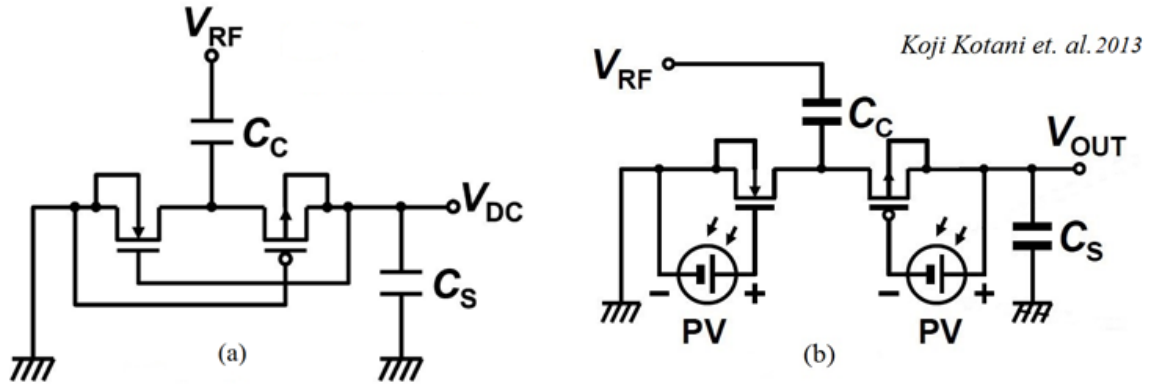


Fig. 3.5 CMOS threshold-compensation schemes. (a) Self- V_{th} cancellation. (b) Photovoltaic-assisted rectifier. Both circuits are voltage doublers using diode-connected nMOS and pMOS transistors. [92]

3.3. Closely-related work: waveform design for improved efficiency

According to the previous literature review, it is clear that the non-zero turn-on voltage is the main cause of efficiency degradation in existing rectifying devices operating at low input power levels, and researchers (specially in the CMOS field) have attempted a number of circuit strategies to deal with this issue.

As an alternative to circuit approaches, waveform design optimization has been investigated to improve WPT efficiency. The use of High PAPR waveforms, with high peak voltage swings and low average power, allows to efficiently overcome the threshold barrier of rectifying devices, while keeping a low average power that complies with regulations and reduces the overall power consumption of the system. This strategy has been recently investigated by using non-conventional waveforms including intermittent CW signals, Ultra Wide Band (UWB) signals, Power-Optimized Waveforms (POW), chaotic signals, white noise, modulated signals and multi-carrier signals [93-99][IV].

In this thesis, we evaluate in-phase high PAPR MS signals, which can provide improved RF-DC conversion efficiency in existing rectifier circuits, specially under low average power conditions, compared to traditional CW signals. Previous work by Trotter et. al. explored a similar concept called POW [96][97]. Recently, C. Valenta also investigated POW for 5.8 GHz energy harvesting circuits [100-101].

References

- [1] Iker Mayordomo, Josef Bernhard, “*Implementation of an adaptive Leakage Cancellation Control for passive UHF RFID Readers*,” IEEE International Conference on RFID, pp. 121-127, April 2011, Orlando.
- [2] Deogracias P. Villame and Joel S. Marciano, Jr., “*Carrier Suppression Locked Loop Mechanism for UHF RFID Readers*,” IEEE RFID 2010, p.p.: 141-145, Orlando, FL, April 2010
- [3] Bin You, Bo Yang, Xuan Wen, and Liangyu Qu, “*Implementation of Low-Cost UHF RFID Reader Front-Ends with Carrier Leakage Suppression Circuit*,” International Journal of Antennas and Propagation, p.p.: 1-8, Volume 2013, Article ID 135203, October 2013.
- [4] Robert Langwieser, Gregor Lasser, Christoph Angerer, Michael Fischer, and Arpad L. Scholtz, “*Active Carrier Compensation for a Multi-Antenna RFID Reader Frontend*,” IEEE, MTT-S, International Microwave Symposium 2012, p.p.:1532-1535, Anaheim – CA, May 2010.
- [5] Thomas Brauner and Xiongwen Zhao, “*A Novel Carrier Suppression Method for RFID*,” IEEE Microwave and Wireless Components Letters, Vol. 19, NO. 3, p.p.: 128-130, MARCH 2009.
- [6] M. Koller et al, “*Adaptive Carrier Suppression for UHF RFID using Digitally Tunable Capacitors*”, EuMC, p.p.: 943-946, Oct 2013, Nuremberg.
- [7] J Lee, j Choi, KH Lee, B Kim, M Jeong, Y Cho, H Yoo, K Yang, S Kim, SM Moon, JY Lee, S Park, W Kong, J Kim, TJ Lee, BE Kim, BK Ko. “*A UHF mobile RFID reader IC with self-leakage canceller.*” IEEE Radio Frequency Integrated Circuits RFIC Symposium, Honolulu, June 2007 (IEEE,Piscataway, 2007), pp. 273–276.
- [8] V. Pillai, H. Heinrich, D. Dieska, P. V. Nikitin, R. Martinez, and K. V. S. Rao, “*An Ultra-Low-Power Long Range Battery/Passive RFID Tag for UHF and Microwave Bands With a Current Consumption of 700 nA at 1.5 V*,” IEEE Transactions on Circuits and Systems I: Regular Papers, vol. 54, no. 7, pp. 1500–1512, 2007.
- [9] J. P. Curty, N. Joehl, C. Dehollain, and M. J. Declercq, “*Remotely Powered Addressable UHF RFID Integrated System*,” IEEE Journal of Solid-State Circuits, vol. 40,no. 11, pp. 2193–2202, 2005.
- [10] U. Karthaus and M. Fischer, “*Fully Integrated Passive UHF RFID Transponder IC with 16.7- μ W Minimum RF Input Power*,” IEEE Journal of Solid-State Circuits,vol. 38, no. 10, pp. 1602–1608, 2003.
- [11] K. V. S. Rao, P. V. Nikitin, and S. F. Lam, “*Antenna Design for UHF RFID Tags: AReview and a Practical Application*,” IEEE Transactions on Antennas and Propagation,vol. 53, no. 12, pp. 3870–3876, 2005.
- [12] Y. Zhang, M. G. Amin, and S. Kaushik, “*Localization and Tracking of Passive RFID Tags Based on Direction Estimation*,” International Journal of Antennas and Propagation, vol. 2007, Article ID 17426, 9 pages, 2007. doi:10.1155/2007/17426.
- [13] Ales Povalac, “*Spatial Identification Methods and Systems for RFID Tags*”, Ph.D. Thesis, Brno Univerisity of Technology, Brno 2012.
- [14] Gonçalves, R., Carvalho, N. B., Magueta, R., Duarte, A. Pinho, P., “*UHF RFID tag antenna for bottle labeling*”, IEEE Antennas and Propagation Society International Symposium (APSURSI), p.p.: 1520-1521, July 2014.
- [15] Gonçalves, R., Carvalho, N. B., Magueta, R., Duarte, A. Pinho, P., “*Investigation into cork substrate printed antennas for RFID applications*”, 7º Congresso Comité Português da URSI, Nov. 2013, Lisboa.
- [16] Orecchini, G., Yang, L., Rida, A., Alimenti, F., Tentzeris, M.M., Roselli, L.: “Green Technologies and RFID: present and future”, Appl. Comput. Electromagn. Soc. J., 2010, 25, (3), pp. 230–238.
- [17] G. Orecchini, F. Alimenti, V. Palazzari, A. Rida, M.M. Tentzeris and L. Roselli, “*Design and fabrication of ultra-low cost radiofrequency identification antennas and tags exploiting paper substrates and inkjet printing technology*”, IET Microw. Antennas Propagation Journal, 2011, Vol. 5, Issue.: 8, pp. 993 – 1001, 2011.

- [18] S.-R. Lee, S.-D. Joo, and C.-W. Lee, "An Enhanced Dynamic Framed Slotted ALOHA Algorithm for RFID Tag Identification," in Proceedings of the Second Annual International Conference on Mobile and Ubiquitous Systems: Networking and Services (MobiQuitous05), 2005, pp. 166–172.
- [19] A. Rohatgi and G. D. Durgin, "Implementation of an Anti-Collision Differential-Offset Spread Spectrum RFID System," in Proceedings of the IEEE Antennas and Propagation Society International Symposium, 2006, pp. 3501–3504.
- [20] P. Nikitin and K. V. S. Rao, "Antennas and Propagation in UHF RFID Systems," in IEEE International Conference on RFID, Las Vegas, TX, 2008, pp. 277–288.
- [21] Stewart J. Thomas and Matthew S. Reynolds, "A 96 Mbit/sec, 15.5 pJ/bit 16-QAM Modulator for UHF Backscatter Communication", IEEE International Conference on RFID, p.p.: 185-190, Orlando, FL, April 2012.
- [22] Ettus Research: www.ettus.com, online 29-08-2015.
- [23] L. Catarinucci, D. De Donno, et.al., "A cost-effective SDR platform for performance characterization of RFID tags," IEEE Transactions on Instrumentation and Measurement, vol. 1, no. 4, pp. 903-911, April 2012.
- [24] M. Buettner and D. Wetherall, "A software radio-based UHF RFID reader for PHY/MAC experimentation," IEEE International RFID Conference, pp.: 134-141, Orlando, April 2011.
- [25] Bo Berglund, Jan Johansson and Thomas Lejon, "High efficiency power amplifiers", Ericsson Review No. 3, 2006.
- [26] N.D. Lopez, J. Hoversten, M. Poulton, Z. Popovic, "A 65-W High-Efficiency UHF GaN Power Amplifier", IEEE International Microwave Symposium, Atlanta, June 2008.
- [27] Johan Sommarek, "Transmitter Architectures with Digital Modulators, D/A Converters and Switching-Mode Power Amplifiers", Ph.D. Thesis, Helsinki University of Technology (Espoo, Finland), June 2007.
- [28] Jason T. Stauth, "Energy Efficient Wireless Transmitters: Polar and Direct-Digital Modulation Architectures", Ph.D. Thesis, Electrical Engineering and Computer Sciences University of California at Berkeley, Feb. 2009.
- [29] Zoya Popovic, David R. Beckett, Scott R. Anderson, Diana Mann, Stuart Walker, Sheldon Fried, "Lunar Wireless Power Transfer Feasibility Study", March 2008.
- [30] Naoki Shinohara, "Beam Control Technologies With a High-Efficiency Phased Array for Microwave Power Transmission in Japan", Proceedings of the IEEE, p.p.: 1448-14-63, Vol. 101, No. 6, June 2013.
- [31] Mehmet Abbak and Ibrahim Tekin, "RFID Coverage Extension Using Microstrip Patch Antenna Array", IEEE Antennas and Propagation Magazine, Feb. 2009.
- [32] Mojix Inc., "Next-generation UHF systems promise to bring a New level of performance", RFID Journal, March/April 2008. Available online, 13-08-2015:
http://www.mojix.com/pdf/RFIDJrnl_PD_MarApr08.pdf
- [33] Graham P. Eloy, US Patent, *Steerable phase array antenna RFID tag locator and tracking system and methods*, US 8742896 B2.
- [34] Daniel Megnet, Heinz Mathis, "Circular Polarized Patch Antenna for 5.8 GHz Dedicated Short-Range Communication", Proceedings of the 39th European Microwave Conference, Rome 2009.
- [35] Bin Lua, Peng Li, "Design of Circular Polarization Microstrip Antenna in RFID Reader for 5.8GHz Electronic Toll Collection Application", International Conference on Microwave Technology and Computational Electromagnetics, 2009.
- [36] Impinj Speedway xPortal Brochure, Available online, 13-08-2015:
<https://support.impinj.com/hc/en-us/articles/202755418-Speedway-xPortal-Brochure>

- [37] James O. McSpadden and Kai Chang, "A dual Polarized Circular Patch Rectifying Antenna at 2.45 GHz for Microwave Power Conversion and Detection", Microwave Symposium Digest, 1994., IEEE MTT-S International, 1994.
- [38] T. Paing, J. Morroni, A. Dolgov, J. Shin, J. Brannan, R. Zane, Z. Popovic "Wirelessly-Powered Wireless Sensor Platform", European Microwave Conference 2007.
- [39] D. Duan and D. Friedman, "Cascaded DC voltages of multiple antenna RF tag front-end circuits", US patent 6243013.
- [40] J. Hyde et al., "RFID tags combining signals received from multiple RF ports", US patent application 20060049917.
- [41] Impinj Monza X-2K Dura Datasheet Rev 1.51 March 24th , 2014. Available 14-08-2015:
<https://support.impinj.com/hc/en-us/articles/202756848-Monza-X-2K-Dura-Datasheet>
- [42] Pavel V. Nikitin and K. V. S. Rao, "Performance of RFID Tags with Multiple RF Ports", IEEE Antennas and Propagation Society International Symposium, p.p.: 5459-5462, June 2007.
- [43] Alien RFID Reader, Hardware Setup Guide ALR-9800, Feb. 2008. Available online 14-08-2015
<ftp://ftp.alientechnology.com/pub/readers/alr9800/docs/Guide,%20Hardware%20Setup,%20ALR-9800.pdf>
- [44] Jin Mitsubi, "UHF Band RFID Readability and Fading Measurements in Practical Propagation Environment", Auto-ID Lab Japan, White Paper Series, Edition 1.
- [45] Joshua David Griffin, "High-Frequency Modulated-Backscatter Communication Using Multiple Antennas", Ph.D. Thesis, Georgia Institute of Technology, May 2009.
- [46] Joshua D. Griffin and Gregory D. Durgin, "Multipath Fading Measurements for Multi-Antenna Backscatter RFID at 5.8 GHz", IEEE International RFID Conference, p.p.: 322-329, Orlando FL., April 2009.
- [47] Deock Ho Ha et al, "A Multi-polarized Antenna system for Combating Multipath Fading in UHF/RFID Frequency Band in Moving Vehicles", 2010 International Conference on Communications and Mobile Computing (CMC), p.p.: 63-67, Shenzhen, April 2010.
- [48] Jun-Seok Park, Jin-Woo Jung, Si-Young Ahn, Hyoung-Hwan Roh, Ha-Ryoung Oh, Yeung-Rak Seong, Yoon-Deock Lee and Kyoung Choi, "Extending the Interrogation Range of a Passive UHF RFID System With an External Continuous Wave Transmitter", IEEE Transactions on Instrumentation and Measurement, p.p.: 2191-1297, Vol. 58, Issue 8, Aug 2010.
- [49] Mojix, "UHF RFID (Mojix) Technology for the Scania Parts Center", Available online, 13-08-2015:
http://mielooandalexander.com/userfiles/projectsfiles/1424190277-20141021_m&a_description_scania_def-web.pdf
- [50] Mojix STAR 3000 System, Available online, 14-08-2015: <http://www.mojix.com/products/>
- [51] A. Georgiadis and A. Collado, "Improving Range of Passive RFID Tags Utilizing Energy Harvesting and High Efficiency Class-E Oscillators", Proc. EuCAP 2012, Prague, March 2012.
- [52] NXP RFID Tag, UCODE G2iL and G2iL+ Product datasheet, Ver. 4.4, 17 March 2014.
Available online, 15-08-2015: http://www.nxp.com/documents/data_sheet/SL3S1203_1213.pdf
- [53] A.P. Sample, J. Braun, A. Parks, J.R. Smith, "Photovoltaic enhanced UHF RFID tag antennas for dual purpose energy harvesting," 2011 IEEE International Conference on RFID (RFID), pp.146-153, 12-14 April 2011.
- [54] Karthaus, U., Fisher, M. "Fully Integrated Passive UHF RF ID Transponder IC with 16.7 μ W Minimum RF Input Power". IEEE J. Solid-State Circ. 2003, 38, 1602-1608.
- [55] Koji, K., Atsushi, S., Takashi, I. "High-Efficiency Differential-Drive CMOS Rectifier for UHF RFIDs". IEEE J. Solid-State Circ. 2009, 44, 3011-3017.

- [56] Huichu Liu et. al. "Tunnel FET RF Rectifier Design for Energy Harvesting Applications", IEEE Journal on Emerging and Selected Topics in Circuits and Systems, Vol.: 4, Issue: 4, p.p.: 400-411, Oct. 2014.
- [57] Zhu, Z.; Jamali, B.; Peter, H.C. "Brief Comparison of Different Rectifier Structures for HF and UHF RFID (Version 1.0)", Auto-ID Lab, University of Adelaide, Australia, 2004.
- [58] Alexander Vaz, Aritz Ubarretxena, Daniel Pardo, Ifiaki Sancho, Roc Berenguer, "Design Methodology of a Voltage Multiplier for Full Passive Long range UHF RFID", 3rd European Workshop on RFID Systems and Technologies (RFID SysTech), 2007
- [59] Yeager, D.J.; Holleman, J.; Prasad, R.; Smith, J.R.; Otis, B.P. "Neural WISP: A Wirelessly Powered Neural Interface with 1-m Range. IEEE Trans. Biomed. Circ. Syst. 2009, 3, 379-387.
- [60] De Vita, G.; Iannaccone, G. "Design Criteria for the RF Section of UHF and Microwave Passive RFID Transponders". IEEE Trans. Microw. Theor. Tech. 2005, 53, 2978-2970.
- [61] A. Shameli, A. Safarian, A. Rofougaran, M. Rofougaran, and F. De Flaviis, "Power harvester design for passive UHF RFID tag using a voltage boosting technique," IEEE Trans. Microwave Theory Tech., vol. 55, no. 6, pp. 1089-1097, June 2007.
- [62] D. Liu, F. Li, X. Zou, Y. Liu, X. Hui, and X. Tao, "New analysis and design of a RF rectifier for RFID and implantable devices," Sensors, vol. 11, pp. 6494-6508, June 2011.
- [63] G. Vera, A. Georgiadis, A. Collado, and S. Via, "Design of a 2.45GHz rectenna for electromagnetic (EM) energy scavenging," in Proc. IEEE Radio and Wireless Symp., 2010, pp. 61-64.
- [64] Bemdie Strassner and Kai Chang, "5.8 GHz circular polarized rectenna for microwave power transmission", Energy Conversion Engineering Conference and Exhibit, 2000.
- [65] C. Chin, Q. Xue, and C. Chan, "Design of a 5.8-GHz rectenna incorporating a new patch antenna," IEEE Antennas Wireless Propag. Lett., vol. 4, pp. 175-178, June 2005.
- [66] M. Furukawa, Y. Takahashi, T. Fujiware, S. Mihara, T. Saito, Y. Kobayashi, S. Kawasaki, N. Shinohara, Y. Fujino, K. Tanaka, and S. Sasaki, "5.8-GHz planar hybrid rectenna for wireless powered applications," in Proc. 2006 Asia-Pacific Microwave Conf., Dec., pp.1611-1614.
- [67] Fang Zhang, Hee Nam and Jong-Chul Lee, "A novel compact folded dipole architecture for 2.45 GHz rectenna application", Microwave Conference, Asia Pacific, 2009
- [68] U. Olgun, C. Chen, and J. Volakis, "Wireless power harvesting with planar rectennas for 2.45 GHz RFIDs," in Proc. 2010 URSI Int. Symp. Electromagnetic Theory, 2010, pp. 329-331.
- [69] Y. Ren, M. Li, and K. Chang, "35 GHz rectifying antenna for wireless power transmission," Electron. Lett., vol. 43, no. 11, pp. 602-603, Nov. 2007.
- [70] W. C. Brown, "Electronic and mechanical improvement of the receiving terminal of a free-space microwave power transmission system," Raytheon Company, Wayland, MA, Tech. Rep. PT-4964, NASA Rep. CR-135194, Aug. 1977.
- [71] W. C. Brown and J. F. Triner, "Experimental thin-film, etchedcircuit rectenna", IEEE MTT-S Int. Microwave Symp. Dig., Dallas, TX, June 1982, pp. 185-187.
- [72] P. Koert, J. Cha, and M. Macina, "35 and 94 GHz rectifying antenna systems", SPS 91-Power from Space Dig., Paris, France, Aug. 1991, pp. 541-547
- [73] T. Le, K. Mayaram, and T. Fiez, "Efficient far-field radio frequency energy harvesting for passively powered sensor networks," Solid-State Circuits, IEEE Journal of, vol. 43, no. 5, pp. 1287-1302, 2008.
- [74] S. Scorpion, L. Larcher, A. Bertacchini, L. Vincetti, and M. Maini, "An integrated rf energy harvester for uhf wireless powering applications," in Wireless Power Transfer (WPT), 2013 IEEE, 2013, pp. 92-95.
- [75] J. Lee, B. Lee and H. Kang "A high sensitivity, CoSi₂-Si Schottky diode voltage multiplier for UHF-band passive RFID tag chips", IEEE Microw. Wireless Compon. Lett., vol. 18, no. 12, pp.830 -832 2008.

- [76] G. Papotto, F. Carrara, and G. Palmisano, "A 90-nm CMOS Threshold-Compensated RF Energy Harvester", IEEE J. Solid-State Circuits, Vol. 46, pp.1985-1997, 2011.
- [77] J. O. McSpadden, L. Fan and K. Chang "Design and Experiments of a High-Conversion Efficiency 5.8-GHz Rectenna", IEEE Trans. Microwave Theory Tech., vol. 46, pp.2053 -2060 1998.
- [78] Erez Falkenstein, Michael Roberg, and Zoya Popović, "Low-Power Wireless Power Delivery", IEEE Transactions on Microwave Theory and Techniques, Vol.: 60, No.: 7, July 2012.
- [79] C. R. Valenta and G. D. Durgin, "Harvesting wireless power: Survey of energy-harvester conversion efficiency in far-field, wireless power transfer systems", IEEE Microw. Mag., Vol. 15, No. 4, pp.108 - 120 2014.
- [80] HSMS-285x Series, Surface Mount Zero Bias Schottky Diodes, Datasheet, Avago Technologies: <http://www.avagotech.com/>.
- [81] Chong-Yi Liou et. al. "High-Power and High-Efficiency RF Rectifiers Using Series and Parallel Power-Dividing Networks and Their Applications to Wirelessly Powered Devices", IEEE Transactions on Microwave Theory and Techniques, Vol.: 61, No.: 1, p.p.: 616-624, Jan 2013.
- [82] C. Gómez, José A. García, A. Mediavilla, and A. Tazón, "A High Efficiency Rectenna Element using E-pHEMT Technology", 12th GAAS Symposium, Amsterdam 2004.
- [83] Qiang Li, Junyu Wang, Yifeng Han, Hao Min, Feng Zhou, "Fabrication of Schottky Diode in Standard CMOS Process", Available Online, 01-09-2015: ResearchGate.
- [84] Brown, W.C, "Rectenna technology program: ultra light 2.45 GHz rectenna and 20 GHz rectenna," Raytheon Company, Tech. Rep., 1987.
- [85] Zied Harouni, Lotfi Osman and Ali Gharsallah, "Efficient 2.45 GHz Rectenna Design with High Harmonic Rejection for Wireless Power Transmission", IJCSI International Journal of Computer Science Issues, Vol. 7, Issue 5, September 2010
- [86] Shohei et. al. "Efficiency and harmonics generation in microwave to DC conversion circuits of half-wave and full-wave rectifier types", Microwave Workshop Series on Innovative Wireless Power Transmission: Technologies, Seystems, and Applications, p.p.: 15-18, Kyoto, Japan, May 2011.
- [87] Ken Hatano, Naoki Shinohara, Tomohiko Mitani, Kenjiro Nishikawa, Tomohiro Seki, Ken Hiraga, "Development of Class-F Load Rectennas", International Microwave Workshop Series on Innovative Wireless Power Transmission: Technologies, Systems, and Applications (IMWS), 2011.
- [88] Andrei Grebennikov, "Load Network Design Technique for Class F and Inverse Class F PAs", High Frequency Electronics, May 2011.
- [89] Hucheng Sun, Zheng Zhong, and Yong-Xin Guo, "An Adaptive Reconfigurable Rectifier for Wireless Power Transmission", IEEE Microwave and Wireless Components Letters, Vol.:23, No.: 9, September 2013.
- [90] Alexander Vaz, Aritz Ubarretxena, Daniel Pardo, Ifiaki Sancho, Roc Berenguer, "Design Methodology of a Voltage Multiplier for Full Passive Long range UHF RFID", 3rd European Workshop on RFID Systems and Technologies (RFID SysTech), 2007
- [91] T. Feldengut, R. Kokozinski, and S. Kolnsberg, "A UHF Voltage Multiplier Circuit Using a Threshold-Voltage Cancellation Technique," in Research in Microelectronics and Electronics, July 2009, pp. 288 – 291.
- [92] Koji Kotani, "Highly Efficient CMOS Rectifier Assisted by Symmetric and Voltage-Boost PV-Cell Structures for Synergistic Ambient Energy Harvesting", IEEE Custom Integrated Circuits Conference, p.p.: 1-4, San Jose, CA, Sept. 2013.
- [93] Hisanori Matsumoto and Ken Takei, "An Experimental Study of Passive UHF RFID System with Longer Communication Range", Proceedings of Asia-Pacific Microwave Conference 2007.
- [94] Chun-Chih Lo, Yu-Lin Yang, Chi-Lin Tsai, Chieh-Sen Lee, and Chin-Lung, Yang, "Novel Wireless Impulsive Power Transmission to Enhance the Conversion Efficiency for Low Input Power", Microwave Workshop Series on Innovative Wireless Power Tansmission, 20011.

- [95] Yu-Lin Yang, Chin-Lung Yang, Chi-Lin Tsai, and Chieh-Sen Lee, "*Efficiency Improvement of the Impulsive Wireless Power Transmission*", Microwave Workshop Series on Innovative Wireless Power Transmission, 20011.
- [96] M. S. Trotter, J. D. Griffin and G. D. Durgin, "*Power-Optimized Waveforms for Improving the Range and Reliability of RFID Systems*", 2009 IEEE International Conference on RFID.
- [97] M.S. Trotter, G.D. Durgin, "*Survey of Range Improvement of Commercial RFID Tags With Power Optimized Waveforms*", IEEE International Conference on RFID, 2010.
- [98] Ana Collado and Apostolos Georgiadis, "*Improving Wireless Power Transmission Efficiency Using Chaotic Waveforms*", International Microwave Symposium - IMS2012, Moteréal, Canadá, June 2012.
- [99] A. Collado, A. Georgiadis, "Optimal Waveforms for Efficient Wireless Power Transmission," Microwave and Wireless Components Letters, IEEE , vol.24, no.5, pp.354,356, May 2014.
- [100] C.R.Valenta, G.D. Durgin, "*Rectenna performance under power-optimized waveform excitation*," RFID (RFID), 2013 IEEE International Conference on , vol., no., pp.237,244, April 30 2013-May 2 2013.
- [101] C. R. Valenta, "*Microwave-Energy Harvesting at 5.8GHz for Passive Devices*", Ph.D. Thesis, School of Electrical and Computer Engineering, Georgia Institute of Technology, August 2014.

4. UNCONVENTIONAL WAVEFORM DESIGN FOR WIRELESS POWER TRANSFER

4.1. Introduction

This chapter addresses the first question formulated in the introduction section of this thesis “*Can the same effect that leads to errors in power probe measurements of high PAPR signals be used to boost the efficiency of similar RF-DC converter circuits used in WPT?*”.

Traditionally, WPT has been carried out using constant envelope CW signals. However, it has been shown recently that high PAPR waveforms can improve the efficiency of existing rectifying circuits, especially at low average power levels. This can potentially increase the reading range of passive-backscatter systems. Curiously, the first electromagnetic signals successfully generated, transmitted and detected by Heinrich Hertz were damped waveforms with non-constant envelope [1], which were utilized for many years in wireless telegraphy and also in some WPT experiments conducted by Tesla [2]. However, due to large spectrum occupancy, damped waves were banned later. They were replaced with CW signals (first generated by Ernst Alexanderson in 1902 [3]) which have been adopted for power transfer since Brown’s MPT experiments in the 1960’s.

The theoretical analysis of CW radio path presented in chapter 2 [equations (2.25) and (2.26), and Fig. 3.4] shows that, unlike conventional wireless communication systems, which are mainly limited by noise and receiver sensitivity, passive-backscatter systems are primarily limited by the power downlink, i.e., the reader-to-transponder energy transfer. This was also theoretically predicted in [4][5], and confirmed by practical experiments in [6], where a far RFID listener device was used to capture the signal backscattered from a tag while being interrogated by a closer principal RFID reader. In that experiment, the RFID listener was able to receive and decode the uplink/backscattered signal 35 meters away from the tag, a distance well beyond the maximum attainable range of current RFID systems (up to 10m). This shows that the more stringent limit on range is in fact imposed by downlink. A closer look reveals that the downlink limitation lies on the reduced RF-DC conversion efficiency of existing energy harvesting circuits at low power level regime. Because Schottky diodes and CMOS devices commonly used in rectifier circuits exhibit a non-zero turn-on voltage, a certain amount of energy is needed to overcome the electrical barrier of the device and thereby the RF-DC conversion efficiency at low input power levels is degraded. This is evident in the state-of-the-art efficiency values presented in Fig. 3.4 of chapter 3.

In order to maximize the RF-DC conversion efficiency, circuit level optimization is conventionally carried out (several techniques are reviewed in the previous chapter). Alternatively, the RF-DC conversion efficiency can be boosted by selecting properly formatted waveforms, such as high PAPR in-phase MS signals, that are capable of efficiently surpassing the turn-on voltage of rectifying devices at low average power levels. In [V], we have presented a survey on the use non-

conventional waveforms for WPT, including chaotic signals, intermittent CW, UWB signals, multi-carrier signals, harmonic signals, modulated signals and white noise.

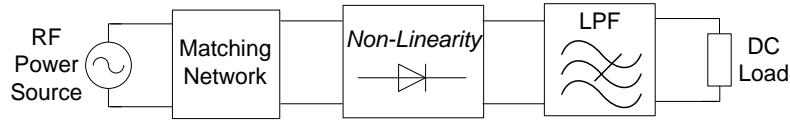


Fig. 4.1 Basic blocks of an RF-DC conversion circuit

4.2. RF-DC power conversion basics

Figure 4.1 depicts the block diagram of an RF-DC converter system, composed of an RF power source, a matching circuit to allow maximum power transference, a non-linear rectifying device, that is the main component of the circuit, followed by a low-pass filter and a DC load. The non-linear device transforms the input AC signal at frequency f_0 into a DC component plus fundamental and harmonic components: $y_{out} = NL[x_{in}] = Y(DC) + Y(f_0) + Y(2f_0) + Y(3f_0) + \dots + Y(nf_0)$. In order to depurate only the DC component, a low-pass filter is used to remove the AC components of the rectified signal.

4.3. Typical RF-DC converter topologies

Figure 4.2 depicts the most popular harvester topologies, namely the shunt diode rectifier [Fig.4.2(a)], the series diode rectifier [Fig.4.2(b)], and the N-stage Dickson voltage multiplier or charge pump [Fig.4.2(d)]. Charge pumps are typically employed in passive RFID tags and single diode rectifiers, especially the microwave version of the shunt rectifier, are commonly used for EM ambient energy harvesting and MPT applications.

The voltage doubler or single-stage charge pump [dashed circuit in Fig.4.2(d)], which is the cell unit of a Dickson charge pump, is composed of a pumping capacitor at the input, a shunt diode, a series diode and a storage capacitor at the output. It operates as follows: when the capacitors are uncharged and the input signal with peak amplitude V_p is in the negative cycle, the series diode is cut and the pumping capacitor is charged with a voltage $-V_p$ through the shunt diode; when the input waveform swings to its positive cycle, the shunt diode is cut, the series diode conducts, and the peak amplitude of the input signal, $+V_p$, is summed to the pre-charged voltage, yielding a voltage of $2V_p$ in the output storage capacitor. The charge pump has a similar operation, being the DC output of each voltage doubler stage used as a reference level for the next stage, such that the maximum voltage at the output of the N -th stage is given by $(2N-1)(V_p - 2V_D)$, where N is the number of stages, V_p is the peak amplitude of the AC signal and V_D is the voltage drop in the diodes.

Typical efficiency curves of different RF-DC converter circuits are presented in Fig.4.3, from which two main conclusions can be drawn. First, the efficiency depends on the selected circuit

topology, and the lower the number of devices, the higher the efficiency. This is explained because of the need for a minimum amount of input power to switch on the rectifying devices and also due to the increase in parasitic losses as the number of devices increases. Nevertheless, the higher the number of stages, the higher the collected DC voltage. For this reason, charge pumps are used in RFID tags to boost the output DC to a level compliant with tag electronics. Second, the efficiency depends on the available power at the input of the circuit: for low power levels the efficiency is low because the rectifying device is not completely switched on. As the input power increases the efficiency increases and reaches a maximum value right before the input amplitude reaches the diode breakdown voltage. After this point, diode reverse current starts to be significant and the efficiency starts to drop. Losses due to higher order harmonics also increase with the increase in the input power level.

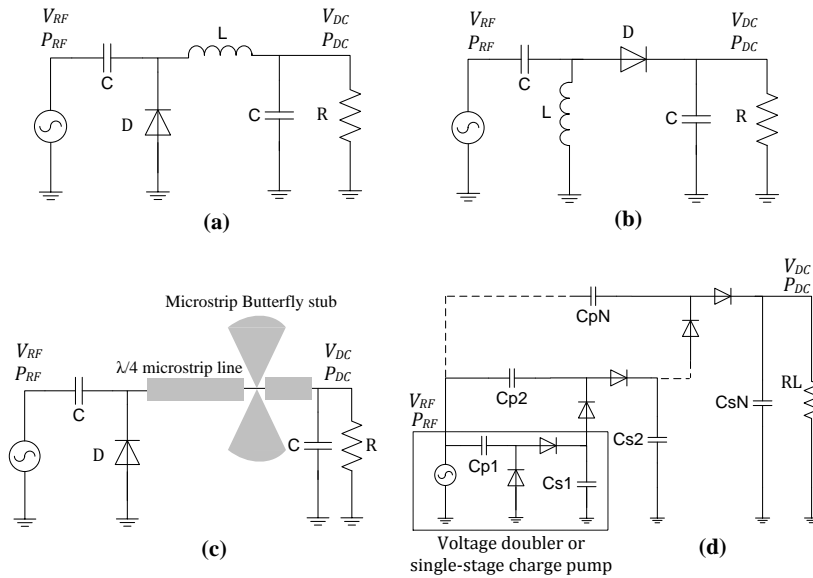


Fig. 4.2 Typical energy harvesting circuit topologies. (a) Shunt diode rectifier. (b) Series diode rectifier. (c) Shunt diode rectifier using microstrip $\lambda/4$ stubs. (d) N-stage Dickson voltage multiplier.

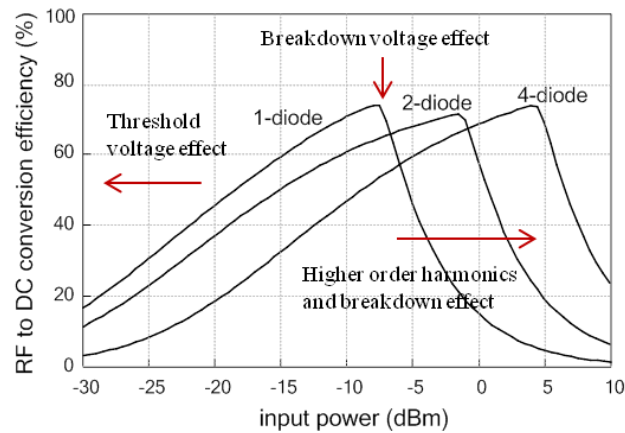


Fig.4.3 Typical efficiency curves of different rectifying circuits.

4.4. Rectifying device characterization and modeling

The Schottky diode is the key component of many rectifying circuits. Its circuit model (Fig.4.4) comprehends a nonlinear junction current source $i_j(v_j)$, shunted by a nonlinear junction capacitance $C_j(v_j)$ and a series parasitic resistance R_s . Packaged diodes also include a parasitic package capacitance (C_p) and inductance (L_p).

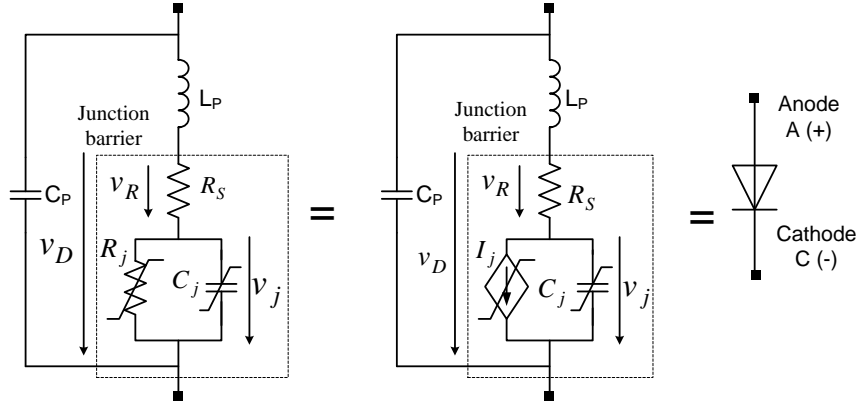


Fig. 4.4 Physical model of a Schottky diode

The non-linear forward and reverse breakdown I-V characteristics (I_f and I_{br}) of the junction barrier can be described respectively by (4.1) [7] and (4.2) [8], and the total diode current is given by (4.3).

$$I_f = I_S(e^{\frac{qV_j}{\eta kT}} - 1) = I_S(e^{\frac{V_j}{\eta V_t}} - 1) = I_S(e^{\frac{V_D - R_S I_f}{\eta V_t}} - 1) \quad (4.1)$$

$$I_{br} = I_{BV} e^{-\frac{V_j + V_{br}}{V_t}} = -I_{BV} e^{-\frac{V_D - R_S I_{br} + V_{br}}{V_t}} \quad (4.2)$$

$$I_D = I_f + I_{br} \quad (4.3)$$

where I_S is the diode reverse saturation current, k is the Boltzmann constant ($1.3806488 \times 10^{-23} \text{ m}^2 \text{ kg s}^{-2} \text{ K}^{-1}$), $V_t = kT/q$ is the thermal voltage ($\approx 26\text{mV}$ @ room temperature), T is the junction temperature in Kelvin (room temperature = 298K), q is the electron charge ($1.60217657 \times 10^{-19}$ coulombs), η is the diode ideality factor, used to model imperfections in the junction, V_j is the voltage across the junction barrier, which is equal to an external voltage applied to the diode, V_D , minus the voltage drop in the parasitic series resistor R_s , V_{bi} is the built-in potential, V_{br} is the reverse breakdown voltage and I_{BV} is the breakdown saturation current. Note that (4.1) and (4.2) are

both non-linear equations that do not have a closed-form analytical solution and are treated numerically in the RF-DC model presented in Appendix A.

Figure 4.5 shows the typical I-V characteristic curve described by equations (4.1)-(4.3). According to (4.1), at low forward (positive) current, the voltage drop across the parasitic series resistance is insignificant and the diode behavior is dominated by the non-linear resistance of the Schottky barrier. At very high positive bias levels, the ohmic resistance R_S dominates, and the I-V curve assumes a linear relationship. For negative bias levels above the breakdown voltage, the exponential terms in (4.1) and (4.2) are negligible and the total diode current (4.3) approximates a constant value equal to $-I_S$. Below the breakdown voltage, equation (4.2) governs the diode behavior. Depending on the input power level, the zero-bias Schottky detector operates in different regimes as illustrated in Fig. 4.6: at very low power level (typically below -20 dBm, 20mV), the diode operates in the square-law region where it produces an average DC output proportional to the average input power [9]. Above 0 dBm (>300mV), the diode enters into forward conduction in each positive cycle of the carrier, and the peak RF voltage is held by the output smoothing capacitor [see Fig. 4.7(a)]. In this regime, known as linear, the rectifier behaves as a peak or envelope detector, and the output DC is proportional to the input peak amplitude minus the voltage drop across the diode. The region between -20 dBm and 0 dBm is said to be a transition region. At very high input power levels, the DC output compresses due to the breakdown effect (described next).

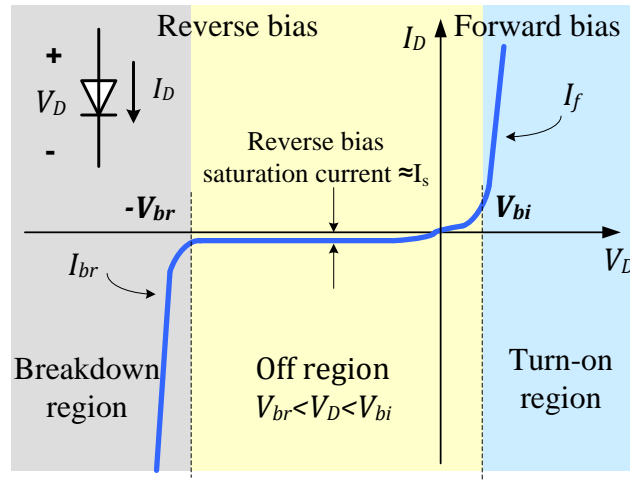


Fig. 4.5 Typical DC I-V curve of a Schottky diode and respective operating regions

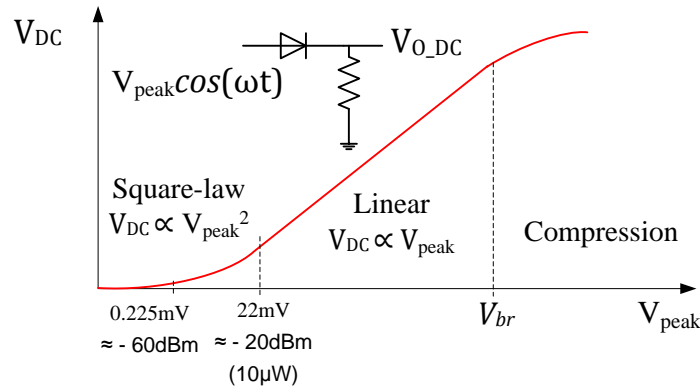
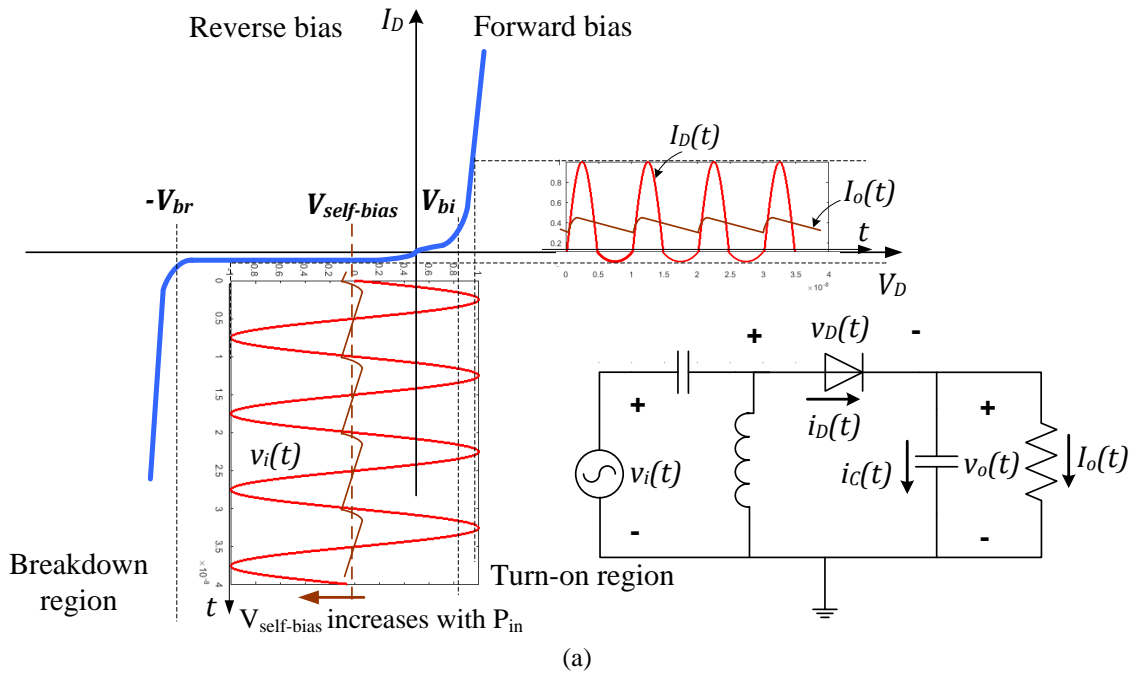


Fig. 4.6 Typical RF-DC characteristic of a detector circuit, illustrating the operation in square-law, linear and compression regions.

4.5. CW envelope detection

The rectification of a single RF carrier in an envelope detector (linear regime) is illustrated in Fig.4.6: in the positive cycle of the input signal $v_i(t)$, whenever the total signal across the diode $v_D(t)$ (input signal minus the generated DC output) is larger than the diode turn-on voltage ($v_D(t) > V_{bi}$), the output capacitor is charged through the diode and the peak RF voltage (minus the drop in the diode) is held by the output smoothing capacitor. In the negative cycles of the input signal ($v_D(t) < V_{bi}$), the charge stored in the output capacitor bleeds thorough the load resistance. The low-pass filter, formed of the output capacitor and load resistance, ideally filters out all the RF components generated in the rectification process, allowing only the DC component to reach the load.



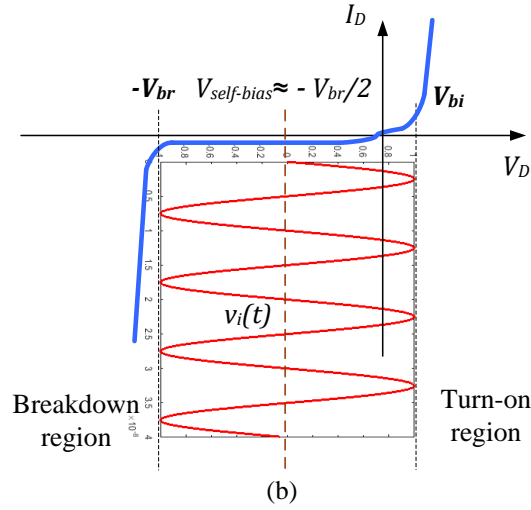


Fig. 4.7 (a) Illustration of single-carrier rectification in a series diode detector. (b) Breakdown effect.

4.5.1. Self-biasing and breakdown effects

Although the rectifying devices used in WPT applications are not intentionally biased (since a local DC source is not available in battery-less applications), diode rectifiers present a self-biasing mechanism via the DC voltage collected from the RF signal. Initially, the output capacitor is uncharged, the diode is zero-biased and the total signal $V_D(t)$ applied to the diode is solely due to the input signal $v_i(t)$. When the input signal satisfies the turn-on condition, the output capacitor starts charging and the total voltage applied to the diode becomes equal to $v_D(t) = v_i(t) + V_{self-bias}$, where $V_{self-bias}$ is the self-bias voltage, which is given by the mean value of the signal across the diode (equation 4.4). If the turn-on condition maintains ($v_i(t) + V_{self-bias} > V_{bi}$) and the input signal continue to increase, then the DC output and thereby the self-bias will continue to increase (Fig. 4.7). Once the amplitude of the signal across the diode reaches the diode threshold voltage V_{br} , a significant amount of reverse current will start to flow through the diode in the negative cycles of the input signal, which contributes to decrease the average current across the diode and to degrade the RF-DC efficiency as the input signal increases (see Fig. 4.7). From this point on, regardless of any increase in the input signal, the generated DC voltage will be fixed to a maximum value of approximately $V_{br}/2$. Therefore, the maximum DC power produced by a single diode rectifier is limited by (4.5).

$$V_{self-bias} = \langle v_D(t) \rangle = \frac{1}{2\pi} \int_0^{2\pi} (v_i(t) - V_{DC}) d\varphi = -V_{DC} \quad (4.4)$$

where the operator $\langle . \rangle$ denotes the average over time, and V_{DC} is the output DC voltage produced by the rectifier. Note that the diode is biased with a voltage symmetrical to its own generated DC.

$$P_{DC_MAX} = \frac{V_{br}^2}{4R_L} \quad (4.5)$$

4.6. High PAPR signal rectification

High PAPR waveforms are able to enhance the RF-DC conversion efficiency of energy harvesting circuits, especially at low input power level. This is due to their greater ability to overcome the built-in potential of the rectifying devices when compared to constant envelope CWs. In order to evaluate the impact of the high PAPR feature in an envelope detector circuit, an analytical-numerical model [based on the diode equations (4.1)-(4.3)] is derived in Appendix A. The model uses a pulsed signal with a variable amplitude and duty-cycle to mimic a general high PAPR signal. Given the input signal amplitude and duty-cycle (which determine the signal's PAPR) and the diode parameters, the model was used to predict the output DC voltage, RF-DC conversion efficiency and efficiency gain, as functions of input average power and PAPR. The following conclusions were drawn from the preliminary model results [please refer to Fig.A.3 in appendix A]:

- 1) At low power levels, as the PAPR increases, the RF-DC conversion efficiency increases, which is attributed to the greater ability to overcome the built-in potential of the diode.
- 2) For higher power levels, however, the increase in PAPR degrades the efficiency. This effect is due to an increased voltage drop across the diode series resistance and consequent resistive loss.
- 3) Moreover, as the PAPR increases, the breakdown is reached earlier and the maximum efficiency is significantly decreased.

In this work, the high PAPR feature is achieved by constructively summing several sinusoidal carriers to form a time-domain waveform with high peaks and low average power level. The rectification of such MS signal is discussed in the next section. Note that although the model presented in Appendix A considers a general high PAPR signal, the conclusions drawn from that model are valid for high PAPR MS signals. This is confirmed by the similarities between the model predictions on Fig. A.3 (d)-(e) and the simulated and measured gain curves obtained in the next section for the MS signals.

4.7. Using multi-sines for wireless power transfer

4.7.1. MS signal definition

A MS signal results from the sum of several sine waves each with a given amplitude, phase and frequency. In order to create a high PAPR signal, the sine waves must be constructively combined in phase. In this case, the higher the number of subcarriers, the higher the PAPR and the higher the signal bandwidth. A MS signal can be expressed in the time-domain as

$$S_{MS}(t) = \sum_{n=1}^N V_n \exp(j(\omega_{min} + (n-1)\Delta\omega)t + \varphi_n)) \quad (4.6)$$

where V_n , $\omega_{min} + (n-1)\Delta\omega$, and φ_n are respectively the amplitude, frequency and phase of the individual subcarriers, ω_{min} is the lowest frequency component, N is the number of subcarriers, and $\Delta\omega$ is the frequency spacing between them. The total signal bandwidth, the maximum² peak amplitude ($V_{peakMAX}$), the peak and average power, and the maximum PAPR of the MS signal are affected by the number of subcarriers, their amplitudes, phases and frequency spacing, and are given respectively by:

$$\begin{aligned} B_w &= (N-1)\Delta\omega \\ V_{peakMAX} &= NV_n \\ P_{peak} &= \frac{1}{R_L} N^2 V_n^2 \\ P_{AV} &= \frac{1}{2R_L} N V_n^2 \\ PAPR &= \frac{P_{peak}}{P_{AV}} = 2N \Rightarrow PAPR(dB) = 10 \log_{10}(2N) \end{aligned} \quad (4.7)$$

It may be convenient to design the MS with the same average power as a given CW signal. This can be done by making $V_1 \dots V_N = V_{CW}/\sqrt{N}$, where V_{CW} is the peak amplitude of the CW signal and N is the number of subcarriers of the MS signal. The top of Fig. 4.8 shows a 4-tone MS signal with a random phase arrangement (left) and a 4-tone MS with 0° phase arrangement overlapped with an average power-equivalent CW (right). The respective frequency spectra are depicted on the bottom of Fig. 4.8. Notice the higher peak amplitudes of the MS in the time-domain waveform, which implies the spreading of the spectrum with respect to a CW with the same average power. Note also that, although the 0° phase arrangement provides the highest PAPR, the random phase arrangement is still overpassing the CW in terms of PAPR.

² Maximum peak is obtained when the subcarriers are phase-synchronized, which occurs for a constant phase progression as discussed later.

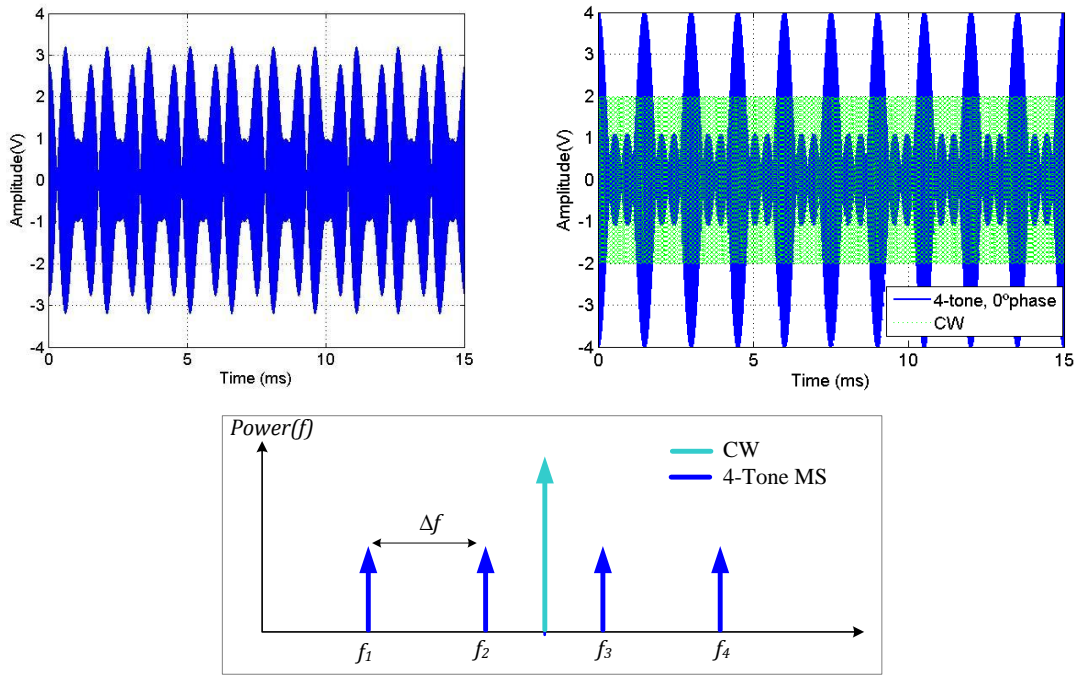


Fig. 4.8 (a) Time-domain waveform of a 4-tone MS with random phase arrangement. (b) 4-tone MS with 0° phase arrangement (blue signal) overlapped with a CW with same average power (green signal). (c) frequency spectrum of a CW and MS signal.

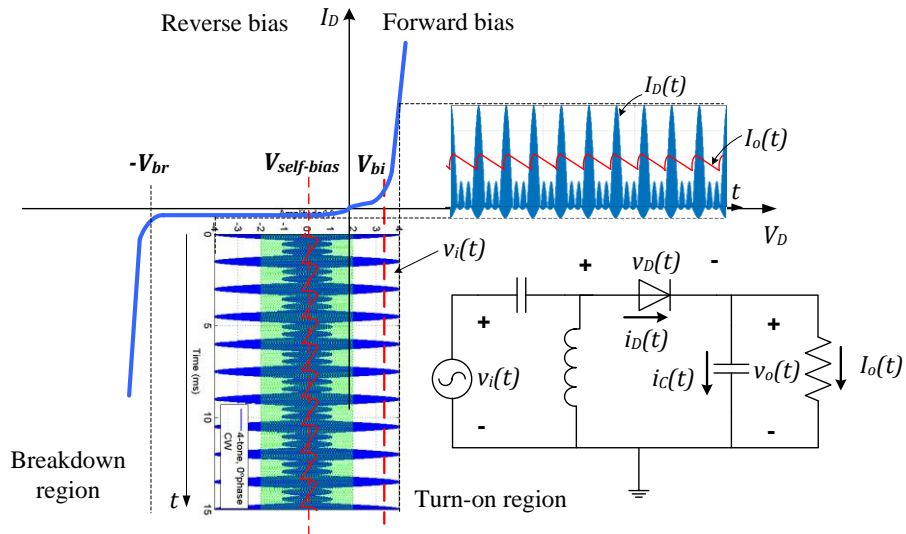


Fig.4.9 CW (green signal) versus MS (blue signal) rectification.

4.7.2. Multi-sine rectification

The rectification of a high PAPR MS signal is illustrated in Fig. 4.9. In comparison with a CW signal with the same average power, the high PAPR MS signal provides higher time-domain peaks. As a consequence, for low average power levels (similarly to the general high PAPR signals

evaluated in Appendix A), the MS can more easily overpass the device turn-on voltage and force it into a more efficient regime than a CW with the same average power would do.

4.7.3. Memoryless model to describe MS RF-DC conversion

In the forthcoming analysis, the Schottky diode current is approximated by a memory-less Taylor polynomial expansion around a quiescent bias point (V_{bias} , I_{bias}) as done in [IV]. Although simple, this model is useful to understand the general non-linear behavior of the rectifier under CW and MS signals, and also to assess the impact of MS parameters such as phase arrangement. The current across the diode is given by:

$$i_D(t) \approx \sum_{i=0}^N k_i (v_D(t) - V_{bias})^i = \sum_{i=0}^N k_i (v_i(t) - v_o(t) - V_{bias})^i \quad (4.8)$$

where $v_D(t) = v_i(t) - v_o(t)$, the bias point is taken as the self-bias voltage as given by equation (4.4), and k_0, k_1, \dots, k_N are the coefficients of the Taylor model, which are obtained from the successive derivatives of the diode current with respect to the diode voltage, taken at the bias point [7]:

$$k_0 = I_{bias} = I_S(e^{\frac{V_{bias}}{nV_t}} - 1); \dots; k_i = \frac{1}{i!} \frac{\partial^i I_D}{\partial V_D^i} \Big|_{V_D=v_{bias}} = \frac{I_S}{i!} \frac{e^{\frac{V_{bias}}{nV_t}}}{(nV_t)^i} \quad (4.9)$$

By assuming that the output capacitor is high enough such that the steady-state output voltage is constant [$v_o(t) = V_{DC}$], and by taking the self-bias quiescent point ($V_{bias} = -V_{DC}$), it follows that,

$$\begin{aligned} i_D(t) = & I_S(e^{\frac{-V_{DC}}{nV_t}} - 1) + \frac{I_S}{1!} \frac{e^{\frac{-V_{DC}}{nV_t}}}{(nV_t)^1} v_i(t) + \frac{I_S}{2!} \frac{e^{\frac{-V_{DC}}{nV_t}}}{(nV_t)^2} (v_i(t))^2 + \frac{I_S}{3!} \frac{e^{\frac{-V_{DC}}{nV_t}}}{(nV_t)^3} (v_i(t))^3 \\ & + \frac{I_S}{4!} \frac{e^{\frac{-V_{DC}}{nV_t}}}{(nV_t)^4} (v_i(t))^4 + \dots \frac{I_S}{i!} \frac{e^{\frac{V_{bias}}{nV_t}}}{(nV_t)^i} (v_i(t))^i \end{aligned} \quad (4.10)$$

For the purpose of finding the output DC using the model (4.10), only the even order terms are considered ($i=0,2,4,6,\dots$), as the odd order ones do not contribute to the DC component. Considering the first even terms up to the fourth order as done previously in [IV], and exciting the system (4.10) with a single tone signal with frequency ω_1 , amplitude V_A and phase φ_1 ,

$$v_i(t) = V_A \cos(\omega_1 t + \varphi_1) \quad (4.11)$$

the following output current is produced:

$$i_D(t) \approx k_0 + \frac{1}{2}V_A^2k_2 + \frac{3}{8}V_A^4k_4 + \frac{1}{2}V_A^2k_2\cos(2\omega_1t + 2\varphi_1) + \frac{1}{2}V_A^4k_4\cos(2\omega_1t + 2\varphi_1) + \frac{1}{8}V_A^4k_4\cos(4\omega_1t + 4\varphi_1) \quad (4.12)$$

Recalling the assumption of constant DC output imposed by the output low-pass filter, the current components at RF frequencies, namely at $2\omega_1$ and $4\omega_1$, are eliminated, and the remaining term is a pure DC component that gives the average value of the diode current:

$$I_{DC} \approx k_0 + 0.5V_A^2k_2 + 0.375V_A^4k_4 = \frac{V_{DC}}{R_L} \quad (4.13)$$

At low power regime (square-law), the second order term k_2 dominates, and the output DC can be approximated by $\frac{1}{2}V_A^2k_2$, which provides power information since it is proportional to the square of the input amplitude. This is the key rule for average power measurements at low power levels.

Now, in order to evaluate the system (4.10) under MS excitation, consider an evenly-spaced 4-tone MS signal (4.14) whose individual subcarriers have amplitudes $V_1 = V_2 = V_3 = V_4 = V_B$, relative phases $\varphi_1, \varphi_2, \varphi_3$ and φ_4 , and evenly-spaced frequencies $\omega_1, \omega_2 = \omega_1 + \Delta\omega, \omega_3 = \omega_1 + 2\Delta\omega$ and $\omega_4 = \omega_1 + 3\Delta\omega$, where $\Delta\omega$ is a constant subcarrier frequency spacing:

$$v_i(t) = V_B\cos(\omega_1t + \varphi_1) + V_B\cos(\omega_2t + \varphi_2) + V_B\cos(\omega_3t + \varphi_3) + V_B\cos(\omega_4t + \varphi_4) \quad (4.14)$$

Substituting (4.14) in (4.10), and after low-pass filtering, the following output DC component is obtained:

$$I_{DC}(\varphi_1, \varphi_2, \varphi_3, \varphi_4) \approx k_0 + \frac{1}{2}(4V_B^2k_2 + 21V_B^4k_4 + 3V_B^4k_4\cos(2\varphi_3 - \varphi_2 - \varphi_4) + 3V_B^4k_4\cos(-2\varphi_2 + \varphi_1 + \varphi_3) + 6V_B^4k_4\cos(\varphi_1 - \varphi_2 - \varphi_3 + \varphi_4)) \quad (4.15)$$

In order to set MS signal to be the same average power as the single-carrier, we make $V_B = V_A/\sqrt{N}$, where $N = 4$ is the number of tones. Accordingly, (4.15) can be rewritten as:

$$I_{DC}(\varphi_1, \varphi_2, \varphi_3, \varphi_4) \approx k_0 + 0.5V_A^2k_2 + 0.65625V_A^4k_4 + 0.09375V_A^4k_4\cos(2\varphi_3 - \varphi_2 - \varphi_4) + 0.09375V_A^4k_4\cos(-2\varphi_2 + \varphi_1 + \varphi_3) + 0.1875V_A^4k_4\cos(\varphi_1 - \varphi_2 - \varphi_3 + \varphi_4) \quad (4.16)$$

The following conclusions can be drawn from the previous analysis:

- 1) The phase-independent component in (4.16) is greater than (4.13).
- 2) The phase-dependent term can be maximized by choosing an optimal phase arrangement.
- 3) Considering the same input average power for the CW and MS signals, (4.16) provides a higher output DC level than that provided by (4.13), guaranteed that 2) is fulfilled.

4.7.4. Waveform optimization: MS phase arrangement optimization

In order to maximize (4.16), the arguments of all the three cosines (4.17) must be simultaneously set to zero.

$$\begin{cases} Arg1 = 2\varphi_3 - \varphi_2 - \varphi_4 \\ Arg2 = -2\varphi_2 + \varphi_1 + \varphi_3 \\ Arg3 = \varphi_1 - \varphi_2 - \varphi_3 + \varphi_4 \end{cases} \quad (4.17)$$

As stated in [IV], the most trivial phase arrangement that equals equations (4.17) to zero and maximizes equation (4.16) is $\varphi_1 = \varphi_2 = \varphi_3 = \varphi_4 = 0^\circ$. In fact, this a particular case; in general, (4.16) can be maximized by imposing a constant phase progression, as in the case of the phase-locked antenna array presented in [VI]:

$$\varphi_{i+1} - \varphi_i = \Delta\varphi \quad (4.18)$$

where $\Delta\varphi$ is a constant phase value. Considering (4.18) and taking the phase of the first subcarrier (φ_1) as the reference ($\varphi_2 = \varphi_1 + \Delta\varphi$; $\varphi_3 = \varphi_1 + 2\Delta\varphi$; $\varphi_4 = \varphi_1 + 3\Delta\varphi$), the zero condition for all the three arguments (4.17) can be simultaneously satisfied:

$$\begin{cases} Arg1 = 2(\varphi_1 + 2\Delta\varphi) - (\varphi_1 + \Delta\varphi) - (\varphi_1 + 3\Delta\varphi) = 0 \\ Arg2 = -2(\varphi_1 + \Delta\varphi) + \varphi_1 + (\varphi_1 + 2\Delta\varphi) = 0 \\ Arg3 = \varphi_1 - (\varphi_1 + \Delta\varphi) - (\varphi_1 + 2\Delta\varphi) + (\varphi_1 + 3\Delta\varphi) = 0 \end{cases} \quad (4.19)$$

The general condition stated by (4.18) as well as the 0° phase condition in [IV] are consistent, as they also provide the MS signal with the maximum PAPR. Subcarriers' amplitudes may also be optimized as in [10]. Other aspects such as optimal MS bandwidth are discussed in [VII].

4.8. Defining a FOM to evaluate the efficiency gain

In order to evaluate the improvements obtained with the MS signals, compared to CWs, a FOM (figure of merit) is defined, namely the RF-DC efficiency gain (G_η), which relates the DC power collected from a single-carrier with the DC power obtained with a MS waveform with the same average power ($P_{RF(CW)} = P_{RF(MS)}$).

$$\begin{aligned} G_\eta(dB) &= 10 \log_{10} \left(\frac{\eta_{MS}}{\eta_{CW}} \right) = 10 \log_{10} \left(\frac{P_{DC(MS)}/P_{RF(MS)}}{P_{DC(CW)}/P_{RF(CW)}} \right) \\ &= 10 \log_{10} \left(\frac{P_{DC(MS)}}{P_{DC(CW)}} \right) = 10 \log_{10} \left(\frac{V_{DC(MS)}^2}{V_{DC(CW)}^2} \right) \end{aligned} \quad (4.20)$$

where, η_{CW} and η_{MS} are the efficiency of the CW and MS signal respectively, $P_{DC(CW)}$ and $P_{DC(MS)}$ refer to the output DC power obtained in a rectifier circuit when using respectively a CW and a MS signal at its input. It should be stressed that the second part of (4.20) is valid when the average input power level and the output DC load are the same for the CW and MS signals. The previously derived equation for the power received by the transponder chip (2.25) can now be combined with the usual RF-DC efficiency under CW excitation and the RF-DC efficiency gain (4.20) to obtain an estimation³ of the received DC power under MS excitation:

$$P_{tagDC}^m = P_{TX} + G_{TX} + G_{tag} + 20 \log_{10}\left(\frac{\lambda}{4\pi d}\right) + 10 \log_{10}\left(1 - \frac{1}{2}(|\Gamma_1|^2 + |\Gamma_2|^2)\right) + \Theta_f - F_f + 10 \log_{10}(\eta_{RF-DC}) + G_\eta [\text{dBm}] \quad (4.21)$$

where η_{RF-DC} is the RF-DC efficiency under CW excitation, which is between 0 and 1. If N equal amplitude subcarriers are used and the reader receiver only demodulates the central subcarrier, then the received power (2.24) should be re-written to account for the reduction in the received power level compared to a power-equivalent CW signal:

$$P_{RX-MS}^m = P_{TX} + G_{TX} + G_{RX} + 2G_{tag} + 40 \log_{10}\left(\frac{\lambda}{4\pi d}\right) + 10 \log_{10}\left(\frac{1}{4} |\Gamma_1 - \Gamma_2|^2\right) + \Theta_f + \Theta_b - F_f - 10 \log_{10}(N) [\text{dBm}] \quad (4.22)$$

Although there is a reduction in the received power level by a factor of N (4.22), it is expected that the extra sensitivity capability of typical readers will compensate for this reduction (see Fig. 2.10). Nevertheless, as demonstrated later in chapter 7, it is possible to demodulate the tag information backscattered on top of all the subcarriers by using a MS matched filter. This will strengthen the overall signal received from the tag.

4.9. Simulations

The circuit of Fig. 4.10(a) is used in ADS to evaluate the RF-DC conversion using CW and MS signals. For this purpose, two situations were simulated using multi-frequency Harmonic Balance (HB). In the first case, a CW was used as the input signal, and in the second, an evenly-spaced N -tone MS signals with zero phase shift between the subcarriers was applied. The average power of the MS signals was set to the same value as the CW average power by doing $P_{CW} = P_{w1} + P_{w2} + \dots + P_{wN}$, where P_{CW} (in dBm) is the average power of the CW signal, and $P_{w1}, P_{w2}, \dots, P_{wN}$ are the power levels of the individual MS subcarriers. A central frequency and tone spacing of 2.4 GHz and 1 MHz respectively was considered. For the sake of an efficient HB simulation, the frequency

³ This estimation assumes perfect MS synchronization at the receiver site. If the MS is affected by multipath fading, then the actual gain at the receiver site may be lower than that obtained in the cabled measurements.

mapping of Fig. 4.10(b) was used, allowing to evaluate the CW and all the MS signals in a single HB run.

Figure 4.11 depicts the input and output time-domain waveforms corresponding to a CW, a 2-tone and a 4-tone MS input signals. First, it can be observed that the output ripple follows the envelope of the input signal and it is strongly dependent on the time constant of the output filter. In the CW case, the output ripple is insignificant (blue curves), as the RF signal period ($T_{RF} = 1/f_{RF} \approx 0.4ns$) is very small compared to the time-constant of the output RC filter ($\tau = RC = 4.7ms$). On the other hand, the 2-tone and 4-tone MS signals are affected by a considerably larger output ripple (red and green curves). This is due to the much slower envelope of the MS signal, whose periodicity is related to the frequency spacing between the subcarriers ($T_{env} = 1/\Delta\omega$). Therefore, the output filter has to be optimized to account for the MS envelope frequency rather than the RF frequency. As seen in Fig. 4.11(b) and Fig. 4.11(d), by increasing the time-constant of the output filter (e.g., increasing C from 47pF to 150pF), it is possible to reduce the output ripple (curve with circles). The simulated output DC voltages and efficiency gains as given by equation (4.20) are depicted respectively in Fig. 4.12(a) and Fig. 4.12(b), as a function of the input average power. A maximum gain of 5 dB is obtained for a 8-tone MS for the series diode configuration tested here, and a similar gain was obtained in [IV] for a shunt diode simulated at 5.8 GHz.

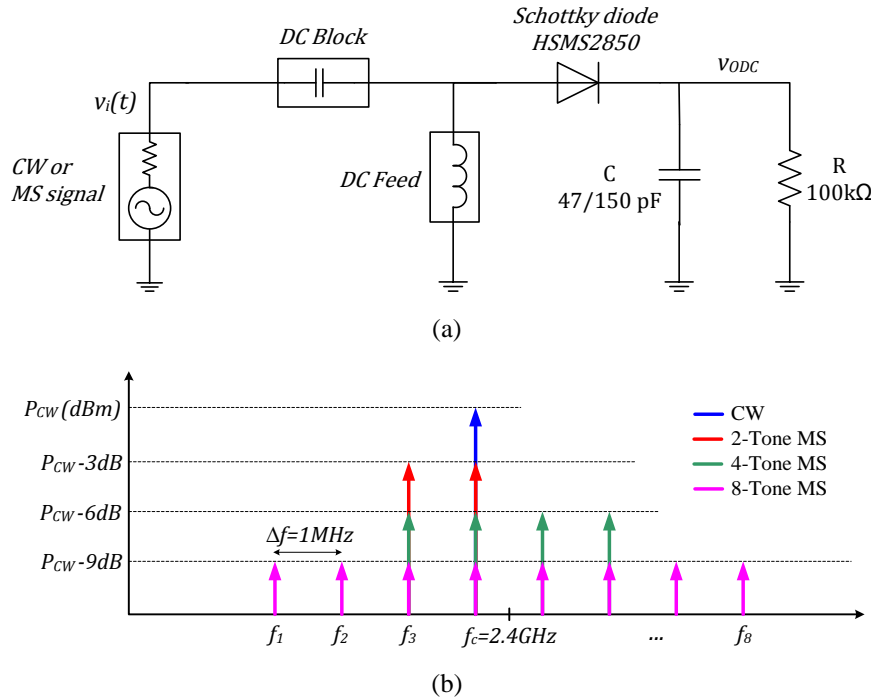


Fig. 4.10 (a) Simple series diode rectifier used in ADS HB simulations. (b) Frequency mapping of the input signals used in the HB simulations.

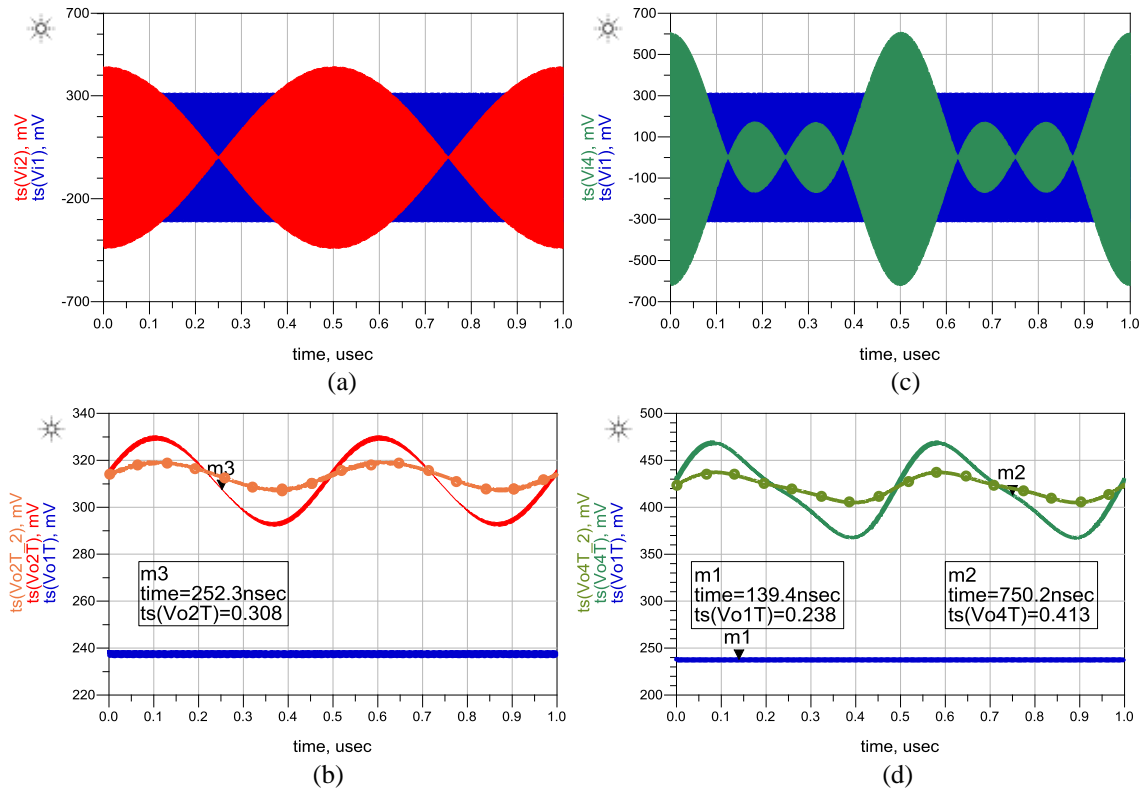
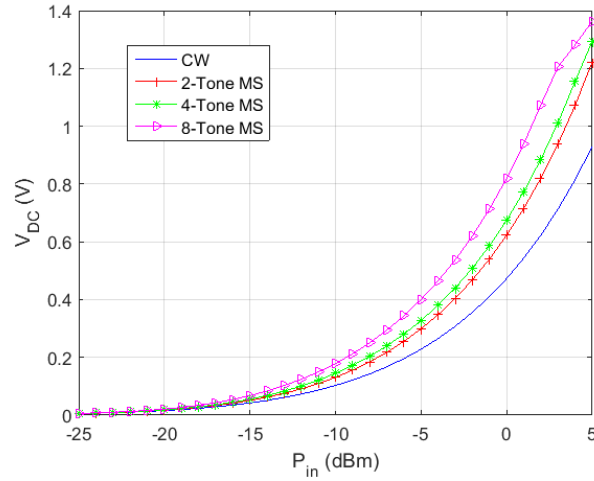
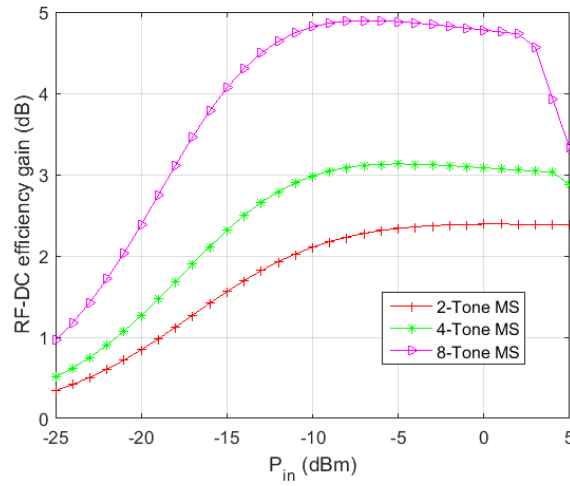


Fig. 4.11 Time-domain waveforms obtained in the HB simulations. (a) Input 2-tone MS signal overlapped with a CW signal with the same average power, and (b) respective output waveform. (c) Input 4-tone MS signal overlapped with a CW signal with the same average power, and (d) respective output waveform. In (b) and (d), the constant curve (blue) corresponds to the CW signal and the rippled waveforms (read and green) corresponds to the MS signals.



(a)



(b)

Fig. 4.12 (a) Simulated DC voltage as a function of average input power for several input excitation signals. (b) Efficiency gain as a function of average input power.

A more accurate efficiency metric that accounts for the actual average power being inputted to the rectifier circuit can be used (4.23). Simulation results using this definition and the matched rectifier circuit of Fig. 4.13(a) are exhibited in Fig. 13(b). These results also evidence an efficiency increase when using MS signals.

$$\eta = \frac{P_{out}}{P_{in'}} = \frac{\int_0^{NT} v_o(t) i_o(t) dt}{\int_0^{NT} v_i(t) i_i(t) dt} \quad (4.23)$$

where $v_i(t)$ and $i_i(t)$ are respectively the input voltage and current, $v_o(t)$ and $i_o(t)$ are respectively the voltage and current at the output DC load, and NT is an integer number of CW carrier periods or an integer number of periods of the MS envelope.

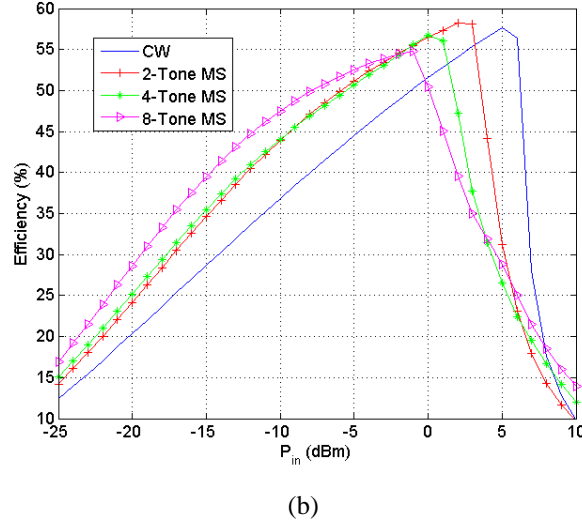
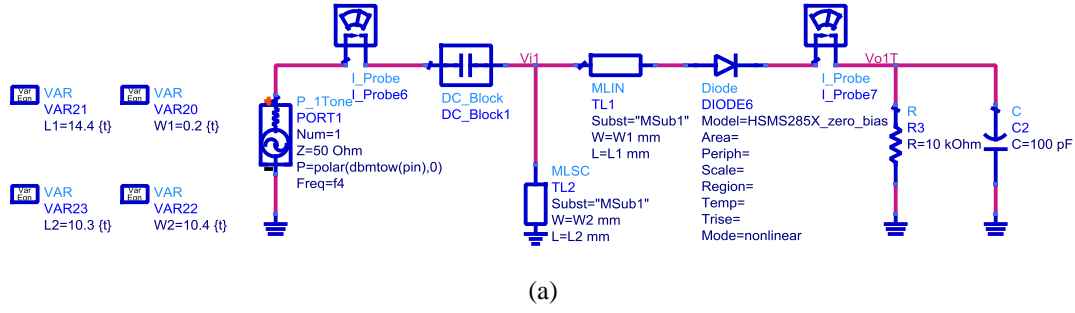


Fig. 4.13 (a) Rectifier circuit matched to the source impedance at 2.4 GHz. (b) Efficiencies under CW and MS excitations as a function of the average input power and number of tones. In this case, the actual average input power level is calculated based on the voltage and current at the input of the circuit as in (4.23).

4.10. Measurements

A set of measurements was conducted to evaluate the efficiency gains obtained in two RF-DC converter circuits under several MS signal excitations. For this purpose, a single diode detector operating at 2.3 GHz [see Fig. 4.14(a)] and a five-stage charge pump voltage multiplier working at 866 MHz [see Fig. 4.14(b)] were tested. The respective simulated and measured return loss of the circuits under test are also depicted in Fig. 4.14. In order to evaluate the performance under several excitation signals, both rectifying circuits were first fed with a CW signal and then with a MS signal with the same average power as the CW. This was done over a range of input power, input signal bandwidth and MS phase arrangements. Figures 4.15 and 4.16 present the DC output voltages and efficiency gains as defined by equation (4.20). The measurement results support the initial premise that MS signals can provide an efficiency gain over CW signals. This is valid for the single diode rectifier (both series and shunt configurations) which showed an efficiency gain up to 6 dB, as well as for the charge pump circuit which exhibited a gain up to 2.75 dB. These results

suggest that this scheme can potentially extend the range of passive RFID systems. This is further explored in the next chapters.

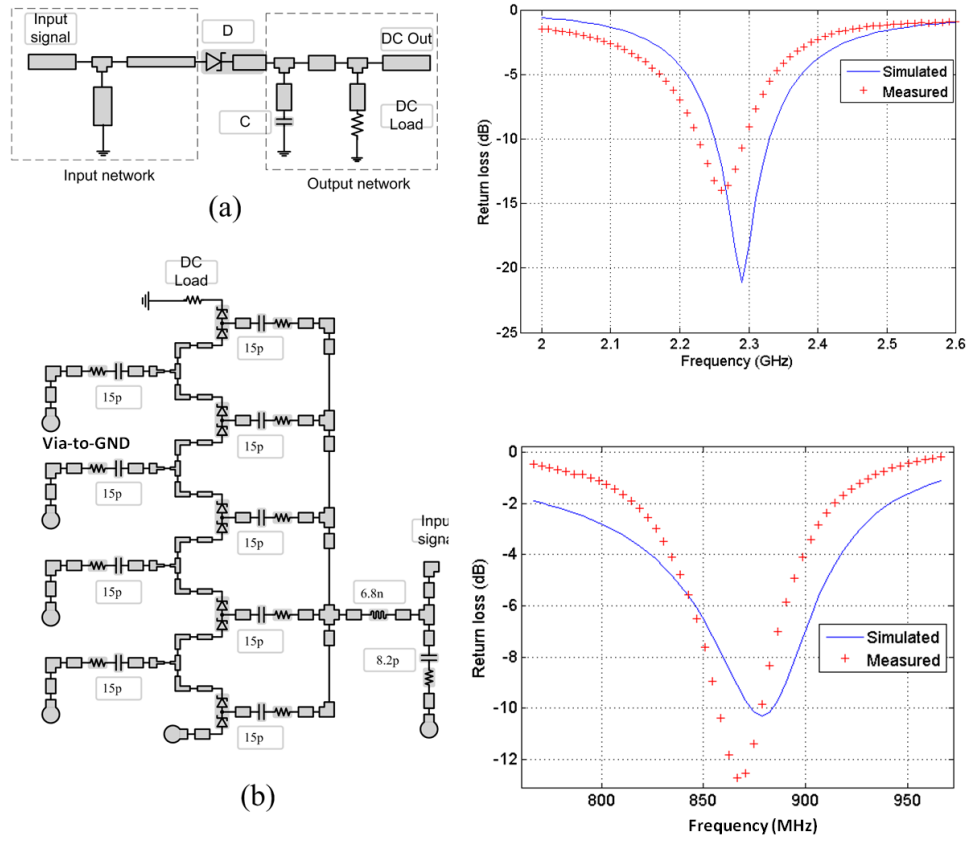
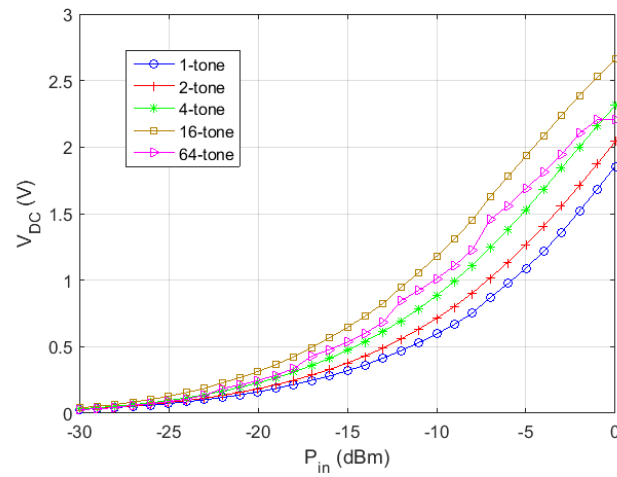
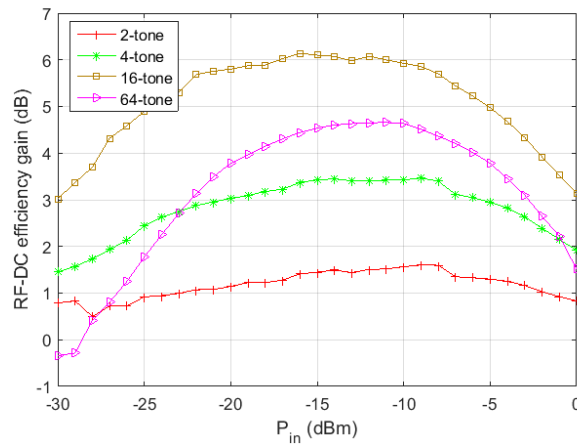


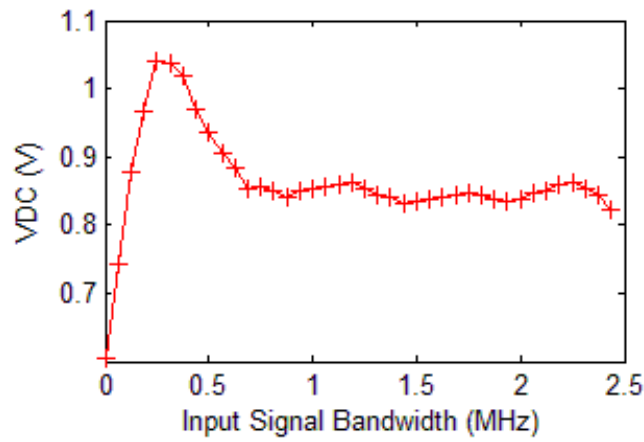
Fig. 4.14 Rectifying circuits used in the cabled measurements and respective input return loss (simulated and measured). (a) Single diode detector operating at 2.3 GHz band. (b) Charge pump rectifier with 866 MHz center frequency.



(a)

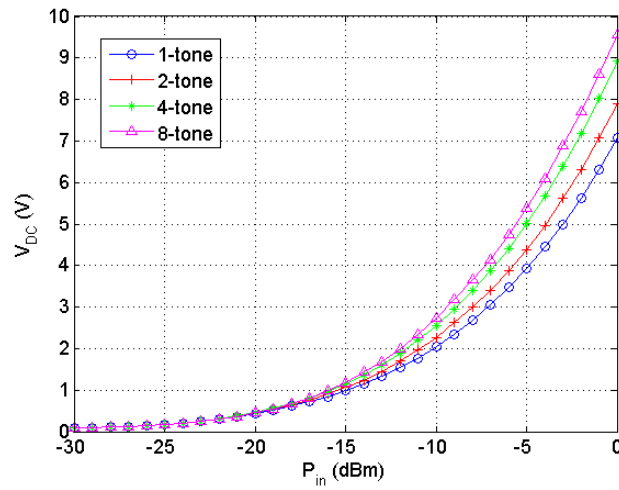


(b)

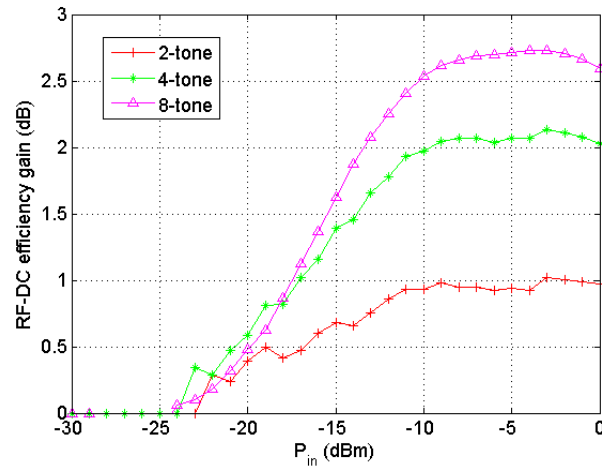


(c)

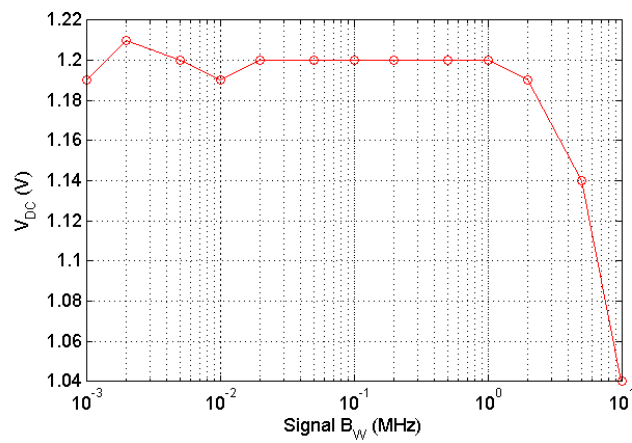
Fig. 4.15 (a) Measured DC output voltage of the single diode detector, as a function of average input power. (b) Efficiency gain of the single diode detector, as a function of average input power. Except for the 64-tone MS, as the number of tones and the PAPR increase, the gain also increases. (c) Output DC voltage as a function of the input signal bandwidth. It is visible that there is an optimal MS bandwidth that produces a maximum output DC.



(a)



(b)



(c)

Fig. 4.16 (a) Measured DC output voltage of the charge pump, as a function of average input power. (b) Efficiency gain of the charge pump, as a function of average input power. (c) Output DC voltage as a function of the input signal bandwidth.

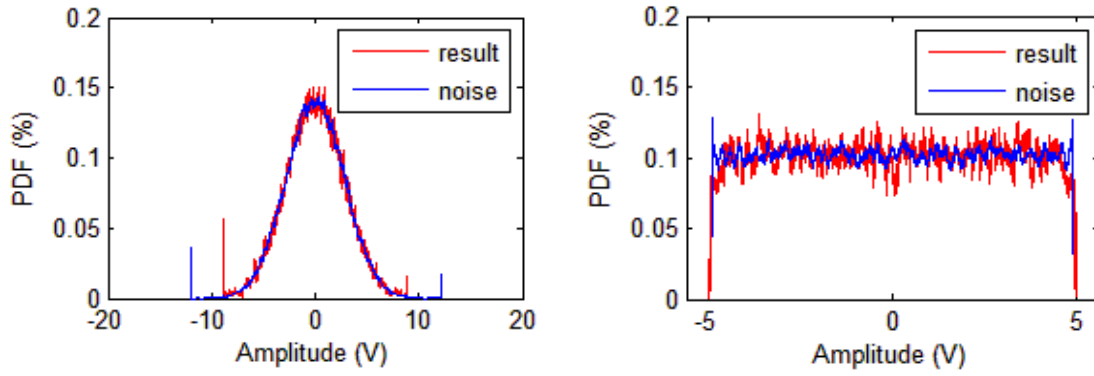


Fig. 4.17 Probability density functions of noise and synthesized MS signals. (a) Normal distribution. (b) Uniform distribution.

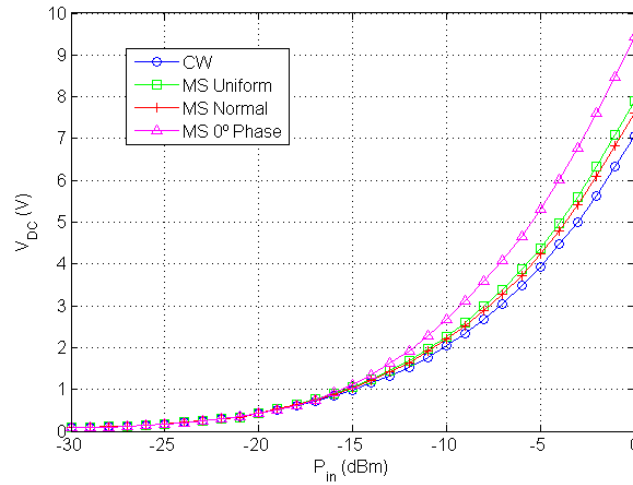


Fig. 4.18 Measured DC output voltage of the charge pump, for a CW signal, and a 16-tone MS with uniform and normal amplitude distributions, and with 0° phase arrangement.

A. The impact of input signal statistics

The circuits under test were also evaluated using different input amplitude statistics, including a 16-tone MS with 0° phase, normal amplitude distribution and uniform amplitude distribution. To achieve a given amplitude distribution, the algorithm outlined in [11] was used to synthesize MS signals from noise signals with the desired amplitude statistics. The algorithm returns the phases of a MS with the same amplitude statistics as the reference noise signal. The Probability Density Functions (PDF) of the noise and MS with normal and uniform distributions are depicted in Fig. 4.17. Figure 4.18 shows the measured output DC voltage of the charge pump, for a CW, and a 16-tone MS with 0° phase arrangement, normal and uniform amplitude distributions. As can be seen in Fig. 4.18, the 0° phase MS provides the best performance, followed by the MS with normal amplitude distribution. A similar result is obtained for the single diode detector.

4.11. Conclusions

This chapter answers affirmatively to the first question formulated in the introductory chapter of this thesis. The major conclusions can be summarized as follows:

- ❖ When compared to conventional CWs, high PAPR signals are able to more efficiently overpass the turn-on voltage of existing rectifying devices, especially at low power levels, yielding an improved RF-DC conversion efficiency. High PAPR MS signals provide higher DC power compared to a CW with the same average power level. This results in an efficiency gain which increases with the increase in PAPR at low average power. However, for very high PAPR values, as predicted by the model in Appendix A, the efficiency is significantly degraded.
- ❖ The MS time-domain waveform is impacted by the phase arrangement, number of tones and their frequency domain distribution. If the subcarriers are phase-synchronized, the higher the number of tones, the higher the PAPR and the higher the efficiency gain at low power levels. The peak repetition rate in time-domain is inversely proportional to the tone separation in the frequency domain, and thus, a decrease in tone separation imposes an increase in the output ripple. On the other hand, a very large tone separation may cause the total MS bandwidth to exceed the input bandwidth of the circuit, resulting in an efficiency drop. Therefore, an optimal tone separation should be selected.
- ❖ Contrary to the cabled measurements conducted in this chapter, in which we have full control over the MS parameters, in open air experiments, we lose control over the subcarrier phases and amplitudes, especially due to multipath fading. Nevertheless, measurements show that even with a random phase arrangement, the MS signal can outperform the CW signal. This aspect is further investigated in the field experiments conducted in the next chapters.
- ❖ While the output filter design is not critical for CW operation (as a relatively small output capacitor is sufficient to smoothen the output ripple), for MS operation, the output filter design is important and should take into account the MS signal envelope. The output ripple follows the MS envelope, and the average output DC depends on the time-constant of the output filter.
- ❖ Not less important, the use of a MS transmitter represents an increased complexity and the amplification of high PAPR signals is challenging because it may occur non-linear distortion (amplitude clipping, spectrum regrowth) and efficiency degradation. For this reason, space power combining is proposed in the next chapter as an efficient way to create and radiate high PAPR MS signals.

References

- [1] Anton A. Huurdeman, *The worldwide history of Telecommunications*, John Wiley & Sons, Inc., Hoboken, New Jersey, 2003.
- [2] N. Tesla, “*The Transmission of Electric Energy Without Wires*” (The Thirteenth Anniversary Number of the Electrical World and Engineer). New York: McGraw-Hill, Mar. 5, 1904.
- [3] Biography of Ernst F. W. Alexanderson, IEEE Global History Network. [http://www.ieeeahn.org/wiki/index.php/Ernst F. W. Alexanderson](http://www.ieeeahn.org/wiki/index.php/Ernst_F._W._Alexanderson)
- [4] Pavel V. Nikitin and K. V. S. Rao, “*Performance Limitations of Passive UHF RFID Systems*”, IEEE Antenna and Propagation International Symposium 2006, p.p.: 1011-1014, July 2006.
- [5] Pekka Pursula, “*Analysis and Design of UHF and Millimetre Wave Radio Frequency Identification*”, PhD Thesis, VTT Technical Research Centre of Finland, Dec. 2008.
- [6] D. De Donno, F. Ricciato, and L. Tarricone, “*Listening to Tags: Uplink RFID Measurements with and Open-Source Software-Defined Radio Tool*,” IEEE Transactions on Instrumentation and Measurement, vol. 62, no. 1, pp. 109–118, Jan. 2013.
- [7] J. C. Pedro and N. B. Carvalho, *Intermodulation Distortion in Microwave and Wireless Circuits*, 1st ed. Norwood, MA: Artech House, 2003.
- [8] Application note: PIN Diode Model Parameter Extraction from Manufacturers’ Data Sheets © 1997 Ansoft Corp.
- [9] Principles of Power Measurement, A Primer of RF & Microwave Power Measurement, Wireless Telecom Group, US, 2011.
- [10] M. S. Trotter, J. D. Griffin and G. D. Durgin “*Power-Optimized Waveforms for Improving the Range and Reliability of RFID Systems*”, IEEE International Conference on RFID, p.p.: 80-87, 2009.
- [11] José C. Pedro and Nuno Borges Carvalho, “*Designing Band-Pass Multisine Excitations for Microwave Behavioral Model Identification*”, Microwave Symposium Digest, 2004 IEEE MTT-S International

5. SPATIAL POWER COMBINING OF MULTI-SINE SIGNALS FOR WPT APPLICATIONS

5.1. Introduction

This chapter addresses the second challenge posed at the beginning of this thesis, namely “*How can we efficiently generate and transmit such high PAPR waveforms?*”.

Although considerable research has been dedicated to the receiver side of WPT systems, rather less attention has been paid to the transmitter side. Concerning the use of high PAPR signals, investigations have been confined only to the study of the (receiver) RF-DC conversion efficiency. However, the high PAPR scheme is effective only if the high PAPR waveform reaches the receiver. Thus, the transmitter should be capable of transmitting the signal without clipping it, preserving the high PAPR feature of the time-domain waveform, that is responsible for the improvement of the RF-DC conversion efficiency in rectifier circuits. However, high PAPR signals can push traditional power amplifier architectures to saturation/clipping leading to non-linear distortion and spectrum regrowth. These non-linear effects may not only destroy the desired high PAPR time-domain shape, they can degrade the energy efficiency and the spectral efficiency of the system. Therefore, improved architectures for high PAPR signals transmission are necessary.

This chapter presents two architectures for efficient generation and transmission of high PAPR MS signals, which have demonstrated to improve the RF-DC conversion efficiency of rectifying circuits. In order to overcome the challenges associated to the amplification of high PAPR signals, the proposed schemes make use of the spatial power combining concept, in which the individual subcarriers are separately amplified, radiated and then passively combined in free-space. With this concept, first introduced in [VI][VIII][1], no special constraints are imposed on the power amplifier stage that only handles CW signals. In order to achieve the desired high PAPR feature, proper synchronization of the individual subcarriers is required. Accordingly, two synchronization mechanisms are proposed in this chapter: the first one is based on the transmission of single tone signals that are externally locked to a common reference signal that establishes the necessary phase reference; the second architecture is based on a mode-locked oscillator scheme that requires no external reference signal. Instead, this scheme takes advantage of the self-synchronization phenomena in coupled oscillator circuits to establish the phase reference. Measurements are presented to validate both schemes and to show their effectiveness in improving the RF-DC conversion efficiency in rectifier circuits.

5.2. Spatial power combining: spatially-combined MS signals

Power combining is a technique commonly used in millimeter-wave technology to achieve moderate to high power levels [2-4]. Millimeter-wave components and devices, such as power amplifiers, have small sizes; therefore, their dissipation capabilities are very limited. For this reason, it is difficult to achieve high power levels with a single component/device, and power combining techniques are used to obtain higher power levels. The traditional approach consists of splitting the input signal into N branches, amplifying them separately and combining them again to obtain an amplified version of the input signal. Since the splitting and combining stages are usually implemented using lossy transmission line circuits, this approach becomes inefficient as the number of branches increases. Spatial power combining has been proposed to overcome this drawback [2-4] by passively combining the signal components in free-space.

A spatially-combined MS transmitter can be implemented as an array of oscillators externally synchronized to a common reference source that establishes the phase reference for the system, or alternatively, using mode-locked coupled oscillators, where the coupling between adjacent elements allows for frequency locking and at the same time establishes the system phase reference [4]. In this paper, both architectures are considered in order to implement spatially-combined high PAPR MS signals for WPT. Figure 5.1 depicts the proposed transmitter architectures considering $N = 2n+1$ synchronized signal sources that generate a MS E -field by means of space power combining. Assuming far-field observation [5], and considering a small spacing between adjacent antenna elements, the total E -field at a distance r is given by:

$$E(t, \theta, r) = \sum_{i=-n}^n E_i G_i(\theta) e^{j[\omega_i t + kr + \phi_i]} \quad (5.1)$$

where k is the propagation constant, ω_i and ϕ_i are the frequency and phase of each signal source, E_i is the amplitude of each E -field component and $G_i(\theta)$ is the gain of each antenna.

In order to achieve a MS E -field with maximum PAPR, the conditions of equally-spaced frequencies ($\omega_i = \omega_0 + i\Delta\omega$) and constant phase distribution ($\phi_{i+1} - \phi_i = \Delta\phi$) must be met [IV][4]. Notice that this is the same set of conditions established before in chapter 4 [equations (4.14) and (4.18)].

In the next section, an externally synchronized MS signal generation scheme is presented, in which the constant frequency progression between the sines is guaranteed by properly setting the signal generators frequencies, and the phase distribution condition is externally imposed by using a 10 MHz reference signal as shown in Fig. 5.1(a).

An alternative transmitter scheme that allows to establish a phase reference without the need for an external reference source is by using active antenna arrays of coupled oscillators, in which the

oscillators are coupled by means of radiative coupling through the antenna elements [see Fig. 5.1(b)]. This coupling allows to synchronize the oscillators in the so-called mode-locked state. In this state a phase reference is established, and at the same time it is possible to synthesize different phase-shift distributions between the oscillator elements [1] such as the required constant phase shift distribution necessary to achieve high PAPR signals. Section 5.4 is dedicated to these type of active antenna arrays operating in mode-locked regime for their use in MS signal generation.

In order to evaluate the improvements obtained in a rectifier circuit when using the proposed MS transmitter schemes, compared to a single-carrier transmitter, the same FOM defined in chapter 4 (equation 4.20) is used.

5.3. Externally-synchronized spatially-combined MS transmitters

In the first spatially-combined MS transmitter architecture, each of the elements is composed of a VSG and an antenna, and all the elements in the transmitting array are synchronized to a common 10 MHz reference signal that establishes a phase reference.

5.3.1. Spatially-combined two-tone signal

In order to provide a first validation of the concept, a two-tone experiment was conducted. A rectenna (a dipole antenna connected to a five-stage voltage multiplier circuit) is placed between two transmitting antennas that are connected to two signal generators (Fig. 5.2). Each of the transmitting antennas is placed at a distance $r = 35$ cm from the receiving rectenna. First, one of the transmitting antennas is fed with a single-carrier at 879 MHz with power P_{CW} . Afterward, the two transmitting antennas are fed with two tones at 878 MHz and 880 MHz. In this case, the power of each tone is set to $P_{2T} = P_{CW} - 3$ dB, such that the total average power is the same as in the single-carrier experiment. For both experiments, the DC voltage at the output of the rectifier is measured and the RF-DC efficiency gain (G_η) was calculated according to (4.20). The results are presented in Table 5.1. Note that, unlike scenarios with more than two tones, in the case of two-tone signals the phase relationship between the sines is not important since it does not affect the PAPR of the signal. Therefore, no external reference signal is required.

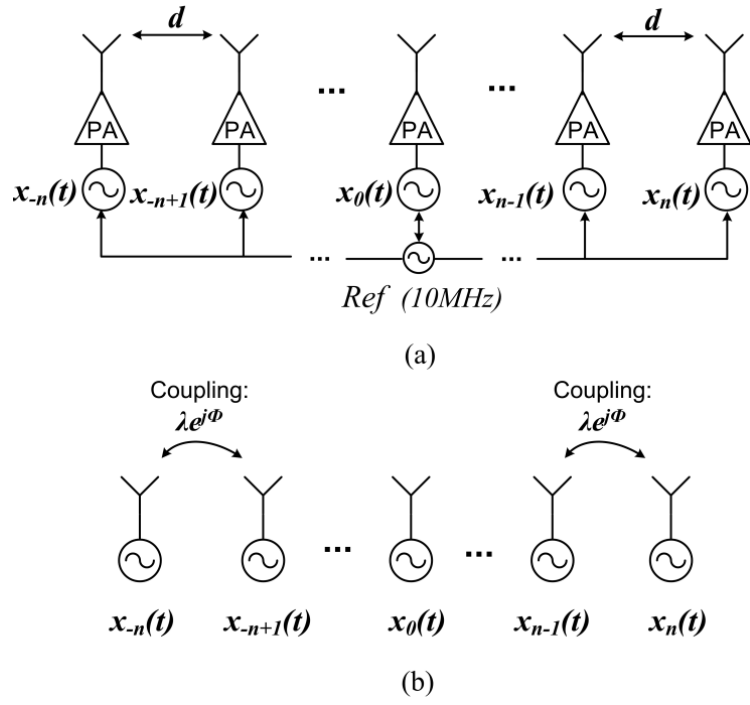


Fig. 5.1 (a) Externally-synchronized multi-sine transmitter. (b) Mode-locked coupled-oscillator array with coupling through the antennas.

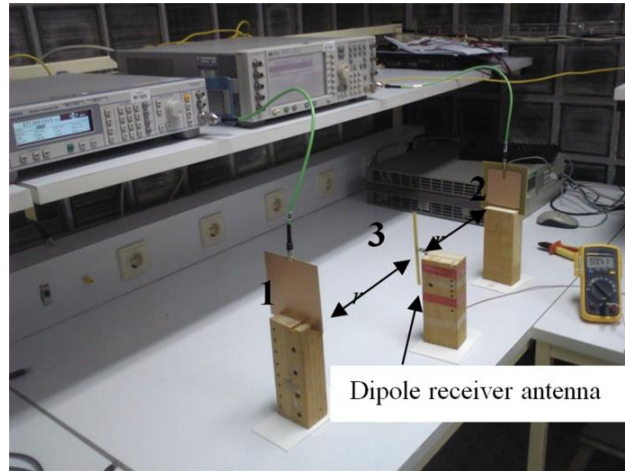


Fig. 5.2 Measurement setup to evaluate rectifier performance under two-tone and CW signal ($r = 35cm$).

Table 5.1 presents the measured output DC voltages of the five-stage voltage multiplier with a 510 k Ω load. Considering the same transmitted average power for the single-carrier and for the two-tone signal, the obtained DC voltage is higher for the two-tone case. However, the RF-DC efficiency gain G_η obtained is not very expressive. This is mainly due to the fact that only two tones is used in the MS signal, which does not provide a very high PAPR. In order to obtain a higher gain, a higher order MS is considered (see next section).

TABLE 5.1
DC VOLTAGE AT THE RECTIFIER OUTPUT AND EFFICIENCY GAIN

P_{CW} (dBm)	V_{DC_CW} (Volt)	$P_{2T} =$ $P_{CW} - 3 \text{ dB}$ (dBm)	V_{DC_2T} (Volt)	G_η (dB)
10.7	1.090	7.7	1.090	0
11.7	1.288	8.7	1.293	0.034
12.7	1.501	9.7	1.509	0.046
13.7	1.726	10.7	1.762	0.179
14.7	1.940	11.7	2.056	0.504
15.7	2.203	12.7	2.381	0.675
16.7	2.480	13.7	2.731	0.837

5.3.2. Spatially-combined three-tone signal

Experiments using more than two tones MS signals were conducted in order to evaluate the impact of the phase arrangement and synchronization of the individual sources. The setup used for this experiment is shown in Fig. 5.3, where a three-tone signal is generated by spatial power combining. At the transmitter side, the subcarriers are generated using independent signal sources that are then amplified and transmitted by three antenna elements. In order to guarantee a constant phase progression between the sources, they must be phase-synchronized to a common reference. For this purpose, one of the generators is used as the reference, providing a 10 MHz reference signal for all the sources. To guarantee that the synchronization is achieved and kept during the measurements, the following is required: 1) the generator with the best output reference signal is chosen as the reference; 2) the cables used to distribute the reference signal are identical; additionally, 3) an oscilloscope is used at the receiver side to monitor the received signal in order to check if the sources are synchronized.

In this experiment, the frequencies of the subcarriers are set to $f_1 = 876 \text{ MHz}$, $f_2 = 877 \text{ MHz}$, $f_3 = 878 \text{ MHz}$, and the total average power (measured at the input of the rectifier circuit) is set to same value as the single-carrier signal ($P_{tone1} + P_{tone2} + P_{tone3} = P_{CW}$, $P_{tone1} = P_{tone2} = P_{tone3}$). The RF-DC efficiency gain (G_η) of the MS relative to the single-carrier is given by (4.20).

For a small spacing (d) between the antennas, and considering far-field conditions ($r_{antenna1} \approx r_{antenna3} \approx r$) and free-space power combining, the *E-field* at the receiver location can be modelled by (5.1). At the receiver side, the spatially-combined signal is collected by a dipole antenna and rectified by a five-stage voltage multiplier whose output DC voltage is measured by using a voltmeter. A sample of the received RF signal (obtained through a directional coupler) is displayed in a Spectrum Analyzer (SA) or in an RF oscilloscope. The SA is used to visualize the received subcarriers in the frequency domain, and to determine the amount of power that is reaching the rectifier circuit. The oscilloscope serves to visualize the time-domain waveform and to verify

whether the tones are locked in phase or not. When the tones are perfectly synchronized, the resulting time-domain signal waveform exhibits the maximum PAPR value as in Fig. 5.4(b); on the other hand, if the tones are not properly synchronized, the PAPR is lowered [see Fig. 5.4(c)].

The measured RF-DC efficiency gain (G_η) values are depicted in Fig. 5.5 for the synchronized and unsynchronized case. For the synchronized MS signal, a maximum gain of 1.72 dB relative to the power-equivalent single-carrier is obtained. This means that the DC power collected when using a three-tone signal is approximately 49% higher than when using a single-carrier signal, both cases with the same average power being delivered to the rectifier circuit.

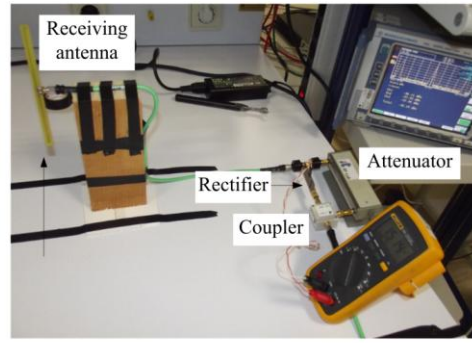
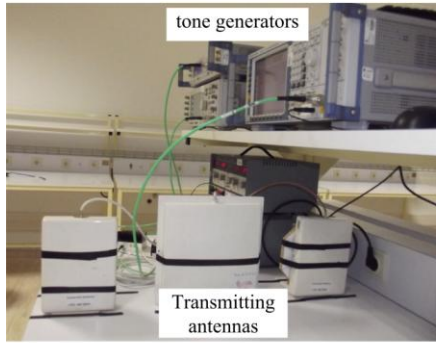
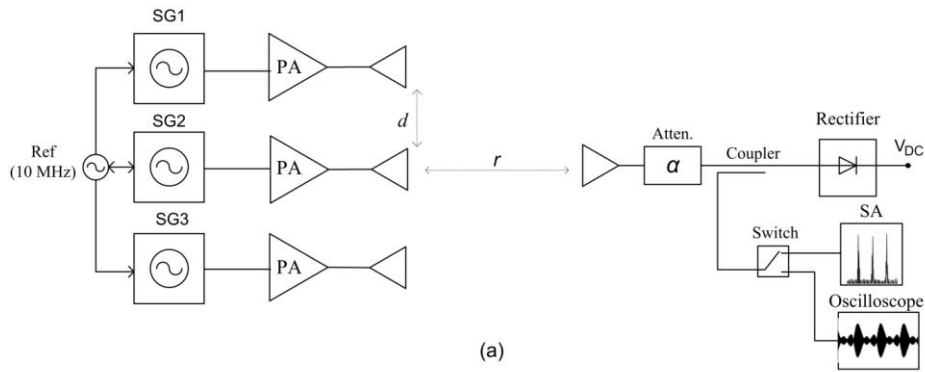


Fig. 5.3 (a) Diagram of the multi-sine measurement setup. (b) Multi-sine transmitter. (c) Receiver. $d = 9\text{cm}$, $r = 70\text{cm}$.

5.3.3. The effect of phase synchronization

While the phases of the tones are not important in the two-tone case, for more than two tones the phase arrangement has a direct impact on the output DC voltage of the rectifier circuit and consequently on the achieved RF-DC efficiency gain G_η . This section analyzes how the phase distribution between the tones affects the obtained RF-DC efficiency gain G_η .

Figure 5.4 depicts the time-domain waveforms of a single-carrier, a synchronized three-tone signal and an unsynchronized three-tone signal. As can be observed, the synchronized signal exhibits the highest PAPR value, which maximizes the efficiency gain. Unlocking the phases leads to a much lower PAPR value and consequently to a non-optimal efficiency gain. This can be observed in Fig.

5.5, which shows the measured efficiency gain G_η versus the available average power level at the rectifier input. Solid and dashed lines show the moving average of the measured values, while squares and triangles correspond to the actual measured values. In the unsynchronized case, the common reference signal is turned off, and therefore the individual tones assume random phases. Consequently, a lower efficiency gain with a larger standard deviation (squares) is observed. On the other hand, when the three tones are synchronized in-phase the efficiency gain is maximized. A residual phase variation is verified in this case, however with little impact on the gain (triangles). Figure 5.5 also shows that the efficiency gain increases with the input power delivered to the rectifier, reaches a maximum value, and then starts to decrease. This effect is due to the non-linear behaviour of the rectifying diode. This same behaviour is also observed in section 5.4.

5.4. Mode-locked coupled-oscillator arrays⁴

An alternative way to create a multi-tone signal is to use mode-locked coupled oscillator arrays where an active array of antenna oscillators is used as the transmitting source. Mode-locked coupled oscillator arrays can synthesize MS signals without the need of an external reference signal to establish the phase reference. This is possible due to the existence of radiative coupling through the antennas (Fig. 5.6) that allows synchronizing the oscillator elements, and consequently, makes it possible to establish the required phase reference [6-8]. Additionally, if the oscillators have a frequency tuning mechanism, varying the free-running frequencies of the oscillators leads to different phase-shift distributions along the elements in the array.

The coupling strength and coupling phase between the oscillator elements play an important part in the synchronization properties of the array of active antenna oscillators, and it is important to properly select them. The coupling strength and phase directly limit the range of phase-shift distributions that can be synthesized, which in practice limits the type of signals that can be generated.

A 4x1 array of active antenna oscillators operating in mode-locked regime has been designed. The core element of the proposed mode-locked active antenna array is an active antenna oscillator where a patch antenna is aperture coupled to an oscillator element [see Fig. 5.6(a)]. The proposed array operates in the C-band. The antenna patches are fabricated on 0.5 mm Arlon A25N substrate with dielectric constant 3.38 and loss tangent 0.0025. The active circuitry and coupling slots layer are fabricated in Rogers 4003C (0.5 mm thickness) with dielectric constant 3.38 and loss tangent 0.0027. The two substrates are separated with a 3mm Rohacell foam layer and the three layers are

⁴ All the prototypes designed in this section and respective measurements were performed in CTTC (Barcelona, Spain) by Profs. Apostolos Georgiadis and Ana Collado, in the scope a collaborative work between our groups, which is published in [VI].

bonded using a 3M spray adhesive [see Fig. 5.6(b)]. The selected VCO is the commercial Z-COMM 6200L-LF with an output power of approximately 3 dBm.

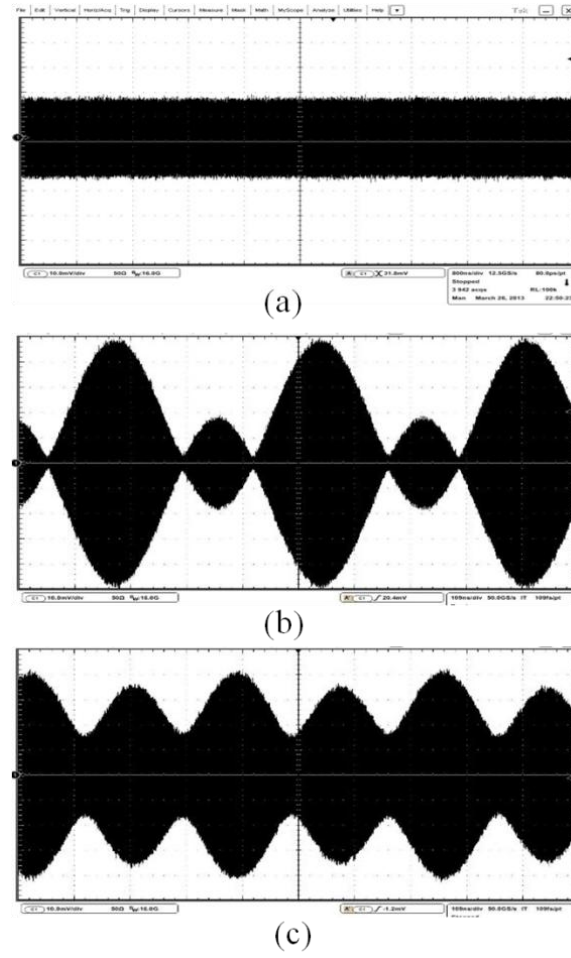


Fig. 5.4 Time-domain waveform of the received signals. (a) Single-carrier. (b) Three-tone signal with synchronized subcarriers. (c) Three-tone signal with unsynchronized subcarriers.

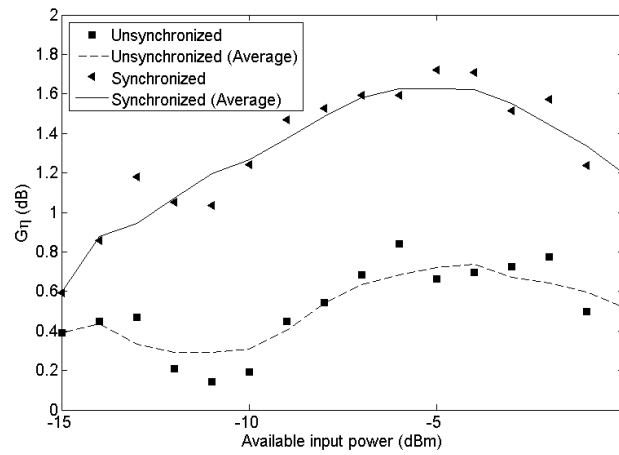


Fig. 5.5 RF-DC efficiency gain G_{η} of synchronized and unsynchronized three-tone signals

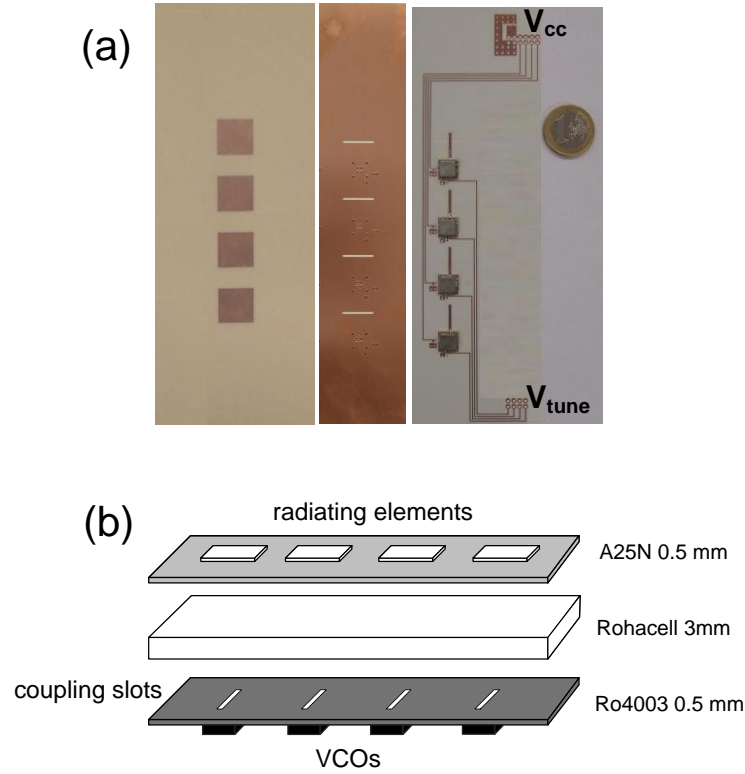


Fig. 5.6 4x1 array of active antenna oscillators. (a) Implemented array. (b) Layer scheme of the 4x1 array. [built in CTTC, Spain].

5.4.1. Mode-locked multi-sine signal synthesis

In order to synthesize a mode-locked MS signal using the 4x1 array, the free-running frequencies of the four oscillator elements are selected to have a frequency spacing such that they are not synchronize to a common frequency. For this, a significant frequency spacing must be used.

Initially, only two oscillator elements are turned on, and their frequencies are set to 6.18 GHz and 6.23 GHz [see Fig. 5.7(a)]. A spacing of 50 MHz is selected to avoid synchronization to a common frequency of the two oscillators. Due to the presence of the two frequencies, mixing products appear at 6.13 GHz and 6.28 GHz. In a second step, the other two oscillators of the array are turned on one at a time. If their frequencies are set close enough to the mixing products of 6.13 GHz and 6.28 GHz, they will synchronize to them, creating a four-tone signal where the four tones are equally spaced and have a phase shift distribution among them that appears due to the synchronization phenomena [6][7]. Figure 5.7(b) shows the third oscillator synchronized to the 6.13 GHz mixing product and Fig. 5.7(c) shows the four oscillators operating in a mode-locked regime.

Once the mode-locked state is reached, it is possible to vary the free-running frequencies of the oscillator elements of the array within a certain frequency range in order to establish different phase-shift distributions among the oscillators. Additionally, selecting free-running frequencies of

the oscillators that are closer or farther to each other makes it possible to synthesize four-tone signals with smaller or larger frequency spacing.

It has to be noted that the minimum spacing possible between the tones is limited by the synchronization bandwidth of the oscillator elements in the array. This synchronization bandwidth directly depends on the coupling strength through the antenna elements. In this case, the synchronization bandwidth of the oscillators was measured to be approximately 90 MHz, which means that a frequency spacing of less than 45 MHz between the tones would make the oscillators to synchronize to a common frequency and no mode-locked state would be possible. If smaller frequency spacing between the tones is desired, the active antenna oscillator array should be designed to have smaller synchronization bandwidth, which can be done by reducing the amount of coupling through the antenna elements. However, it has to be taken into account that the smaller the synchronization bandwidth the more sensitive the system will be to interferences that may affect the mode-locked regime.

Using the 4x1 array, two different mode-locked four-tone signal are generated. One of the signals has frequency spacing between the tones of 75 MHz and the other of 45 MHz. The free-running frequencies of the four oscillators are properly selected to achieve the desired frequency spacing and at the same time maintaining the four tones in-phase in order to create a high PAPR four-tone signal. The signals in Fig. 5.8 and Fig. 5.9 exhibit a PAPR of approximately 8.9 dB.

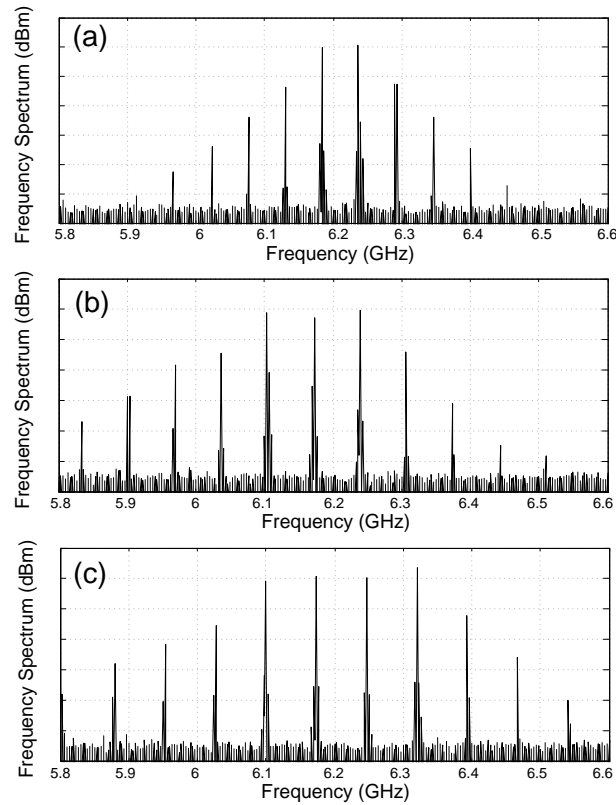


Fig. 5.7 Measured mode-locked synchronization phenomena. (a) Two oscillators. (b) Three oscillators. (c) Four oscillators. Subcarrier frequency spacing is initially set to 50 MHz.

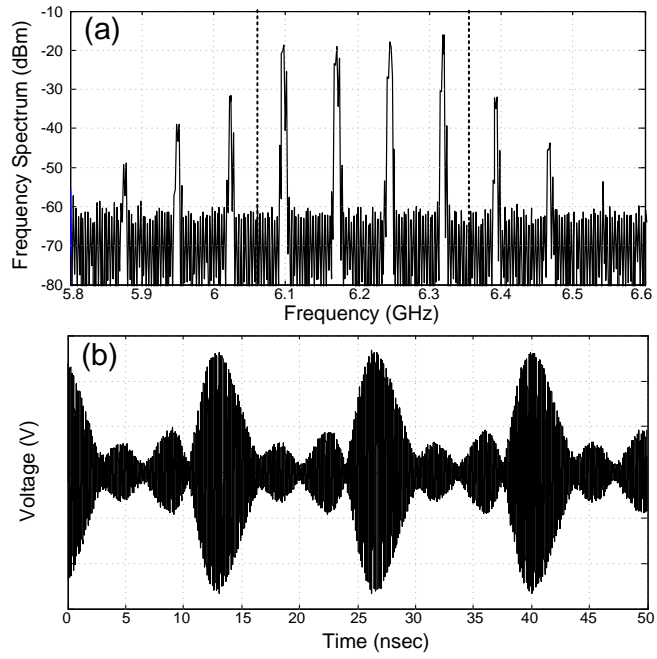


Fig. 5.8 Measured mode-locked multi-tone signal with frequency spacing 75 MHz. (a) Frequency spectrum. (b) Time-domain waveform.

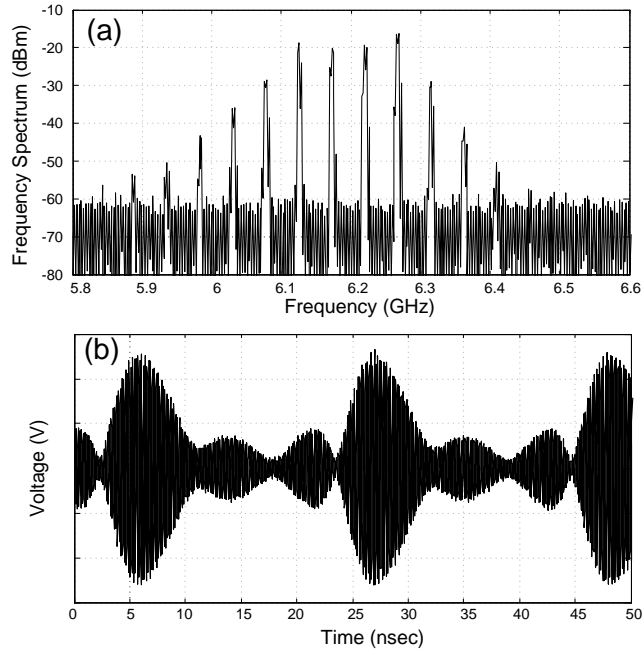


Fig. 5.9 Measured mode-locked multi-tone signal with frequency spacing 45 MHz. (a) Frequency spectrum. (b) Time-domain waveform.

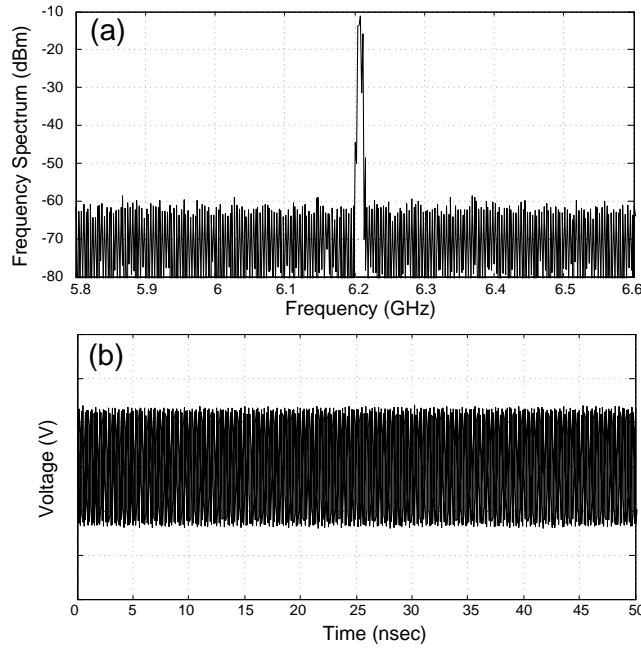


Fig. 5.10 Measured single-carrier signal. (a) frequency spectrum (b) time-domain waveform.

5.4.2. Single-carrier signal synthesis

In order to maintain the same setup for the performance evaluation experiment the single-carrier signal is synthesized using the same 4x1 array. In contrast to the case of mode-locked MS signals, the synthesis of a single tone signal requires that all the oscillators synchronize to a common frequency. This can be done by setting the free-running frequencies of all the oscillators to the same value (in this case 6.2 GHz). The obtained signal is shown in Fig. 5.10.

5.4.3. Performance evaluation

The four-tone mode-locked signal with frequency spacing of 75 MHz and PAPR = 8.9 dB is used as the transmitting signal of a WPT system at 6.2 GHz. In the receiving end, a 6.2 GHz rectifier circuit is placed in order to evaluate the performance of the system.

The selected rectifier is an envelope detector with an LC matching network at the input. The rectifying device is the MACOM MA2502L Schottky diode. The matching network and the load ($R_L = 10 \text{ k}\Omega$) of the rectifier were optimized to maximize the RF-DC conversion efficiency at 6.2 GHz.

The setup used for the experiment is shown in Fig. 5.11. The transmitter consists of the 4x1 active antenna oscillator array of Fig. 5.6. The receiver is formed by a standard horn antenna and the rectifier circuit. The transmitter and the receiver are separated approximately 30 cm. In order to recreate the effect of larger distances between the transmitter and receiver, two variable attenuators, α_1 and α_2 , with 1 dB and 10 dB steps are used in the receiver between the receiving horn antenna and the rectifier [see Fig. 5.11].

During the experiment, the attenuation values α_1 and α_2 are varied and the obtained DC output voltage (V_{DC}) is measured using a multimeter (Fig. 5.11). At the same time, the available power at the input of the rectifier is measured using a 10 dB directional coupler and an oscilloscope (Agilent DSO81004A) with 50 Ohm input impedance. For this measurement, only the power in the frequency band that covers the four main carriers of the MS signal (marked by two vertical dashed lines in Fig. 5.8) is considered.

The same experiment was performed using a single-carrier signal in order to calculate the RF-DC efficiency gain (G_η) when using the mode-locked four-tone signal in comparison with a single-carrier signal. The same setup was used for this experiment. The attenuation values are selected to set the power level of the single-carrier signal to the same values that were measured for the four-tone mode-locked signal. The DC output voltage values obtained for the single-carrier signal are recorded.

Since the same average input power at the rectifier is considered for the mode-locked four sine signal and for the single-carrier signal, the previously defined efficiency gain FOM (4.20) can be used. The obtained results of G_η versus available input power at the rectifier are shown in Fig. 5.12, showing that there is a clear improvement in the obtained DC voltage when using the mode-locked four-tone signal in comparison with the single-carrier signal. The same comparison was performed for a four-tone mode-locked signal with a frequency spacing of 45 MHz (Fig. 5.9). The G_η obtained is also shown in Fig. 5.12.

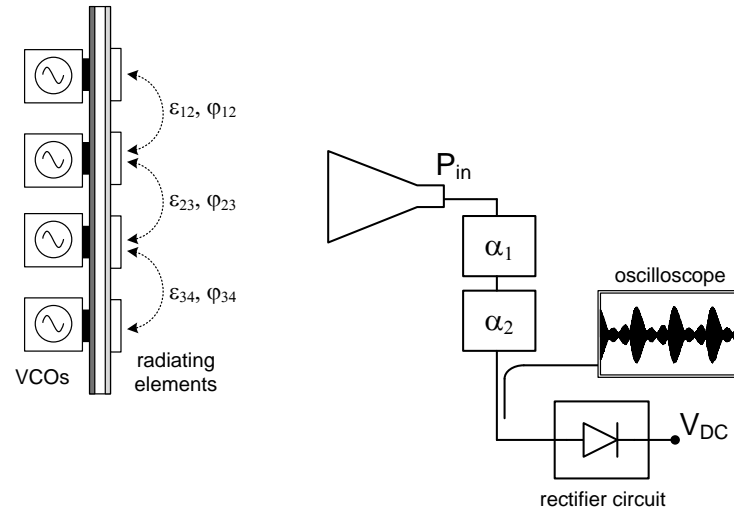


Fig. 5.11 Measurement setup used for the performance evaluation of the rectifier circuit when using the mode-locked active antenna array as transmitting source.

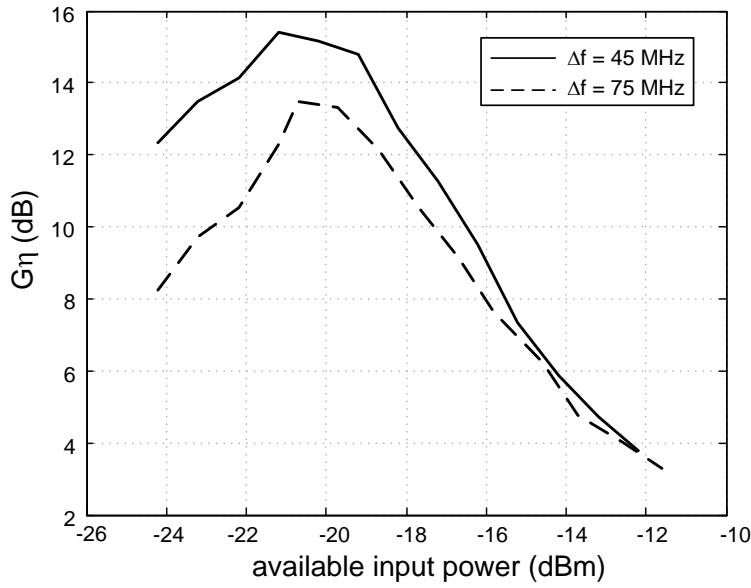


Fig. 5.12 Measured RF-DC efficiency gain (G_η) versus available input power at the rectifier.

5.5. Conclusions

This chapter has presented two architectures for MS signal generation to be used in WPT transmitters. These architectures aim at creating high PAPR MS signals for maximizing the RF-DC conversion efficiency in rectifier circuits located in the receiving end of a WPT system. The proposed schemes overcome the problem of amplifying large PAPR signals by using spatial power combining, where the individual tones are amplified, radiated and then the MS signal is passively created by spatial power combining. One of the proposed architectures is based on mode-locked oscillators that avoid the use of an external phase reference signal to set the adequate phase condition for synthesizing high PAPR MS waveforms by using the synchronization phenomenon in oscillators.

References

- [1] A. Georgiadis, A. Collado, "*Mode locked oscillator arrays for efficient wireless power transmission*", IEEE Wireless Power Transmission Conference 2013, pp. 73-75, Perugia, Italy, May 2013
- [2] J. Harvey, E.R. Brown, D.B. Rutledge, R.A. York, "*Spatial Power Combining for High Power Transmitters*", IEEE Microwave Magazine, December 2000.
- [3] J. Harvey, E.R. Brown, D.B. Rutledge, R.A. York, "*Spatial power combining for high-power transmitters*," Microwave Magazine, IEEE , vol.1, no.4, pp.48,59, Dec 2000
- [4] R. A. York, R. Compton, "*Coupled-Oscillator Arrays for Millimeter-Wave Power-Combining and Mode-Locking*", IEEE International Microwave Symposium, California USA, 1992.
- [5] C. A. Balanis, *Antenna Theory: Analysis Design*, 3th Edition, John Wiley & Sons, 2005.
- [6] R.A. York, R.C.Compton, "*Experimental observation and simulation of mode-locking phenomena in coupled-oscillator arrays*," Journal of Applied Physics , vol.71, no.6, pp.2959,2965, Mar 1992.
- [7] R.A.York, R.C. Compton, "*Mode-locked oscillator arrays*," Microwave and Guided Wave Letters, IEEE , vol.1, no.8, pp.215,218, Aug. 1991.
- [8] R.A.York, R.C. Compton , "*Measurement and modelling of radiative coupling in oscillator arrays*," Microwave Theory and Techniques, IEEE Transactions on , vol.41, no.3, pp.438,444, Mar 1993

6. JOINT WIRELESS POWER TRANSFER AND BACKSCATTER COMMUNICATION USING MS SIGNALS

6.1. Introduction: extending the reading range of commercial RFID readers

This chapter and the next answer to the third question formulated in the introduction section of this thesis: “*Can properly designed waveforms improve the coverage range of passive-backscatter systems such as passive RFID?*”.

Several circuit and system level approaches have been attempted to extend the reading range of passive RFID systems. Some of these approaches, reviewed in chapter 3, include the use of antenna beamforming [1], external CW transmitters [2], CMOS threshold compensation [3][4] and synergistic energy harvesting [4][5]. Recently, waveform design has been explored to increase the RF-DC conversion of rectifying circuits, and has also been applied to extend reading range [6-9].

This chapter evaluates joint WPT and backscattering data communication using MS signals to extend the reading range of RFID readers [V-VII]. First, a mathematical description is presented in order to show the ability of MS signals to communicate data, with minimal changes in the downlink path, while no changes are required in the conventional tag architecture. Moreover, and most importantly, if a proper MS design is performed, a conventional reader receiver is still able to demodulate and decode the backscattered MS signal from the tag, without any hardware change. Thus, guidelines are presented for MS design, including MS nature, central tone positioning, tone separation, and bandwidth requirements.

After, a commercial RFID reader is equipped with an external MS front-end that implements the previous mathematical proposals [IX][X]. In order to evaluate the reading range improvement, when compared with the conventional single-carrier approach with the same average power, two experiments are conducted: in the first one, an oscilloscope is used to visualize the tag response and to determine whether the tag does or does not respond. In the second measurement scenario, the downlink path is implemented by the reader combined with the front-end, and the uplink is implemented solely by the reader. In this case, the decision on successful tag response is taken when the reader actually accesses the tag identification (ID) number. The first measurement scenario has pointed out for a maximum reading range improvement of near 43% for a 8-tone MS signal with 2 MHz tone separation. In the second scenario, a more realistic one, a reading range improvement of almost 25% has been obtained for a 8+1 tones MS. In this chapter:

- 1) A mathematical model/description is provided for downlink and uplink using MS signals;
- 2) MS design requirements are presented to allow communication with a commercial reader;
- 3) The MS scheme is integrated in a commercial RFID reader. According to 1) and 2), the reader is still able to receive a backscattered MS signal without the deployment of new hardware in the receiver path.

6.2. The radio link using multi-sine signals

The radio link of passive RFID systems exhibits very peculiar characteristics [10][11]. Since a passive tag has no batteries, and it is entirely powered by the RF power radiated by the reader, the downlink operation has a twofold goal: data communication and power transfer. Moreover, since the passive tag has no local oscillator (LO), the uplink communication is implemented by backscatter mechanism as described in chapter 2 [11]. In this section, we analyze the data downlink and data uplink when using MS excitations instead of a conventional single-carrier. For the following mathematical description, consider the basic architecture of an RFID reader plus a MS front-end as depicted in Fig. 6.1 and a passive RFID transponder as described in chapter 2.

6.1.1. Multi-sine data downlink

As shown in chapters 4 and 5, from the viewpoint of WPT, high PAPR MS signals are beneficial since they provide increased RF-DC efficiency in diode detectors and charge pumps circuits commonly used in passive RFID transponders. This can potentially improve the communication range of RFID systems. However, in order to still guaranteeing data communication, the MS must be properly designed. In this section, we analyze the downlink data communication and we present design rules to guarantee communication with MS signals. In the following analysis, the transponder envelope detector and charge pump will be modelled by an even order polynomial series. In addition, all link factors are ignored and the effective length of the antennas are assumed to be unitary such that the electric field and voltage at their interfaces are interchangeable.

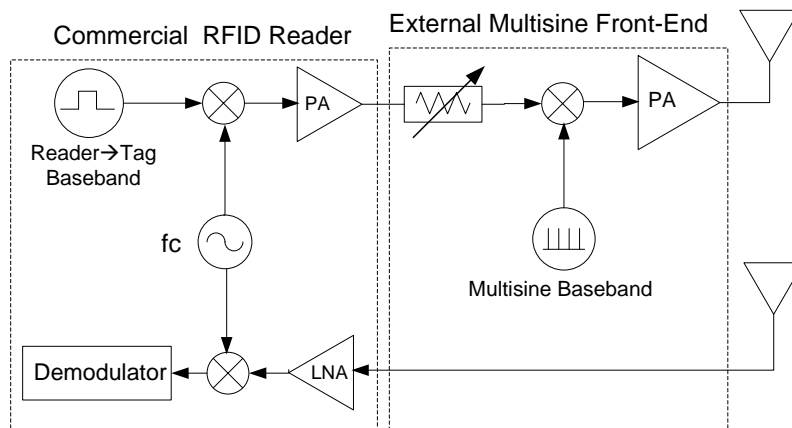


Fig. 6.1 Architecture of an RFID reader plus external multi-sine front-end. Using a proper MS design, the transponder response can be directly forward to the reader receiver. The attenuator in the forward path is used to find the minimum activation power level of the transponder.

The externally generated baseband MS [see Fig. 6.1] is a sum of N baseband subcarriers harmonically spaced by $\Delta\omega$:

$$S_{MB}(t) = \sum_{n=1}^N V_n \cos(n\Delta\omega t + \varphi_n) \quad (6.1)$$

where N is the number of tones, $\Delta\omega$ is the frequency separation between tones, V_n and φ_n are respectively the amplitude and phase of each tone. In the next analysis, all signals are represented in their Euler equivalent form. The modulated MS signal at the transmitter antenna [Fig. 6.1] is given by the mixture of the RFID baseband signal $m(t)$ and the reader LO signal with amplitude V_C and frequency ω_c , followed by a mixture with a zero phase⁵ baseband MS:

$$S_{MS}(t) = m(t) \left\{ \sum_{n=1}^N V_n \frac{e^{jn\Delta\omega t} + e^{-jn\Delta\omega t}}{2} \right\} \left\{ V_C \frac{e^{j\omega_c t} + e^{-j\omega_c t}}{2} \right\} \quad (6.2)$$

For instance, if a two-tone baseband MS is used ($N = 2$), the bandpass modulated MS $S_{MS}(t)$ will have spectral components at $-(\omega_c + 2\Delta\omega)$, $-(\omega_c + \Delta\omega)$, $-(\omega_c - \Delta\omega)$, $-(\omega_c - 2\Delta\omega)$, $(\omega_c - 2\Delta\omega)$, $(\omega_c - \Delta\omega)$, $(\omega_c + \Delta\omega)$, $(\omega_c + 2\Delta\omega)$:

$$S_{MS}(t) = m(t) \left\{ \begin{aligned} & \frac{V_1 V_C}{4} e^{j(\omega_c + \Delta\omega)t} + \frac{V_1 V_C}{4} e^{j(\omega_c - \Delta\omega)t} \\ & + \frac{V_1 V_C}{4} e^{-j(\omega_c - \Delta\omega)t} + \frac{V_1 V_C}{4} e^{-j(\omega_c + \Delta\omega)t} \\ & + \frac{V_2 V_C}{4} e^{j(\omega_c + 2\Delta\omega)t} + \frac{V_2 V_C}{4} e^{j(\omega_c - 2\Delta\omega)t} \\ & + \frac{V_2 V_C}{4} e^{-j(\omega_c - 2\Delta\omega)t} + \frac{V_2 V_C}{4} e^{-j(\omega_c + 2\Delta\omega)t} \end{aligned} \right\} \quad (6.3)$$

The frequency spectrum of $S_{MS}(t)$ is depicted in Fig. 6.2. As can be seen, the frequency separation between tones $\Delta\omega$ must be higher than the bandwidth of the data signal f_{BB} , such that the information can be successfully recovered at transponder side. Ideally, $\Delta\omega$ should be much higher than f_{BB} ($\Delta\omega \gg f_{BB}$). As an example, the EPC standard allows baseband data rates ($f_{BB}/2$) of 26.7 to 128 kbps [12], which requires a bandwidth f_{BB} of 53.4 to 256 kHz. In our experiments, the minimum tone separation used is 500 kHz, that is higher than the maximum bandwidth allowed by the standard. The increased bandwidth is one of the drawbacks of the MS scheme, however, the maximum bandwidth used in this work is compliant with ISM UHF regulations.

⁵ Zero phase arrangement and constant phase progression arrangement are the most efficient ones.

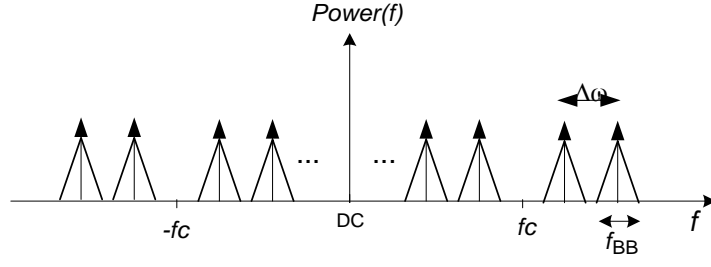


Fig. 6.2 Spectrum of a modulated multi-sine signal. The tone separation in the multi-sine must be higher than the bandwidth of the reader-to-transponder baseband signal in order to avoid spectrum overlapping that prevent the transponder to recover the reader's baseband information.

In order to understand the MS downlink operation, assume a unitary reader-to-transponder channel response and consider that the envelope detector of the transponder behaves as a pure squarer, $LN[S_{MS}(t)] = k_2[S_{MS}(t)]^2$ (a second order model is sufficient to describe the basic ASK demodulation operation). By squaring (6.3), baseband components will be generated from the product of the symmetric frequency components, $-(\omega_c + 2\Delta\omega) * (\omega_c + 2\Delta\omega)$, $-(\omega_c + \Delta\omega) * (\omega_c + \Delta\omega)$, $-(\omega_c - \Delta\omega) * (\omega_c - \Delta\omega)$, $-(\omega_c - 2\Delta\omega) * (\omega_c - 2\Delta\omega)$, yielding the following DC-centred baseband signal at the output of the transponder envelope detector (after low-pass filtering):

$$S_{TB}(t) = \frac{k_2}{4} [m(t)]^2 (V_1^2 V_c^2 + V_2^2 V_c^2) \quad (6.4)$$

According to (6.4), the transponder's detector is able to recover the baseband information $m(t)$ sent by the reader through the MS signal, provided that the condition $\Delta\omega > f_{BB}$ is satisfied. If the reader baseband information is an ASK signal formed of two levels ($a_k = 0$, $a_k = 1$) with bit period T [12],

$$m(t) = \sum_{k=-\infty}^{+\infty} a_k \delta(t - kT), \text{ then } [m(t)]^2 \text{ contains essentially the same binary information as } m(t). \text{ It is}$$

important to note that no changes are needed in the architecture of a typical transponder in order to demodulate these new kind of signals. In the transmission path, changes are only required on the reader side, namely to incorporate the MS signal. In this stage, MS signals are incorporated by using an external front-end as in Fig. 6.1. In the following chapter, this is efficiently implemented by using a SDR approach.

6.1.2. Multi-sine data uplink

As previously described in chapter 2, transponder-to-reader data communication is realized by power reflection: first the reader illuminates the transponder with an un-modulated carrier (a MS carrier in this case) and second, the transponder modulates its antenna reflection coefficient according to the information to be sent to the reader. Transponder information can be represented

by a time-varying reflection coefficient $\Gamma(t)$. Consider now that the transponder is illuminated with an un-modulated 3-tone MS signal, where the amplitudes of the subcarriers are respectively V_1 , V_0 and V_2 , and the phase relation between the subcarriers is 0° . This MS is designed in such way that the central subcarrier with amplitude V_0 is at the same frequency as the reader local oscillator. Thus, unlike signal (6.3) that has an odd number of tones and has no subcarrier at the local oscillator frequency, the bandpass version of this signal will exhibit additional spectral components at ω_c and $-\omega_c$ as can be seen in (6.5). In fact, this is the necessary condition to allow a conventional receiver to demodulate the reflected MS signal from the transponder without any hardware change. In order to better understand this operating mechanism, consider the transponder backscatter modulator (typically, a switching transistor as previously described in chapter 2), which modulates the MS subcarriers by acting on the reflection coefficient of the antenna at the different subcarrier frequencies, according to the baseband information to be sent to the reader. The reflected MS signal from the transponder comes as follows:

$$\begin{aligned}
S_{Back}(t) = & \left\{ \Gamma_0(t) \frac{V_0 V_C}{2} e^{j\omega_c t} + \Gamma_0(t) \frac{V_0 V_C}{2} e^{-j\omega_c t} + \Gamma_1(t) \frac{V_1 V_C}{4} e^{j(\omega_c + \Delta\omega)t} \right. \\
& + \Gamma_2(t) \frac{V_1 V_C}{4} e^{j(\omega_c - \Delta\omega)t} + \Gamma_2(t) \frac{V_1 V_C}{4} e^{-j(\omega_c - \Delta\omega)t} + \Gamma_1(t) \frac{V_1 V_C}{4} e^{-j(\omega_c + \Delta\omega)t} \\
& + \Gamma_3(t) \frac{V_2 V_C}{4} e^{j(\omega_c + 2\Delta\omega)t} + \Gamma_4(t) \frac{V_2 V_C}{4} e^{j(\omega_c - 2\Delta\omega)t} + \Gamma_3(t) \frac{V_2 V_C}{4} e^{-j(\omega_c + 2\Delta\omega)t} \\
& \left. + \Gamma_4(t) \frac{V_2 V_C}{4} e^{-j(\omega_c - 2\Delta\omega)t} \right\}
\end{aligned} \tag{6.5}$$

where $\Gamma_0(t)$, $\Gamma_1(t)$, $\Gamma_2(t)$, $\Gamma_3(t)$ and $\Gamma_4(t)$ are the time-varying reflection coefficients seen by each MS frequency component. Assuming again no link losses, the signal $S_{Back}(t)$ reaches the reader receiver antenna and it is forwarded to the down-conversion mixer [see Fig. 6.1] where it is mixed with the local oscillator at frequency ω_c , resulting in the following signal at the mixer output:

$$\begin{aligned}
S_{IF}(t) = & \left\{ \Gamma_0(t) \frac{V_0 V_C}{2} e^{j\omega_c t} + \Gamma_0(t) \frac{V_0 V_C}{2} e^{-j\omega_c t} + \Gamma_1(t) \frac{V_1 V_C}{4} e^{j(\omega_c + \Delta\omega)t} \right. \\
& + \Gamma_2(t) \frac{V_1 V_C}{4} e^{j(\omega_c - \Delta\omega)t} + \Gamma_2(t) \frac{V_1 V_C}{4} e^{-j(\omega_c - \Delta\omega)t} \\
& + \Gamma_1(t) \frac{V_1 V_C}{4} e^{-j(\omega_c + \Delta\omega)t} + \Gamma_3(t) \frac{V_2 V_C}{4} e^{j(\omega_c + 2\Delta\omega)t} \\
& + \Gamma_4(t) \frac{V_2 V_C}{4} e^{j(\omega_c - 2\Delta\omega)t} + \Gamma_3(t) \frac{V_2 V_C}{4} e^{-j(\omega_c + 2\Delta\omega)t} \\
& \left. + \Gamma_4(t) \frac{V_2 V_C}{4} e^{-j(\omega_c - 2\Delta\omega)t} \right\} \left\{ V_C \frac{e^{j\omega_c t} + e^{-j\omega_c t}}{2} \right\}
\end{aligned} \tag{6.6}$$

Note that, the only components of $S_{IF}(t)$ falling on baseband (centred on DC) result from the product of frequency components at ω_c and $-\omega_c$. After passing the signal $S_{IF}(t)$ through a low-pass filter (present in traditional receiver architectures) with a cut-frequency f_{BB} , a sample of the transponder's baseband information can be obtained as, $\Gamma_0(t)$ – reflection coefficient of the central frequency component:

$$S_{RB}(t) = \frac{1}{2} \Gamma_0(t) V_0 V_c^2 \quad (6.7)$$

The result in (6.7) shows that the received signal at the output of the low-pass filter is related to the amplitude of the local oscillator (V_c^2), but it is also related to the amplitude of the central component of the reflected MS signal $[V_0 \Gamma_0(t)]$, which contains the transponder baseband information. With the exception of a narrow bandpass filter at the input of the receiver to accept only the MS central tone and improve the system performance, with this approach no further changes are needed in the architecture of the receiver. Therefore, conventional RFID readers are still able to decode the transponder information on top of the MS signal. The previous description is illustrated in Fig. 6.3: in the first case, the reader transmits a MS carrier with an even number of tones without a component at the local oscillator frequency as in Fig. 6.3(a). In this scenario, although the transponder modulates and backscatters information on top of all the subcarriers, a conventional reader is not able to recover the transponder information, because after down-conversion the transponder baseband is not DC-centred and most probably falls out of the receiving low-pass band. However, in the second case [see Fig. 6.3(b)], the transponder is illuminated with a MS carrier with an odd number of tones, where the central tone coincides with reader's local oscillator. In this case, a conventional reader is able to demodulate and decode the transponder baseband information in the same manner it would do for a single-carrier. Note that the frequency position of the MS central component, coinciding with the LO frequency, is the necessary condition to allow a conventional reader to demodulate/decode MS signals, while the odd number of tones is an additional condition to guarantee spectrum symmetry and to simplify the MS signal generation and hardware design. Additionally, the bandwidth of the receiver low-pass filter should be tight enough to reject all the lateral MS components (that otherwise act as noise), leaving only the DC-centred component.

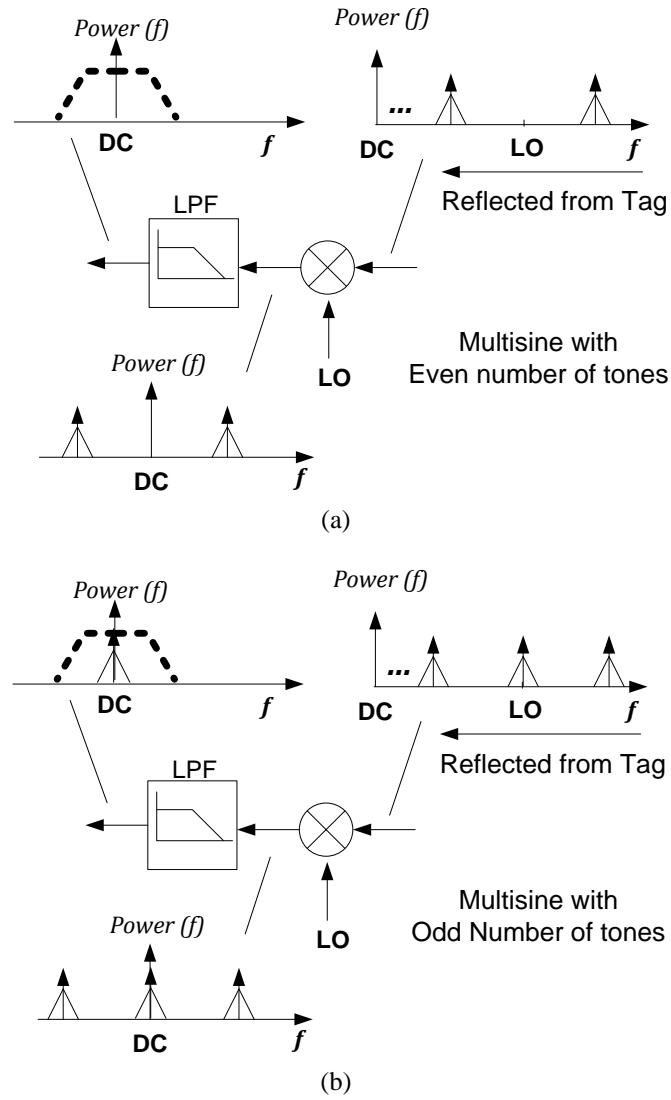


Fig. 6.3 (a) Even number of tones scheme. (b) Odd number of tones scheme. Dashed line represents the low-pass filter. In the first case (even MS), a conventional reader is not able to recover the transponder baseband information, while in the second case (odd MS), a common reader is allowed to access and process the transponder response.

6.3. Laboratorial setup and measurements

In order to evaluate the reading range improvement in comparison to the conventional single-carrier approach with the same average power, two experiments are conducted: in the first one, an oscilloscope is used to capture the transponder response and to determine whether the transponder does or does not respond. In the second measurement scenario, the downlink path is implemented by the reader combined with the MS front-end and the uplink is fully implemented by the reader, by using the previous MS design rules. In this case, the decision on successful tag response is taken when the reader actually accesses the tag ID.

6.1.3. Measurement setup 1

In this measurement scenario, a commercial RFID reader [13][14], compliant with ISO/IEC 18000-6 and EPC Global Class-1 Generation-2 protocols [12], is equipped with an external front-end that incorporates the MS waveform in the built-in reader signal. Figures 6.4 and 6.5 show the block diagram and respective laboratory testbed used in the measurements. The setup is similar to the one in [6], except that a commercial RFID reader is used here.

The output of the reader transmitter is mixed with a baseband MS, and then amplified and transmitted. Two power splitters are used, the first one to pick a sample of the transmitted signal to be used as local oscillator for the receiving path, and the second one to provide a measure of the radiated average power. The signal reflected from the transponder is down-converted (mixed with f_c) so that the tag baseband response can be visualized in the oscilloscope. This provides us with the visual information of whether the transponder is or not activated [see tag response in Fig. 6.6]. An attenuator is used to control the radiated power and to find the minimum power level needed to activate the transponder. The receiving antenna and the EPC Global compliant transponder are placed at a fixed distance R of the transmitter antenna.

In order to evaluate the improvements of the MS scheme, a FOM is defined as the difference between the minimum average power required to activate and get a response from the transponder using a single-carrier signal (P_{CW}) and the minimum average power required to activate the transponder using a MS signal (P_{MS}) at the same distance R : $G_P(\text{dB}) = P_{CW} - P_{MS}$. Note that G_P is a sensitivity gain, which is equivalent to the efficiency gain G_η previously defined in chapter 4. In order to determine such gain, first the transponder is illuminated with a single-carrier, and by varying the attenuation of the transmission path the minimum average power (P_{CW}) to activate the transponder at a distance R is found. In the second experiment, the previous procedure is repeated but now using a MS signal. By using the measured gain G_P and Friis equation, it is possible to estimate the expected communication range gain r (in meters): the minimum DC power needed to activate the transponder at a distance R when using a single-carrier is given by $P_{DC_min} = \eta_{CW} P_t G_t G_r \left(\frac{\lambda}{4\pi R} \right)^2$, where η_{CW} is the RF-DC conversion efficiency under CW excitation, P_t is the transmitted power, G_t and G_r are the transmitter and receiver antenna gains respectively, λ is the wavelength and R is the distance between reader and transponder antennas. On the other hand, when using a MS with the same average transmitted power P_t , a power gain G_P is expected and consequently a reading range gain r . Thus, the Friis equation can be re-written as $P_{DC_min} = G_P \eta_{CW} P_t G_t G_r \left(\frac{\lambda}{4\pi(R+r)} \right)^2$. By equalling the two previous Friis equations, an estimation for the reading range gain can be obtained: $r = R(\sqrt{G_P} - 1)$ [m].

Table 6.1 presents the measurement results. Four different signals were used in the measurements, including a single-carrier and three MS signals with two, four and eight tones. Each MS signal was also tested with three different tone separations. The CW reference signal required a minimum transmitted power $P_{CW} = 19.3$ dBm for a reference distance of $R = 1.9$ m. For the fixed distance R , the tag sensitivity gain G_P for each MS signal can be obtained based on the reference power P_{CW} and on the minimum power required for each MS, P_{MS} . Finally, we can estimate the expected reading range gain r . The best result is obtained for the 8-tone MS with an optimal tone separation of 2 MHz, pointing out a communication distance improvement of 43%.

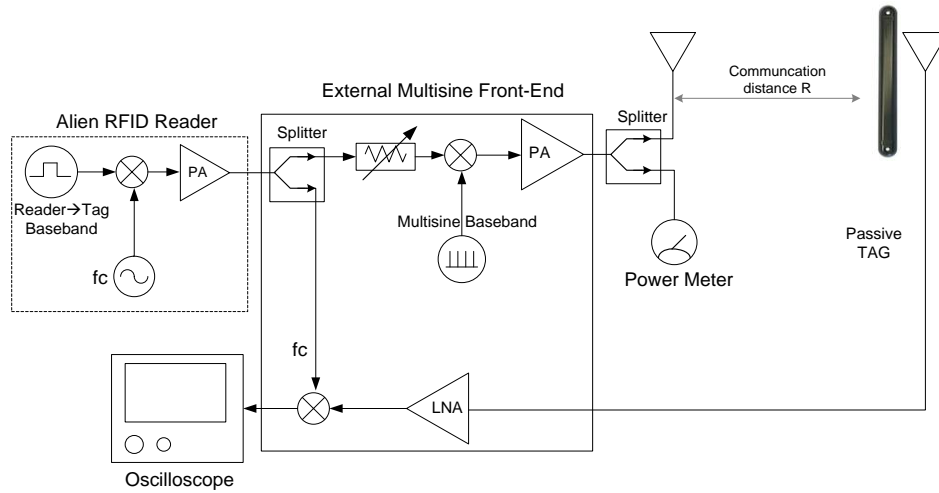


Fig. 6.4 Laboratory setup used to measure tag sensitivity gain.

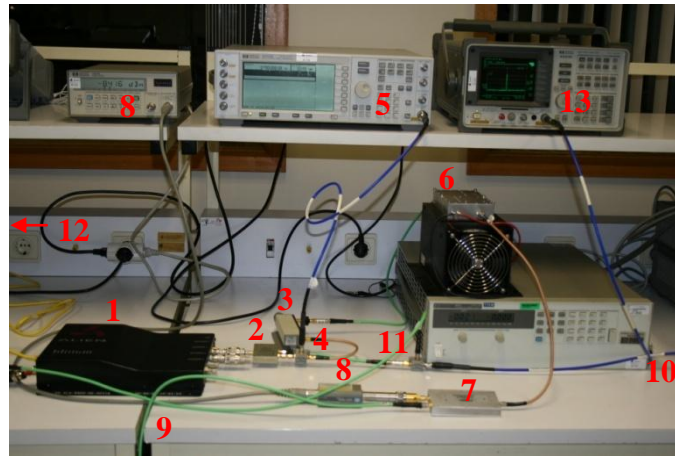


Fig. 6.5 RFID reader and multi-sine front-end setup: 1-RFID reader, 2-power splitter, 3-variable attenuator, 4-mixer, 5-signal generator, 6-power amplifier, 7-power splitter, 8-power meter, 9-cable to the transmitting antenna, 10-cable from the receiving antenna, 11-mixer, 12-oscilloscope, 13-spectrum analyzer.

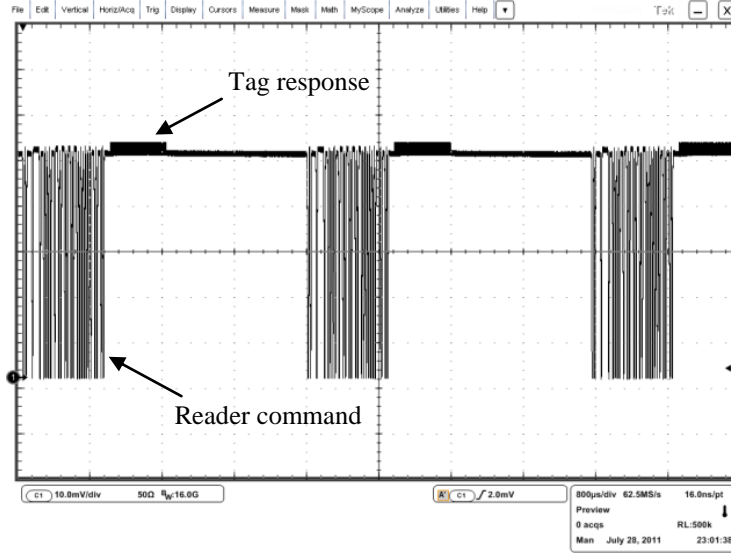


Fig. 6.6 Baseband signal visualized in the oscilloscope: RFID reader commands followed by tag responses.

TABLE 6.1

EXPECTED SENSITIVITY GAINS AND READING RANGE GAINS OBTAINED IN THE FIRST MEASUREMENT SCENARIO

Signal	$\Delta\omega$ (MHz)	P_{min} (dBm)	G_P (dB)	r (m)	r (%)
1-tone		19.3	0.0	0.0	
2-tones	3.0	17.4	+1.9	+0.46	24.2
	2.0	17.5	+1.8	+0.44	23.2
	1.0	17.8	+1.5	+0.36	18.9
4-tones	3.0	16.5	+2.8	+0.72	37.9
	2.0	17.2	+2.1	+0.52	27.4
	1.0	17.7	+1.6	+0.38	20.0
8-tones	2.0	16.2	+3.1	+0.81	42.6
	1.0	16.4	+2.9	+0.75	39.4
	0.5	No response	-----	-----	-----

6.1.4. Measurement setup 2

In this measurement setup, instead of evaluating the tag response using an oscilloscope as did in the previous section, the tag response is forwarded to the reader receiver as in Fig. 6.1. In this case, the downlink path is implemented by the reader combined with the external front-end, but the uplink is implemented solely by the reader, and the decision on successful tag response is taken when the reader actually reads the tag ID. Contrary to a more complex receiver configuration using matched filters (discussed in the next chapter), this is a very simple scheme that does not require any additional hardware to be deployed in the receiving path, provided that the MS design requirements stated before are fulfilled, namely odd number of tones, central tone positioning, tone separation

and bandwidth. The latter requirements are important in order to avoid spectrum overlapping and guarantee compliance with the internal low-pass filter of the reader.

The MS tone spacing plays an important role, as it should fit the filtering stage of the transponder charge pump, as previously discussed in chapter 4, but also it should avoid aliasing between the modulation bandwidth of each modulated subcarrier, as seen in Fig. 6.3. Moreover, as previously mentioned, the baseband MS signal must have a DC component such that its bandpass version exhibits a component at the local oscillator frequency. Since the baseband MS is being provided by a signal generator with a DC-decoupled output, an additional function generator and a bias-tee are used to add a DC component in the baseband MS [See Fig. 6.7(a)]. Hence, the bandpass MS will present a spectral component at the LO frequency, and fulfil the requirements related to odd number of tones and central frequency position. The DC component is varied in order to equate the amplitude of the central tone to the same level as the other subcarriers. Figure 6.7(b) presents an alternative configuration of the transmitter that uses a sample of the reader signal directly forwarded to the PA in order to provide the MS with a central component equal to the reader's carrier. In this alternative setup, a DC component in the baseband MS is no longer needed, and an attenuator can be used to level the central tone. Depicted in Fig. 6.8(a) is the typical frequency spectrum of a 8+1 tones MS. Figure 6.8(b) shows the expected shape of the normalized time-domain waveform.

Table 6.2 presents the measurement results obtained in the second setup, where the RFID reader is actually reading the tag ID. The notation $x+1$ tones stands for a MS with an odd number of tones with x lateral subcarriers plus a central subcarrier. In this case, the distance between the reader and transponder was set to $R = 1.7$ m, and the minimum power to activate the transponder with the single-carrier signal was found to be 16.5 dBm. Although the gains are lower than the first case setup (the reason for this is detailed in the discussion section), an improvement of almost 25% has been achieved with an 8+1 tones MS with 2 MHz tone separation.

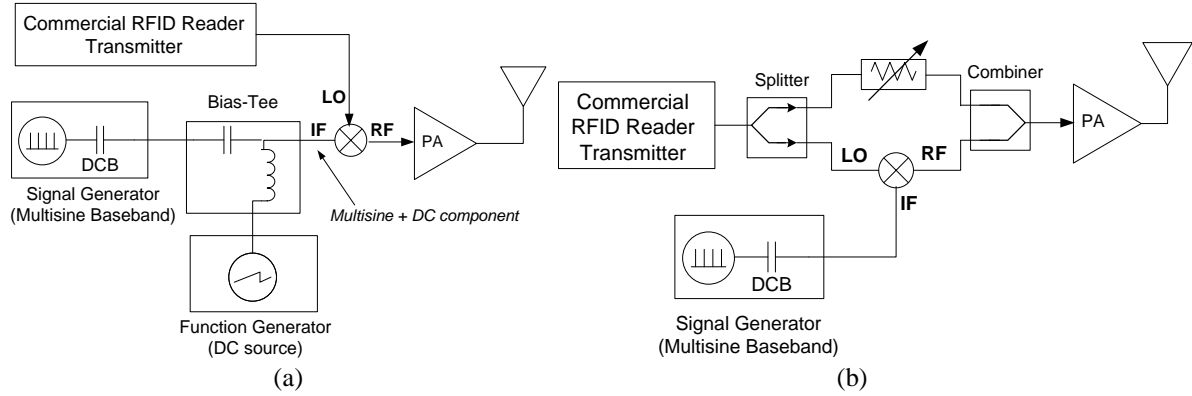


Fig. 6.7 Transmitter configurations. (a) Setup used in the experiments, where a DC component is added to the baseband multi-sine in order to create a central component in the bandpass multi-sine. (b) alternative setup configuration, where a sample of the reader signal is directly transmitted to provide a central component in the multi-sine.

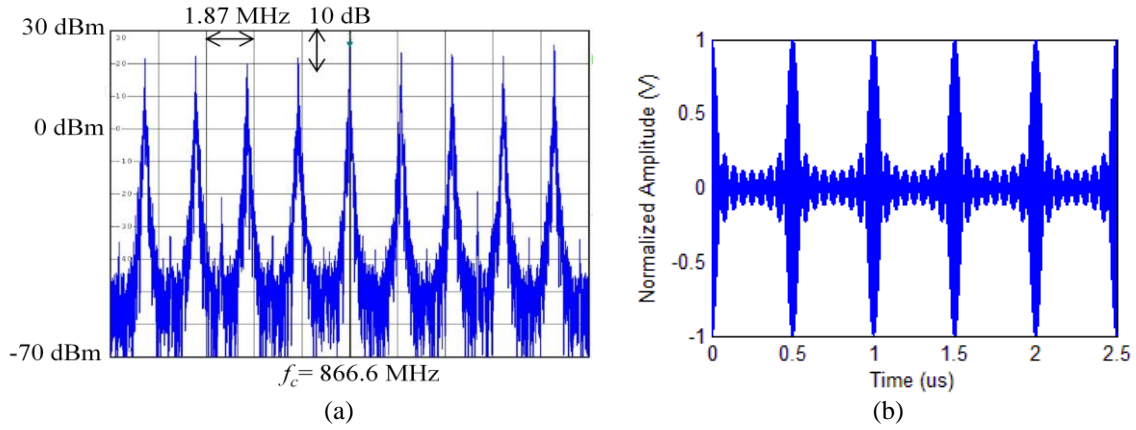


Fig. 6.8 Modulated 8+1 tones multi-sine signal. (a) Frequency spectrum: the 866.6 MHz RF carrier is modulated by an arbitrary ASK signal at 100 kbps and the resultant signal is then mixed with the baseband multi-sine. In this example the baseband multi-sine is a 4-tone (centred at 5 MHz, with 2 MHz tone separation) plus a DC component externally imposed by a function generator. (b) Normalized time-domain waveform.

TABLE 6.2
SENSITIVITY GAINS AND READING RANGE GAINS

Signal	$\Delta\omega$ (MHz)	P_{min} (dBm)	G_P (dB)	r (m)	r (%)
1-tone		16.5	0.0	0.0	
2+1 tones	2.0	15.4	+1.1	+0.23	13.5
	1.0	16.9 (-)	-0.4	-0.08	-4.7
4+1 tones	2.0	14.9	+1.6	+0.34	20.0
	1.0	16.2	+0.3	+0.06	3.5
8+1 tones	2.0	14.6	+1.9	+0.42	24.7
	1.0	16.2	+0.3	+0.06	3.5
	0.5	No response	-----	-----	-----

6.4. Results discussion and conclusions

Tables 6.1 and 6.2 show that the second experiment provides less expressive results. Recall that in the second experiment, the tag information (ID) is actually accessed (demodulated and decoded) by the reader, contrary to the first experiment where we were only interested in observing the tag response in the oscilloscope, without any consideration on the quality of the tag response. A prior investigation [15] showed that, in some situations the tag only returns a partial response and the reader is not able to properly decode the information (please refer to figure 4 of [15]). This effect, associated to the fact that the reader sensitivity is also important in the second case, helps explaining the overestimated results in the first setup.

As a general trend, the gains in both experiments are degraded with the decreasing of the tone separation, and for very low tone separation values, the transponder does not even respond. This is very likely due to the ripple effect on the transponder's RF-DC converter imposed by the low frequency separation between tones in the MS. Figure 6.9 illustrates how the tone separation imposes different time-domain behaviours at the RF-DC converter output. A phase- synchronized MS exhibits a very high PAPR, and thereby high peaks in the time-domain waveform. These time-domain peaks are temporally separated by $T = 1/\Delta\omega$, and consequently, as the tone separation is reduced, the time-domain peaks will separate from each other and the output ripple will increase. The existence of ripple may lead to different kind of problems: first, the average voltage at the charge pump output will be reduced as the ripple increases, and may go below the transponder activation level, as illustrated in Fig. 6.9; second, with the increase of the ripple, non-DC signal components may propagate into the transponder electronics acting as AC interference. Nevertheless, it is expected that the regulation stage of the transponder will attenuate this effect. These effects are visible in the last columns of Table 6.1 and Tables 6.2, where the transponder does not respond for a very low tone separation of 500 kHz. There exist, thus, a minimum tone separation value that is strongly related to the output filtering stage of the tag RF-DC converter. This minimum value can be optimized (lowered) by reducing the ripple effect through the use of a larger capacitance at the output of the RF-DC converter. It is worth mentioning that ripple problem is not critical when using a conventional single-carrier because, in that case, the signal envelope remains constant. However, in the MS scheme, the ripple is imposed by the tone separation (and thereby by the envelope of the MS signal) rather than the RF signal. For instance, a tone separation of 2 MHz imposes a MS peak separation equal to 0.5 μ s [see Fig. 5.8(b)], while an RF carrier at 866 MHz has an RF peak separation of approximately 1.15 ns.

As can be concluded from the experimental results, the gains are directly influenced by the combination of the MS parameters such as number of tones, bandwidth and tone spacing: in principle, as the number of tones increases, the PAPR also increases leading to an increase in the

efficiency of the charge pump, and consequently the coverage range increases. However, at a certain point, the increase of the number of tones provides no extra gain. This is explained by the breakdown effect and by the increased losses in the series resistance of the rectifying devices caused by very high PAPR. On the other hand, for the same tone spacing, as the number of tones increases, the MS bandwidth also increases, having a negative impact on the efficiency because of the limited input bandwidth of the transponders. An optimal frequency separation value exists which is limited by two effects: 1) for the same number of tones, the higher the frequency separation, the higher the input bandwidth and some signal components may be attenuated due to the limited bandwidth of the transponder. 2) the subcarrier separation in the frequency domain directly affects the separation between the signal peaks in the time-domain. Thus, the lower the frequency separation, the higher the ripple effect, which degrades the performance.

Further improvements to the system may include the introduction of a bandpass filter at the output of the power amplifier to avoid out-of-band emissions, and the use of a narrowband filter at the input of the reader receiver to prevent transmitter-to-receiver leakage of the MS lateral components. In this part of the work, a highly-linear amplifier with a high dynamic range is used (Mini Circuits PA ZHL-10W-2G+) in order to avoid signal clipping and to guarantee that the high PAPR signal reaches the tag.

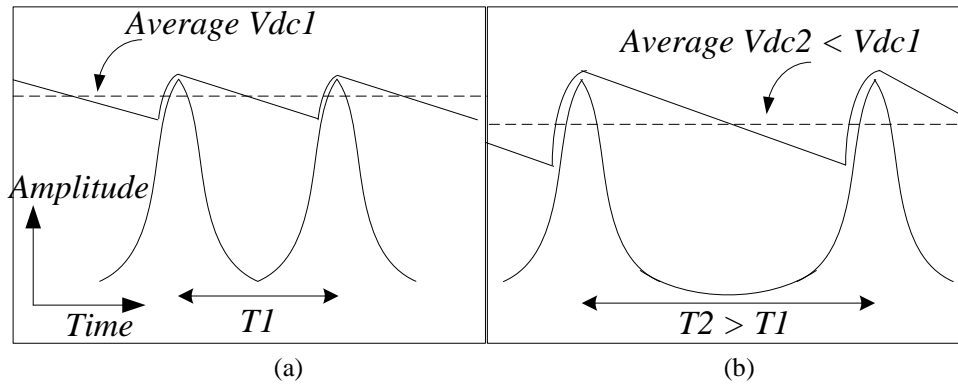


Fig. 6.9 Tone separation effect illustrated in the time-domain. (a) Higher average DC voltage obtained with a lower envelope period (higher tone separation). (b) Lower average DC voltage for higher envelope period. The pulsed signal is the envelope of the high PAPR signal after being rectified, maximum ripple value depends both on tone separation and on the output filter of the RF-DC converter.

References

- [1] Mehmet Abbak and Ibrahim Tekin, “*RFID Coverage Extension Using Microstrip Patch Antenna Array*”, Vol 51, No. 1, p.p.: 185-191, Feb 2009, Antennas and Propagation Magazine, IEEE.
- [2] Jun-Seok Park, Jin-Woo Jung, Si-Young Ahn, Hyoung-Hwan Roh, Ha-Ryoung Oh, Yeung-Rak Seong, Yoon-Deock Lee, and Kyoung Choi “*Extending the Interrogation Range of a Passive UHF RFID System With an External Continuous Wave Transmitter*”, IEEE TRANSACTIONS ON INSTRUMENTATION AND MEASUREMENT, VOL. 59, NO. 8, p.p.: 2191-21-97, AUGUST 2010.
- [3] T. Feldengut, R. Kokozinski, and S. Kolnsberg, “*A UHF Voltage Multiplier Circuit Using a Threshold-Voltage Cancellation Technique*,” in Research in Microelectronics and Electronics, July 2009, pp. 288 – 291.
- [4] Koji Kotani, “*Highly Efficient CMOS Rectifier Assisted by Symmetric and Voltage-Boost PV-Cell Structures for Synergistic Ambient Energy Harvesting*”, IEEE Custom Integrated Circuits Conference, p.p.: 1-4, San Jose, CA, Sept. 2013.
- [5] A. Georgiadis and A. Collado, “*Improving Range of Passive RFID Tags Utilizing Energy Harvesting and High Efficiency Class-E Oscillators*”, Proc. EuCAP 2012, Prague, March 2012.
- [6] M. S. Trotter, J. D. Griffin and G. D. Durgin “*Power-Optimized Waveforms for Improving the Range and Reliability of RFID Systems*”, IEEE International Conference on RFID, p.p.: 80-87, 2009.
- [7] Hisanori Matsumoto and Ken Takei, “*An Experimental Study of Passive UHF RFID System with Longer Communication Range*”, Proceedings of Asia-Pacific Microwave Conference, p.p.: 1-4, 2007.
- [8] Chun-Chih Lo, Yu-Lin Yang, Chi-Lin Tsai, Chieh-Sen Lee, and Chin-Lung Yang, “*Novel Wireless Impulsive Power Transmission to Enhance the Conversion Efficiency for Low Input Power*” , Microwave Workshop Series on Innovative Wireless Power Transmission, 2011.
- [9] Yu-Lin Yang, Chin-Lung Yang, Chi-Lin Tsai, and Chieh-Sen Lee, “*Efficiency Improvement of the Impulsive Wireless Power Transmission*”, Microwave Workshop Series on Innovative Wireless Power Transmission, 2011.
- [10] Finkenzeller, Klaus, *RFID Handbook*, 2nd Edition ed. Wiley, 2003.
- [11] Daniel M. Dobkin, *The RF in RFID: Passive UHF in Practice* , Newnes, Burlington, MA, USA, 2007.
- [12] EPC Class-1 Generation-2 UHF RFID, Protocol for Communications at 860 MHz – 960 MHz, Version 1.2.0, 2008.
- [13] Alien technology, Hardware Setup Guide ALR-8800, 2007.
- [14] Alien technology, Reader Interface Guide, September 2007.
- [15] Xunteng Xu, Lin Guy, Jianping Wang and Guoliang Xing, “*Negotiate Power and Performance in the Reality of RFID Systems*”, IEEE International Conference on Pervasive Computing and Communications, Mannheim, p.p.: 88-97, March 2010.

7. SOFTWARE-DEFINED RADIO RFID READER DESIGN WITH IMPROVED POWERING WAVEFORMS

7.1. Introduction: prior work

Several circuit and system level approaches have been attempted in the literature to improve the reading range of passive RFID systems, including antenna beamforming [1], external CW transmitters [2], CMOS threshold compensation [3][4] and synergistic energy harvesting [4][5] (see chapter 3 for details). For the same reasoning of extending the reading range, waveform design optimization has been explored as an alternative to circuit and system design optimization (this is addressed in chapter 4).

In [6], a bursty CW signal with high PAPR and low duty cycle was used in an RFID reader to reduce the average transmitted power while keeping the same communication distance that would be obtained with an always-ON CW signal with same average power. Although an ON-OFF approach was used in that work to achieve high PAPR, the rigid implementation does not allow for arbitrary waveform design. In [7], passive RFID tags were tested under a category of multi-sine signals (referred to as POW – Power-Optimized Waveforms), which provided an improvement in the reading range. However, the RFID protocol was only partially implemented, consisting of a single reader-tag-reader transaction, namely reader *Query* followed by tag RN16 response. The MATLAB-generated reader baseband plus POW signal was created using a DAC, while the tag response was observed in an oscilloscope. The previous chapter reports on the work conducted in [IX][X], where a MS front-end was integrated in a commercial RFID reader to demonstrate that: 1) the reading range can be improved when using MS signals; 2) MS receiver complexity can be reduced to that of a regular CW receiver if a proper MS design is performed. Nevertheless, only the MS signal was generated externally by using a VSG. Since the RFID protocol was handled by a commercial RFID reader, it was not possible to access the reader internal signals. In [XI], we presented an evaluation of joint wireless power transfer and backscattering communication using MS signals and we first attempted on the design of a custom-designed MS reader⁶. Although the RFID protocol was implemented using a custom SDR design, due to digital hardware limitations⁷, the baseband MS waveform had to be generated externally by using an AWG (Arbitrary Waveform Generator).

SDR RFID reader design offers an increased flexibility and allows to adapt to different standards by simply upgrading the reader software. This approach has been used for RFID research purposes [8][9], RFID characterization and measurements [10], protocol exploration [11], localization [12]

⁶ This RFID reader was also used in the self-jamming evaluation presented in the next chapter.

⁷ A single-core CPU working @ 150MHz was used in contrast to the four-core CPU used here, each core operating @ 200MHz.

and also industry applications [13]. In [XII], a SDR-based MS RFID reader has been designed from scratch for the first time. This chapter reports on such design. In addition to fully implementing the RFID communication protocol in CW mode under EPC Global Gen2/ISO-18000-6C standard [14], the presented SDR reader is capable of generating arbitrary powering waveforms, such as MS signals, that can improve the wireless power transfer capability and thereby increase the coverage range.

Measurements have been conducted using the developed reader, namely to evaluate the self-jamming cancellation scheme used, the proposed MS demodulation approaches, the multipath fading performance and the sensitivity improvement of RFID chips under MS waveforms. A sensitivity gain of more than 3 dB relative to the CW has been obtained for an RFID chip under a 9-tone MS signal with a PAPR of 12.6 dB.

7.2. Theoretical analysis

In the previous chapter, the MS backscatter link was described for unitary channel response and it was shown that traditional RFID tags are able to demodulate a MS signal similar to (7.3). In order to broaden the description to account for arbitrary propagation phase shift, consider the following analysis. Signal (7.3) is a symmetrical 3-tone MS signal, which results from the product of the reader baseband signal $[m(t)]$, the LO carrier $[S_C(t)]$ and an harmonically-related baseband MS signal $[S_{MB}(t)]$.

$$S_{MB}(t) = V_0 + V_1 \cos(\Delta\omega t) \quad (7.1)$$

$$S_C(t) = V_C \cos(\omega_C t) \quad (7.2)$$

$$\begin{aligned} S_{MS}(t) &= m(t)S_{MB}(t)S_C(t) \\ &= \frac{m(t)}{2} V_1 V_C \cos((\omega_C - \Delta\omega)t) + m(t)V_0 V_C \cos(\omega_C t) + \frac{m(t)}{2} V_1 V_C \cos((\omega_C + \Delta\omega)t) \end{aligned} \quad (7.3)$$

where V_0 is a DC component in the baseband MS and $\Delta\omega$ is the MS subcarrier separation. As demonstrated in chapter 4, signal (7.3) can excite the charge pump circuit of the RFID tag in a more efficient way than a CW signal, which can potentially improve the reading range of passive-backscatter systems. During uplink, signal (7.3) is radiated by the reader to power up the tag, and part of this signal, $[S_{Back}(t)]$, is backscattered by the tag according to its baseband information $[I(t) \rightarrow I_0(t), I_1(t), I_2(t)]$. Note that $m(t)$ is held constant during uplink (e.g. $m(t) = 1$). Thus, the backscattered signal is given by:

$$\begin{aligned}
S_{back}(t) &= \Gamma(t)S_{MS}(t) \\
&= \frac{1}{2}\Gamma_1(t)V_1V_C \cos((\omega_C - \Delta\omega)t + \phi_1) + \Gamma_0(t)V_0V_C \cos(\omega_C t + \phi_2) \\
&\quad + \frac{1}{2}\Gamma_2(t)V_1V_C \cos((\omega_C + \Delta\omega)t + \phi_3)
\end{aligned} \tag{7.4}$$

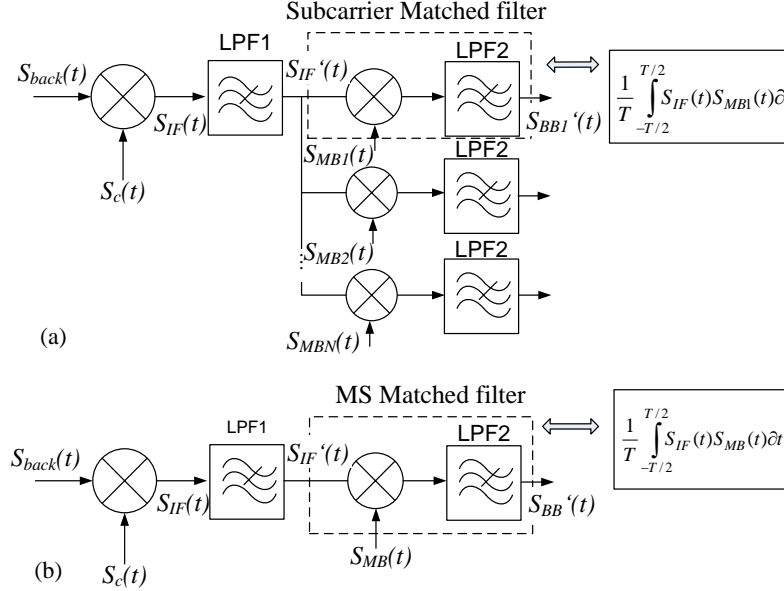


Fig. 7.1 (a) Bank of matched filters. (b) MS matched filter. On the left is the hardware implementation and on the right is the corresponding software version. LPF1 is utilized to remove the RF components and LPF2 is a narrower filter which is part of the matched filter.

where ϕ_1 , ϕ_2 and ϕ_3 are the round trip phase shifts of the subcarriers with respect to the reader LO, and $\Gamma_0(t)$, $\Gamma_1(t)$ and $\Gamma_2(t)$ are the time-varying reflection coefficients seen by each subcarrier. Neglecting all scaling factors, signal (7.4) reaches the reader antenna and then it is down-converted to baseband, resulting in signal (7.5).

$$\begin{aligned}
S_{IF}(t) &= S_{Back}(t)S_C(t) = \frac{1}{4}\Gamma_0(t)V_0V_C^2 \cos(\phi_2) + \frac{1}{4}\Gamma_0(t)V_0V_C^2 \cos(2\omega_C t + \phi_2) \\
&\quad + \frac{1}{4}\Gamma_1(t)V_1V_C^2 \cos(-\Delta\omega t + \phi_1) + \frac{1}{4}\Gamma_1(t)V_1V_C^2 \cos((2\omega_C - \Delta\omega)t + \phi_1) \\
&\quad + \frac{1}{4}\Gamma_2(t)V_1V_C^2 \cos(\Delta\omega t + \phi_3) + \frac{1}{4}\Gamma_2(t)V_1V_C^2 \cos((2\omega_C + \Delta\omega)t + \phi_3)
\end{aligned} \tag{7.5}$$

As the MS is symmetrically designed, with a central subcarrier at the LO frequency, then a sample of the backscattered tag baseband can be retrieved simply by low-pass filtering (7.5) with a cut-off frequency lower than $\Delta\omega$, originating the in-phase tag baseband signal (7.6). This obviates the receiver design and allows a conventional receiver to decode the MS tag response as done in [X]. Note that the quadrature signal is complementary to (7.6).

$$S_{BB}(t) = \frac{1}{4}\Gamma_0(t)V_0V_C^2 \cos(\phi_2)$$

(7.6)

The tag information modulated on the other subcarriers can be retrieved as well by using a bank of matched filters [Fig. 7.1(a)] or a single MS matched filter [Fig. 7.1(b)]. In the first case, each filter is matched to a subcarrier, and in the second case, the correlation pulse is the baseband MS signal (1).

TABLE 7.1
LOW-COST DSP AND MICROCONTROLLER DEVICES SUITABLE FOR THIS WORK

	F28335 (32-bits)	F28377D (32-bits)	C28346 (32-bits)	C5410A (16-bits)	TMS320C67 48 (32-bits)	OMAP-L138 (DSP C674x + ARM)	LPC4370 (32-bits) ARM Cortex- M4 + 2M0	ADSP- BF506F (BlackFin)
Manufacture	TI	TI	TI	TI	TI	TI	NXP	Analog Dev ³
N. of cores	Single	Dual	Single	Single	Single	Dual	Dual	Single
CPU Speed	150MHz	2x 200 MHz	300 MHz	160 MHz	456 MHz (3648 MIPS)	2x456 MHz	2x204 MHz	400 MHz (800MMACS)
Co-processor		2 CLAs at 200 MHz					2 Cortex-M0	
FPU	Yes	Yes						
FLASH	512KB	1MB	External	External	External	External	External	32MB
RAM	64KB	204KB	510KB	128KB	64+256KB	64+256KB	264KB	68KB
ADC	12.5MSP S	3.5 MSPS	NO	NO	NO	NO	80 MSPS	Up to 2 MSPS
DMA	Yes	Yes	Yes	Yes	Yes	Yes	Yes	Yes
USB	NO	Yes	NO	NO	Yes	Yes	Yes	
Ethernet	NO	NO	NO	NO	Yes	Yes	Yes	
Price/Ku	14.25 \$	18 \$	16.4 \$	16.15 \$	11.5 \$	14.90 \$	11 \$	12.2 \$

Assuming that the RF components of signal (7.5) are removed by LPF1, the output of the MS matched filter of Fig. 7.1(b) comes as follows:

$$\begin{aligned}
 S'_{BB}(t) &= \frac{1}{T_{symbol}} \int_{-\frac{T_{symbol}}{2}}^{\frac{T_{symbol}}{2}} S_{IF}(t) S_{BM}(t) dt \\
 &= \frac{1}{4} \Gamma_0(t) V_C^2 V_0^2 \cos(\phi_2) + \frac{1}{4} \Gamma_1(t) V_C^2 V_1^2 \cos(\phi_1) + \frac{1}{4} \Gamma_2(t) V_C^2 V_1^2 \cos(\phi_3)
 \end{aligned} \tag{7.7}$$

Due to random changes in the round trip phase shift [ϕ_2 in (7.6)], the transponder constellation suffers unpredictable rotations before it reaches the reader. Hence, the received constellation must be phase-rotated such that it aligns with the real-axis and thereby it can be demodulated as if it was pure ASK (refer to chapter 2, Fig. 2.11). For this reason, common RFID readers employ quadrature demodulators to recover both the in-phase and quadrature components. On the other hand, the phase diversity present in (7.7), imposed by the different phase shifts of the several MS subcarriers, can be exploited to avoid the use of an *IQ* demodulator. This is evaluated in the measurements section.

7.3. The software-defined radio design

7.3.1. SDR RFID hardware implementation

In the course of this work, two SDR RFID readers were engineered, one based on a single-core MCU/DSP (described in the next chapter) and other based on a dual-core MCU/DSP. The block diagram of the latter is depicted in Fig. 7.2 (a) and the respective hardware is shown in Fig. 7.2 (b). The RF/analog part is built around an integer-N PLL (Phase Locked Loop) with integrated VCO (Voltage Controlled Oscillator) from Analog Devices [15]. The RF front-end, operating in the 840 MHz – 960 MHz band, is composed of frequency synthesizer, *IQ* up- and down-conversion stages, Rx baseband low-pass filters and PGAs (Programmable Gain Amplifiers). The transmitting path uses a modified homodyne architecture in which the RFID bandpass signal (output of Mix1) is mixed with a baseband MS signal similar to that in (7.1) to produce a bandpass signal similar to the one in (7.3). The resulting signal is then amplified by an external PA.

The digital part is implemented in DSP (Digital Signal Processor) technology. A survey on low-cost DSP and microcontroller (MCU) devices in the market suitable for this application is presented in Table 7.1. Taking into account the trade-off between cost, processing speed, memory space and integrated peripherals, a 32-bit four-core MCU/DSP⁸ from Texas Instruments [16] (second column of Table 7.1) was selected for this work. Among the principal features, it includes two main CPU cores plus two co-processors (referred to as CLAs – Control Law Accelerators), an internal multi-channel ADC (Analog-to-Digital Converter) and several other peripherals. This choice offers an increased computational capability in comparison to the one previously used in [XI] (first column of Table 7.1). The four cores running at 200 MHz allow the parallelization of tasks and permit a maximum processing speed of 800 MIPS. Moreover, the integrated peripherals, such as ADCs, DMAs (Direct Memory Access), internal FLASH, etc, greatly reduces the overall size and cost, and eases the implementation.

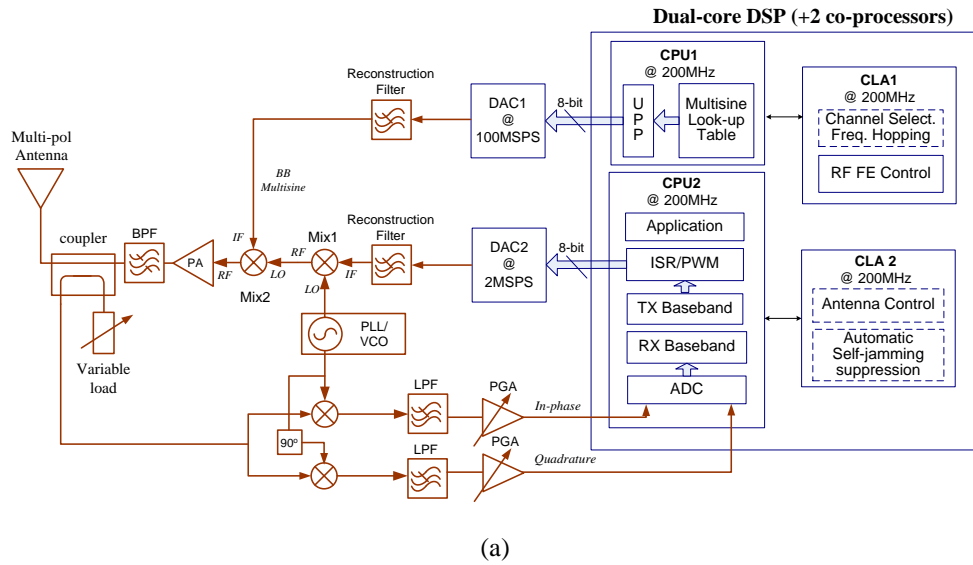
While the analog-to-digital conversion is realized by the DSP internal multi-channel 12/16-bit ADCs, the digital-to-analog conversion is implemented using two external DACs, an *IQ* DAC operating at 2 MSPS (DAC2) for the RFID baseband signal [17], and another DAC working at 100 MSPS (DAC1) for the baseband MS waveform [18]. In both cases, a 8-bit resolution is used. Although the RFID baseband signal and the baseband MS waveform could be mixed directly in software, which would require only one DAC and would dispense the need for the second mixing

⁸ This device is based on Harvard and reduced instruction set (RISC) architecture, and combines digital signal processing capabilities with microcontroller features such as integrated memory and peripherals.

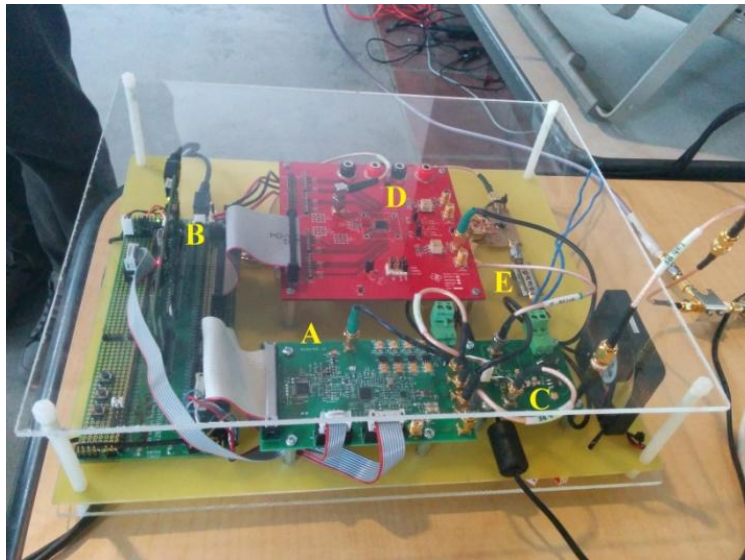
stage (Mix2), in this implementation we have chosen to do it externally in hardware. This choice is justified in the next section.

7.3.2. A multi-polarization antenna scheme

In order to take advantage of the increased efficiency of linear-polarized antennas while guaranteeing the orientation insensitivity, a multi-polarization antenna scheme has been designed to work in conjunction with the SDR reader. This antenna is controlled by the reader through an RF feeding switch in order to continuously switches between several linear polarizations, thereby, delivering 3 dB more power than a circularly-polarized antenna in several orientations [please refer to Fig. 7.2(c)-(d)].



(a)



(b)

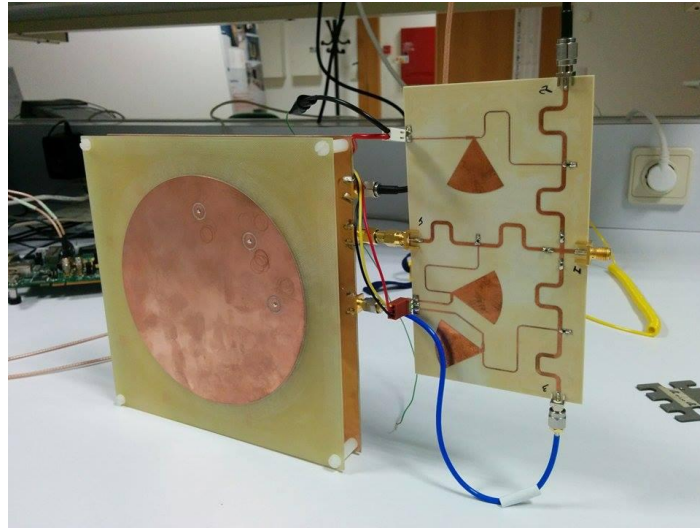
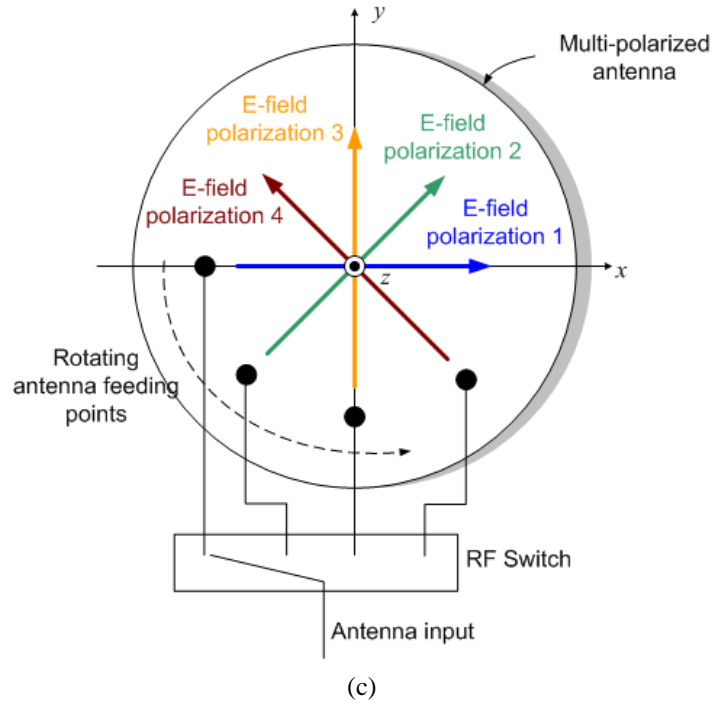


Fig. 7.2 (a) Simplified block diagram of the developed MS SDR RFID Reader platform. The dashed blocks in the digital part are proposed functionalities or CPU allocations that are still to be implemented. (b) Photograph of the developed reader hardware. Main blocks: A – RF/analog part, B – digital signal processing part, C – power amplifier, D – MS DAC, E – MS reconstruction filter. With exception of block B (DSP development board) and block D (DAC evaluation board) all the hardware has been designed from scratch. (c) Multi-polarization antenna concept. (d) The designed multi-polarization antenna⁹ with three feeding points and respective RF switch.

⁹ The antenna design was done in collaboration with Ricardo Gonçalves from IT, and is detailed in [XVIII].

7.3.3. Gen2 RFID protocol and software implementation

EPC Global Gen2/ISO18000-6C protocol [14] is a Reader Talks First (RTF) standard with Aloha-based adaptive collision resolution (Q -algorithm) and variable data rates, data coding schemes and modulation formats for reader and tag transmissions. An inventory round after Gen2 [Fig. 7.3(a)] is started with a *Query(Q)* command broadcasted by the reader with the Q parameter (from 0 to 16). Q specifies the available number of time slots to be used in the anti-collision process (slot count $N = 2^Q$). After receiving the *Query*, each tag in the field randomly chooses a slot number in the range from 0 to $2^Q - 1$. If a tag chooses the slot number 0, it wins the medium and automatically answers with a 16-bit random number (RN16) that identifies it during the inventory round. The reader then broadcasts an acknowledgment command containing the received RN16 [*Ack*(RN16)] to notify the winning tag. After being notified, the winning tag returns its EPC ID (the firmware implementation of *Ack* command followed by EPC response is exemplified in Fig. 7.4). The reader continues the round by issuing successive *QueryRep* commands that cause the remaining tags to decrement their slot counter by 1 after receiving each *QueryRep*. As soon as a tag's slot counter reaches 0, it becomes the winning tag. The choice of Q should represent a trade-off between collision probability reduction and inventory speed, and Q can be dynamically adjusted based on the estimation of number of tags in the field. For the experiments conducted here, Q has been set to 0. Therefore, a single time slot is specified and the first tag to enter the reader's field is automatically selected as the winning tag.

Gen2 protocol timing is critical, especially the time between each tag response and the subsequent reader interrogation transmission [see Fig. 7.3(a)]. After receiving the RN16, the reader must be able to send the *Ack* command during a very short time T_2 . If the reader fails to satisfy this timing, the tag times out and no further communication is possible. The maximum value of T_2 depends on the selected tag Backscatter-Link Frequency¹⁰ (BLF) as follows: $T_{2\text{MAX}} = 20/\text{BLF}$ [14]. Thus, the higher is the tag data rate, the more stringent is the time limitation. In order to be able to timely process higher tag data rates and answer to the tag before it times out, an efficient design of the reader firmware combined with some degree of task parallelization was necessary. For instance, the main CPU core starts processing the received data before the complete tag data frame is received via ADC/DMA. This requires a proper synchronization and an adequate data threshold level, on the one hand, to guarantee that there is enough buffered data to be processed, and on the other hand, to ensure that the main CPU processing does not overpass the DMA transference. Furthermore, some functions are coded in Assembly, and at boot time, all time-critical functions are loaded from the DSP FLASH to RAM memory, which significantly improves the code execution time.

¹⁰ When FM0 encoding is used, BLF coincides with the tag data rate. Otherwise, if a Miller encoding is selected, BLF is the frequency of the Miller subcarrier.

The implemented RFID Gen2 protocol stack is depicted in Fig. 7.3 and the flowchart of the firmware is shown in Fig. 7.4 (dual-core CPU operation) and Fig. 7.5 (EPC protocol handling). For reader-tag communication, PIE (Pulse Interval Encoding) coding and ASK/PR-ASK modulations have been implemented at the maximum allowed downlink bit rate of 128 kbps. For tag-reader link, FM0 encoding has been selected, variable data rates (40 kbps-160 kbps) have been tested, and the tag has been commanded to answer with a pilot carrier prior to preamble and payload data. In the current implementation [Fig. 7.3(b)], both the preamble detection and the FM0 data decoding are based on a Zero-Cross (ZC) detection method similar to that in [19]. Although ZC detection provides a lower tag read success rate than other clock recovery schemes [9], the required complexity is significantly lower. For further details on Gen2, please refer to Appendix B or Gen2 standard documentation [14].

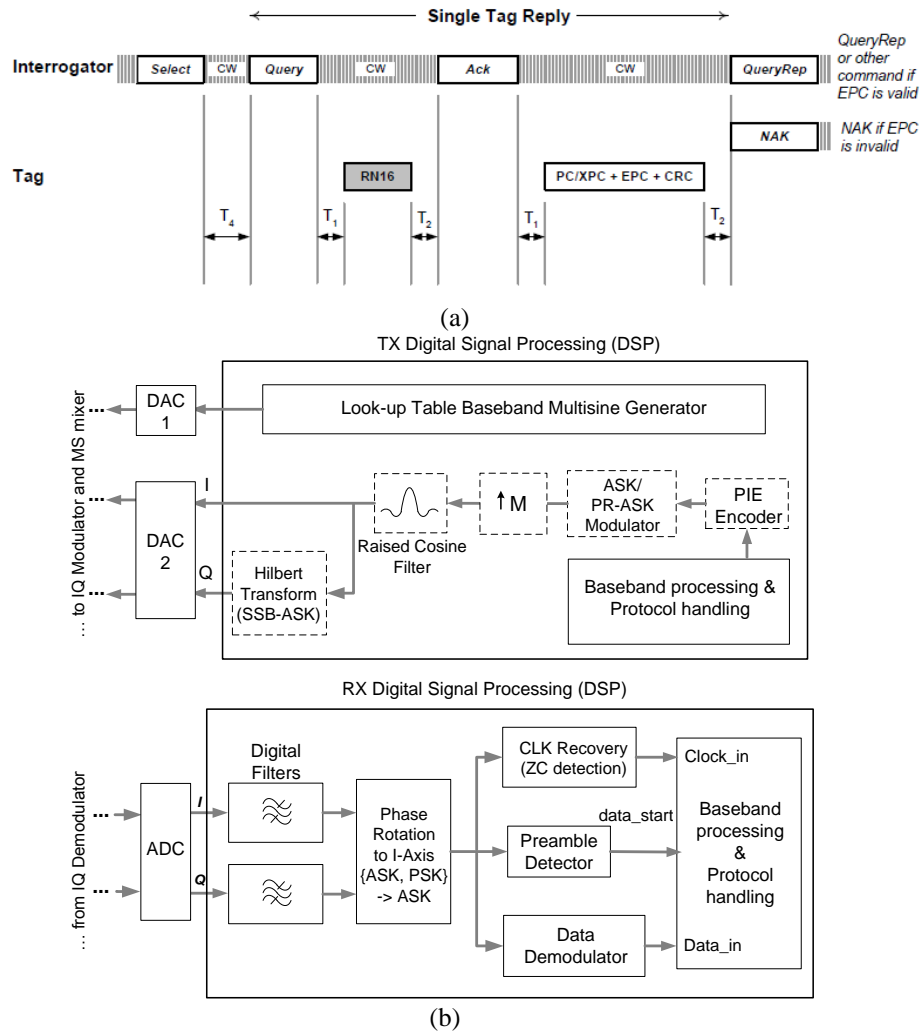


Fig. 7.3 (a) Inventory round after EPC Global Gen2/ISO18000-6C with a single tag reply [14]. (b) Gen2 protocol stack. Dashed blocks in the Tx path are either to be implemented (e.g. the Hilbert transform) or are not implemented in real time; PIE encoding, ASK modulation, interpolation and raised-cosine filtering are

applied to the individual Tx binary pulses, which are then stored in the DSP memory to be used in a look-up table approach. The same approach is used for MS signal generation.

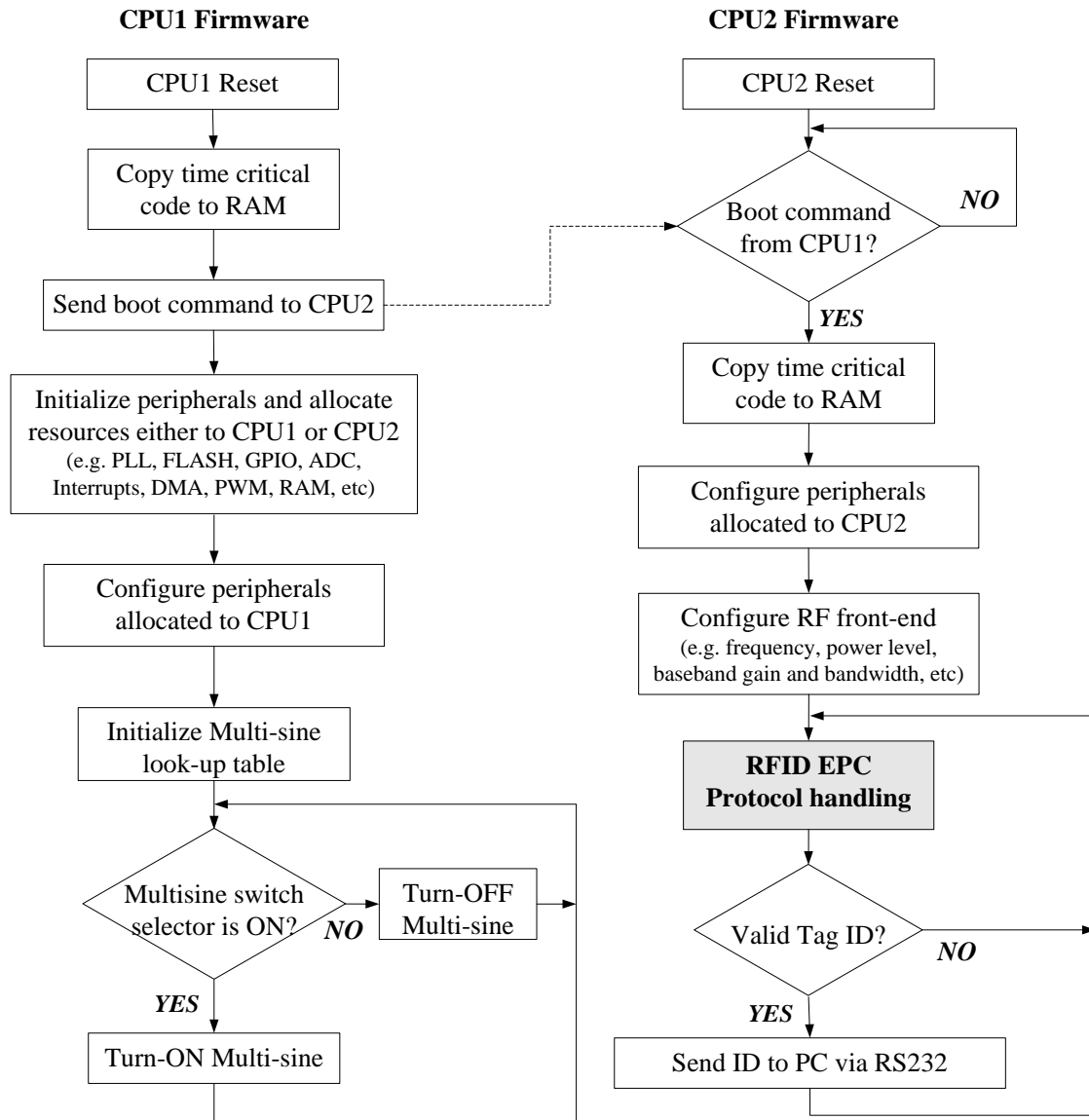


Fig. 7.4 Simplified flowchart of the implemented firmware showing dual-core CPU operation. The EPC protocol handling module (in grey) is detailed in the next figure.

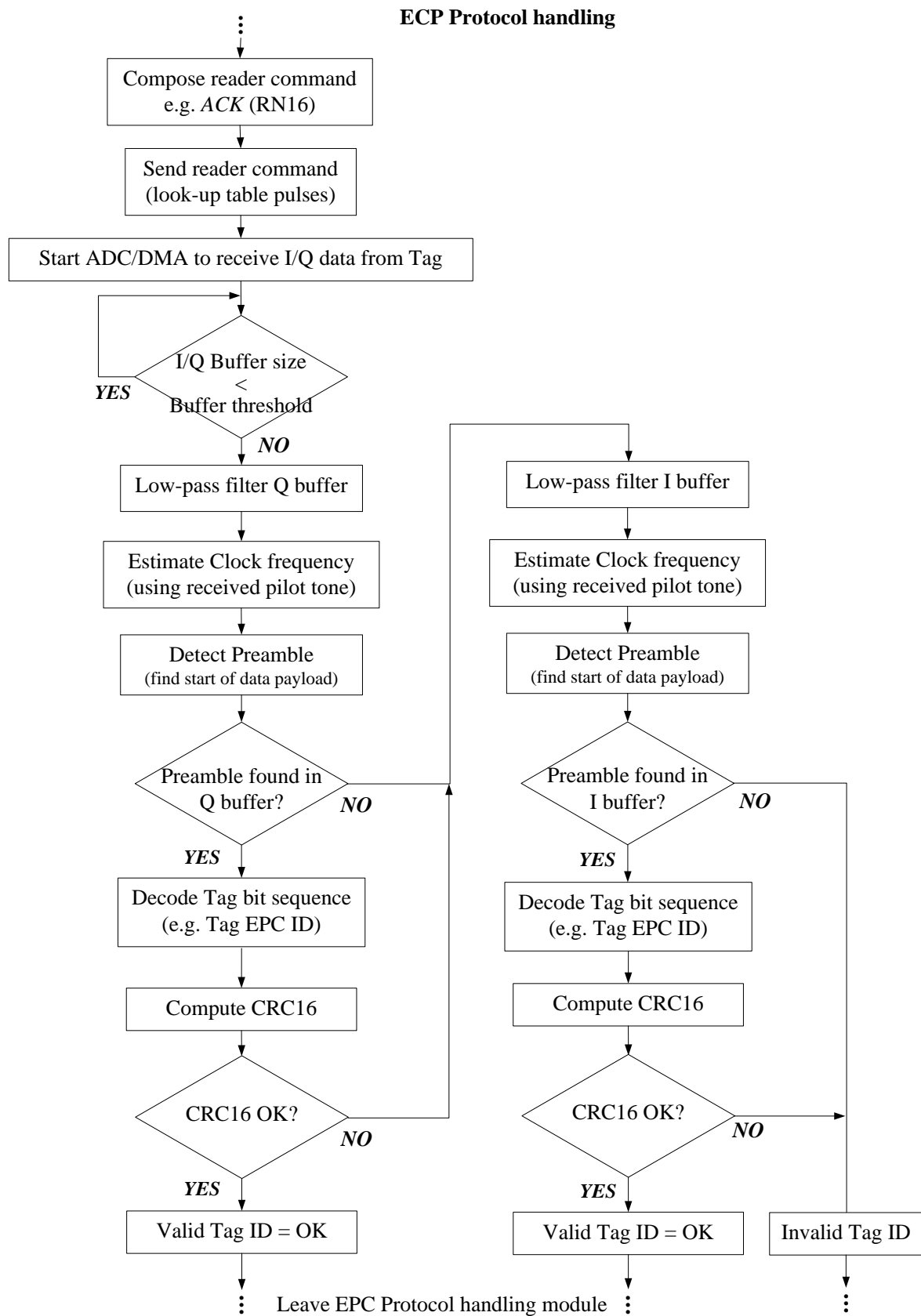


Fig. 7.5 Flowchart of implemented firmware, EPC protocol handling module (grey block in previous figure)

7.3.4. Baseband waveform generation

In order to reduce the real-time processing load, a look-up table approach has been followed to generate both the RFID baseband pulses and the baseband MS waveform. The RFID baseband pulses are filtered in MATLAB using a pulse shaping filter (e.g. a raised-cosine filter), then the samples are stored into the DSP FLASH memory. The used 8-bit DACs allow 256 code levels where code 0 represents the most negative number, 128 represents 0, and 255 represents the most positive number. The analog samples generated in MATLAB are normalized, scaled and quantized according to (7.8).

$$S_D = \lfloor \frac{255}{2} (\frac{S_A}{S_{AMAX}} + 1) \rfloor \quad (7.8)$$

where S_D is the quantized digital word, S_A is the analog sample generated in MATLAB, S_{AMAX} is the maximum value of the generated analog sequence, and $\lfloor \cdot \rfloor$ denotes the quantization to the nearest integer number in the 0-255 range. The baseband MS generation is based on the same look-up table approach. A baseband MS signal similar to (7.1) is generated in MATLAB and then quantized according to (7.8), and the resulting samples are stored into the DSP FLASH memory. Since the MS waveform is periodic, in principle only a single signal period is required to be stored in memory. Note that any other waveform, other than MS signals, can be generated using this approach. Moreover, different waveforms can be simultaneously stored in memory and selected in real-time by the application. In the following experiments and measurements, one switches between several stored MS waveforms with different characteristics (e.g. number of tones).

In this implementation, the RFID signal and the baseband MS signal are externally mixed in hardware rather than internally in software. This is done to reduce the required memory space needed to store the samples of the baseband pulses. As an example, in the current implementation, a reader data rate of 40 kbps at 2 MSPS requires 50 samples per RFID baseband symbol (2 MSPS / 40 kbps). In addition, a single period of a baseband MS with tone spacing $\Delta\omega = 2$ MHz at 100 MSPS requires 50 samples per period. Thus, a total of 100 samples per RFID symbol are enough. On the other hand, if the same RFID baseband symbol was memory-stored containing the MS pulses, rather than being implemented in hardware using Mix2, 2500 samples (100 MSPS / 40 kbps) would be necessary for each RFID symbol.

An alternative to look-up tables is the real-time computation of the MS function, which could be done by using DSP trigonometric libraries and resources. This approach reduces the memory usage but increases the computational load.

A PWM (Pulse Width Modulation) module and respective ISR (Interrupt Service Routine) is used for data interface with the lower sampling rate DAC (DAC2). For this purpose, the PWM is configured to generate interrupts at the same rate as the required data sampling rate (2 MSPS) and

the ISR feeds the data samples to DAC2. However, for the higher sampling rate DAC (DAC1), working at 100 MSPS, this approach is not suitable due to the speed limitation of the PWM module and also due to the ISR execution overhead. In this case, a Universal Parallel Port (uPP) peripheral of the DSP is used, which allows 8-bit parallel interface of high speed data using dedicated data RAMs and DMAs.

7.3.5. Self-jamming Cancellation

The reflective self-jamming cancellation scheme, described in detail in the next chapter, is used in this reader. This method originally proposed for CW cancelation [20] also shows good results for MS self-jamming suppression [XIII]. By un-matching port 3 of the Tx-Rx isolation coupler (which is usually matched to 50Ω), a portion of the transmitted signal is reflected and will cancel the self-jammer signal at port 4. In the preliminary experiments, a 50Ω load and an impedance tuner are used to realized a variable load impedance, and the adjustment for optimal impedance is done manually. In the future, one of the adaptive self-jamming suppression algorithms presented in [XIV] and described in the next chapter will be applied to this reader.

7.4. Measurements

7.4.1. The measurement setup

The setup depicted in Fig. 7.6 was used in the following measurements. Coupler 1 (CPL1) is part of the RFID reader itself, being configured as a circulator to isolate the transmitting and receiving paths. Its isolated port is connected to a variable load impedance which is used to implement the self-jamming cancellation scheme described in the next chapter. Coupler 2 (CPL2) is used to measure the power available to the RFID chip when the reader output is directly connected to the chip, or the power delivered to the reader antenna. The third coupler (CPL3) is used to assist in the self-jamming cancellation experiment, allowing to visualize the received signal after self-jamming suppression and to adjust the impedance tuner accordingly. The variable attenuator inserted in the transmitting path is used to vary the reader output power in order to find the minimum activation power of the transponder. Finally, an oscilloscope is used to access the internal signals of the RFID reader. This is useful, for instance, to visualize the received tag baseband signal.

Fig. 7.7 shows the waveforms in the transmitting path of the MS RFID reader, namely the baseband MS signal, the bandpass MS pulses and the PIE-encoded, ASK-modulated symbols using a CW and MS carrier. Note that a N-tone baseband MS signal plus a DC component originates $2N+1$ bandpass tones after up-conversion. In Fig. 7.7, four baseband tones are used and a tone spacing of 2 MHz is selected.

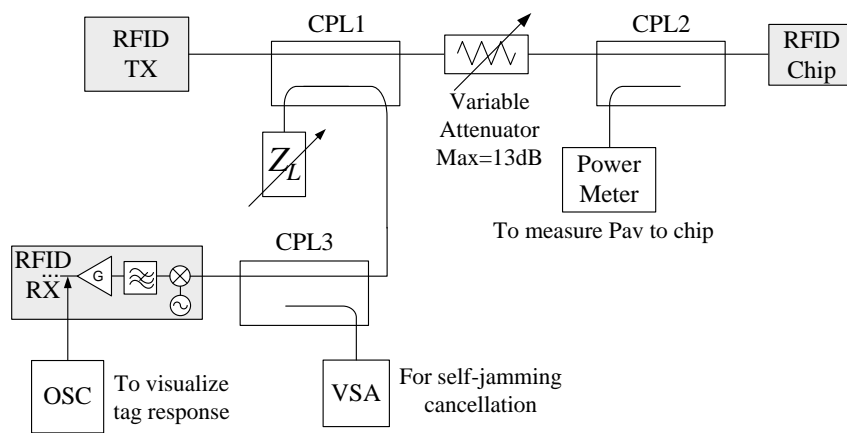
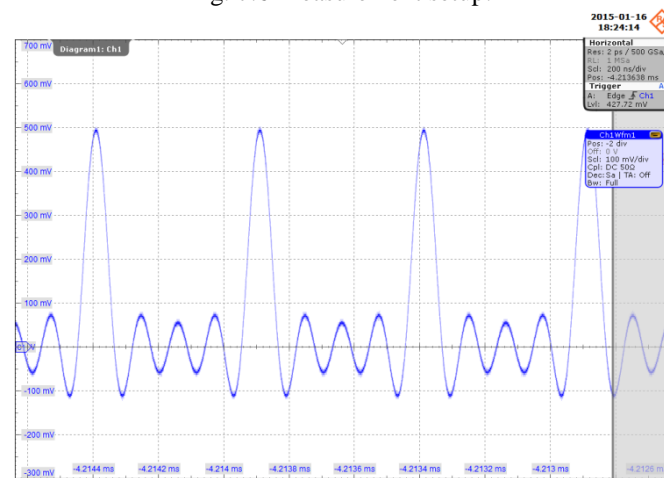
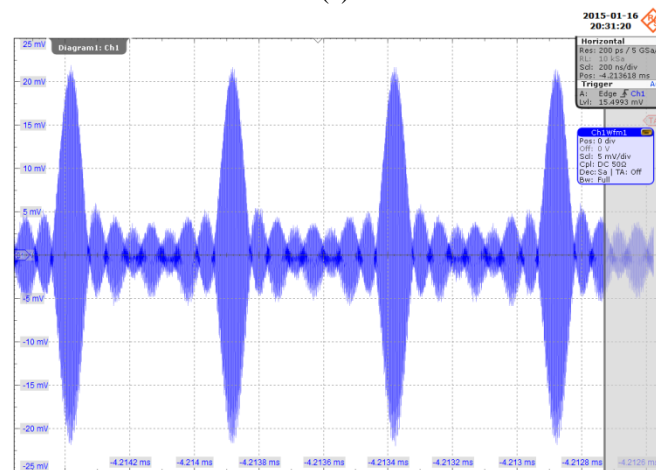


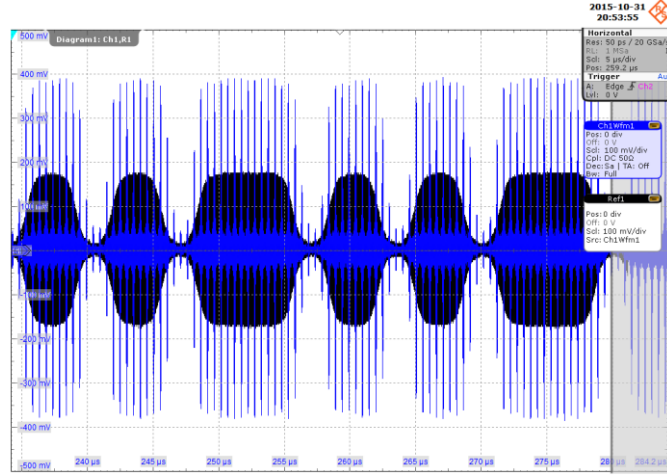
Fig. 7.6 Measurement setup.



(a)



(b)



(c)

Fig. 7.7 Waveforms in the transmitting path of the MS RFID reader. (a) 4-tone baseband MS plus a DC component at the output of the MS DAC. (b) Pulses of the resulting bandpass MS with 8+1 tones which results from the mixture of the baseband MS and the LO RF carrier. (c) RFID PIE-encoded, ASK-modulated symbols using a CW carrier (black signal) and a MS carrier (blue signal) with the same average power. Notice the higher peaks in the MS case.

7.4.2. Measurement of RFID Chip sensitivity improvement

This section intends to measure the chip sensitivity improvement gain obtained with several MS signals. For this purpose, the NXP RFID chip G2XM [21] (without matching network) is directly connected to the output of the RFID reader as shown in Fig. 7.6. Direct connection to the reader output ensures that multipath fading effects do not interfere with the measurement (these effects are evaluated in the next section). Moreover, by using no matching network, it is guaranteed that the MS signal is not affected by the input filter. By varying the attenuation of the transmitting path, it is possible to find the tag sensitivity or minimum power level required to activate the tag with a CW (P_{MIN_CW}) and with a MS signal (P_{MIN_MS}). The difference between these two values corresponds to the sensitivity improvement gain provided by the MS signal ($G_P = P_{MIN_CW} - P_{MIN_MS}$). Note that G_P has the same meaning as the efficiency gain FOM defined in chapter 4 and the power gain defined in the previous chapter. The obtained results are presented in Table 7.2. The gain G_P is calculated with the unmatched measurements. An estimation of the matched activation power level can be obtained from the unmatched activation power level and the unmatched return loss, according to equation (3) of [XV]. A maximum sensitivity gain of 3.3 dB was obtained for the tested RFID chip under a 9-tone MS signal presenting a PAPR of 12.6 dB.

TABLE 7.2
MEASUREMENT OF TAG SENSITIVITY GAIN FOR SEVERAL MS SIGNALS

	CW	3-tone MS	5-tone MS	9-tone MS
PAPR (dB)	3	7.8	10	12.6
$P_{\text{MIN_Unmatched}}$ (dBm)	-4.45	-6.0	-7.1	-7.75
$P_{\text{MIN_Matched}}$ (dBm)	-13	-14.5	-15.6	-16.3
G_P (dB)	0	+1.55	+2.65	+3.3

7.4.3. MS demodulation

The demodulation approaches previously described in section 7.2 namely the central carrier demodulation (7.6) and the MS match filtering (7.7) are evaluated in this section. For the following experiments, the output of CPL2 in Fig. 7.6 is connected to a 7 dBi antenna instead of being directly connected to the RFID chip. Alien ALN-9540 Squiggle tag based on Higgs-2 chip [22] is located at a distance D away from the MS reader. As a first evaluation of the proposed demodulation methods, the tag is interrogated with a *Query* command and the RN16 tag response is captured using an oscilloscope, and afterward processed in MATLAB.

Figure 7.8 (a) shows the received RN16 tag response after down-conversion, where one can notice the tag baseband signal on top of the baseband MS subcarriers. The sample of the tag response modulated on the central subcarrier can be recovered by simply low-pass filtering the down-converted signal with a cut-off frequency lower than $\Delta\omega$. This results in the signal of Fig. 7.8(b). Note that (7.6) is null whenever the round trip phase shift is equal to $\phi_2 = 90^\circ + n180^\circ$ or the tag-reader distance is equal to $D = \lambda/8 + n\lambda/4$. This is shown in Fig. 7.8 (c) where, for a frequency of 866 MHz ($\lambda = 35$ cm.), the distance between consecutive nulls is approximately $D = \lambda/4 = 8.66$ cm, which corresponds to a round trip phase shift of $\lambda/2$ (180°). The first null should theoretically appear at $D = 4.33$ cm ($\lambda/8$), however this is not in the far-field. Due to the appearance of these nulls, this demodulation method requires a quadrature receiver. A specific reader-tag distance case where (7.6) becomes null is shown on Fig. 7.8(d)-top. For the same situation, the MS matched filter (7.7) is able to retrieve the tag information without using a quadrature receiver by taking advantage of the phase diversity present in (7.7) [see Fig. 7.8(d)-bottom].

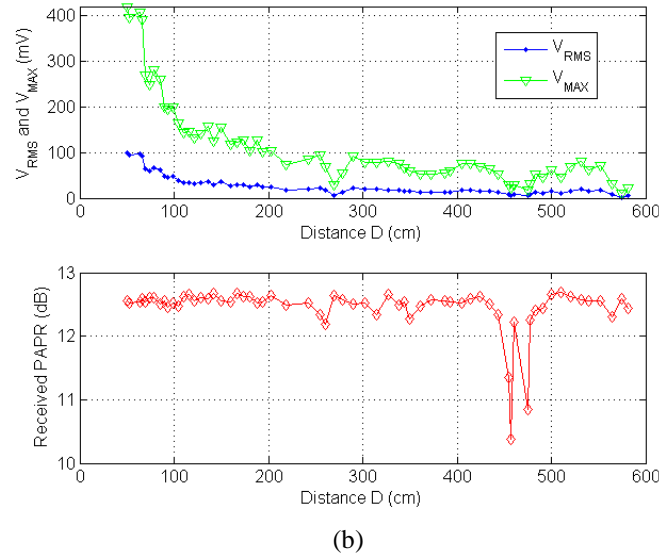
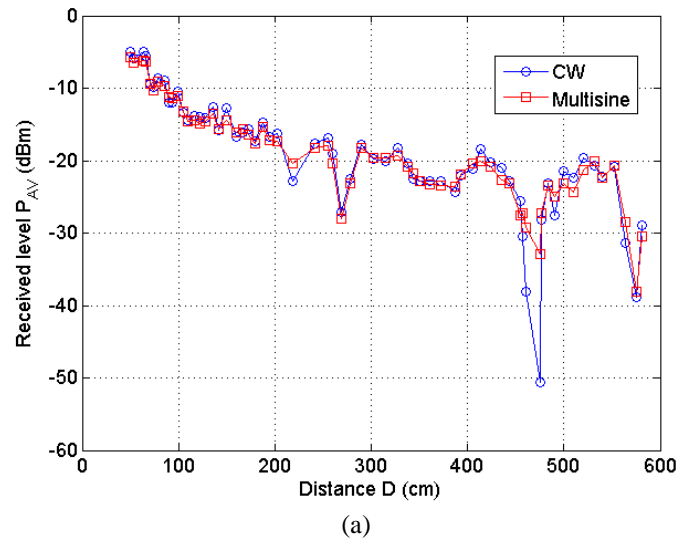


Fig. 7.9 (a) Received average power level in a lab environment as a function of distance from the reader, for a CW and a 9-tone MS with same average power. (b) Received PAPR as a function of the distance, when transmitting a 9-tone MS signal. In both cases, a 7 dBi Tx antenna and a dipole Rx antenna were used. A power meter was used in the first case, and an RF oscilloscope was used in the second measurement.

7.4.5. RFID reader – PC interface

The developed RFID reader communicates with the computer via RS232 to send the data read from the tags (e.g. the EPC IDs) which are displayed by an R232 terminal application. Several tags with different EPC IDs have been used. Figure 7.10 depicts a screenshot of Termite application, showing several tag readings in CW mode. Along with the tag EPC ID it is shown the information of the *IQ* branch used for data demodulation.

improved baseband amplification, by improving MS baseband filtering and by using improved data decoding methods.

The developed platform is a flexible lab tool that allows to conduct many experiments not possible with off-the-shelf readers or commercial ASICs. For instance, it allows for settings adjustment (e.g. power level, frequency and other protocol parameters), which is useful for RFID characterization and measurements, protocol evaluation and research purposes. Moreover, RFID reader design based on SDR also presents significant benefits in terms of industry, as it allows for standard interoperability and upgradability.

References

- [1] Mehmet Abbak and Ibrahim Tekin, "RFID Coverage Extension Using Microstrip Patch Antenna Array", Vol 51, No. 1, p.p.: 185-191, Feb 2009, Antennas and Propagation Magazine, IEEE.
- [2] Jun-Seok Park, Jin-Woo Jung, Si-Young Ahn, Hyoung-Hwan Roh, Ha-Ryoung Oh, Yeung-Rak Seong, Yoon-Deock Lee, and Kyoung Choi "Extending the Interrogation Range of a Passive UHF RFID System With an External Continuous Wave Transmitter", IEEE Transactions on Instrumentation and Measurement, VOL. 59, NO. 8, p.p.: 2191-21-97, Aug. 2010.
- [3] T. Feldengut, R. Kokozinski, and S. Kolnsberg, "A UHF Voltage Multiplier Circuit Using a Threshold-Voltage Cancellation Technique," in Research in Microelectronics and Electronics, July 2009, pp. 288 – 291.
- [4] Koji Kotani, "Highly Efficient CMOS Rectifier Assisted by Symmetric and Voltage-Boost PV-Cell Structures for Synergistic Ambient Energy Harvesting", IEEE Custom Integrated Circuits Conference, p.p.: 1-4, San Jose, CA, Sept. 2013.
- [5] A. Georgiadis and A. Collado, "Improving Range of Passive RFID Tags Utilizing Energy Harvesting and High Efficiency Class-E Oscillators", Proc. EuCAP 2012, Prague, March 2012.
- [6] H. Matsumoto, K. Takei, "An Experimental Study of Passive UHF RFID System with Longer Communication Range", Proceedings of Asia-Pacific Microwave Conference 2007.
- [7] M.S. Trotter, G.D. Durgin "Survey of Range Improvement of Commercial RFID Tags With Power Optimized Waveforms", IEEE International Conference on RFID, 2010.
- [8] Ettus Research: www.ettus.com, online 12/02/2015
- [9] D. De Donno, F. Ricciato, and L. Tarricone, "Listening to Tags: Uplink RFID Measurements with an Open-Source Software-Defined Radio Tool," IEEE Transactions on Instrumentation and Measurement, vol. 62, no. 1, pp. 109–118, Jan. 2013.
- [10] L. Catarinucci, D. De Donno, et.al., "A cost-effective SDR platform for performance characterization of RFID tags," IEEE Transactions on Instrumentation and Measurement, vol. 1, no. 4, pp. 903-911, April 2012.
- [11] M. Buettner and D. Wetherall, "A software radio-based UHF RFID reader for PHY/MAC experimentation," IEEE International RFID Conference, pp.: 134-141, Orlando, April 2011.
- [12] Ales Povalac, "Spatial Identification Methods and Systems for RFID Tags", Ph.D. Thesis, Brno University of Technology, Brno 2012.
- [13] Alien RFID Reader - Hardware Setup Guide ALR-9800, Feb. 2008. Available online 26-10-2015: [ftp://ftp.alientechnology.com/pub/readers/alr9800/docs/Guide,%20Hardware%20Setup,%20ALR-9800.pdf](http://ftp.alientechnology.com/pub/readers/alr9800/docs/Guide,%20Hardware%20Setup,%20ALR-9800.pdf)
- [14] EPC Radio-Frequency Identity Protocols Class-1 Generation-2 UHF RFID, Protocol for Communications at 860 MHz – 960 MHz, Version 1.2.0
- [15] Analog Devices, www.analog.com available online 28-10-2015.
- [16] Texas Instruments, www.ti.com available online 28-10-2015.
- [17] <http://www.analog.com/en/products/digital-to-analog-converters/da-converters/ad9709.html> available online 28-10-2015.
- [18] Texas Instruments, <http://www.ti.com/product/dac5662> available online 28-10-2015.
- [19] D. De Donno, F. Ricciato, L. Catarinucci, A. Coluccia, and L. Tarricone, "Challenge: Towards Distributed RFID Sensing with Software-Defined Radio," ACM MobiCom 2010, September 2010.
- [20] Thomas Brauner and Xiongwen Zhao, "A Novel Carrier Suppression Method for RFID", IEEE MICROWAVE AND WIRELESS COMPONENTS LETTERS, VOL. 19, NO. 3, MARCH 2009.
- [21] UCODE G2XM and G2XL, SL3ICS1002/1202, http://www.nxp.com/documents/data_sheet/SL3ICS1002_1202.pdf available online: 30-10-2015.
- [22] ALN-9540 Squiggle Inlay, http://www.falkensecurenetworks.com/PDFs/DS_ALN_9540_Squiggle_tag.pdf, available online: 30-10-2015.

8. SELF-JAMMING IN PASSIVE-BACKSCATTER RFID SYSTEMS

8.1. Introduction

Self-jamming is perhaps the second most limiting factor in passive-backscatter RFID systems, and thus, this topic deserves special attention in this separate chapter. In passive RFID systems, the interrogator needs to radiate a strong powering signal to remotely supply the transponder, while simultaneously receiving the faint information signal backscattered by the transponder at the same frequency [1]. In order to separate the transmitting and receiving paths, either a bistatic or monostatic antenna configuration can be used. However, these simple isolation schemes suffer from poor transmitter to receiver isolation, which may cause a significant amount of the transmitted power to leak into the receiver, degrading its sensitivity to the weak backscattered information signal from the tag. LO phase noise leakage [1] and saturation of the receiver front components are the main causes of sensitivity degradation. If no self-jamming suppression mechanism is employed, then a high dynamic range capability is required for the front LNA and mixer as well for the baseband amplifiers and ADCs. In order to improve the performance of receivers, self-jamming cancellation techniques have been proposed in the literature [2-11] and used in monolithic RFID reader chips [12-13]. Similar techniques are also employed in radar systems where transmitter and receiver operate simultaneously [14], and more recently in full-duplex wireless communication systems (e.g. full-duplex WiFi) [15-17].

Another unwanted effect of self-jamming in Direct Conversion Receivers (DCR) [18] is the generation of DC-offsets. A DCR directly down-converts the received signal to baseband by mixing it with a local oscillator at the exact same frequency, which creates unwanted DC-offsets. In typical half-duplex wireless and mobile systems, DC-offsets are solely the result of LO leakage (self-mixing) and interferer leakage [19-21]. In DCR-based passive RFID readers, though, self-jamming is the dominant cause of DC-offset generation. The jammer signal that leaks from the transmitter to the receiver is mixed with the LO (at the same frequency) producing a DC component that can be much bigger than the down-converted tag signal. Furthermore, the phase noise of the leaked LO is directly down-converted to baseband.

Similarly to other wireless communication systems [19], passive RFID systems have adopted the use of DCRs due to their low-cost and reduced complexity which make them preferable over heterodyne receivers [18]. Moreover, the increased flexibility makes DCR suitable for Software Defined Radio (SDR) applications [22][23]. DCR has, thus, been the natural choice for passive RFID, being used in commercial RFID reader chips (e.g. AS399x family [24] and R1000/2000 family [25]), as well as in a number of SDR-RFID implementations devoted to research [26], system characterization and measurement [27], protocol exploration [28], and localization [29].

This chapter addresses RF self-jamming and DC-offset generation in passive RFID systems in a comprehensive way. First, a theoretical analysis and evaluation of conventional approaches to deal with these issues is presented, such as the use of directional couplers terminated with variable reflective loads to suppress the jamming signal. Afterward, new hardware and software proposals are presented namely an improved non-linear high-pass filter with pre-charged initial condition to simultaneously cancel the DC-offset and the transient, and a method for transient correction in software. Both the evaluation of existing techniques as well as the validation of the new proposals are accompanied by laboratorial measurements. To complement the study, several techniques commercially used in modern reader ICs are also described. The laboratorial experiments are conducted on two different SDR platforms, one based on DSP/MCU and other based on Field-Programmable Gate Array (FPGA).

8.2. Self-jamming and interference in passive RFID

- Since passive RFID systems operate in full-duplex mode and due to imperfect Tx-Rx isolation, a significant amount of radiated power (up to 2W ERP in EU [30] and 4W EIRP in USA) may leak into the receiver. An early consequence is the saturation of the RF stages (LNA/Mixer).
- After down-conversion, strong self-jammers generate large DC-offsets, which are in many cases, random and much higher than the transponder baseband signal. This challenges the baseband stages (mainly the ADC).
- Moreover, the self-jamming leakage propagates also the LO phase noise into the receiver chain. Actual local oscillators generate phase noise in close proximity to the carrier frequency. Since the tag signal, typically, is also very close to the carrier frequency (few tens to few hundred kHz from the central carrier [31]), the LO phase noise can easily corrupt the tag information, thus limiting the receiver sensitivity [see this effect illustrated in Fig. 8.1 (b)].

The main sources of interference and self-jamming are illustrated in Fig. 8.1 and include:

- Antenna mismatch and imperfect isolation of the circulator (or coupler) in monostatic configurations [Fig. 8.1(a)] and direct Tx-Rx antenna crosstalk in bistatic configurations.
- Reflections from surrounding objects, buildings, walls, people, or cars (vehicular applications)
- Transponder motion and unmodulated or structural reflections from the transponder antenna.
- Interferer signals from neighbor radios (e.g. other RFID readers) in the same frequency band.

Note that, interferer signals at the exact same frequency as the reader can be seen as self-jammer components. On the other hand, in-band interferer signals at a different frequencies are down-

converted to baseband, taking with them the LO phase noise, as illustrated in Fig. 8.1 (b). The amplitude of the interferes and their proximity to the LO frequency will determine their effect.

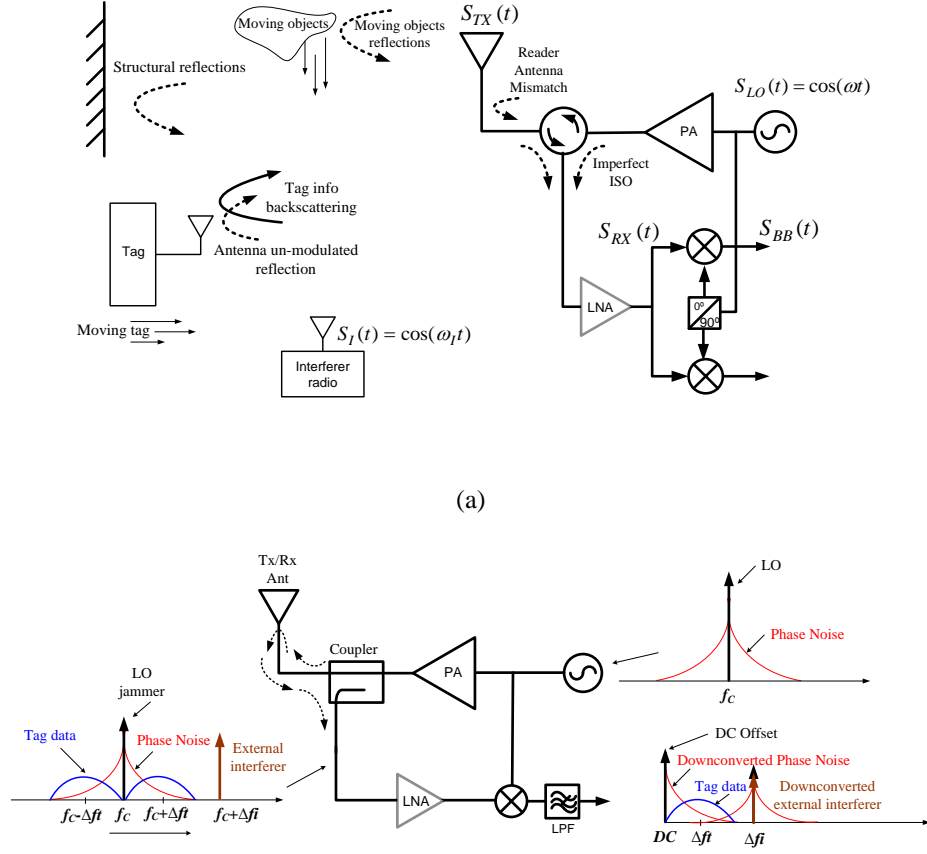


Fig. 8.1 (a) Sources of self-jamming in a bistatic antenna configuration. (b) Self-jamming sources in a monostatic configuration, c) illustration of external interference, LO jammer and phase noise leakage.

8.3. Basic isolation between transmitter and receiver

Two basic configurations are commonly used to isolate the receiver from the transmitter, namely bistatic, which uses two separate antennas to transmit and receive, and monostatic, which shares one antenna for transmitter and receiver through a circulator. In the former, cross-talk between the two antennas dominates the Tx to Rx leakage, while in the latter, leakage is mainly the result of antenna mismatch and imperfect isolation of the circulator (or coupler). Bistatic configurations [32] offer, in principle, better isolation performance (30 - 40 dB), however, due to cost and size, monostatic configurations (offering 15 – 30 dB isolation) are often preferred. The poor isolation and consequent sensitivity degradation is responsible for a reduction of reading range and identification rate [10][12]. For this reason, improved self-jamming suppression techniques are a must.

8.4. RF self-jamming cancellation

It is important to suppress the unwanted leakage in the RF level before it reaches the active parts of the front-end (LNA/mixer), as it may saturate them. If no RF suppression scheme is employed, then the front LNA/mixer must feature high dynamic range in order to properly handle the weak tag signals in the presence of the strong jammer signals. Baseband amplifiers and ADCs must also feature high dynamic range capabilities in order to handle large down-converted DC-offsets.

To suppress the jammer signal in the RF domain, a sample of the transmitted RF signal may be used to cancel out the self-interference in the received signal [2-11]. Two cancellation techniques for application in passive RFID are described next, namely the classical self-jamming suppression using active amplitude and phase control (Fig. 8.2), and the cancellation by using a variable reflective load to terminate the isolating coupler (Fig. 8.3). Adaptive approaches to find the optimal parameters settings for the cancellation, including techniques used in commercial ICs, are also discussed.

8.4.1. Classical self-jamming suppression scheme

Figure 8.2 (a) shows the self-jamming cancellation scheme based on active amplitude and phase control, which is typically used in passive RFID readers [2-9][12]. In this approach, a sample of the transmitted signal, the canceller signal $S_{canceller}(t)$, is set to the same amplitude and opposite phase (180° phase shift) of the jammer signal $[S_{jammer}(t)]$. Then, it is deliberately added to the received signal $[S_{RX}(t)]$, eliminating the jammer signal and leaving only the tag information signal, $S_{Desired}(t)$. In the configuration of Fig. 8.2 (a), a coupler is used to pick up a sample of the Tx signal that is properly shaped and then added to the received signal. The amplitude and phase of the canceller signal can be controlled by using a variable amplifier/attenuator and a phase shifter, respectively [7]. Alternatively, amplitude and phase can be controlled by using vector modulation techniques [see Fig. 8.2(b)]. To add the canceller signal to the received signal, a power combiner or a coupler can be used as an RF summator. A second coupler and a power detector are used to measure the power at the output of the summator. Note that power level information can also be obtained by measuring the DC-offsets of the down-conversion mixers. In this case, the quadrature mixer itself is used as a power detector, which not only dispenses the use of a dedicated power detector, but can also allow the implementation of faster cancellation algorithms by using in-phase and quadrature information of the jammer signal [35]. A control unit is needed to generate the amplitude and phase control information, based on the output power level measured at the output of the summator. The control unit's algorithm, similar to those described later in this section, should automatically and adaptively adjust the amplitude and phase of the canceller signal in order to minimize the residual

power level measured at the output of the summator (after cancellation), supposing that only the jammer signal is present.

A commercial implementation of self-jamming cancellation, similar to the one described here, is found in Impinj RFID reader chip Indy R2000 [13]. The main difference, with respect to Fig. 8.2(a), is that the Indy R2000 uses a vector modulation approach to control the amplitude and phase of the canceller signal, rather than using an amplifier and phase shifter. The input of a vector modulator [Fig. 8.2(b)] is split into in-phase (I) and quadrature (Q) components, with the Q component shifted 90° relative to the I component. These signal components pass through variable amplifiers (or attenuators) that independently scale the I and Q amplitudes. The output of the amplifiers/attenuators are then summed to create the output signal. By controlling the relative gains of the I and Q branches, the magnitude and phase of the output signal can be set as desired. Two examples of vector modulators are QHX220 [33] used in [15][16], and AD8340 [34] used in [8].

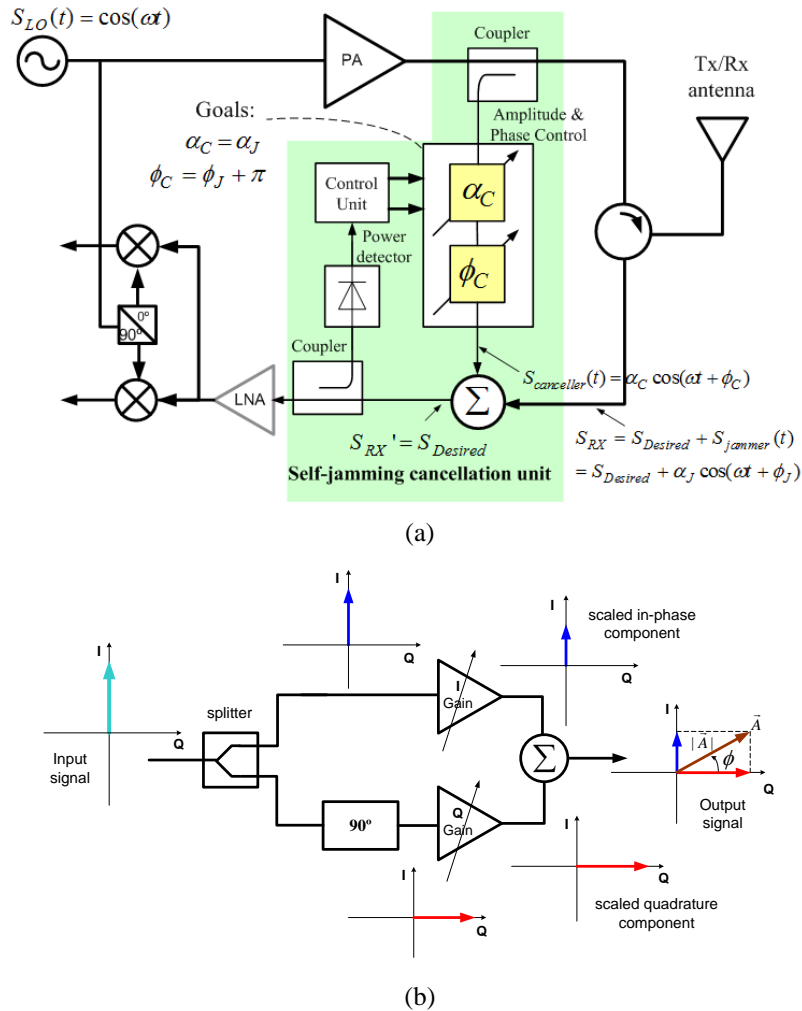


Fig. 8.2 (a) Monostatic reader front-end incorporating a self-jamming cancellation unit. (b) Vector modulator used to control amplitude and phase of the canceller signal.

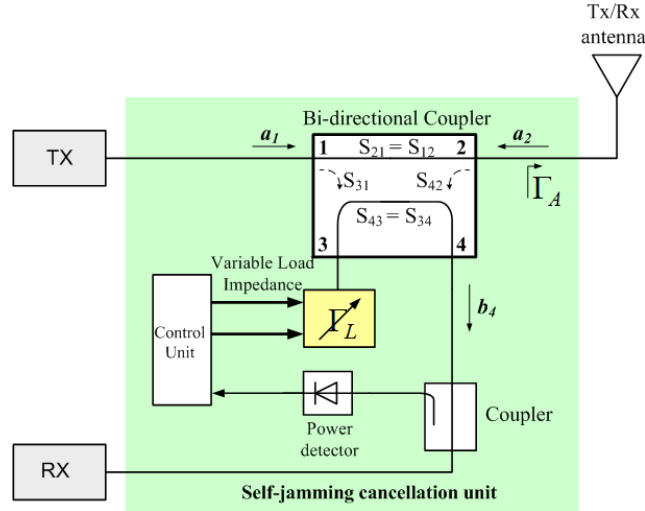


Fig. 8.3 Passive self-jamming cancellation using a coupler terminated with a reflective load

8.4.2. Passive self-jamming cancellation using reflective loads

To realize this scheme proposed in [10][11], a directional coupler is configured as a circulator, and the isolated port 3, which is usually matched to 50Ω , is terminated with an unmatched load [refer to Fig. 8.3]. Cancellation is achieved by properly choosing the terminating impedance value. This is done such that a portion of the transmitter signal coupled into port 3 is reflected toward port 4 where it will cancel out the coupled jammer [10][11]. To better understand this method, consider the received signal at port 4, given by (8.1). Assuming a perfectly symmetrical coupler with transmission coefficients $T=S_{21}=S_{12}=S_{34}=S_{43}$, coupling $C=S_{42}=S_{31}$, and isolation $I=S_{41}=S_{32}$, then (8.1) can be written as (8.2). Now, if the return loss presented to port 3 is symmetrical to the antenna return loss ($\Gamma_L = -\Gamma_A$), then the received signal at port 4 is free of leakage and contains only the desired signal from the transponder ($b_4 = S_{42}a_2$).

$$b_4 = S_{42}a_2 + a_1(S_{21}\Gamma_A S_{42} + S_{31}\Gamma_L S_{43}). \quad (8.1)$$

$$b_4 = S_{42}a_2 + a_1(T\Gamma_A C + C\Gamma_L T). \quad (8.2)$$

The advantages of this method include reduced complexity, high linearity, and low noise performance, since it is completely passive (no active amplification is used). In order to evaluate this self-jamming cancellation approach, a bi-directional coupler was constructed ($T = 0.5$ dB, $C = 12$ dB and $I = 20$ dB) and combined with a load impedance tuner to form a self-jamming cancellation module. This module was then used with the DSP-based RFID reader of Fig. 8.9. The coupler was first characterized using a VNA, both with and without carrier suppression. For this

purpose, a 7 dBi linearly polarized antenna, with a return loss better than 14 dB, was connected to Port 2. The isolated port (3) was first terminated with a 50Ω load as usually done (no carrier suppression) and then with the load impedance tuner. In the first case, the isolation is limited by the intrinsic coupler isolation (around 20 dB). In the second case, the tuner was adjusted for an optimal termination impedance of $19.6+13.5j$ @ 860 MHz, thus improving the overall Tx to Rx isolation to approximately 50 dB (Fig. 8.5). After, the setup of Fig. 8.4 was used to evaluate the self-jamming cancellation in the RFID reader [Fig. 8.9] with a transmitted power of 30.8 dBm. Table 8.1 presents the measured results. Since the wireless channel is constantly changing, the termination impedance should also adaptively change.

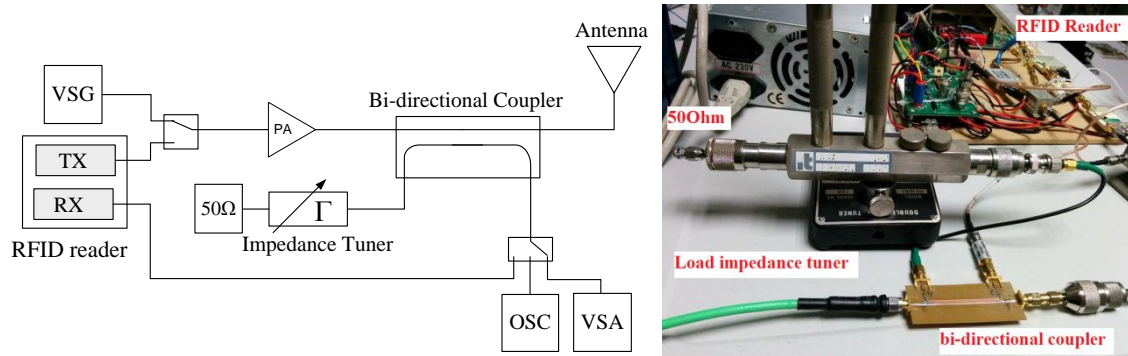


Fig. 8.4 Measurement setup to evaluate the reflective load method. (a) Block diagram. (b) Lab setup using an impedance load tuner, a bi-directional coupler and an RFID reader.

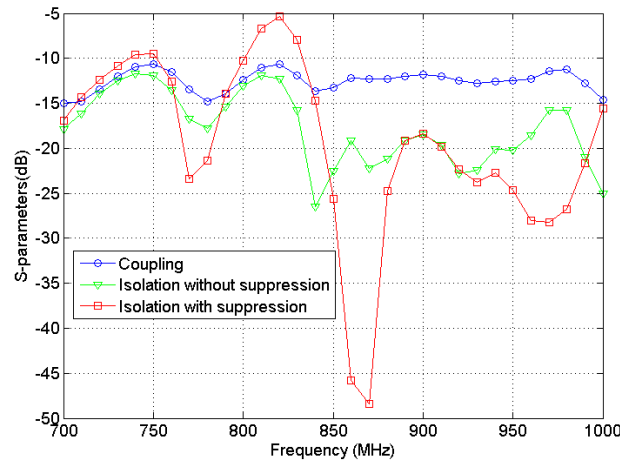


Fig. 8.5 Coupler characterization and evaluation of the cancellation method by using a VNA. Coupling (circles): 12 dB @ 860 MHz, Isolation without carrier suppression (triangles): 19 dB @ 860 MHz, and Isolation with carrier suppression (squares): 46 dB @ 860 MHz.

TABLE 8.1
EVALUATION OF CW ISOLATION

Tuner Impedance Z_L @ Port 3	P_{IN} @ Port 1 (dBm)	P_{CPL} @ Port 4 (dBm)	$ISO = S_{41} = P_{IN} - P_{CPL} $ (dB)
50Ω	30.8	11.0	20.8
(24+14j) Ω	30.8	-10.0	40.8

8.4.3. MS self-jamming suppression

Multi-sine self-jamming cancellation was investigated in [XIII] using the approach described in the previous section. The same setup of Fig. 8.4 was used, but now with a 9-tone MS ($\Delta\omega = 2$ MHz) as the transmitted signal. The Tx and Rx spectra were acquired using the VSA and the optimal load impedance of the coupler was adjusted to minimize the Tx to Rx leakage power. It was found that: 1) the best result is obtained when the suppression is optimized for the central subcarrier. 2) the MS suppression is further improved by using a narrow-band BPF ($F_c = 866$ MHz and $B_w = 2$ MHz), which attenuates the lateral components and also reduces the crest factor of the leakage signal. The results of [XIII] are summarized in Table 8.2 where an isolation of more than 60 dB is observed when using the BPF.

TABLE 8.2
EVALUATION OF MS ISOLATION

Tuner Impedance Z_L @ Port 3	P_{TX_AV} (dBm)	P_{RX_AV} (dBm)	Iso_AV (dB)	P_{TX_fc} (dBm)	P_{RX_fc} (dBm)	Iso_fc (dB)
50Ω	10.8	-10.8	21.6	-3.6	-21.5	21.5
(22+10j) Ω	10.8	-27.5	38.3	-3.6	-58.1	54.5
(22+10j) Ω plus a BPF	10.8	-55.5	66.3			

8.4.4. Adaptive self-jamming cancellation

In the previous section, the self-jamming suppression was performed in a static manner; the optimal setting for the impedance termination was manually found just once and no further adjustment was done. However, as the wireless channel changes (due movement of objects and people, tag motions and arbitrary scattering), the self-jamming signal component also changes and consequently the optimal point is lost. Moreover, for readers using FHSS (Frequency Hopping Spread Spectrum), the channel changes as the frequency is changed. This imposes the need for an adaptive self-jamming cancellation scheme capable of automatically suppressing the jammer and dynamically adapt to the changes of the wireless channel. Hence, the control unit must be able to continuously monitor the residual power level after cancellation and adaptively compute the

optimal control parameters of the canceller signal that minimize the residual power level after cancellation. In order to independently control the amplitude and phase of the canceller signal, two independently-controllable variables or control parameters are required. In Fig. 8.2(a), the control parameters are the amplitude and phase of the canceller signal [7][12]. In this case, the control is achieved directly by using an attenuator/amplifier and a phase-shifter. In Fig. 8.3(b), the in-phase and quadrature components of a vector modulator are used as control parameters [5][8][15]. Other approaches may require the control of the resistance and reactance of a load, as in [11] where two variable capacitors are used to vary the impedance termination presented to a coupler.

In the next examples in this section, we consider the configuration of Fig. 8.3(a), which uses an attenuator and a phase shifter. Fig. 8.6 depicts the theoretical RSSI of the residual signal at the output of the summator, as a function of the attenuation and phase shift of the canceller signal (α_C, ϕ_C) , while the jammer signal is kept unaltered. This set of values, taken around the optimal point, shows that the $RSSI(\alpha_C, \phi_C)$ presents a convex shape with a global minimum at the optimal point. In implementations using vector modulation to control the canceller signal, the RSSI curve presents a similar behavior with respect to the in-phase and quadrature gains of the vector modulator [15]. Next, we present two algorithms that can be used to find the optimal point settings, namely full search and gradient descent search [35].

Table 8.3 summarizes several implementations of self-jamming cancellation found in the literature in terms of achieved isolation, frequency/bandwidth and type of system (including not only passive RFID but also radar and full-duplex wireless communication systems).

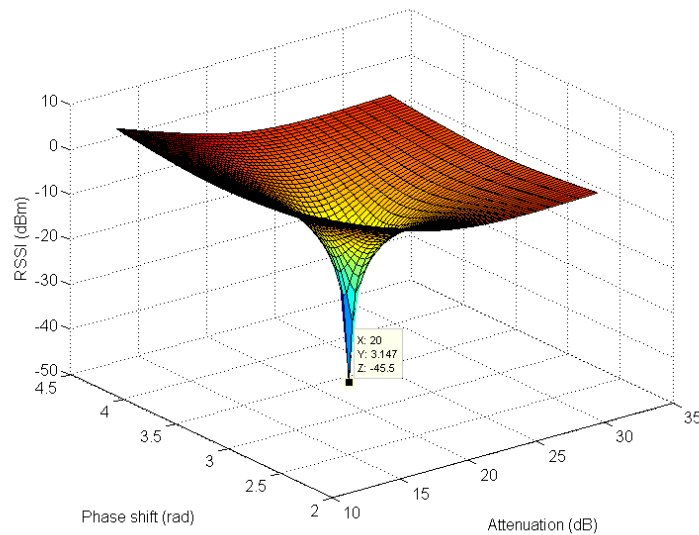


Fig. 8.6 $S(\alpha_C, \phi_C)$ - theoretical RSSI of the residual signal after self-jamming cancellation depending on the attenuation and phase shift of the canceller signal. In this example, the jamming signal has a 0° phase shift and 20 dB attenuation w.r.t. the sample of the Tx signal used for cancellation.

A. Full search algorithm

As the name suggests, “full search” is a brute-force algorithm that evaluates all possible combinations of the control parameters and then selects the one that produces the best result (minimum residual RSSI). For instance, if the control parameters (attenuation and phase) assume N possible values, then a total of N^2 adjustments and measurements are required to find the optimal point. In its primitive form, full search is very time consuming, which can make it unpractical. Depending on the overall time needed to treat each setting point (including parameters setting time and RSSI measurement time), this technique may become extremely slow, which prevents it from following the changes of the medium or even from finding the optimal point [35]. Nevertheless, due to its simplicity, improved versions of this algorithm are employed in commercial ICs, such as the Impinj RFID reader chip Indy R2000 [13]. In order to reduce the scanning time, the algorithm is divided into two steps. In the first step, a full scan search with a coarse grid is performed, in which only a fraction of the N^2 points is evaluated. From this first search, the algorithm identifies the best point. In the second step, a finer search is performed around the previous best setting. This strategy drastically reduces the overall time needed to depurate the optimal point. In the example of Fig. 8.7, we would need to scan only 74 points ($7^2 + 5^2$), rather than $N^2=961$ points ($N=31$). Fig. 8.7 depicts an amplitude-phase constellation and illustrates optimal point search similar to that in Impinj IC [13]. This is based on the combination of a coarse grid search and a fine grid search. Here, the control parameters are attenuation and phase shift, rather than the in-phase and quadrature components of the vector modulator used in Impinj IC [13]. The algorithm first evaluates all the possibilities corresponding to the blue points (coarse grid) and finds the coarse best point, which is a first non-optimal approximation. Afterward, a finer scan is performed in a finer 5x5 grid around the previous best point (red points) in order to find the final optimal point. In order to track the optimal settings, the fine scan should be repeated periodically.

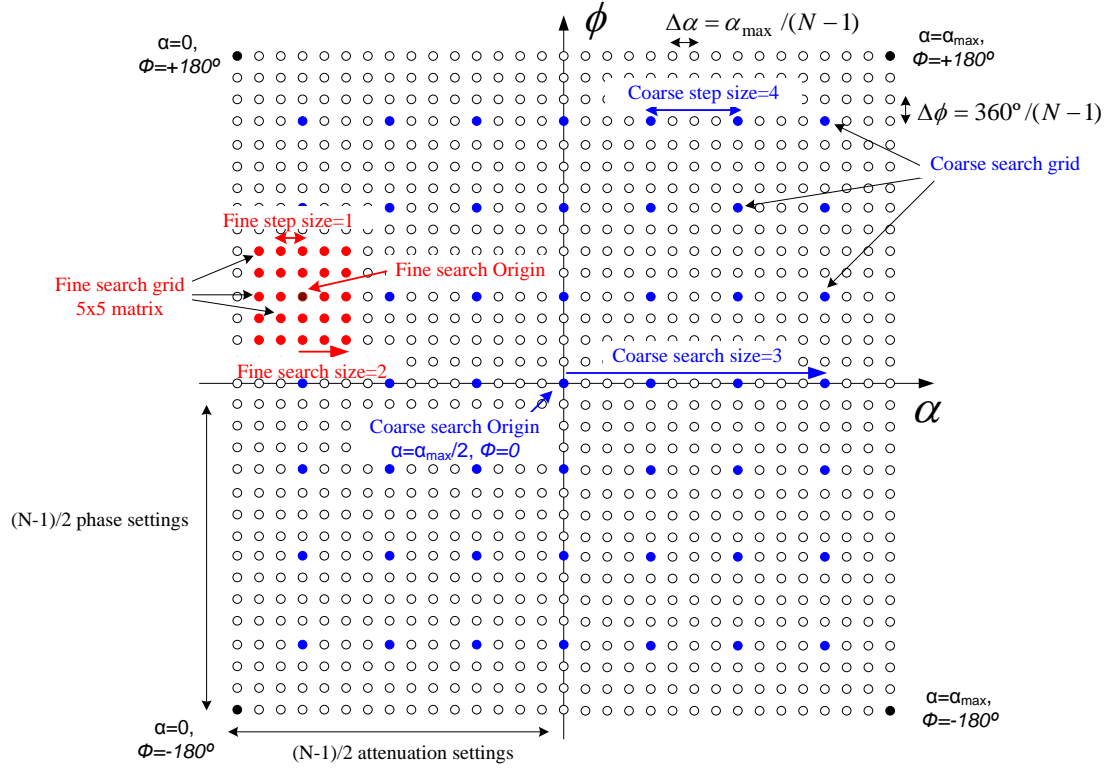


Fig. 8.7 Amplitude-phase constellation: the blue points correspond to the coarse search grid and the red ones correspond to the fine search grid. Note: although the same number of points (N) is considered for both control parameters, different values can be used as convenient.

B. Gradient descent search algorithm

The optimal point can be more efficiently tracked by using the gradient descent algorithm, which is an iterative approach to approximate the minimum of a function, based on its gradient. Some implementations of this method can be found in [5] and [16]. Next, we detail an example (Fig. 8.8) that can be used in the configuration of [Fig. 8.2(a)]. In each step, the algorithm computes the local gradient of the RSSI function in order to determine in which direction the function is decreasing. Based on this information, it then computes the values for the next setting of the control parameters. In our proposal, in order to compute the local gradient, the algorithm samples three points for RSSI. First it samples the current point $\text{RSSI}(\alpha, \phi)$. Then, by separately changing the two control parameters (α and ϕ) by small amounts ($\delta\alpha$ and $\delta\phi$), it samples more two points: $\text{RSSI}(\alpha + \delta\alpha, \phi)$ and $\text{RSSI}(\alpha, \phi + \delta\phi)$. The slope vector or gradient of the RSSI curve with respect to the control parameters $[\nabla\alpha, \nabla\phi]$, is given by equation (8.3). The gradient descent rule is defined by equation (8.4), which is used to determine the value of the control parameters to be used in the next step of the algorithm. The gradient descent equation imposes that the control parameters are always updated in the descendant direction of the function.

$$\begin{aligned}
(\nabla \alpha, \nabla \phi) = \nabla RSSI(\alpha, \phi) &= \left[\frac{\partial RSSI(\alpha, \phi)}{\partial \alpha}, \frac{\partial RSSI(\alpha, \phi)}{\partial \phi} \right] \\
&\approx \left[\frac{RSSI(\alpha + \delta\alpha, \phi) - RSSI(\alpha, \phi)}{\delta\alpha}, \frac{RSSI(\alpha, \phi + \delta\phi) - RSSI(\alpha, \phi)}{\delta\phi} \right]
\end{aligned} \tag{8.3}$$

$$\begin{cases} \alpha = \alpha - \mu_\alpha \nabla_\alpha \\ \phi = \phi - \mu_\phi \nabla_\phi \end{cases} \tag{8.4}$$

where μ_α and μ_ϕ are real positive numbers referred to as step size parameters. After updating the control parameters according to the previous equations, the new residual $RSSI(\alpha, \phi)$ value is sampled. If this value is lower than the current RSSI value, the algorithm continues and then repeats the process, according to (8.3) and (8.4). Supposing that the algorithm converges, the next values will then be closer and closer to the optimal point (minimum RSSI). If, at any point, the new value of the residual RSSI is higher than the previous one, it means that the algorithm is close to the minimum. It then decreases the step size (both the derivation step size $\delta\alpha$ and $\delta\phi$, and the algorithm step size $\mu_\alpha \nabla_\alpha$ and $\mu_\phi \nabla_\phi$), reverses the direction, and attempts to converge to the optimal point. The optimal point is found when the minimum step size is reached. Using variable step size improves the algorithm performance. At the beginning, the step size is set to a relatively large value and, as the algorithm approaches the optimal point, the step size is gradually decreased. The algorithm should also be able to detect false alarms caused by noisy minimums. This can be done, for instance, by discarding minimum values above a predefined threshold value for the minimum. Once a valid minimum is found, the algorithm presented in Fig. 8.8(a)-(b) enters a monitoring state, in which it keeps the control parameters constant (at the optimal point) until a condition change is detected. This is done by continuously measuring the current RSSI and comparing it with the optimal one. If the difference is larger than a predefined value, the algorithm updates the step size according to this difference and begins to search again for the optimal point. Updating the step size according to the deviation from the optimal RSSI improves the algorithm because, if the difference is not big, the algorithm doesn't need to be restarted from the beginning with the largest step size, which would take much more time to converge. Figure 8.8(a) depicts the flowchart of the described gradient descent algorithm, while Fig. 8.8(b) presents an alternative implementation. For improved algorithms with faster convergence, the reader may refer to [35] and [36].

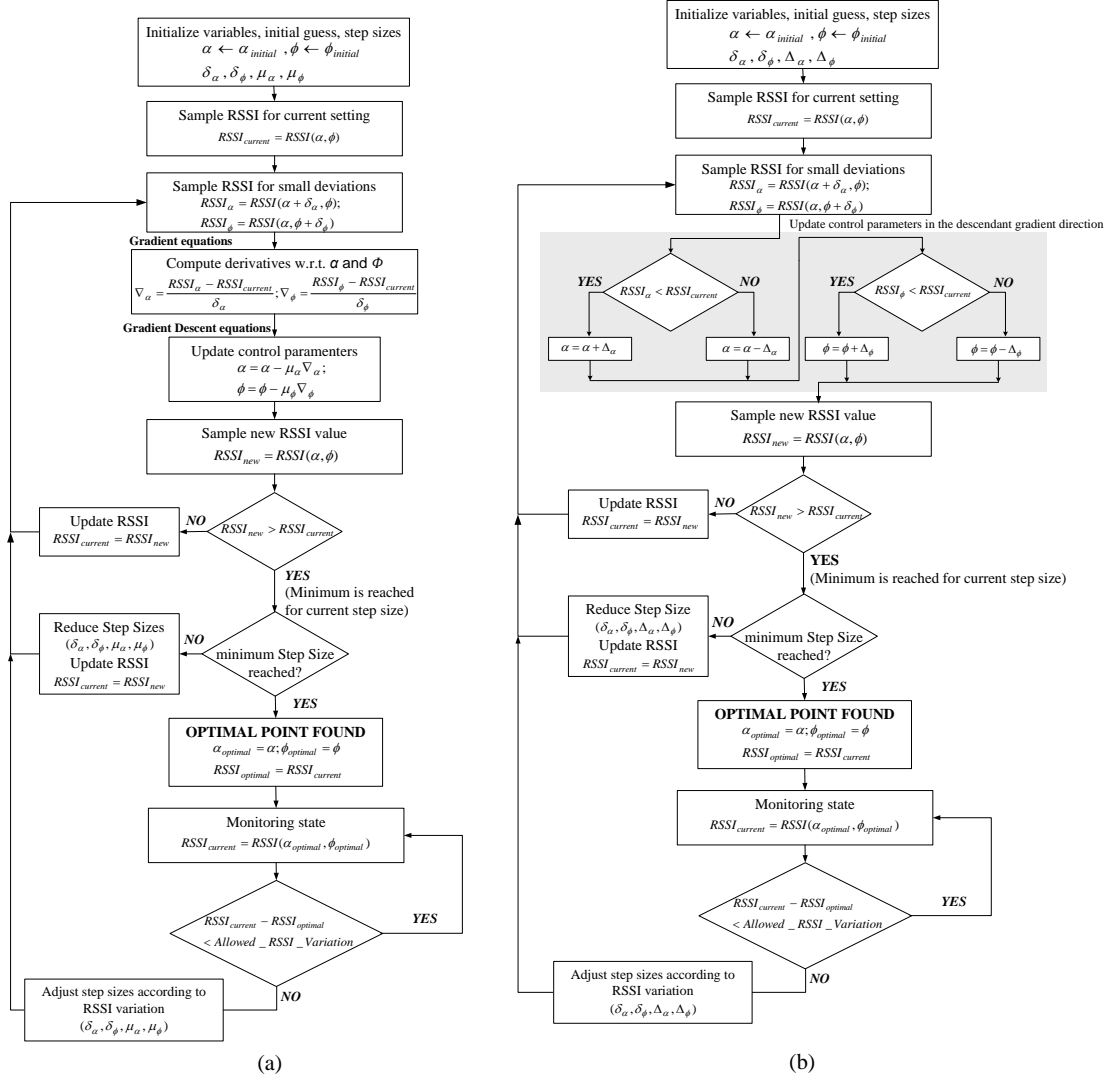


Fig. 8.8 Adaptive cancellation based on gradient descent algorithm. (a) Direct implementation of gradient descent. (b) Alternative implementation.

TABLE 8.3 SUMMARY OF SELF-JAMMING CANCELLATION IMPLEMENTATIONS

Isolation	System	Comment	Ref.
41-46 dB	UHF RFID	Continuous adaptive cancellation	[19]
>30 dB	RADAR	26 GHz, wide bandwidth 1.7 GHz	[14]
40 dB	RFID UHF	Broadband, 82 MHz bandwidth	[8]
up to 50 dB	UHF RFID	Reflective load, static adjustment	This work
70-80 dB	UHF RFID	Single frequency, 919 MHz	[6]
45 dB	Full-duplex WiFi	40 MHz OFDM Tx signal	[15]
up to 73 dB	UHF RFID	Multi-antenna: 1Tx and 2Rx antennas	[9]
50-65 dB	UHF RFID	At least 50 dB @20 MHz bandwidth	[7]

8.5. Baseband DC-offset removal techniques

As a consequence of self-jamming in DCR receivers, DC-offsets may appear at the baseband and may exhibit large values if no self-jamming suppression is used. On the other hand, if the ADC has a limited dynamic range, it is important to remove the DC-offset in the analog domain prior to signal digitalization. However, a simple high pass-filter (simple AC-coupler) may not be effective. The AC-coupler capacitor may be pre-charged with an incorrect initial condition during the reader transmission period and transient effects can then lead to information loss, especially for high data rates [1]. An improved non-linear switched high-pass filter, with pre-charged initial condition is presented in this section. This filter removes both the DC-offset and the transient effect, otherwise imposed by a simple high-pass filter. A mixed analog-digital alternative is also presented, where the DC-offset is removed with an analog high-pass filter and the transient effect is cancelled in the digital domain. If the ADC has enough dynamic range (resolution), the analog filter can be discarded and the DC-offset can be removed in software after baseband digitalization. We evaluated this approach in a high performance FPGA platform (including also high dynamic range ADCs). However, these high performance requirements increase the cost and may not be suitable for low-cost implementations. In our experiments, the down-converted DC-offset and transient effects are moderate since a low power level is transmitted (12 dBm in the DSP platform and 18.30 dBm in the FPGA platform). However, these effects can be more severe for higher transmitted power levels [37].

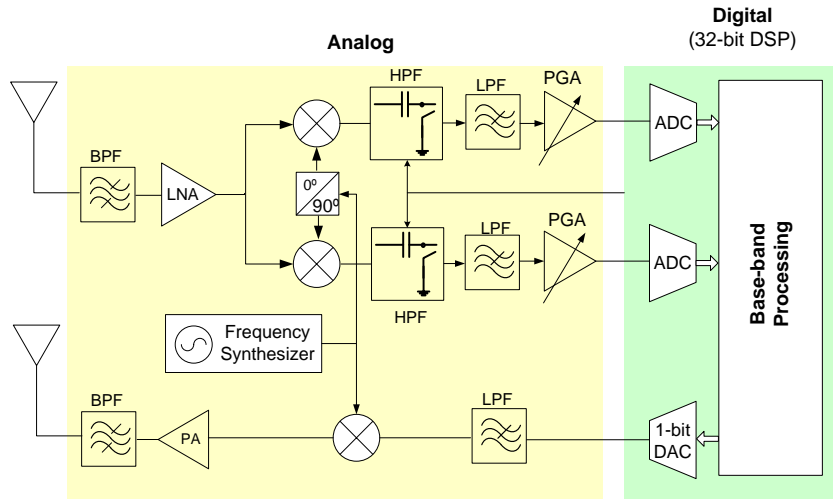
8.5.1. Experimental hardware

Two different SDR hardware platforms were used in the following experiments. The first is one of two the RFID readers built in the scope of this thesis based on DSP/MCU technology and the second is based on FPGA technology. The former is depicted in Fig. 8.9, and details of the latter can be found in [XIV].

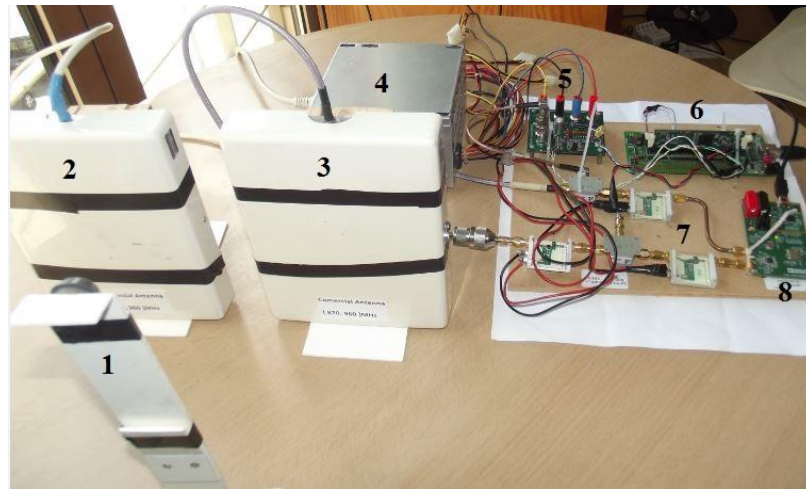
8.5.2. DC-offset elimination and transient issues

DC removal with a simple high-pass filter (HPF) can corrupt the signal received from the tag, due to the transient behavior of the filter. The capacitor value of the filter (Fig. 8.10) should not be too high, as the time constant of the filter would be too long and the transient behavior would be quite accentuated. On the other hand, the value cannot be too low, as this would excessively attenuate important frequency components of the received tag baseband signal. In our experiments, the transponder-to-reader data rate is in the range of 40 kbps to 640 kbps, and a 100nF series capacitor is used.

Two aspects contribute to tag information loss due to transient effect (Fig. 8.11). First, if the filter is pre-charged with a wrong initial condition during the prior reader command period, then the filter will take too long to recover. Second, if the transponder-to-reader data rate is too high, then significant part of the information signal (if not the entire signal) may fall in the transient region and may be lost during the transient period [see Fig. 8.11(b)].



(a)



(b)

Fig. 8.9 (a) Block diagram of the SDR RFID reader. Notice the use of a non-linear switched HPF. (b) Photography of the implemented hardware where the following blocks are visible: 1 – EPC tag mounted in a stand, 2 – Tx antenna, 3 – Rx antenna, 4 – a computer power supply used to supply the reader, 5 – Baseband receiving PGA including filters, 6 – DSP/MCU development board, 7 –RF part including up-converter and down-converter mixers and amplifiers, 8 – VCO/PLL/frequency synthesizer.

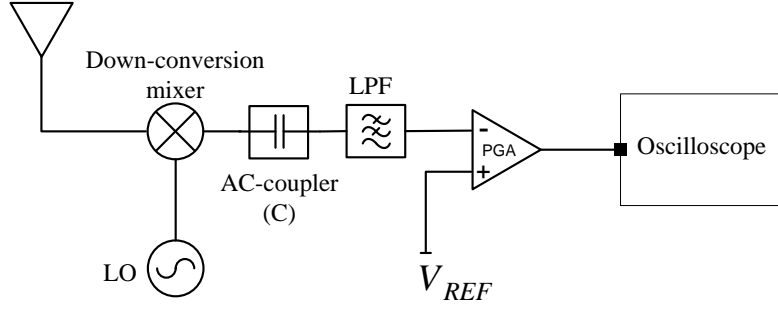


Fig. 8.10 Receiver using a simple high-pass filter capacitor to remove DC-offset before LPF and amplification. This simple HPF imposes a transient effect that corrupts the received signal.

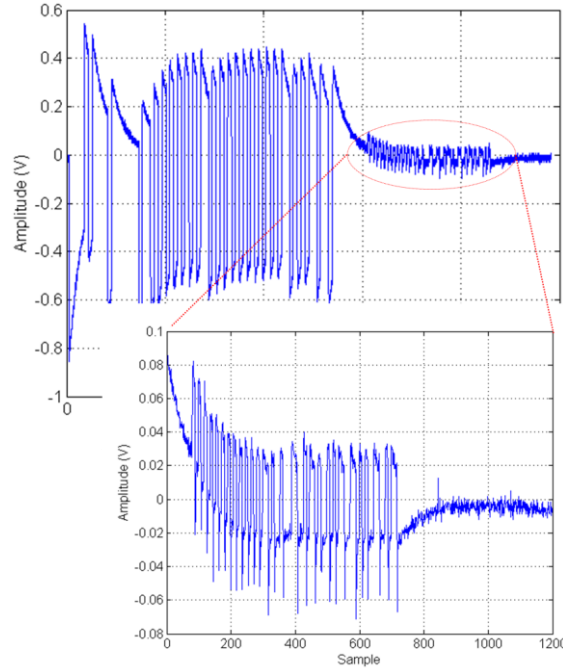


Fig. 8.11 (a) Reader command followed by tag RN16 response. (b) Zoomed tag response. The transient effect imposed by the high-pass filter is visible. The tag data rate used is 320 kbps.

A. DC-offset removal using an analog HPF and transient cancellation in software

Next, we propose a simple approach to correct the transient effect in software. The DC is removed by using a regular analog HPF and the transient-affected signal is then treated in software. The digital transient cancellation is achieved by computing the moving average of the transient-affected signal and subtracting it from the corrupted signal as follows,

$$S_{BB_{Corrected}}(n) = S_{BB}(n) - \frac{1}{w} \left\{ S_{BB} \left(n - \frac{w-1}{2} \right) + \dots + S_{BB}(n-1) + S_{BB}(n) + S_{BB}(n+1) \dots + S_{BB} \left(n + \frac{w-1}{2} \right) \right\} \quad (8.5)$$

where n is the present sample number, the subtracted term is the moving average of the transient-affected signal $[S_{BB}(n)]$, and w is the window or span size of the average. The moving average

performs a low-pass filtering, whose cut-off frequency depends on the size of the window w . This filter can be equivalently implemented as a FIR filter, with coefficients weight equal to $1/w$. Fig. 8.12 depicts the tag response with transient effect and the respective moving average (negative) for two different window sizes (31 and 101 samples). Increasing the window span provides a smoother moving average curve, however the computation time is increased. Fig. 8.13 shows the corrected signal, as given by (8.5). An additional low-pass filter should be used to remove noise and high frequency components as done in the FPGA section. In this example, the reader baseband data is generated in the DSP and the down-converted received signal is captured using an oscilloscope and then is processed in Matlab.

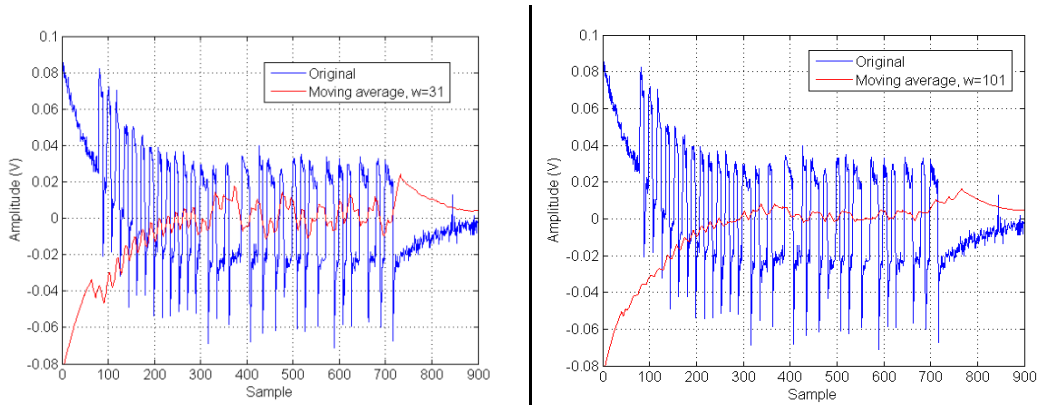


Fig. 8.12 Tag RN16 response with transient effect (blue) and the respective (negative) moving average (red): a) $w = 31$ samples, b) $w = 101$ samples

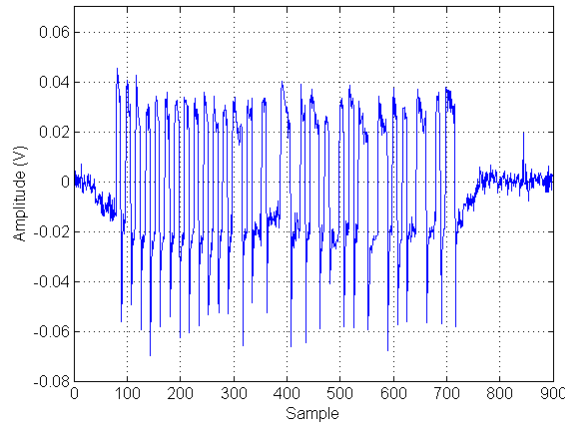


Fig. 8.13 Corrected signal, centered at DC. Additional low-pass filter should be used to remove noise.

8.5.3. Analog DC-offset removal using a non-linear HPF

Figure 8.14 presents an improved non-linear switched high-pass filter, with pre-charged initial condition. This filter removes both the DC-offset and the transient effect otherwise imposed by a simple high-pass filter. Two low-cost C-MOS transistors configured as switches are used in this scheme to control the isolation and the initial condition of the filter. The principle of operation of

the filter and respective waveforms are shown in Fig. 8.15. The series switch (S1) is introduced to isolate the receiver during the reader command transmission period and the shunt switch (S2) is used to control the capacitor charging. During the reader command transmission, switch S1 is open and S2 is closed to isolate the receiver. At the end of the reader command transmission (in the CW transmission period), S1 is closed and S2 is kept closed such that C is grounded and is pre-charged to the DC-offset value generated by the reader CW. During the reception of tag information, S2 is open and S1 is kept closed. Hence, at the initial instant of tag transmission, the pre-charged DC-offset is subtracted from the incoming signal, thus avoiding the transient effect and centering the output signal at 0V. After, the signal is passed through a signal conditioning (to set proper DC level) and amplification stage. The switches are controlled by DSP IO pins and timings are obtained with DSP timers. The transient-free signal obtained with this scheme is presented in Fig. 8.16. It is important to note that the charging time must be properly set such that there is enough time for the capacitor to charge. Compared to a traditional implementation of this filter which uses a single switch (only S2), our implementation offers an improved isolation thanks to the introduction of S1, that completely isolate the receiver during transmission. Figure 8.16(a) depicts a reader command followed by a tag response after passing through the described non-linear high-pass filter. The zoom around the tag response [Fig. 8.16(b)] clearly shows the effectiveness of the approach in both eliminating the transient effect and centering the signal around 0V.

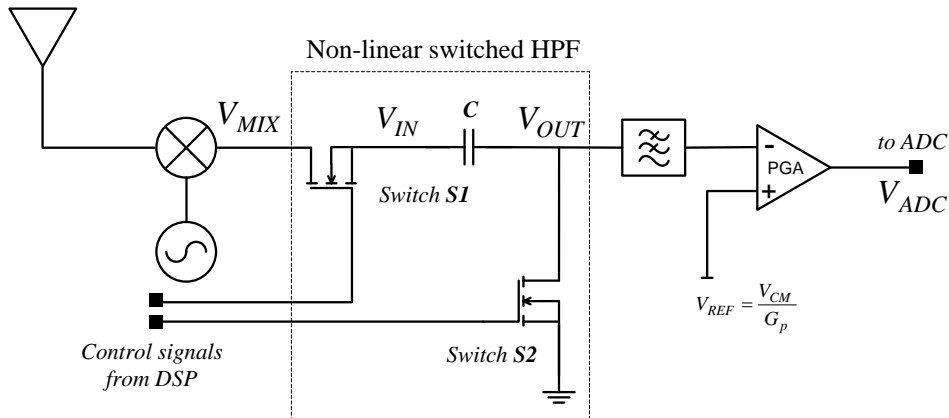


Fig. 8.14 Down-conversion mixer followed by a non-linear switched high-pass filter, with pre-charged initial condition, followed by low-pass filter, signal conditioning and baseband amplification. The output of the PGA is centered at proper DC level for ADC conversion (1.5V provides optimal ADC dynamic range).

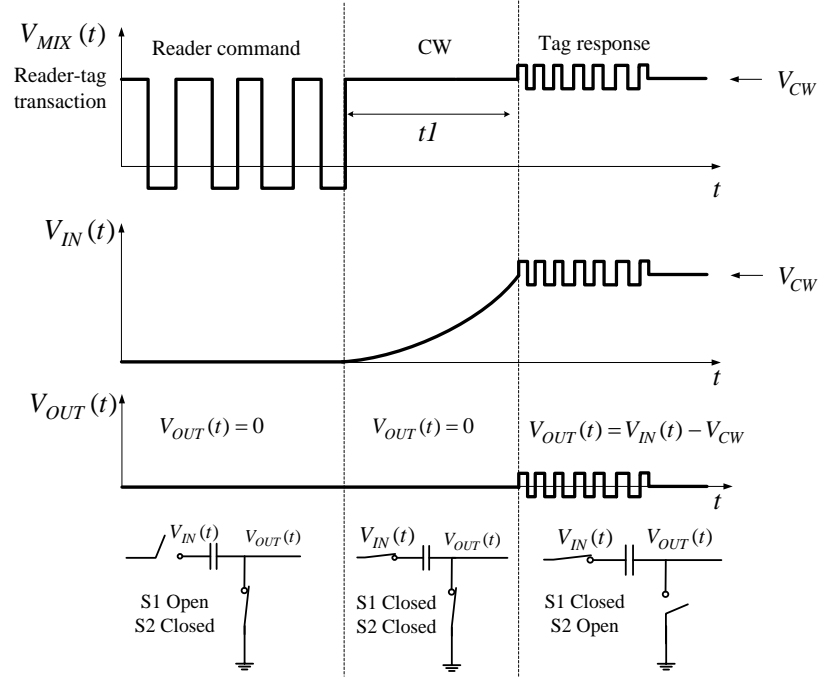


Fig. 8.15 Principle of operation of the non-linear filter and respective waveforms.

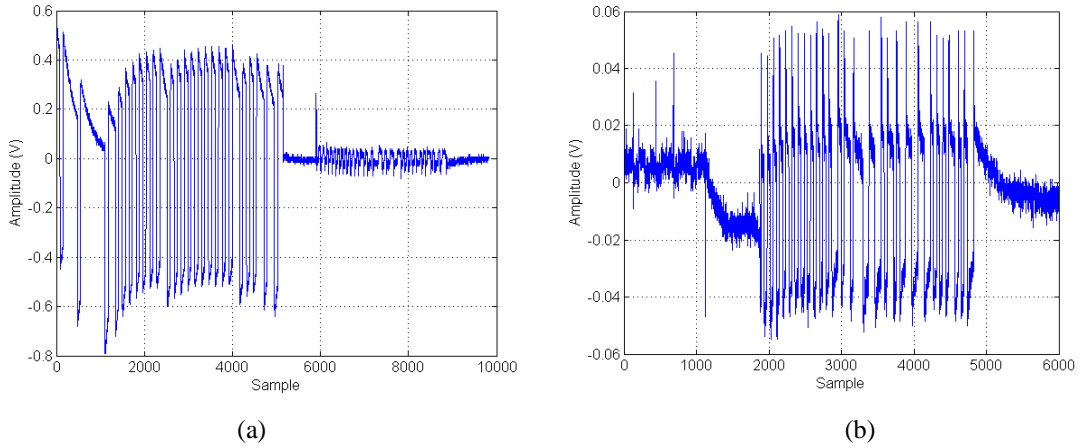


Fig. 8.16 (a) Reader command followed by tag RN16 response after passing through the non-linear high-pass filter. (b) Zoom around tag response. Using the two switches, the pulses of the down-converted reader command are also suppressed.

8.5.4. Software DC-offset removal using a FIR HPF¹¹

In this section, it is assumed that the baseband stages (mainly the ADC) have sufficient dynamic range to properly handle the received signal. The DC removal is performed in the digital domain by using a high-pass Finite Impulse Response (FIR) filter in a FPGA-based platform. The filter bank of the receiver also includes a low-pass FIR filter which is used to filter out noise and higher frequency components. Both filters were designed in Matlab and their coefficients were then imported into the FPGA hardware. The following filter parameters were used to isolate a tag

¹¹ This part of the work was done in collaboration with colleagues from FPGA field (Prof. Arnaldo Oliveira and João Santos). The complete work is presented in [XIV].

response with data rate of 204 kbps: sampling rate after decimation by 20, $F_s = 3.072$ MHz, the cut-off frequency and the order of the high-pass filter were respectively $F_{C_HIGH-PASS} = 60$ kHz and $N_{HIGH-PASS} = 50$, and the cut-off frequency and the order of the low-pass filter were respectively $F_{C_LOW-PASS} = 1$ MHz and $N_{LOW-PASS} = 20$. More implementation details can be found in [XIV].

First, the RN16 (Fig. 8.17) of a ISO18000-6C tag was obtained from a real tag interrogation, then it was imported into Matlab where it was passed through the FIR filter chain. Figure 8.18 shows the signals at different points of the receiving chain. Afterward, the FIR filters were implemented in FPGA hardware. The obtained results are presented in Fig. 8.19.

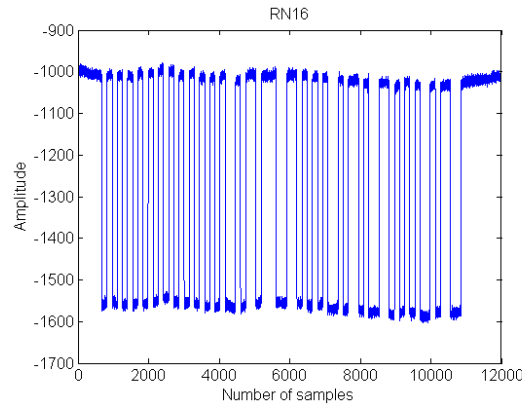


Fig. 8.17 Received tag response (RN16) sampled at 61.440 MSPS. Captured by the FPGA.

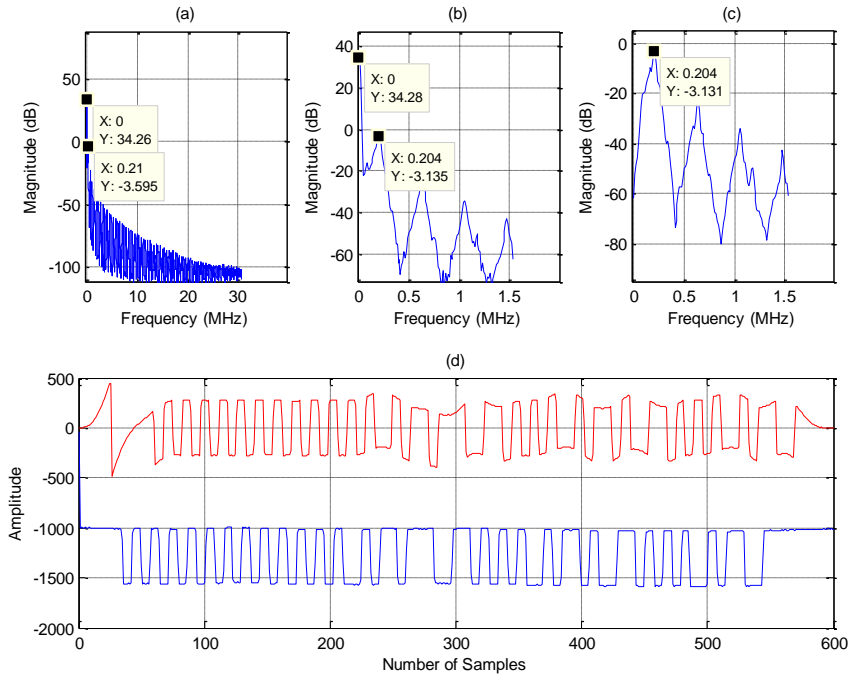
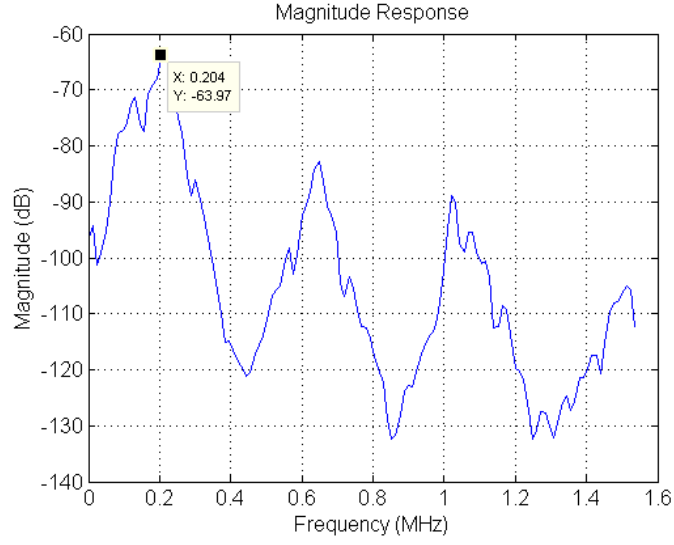
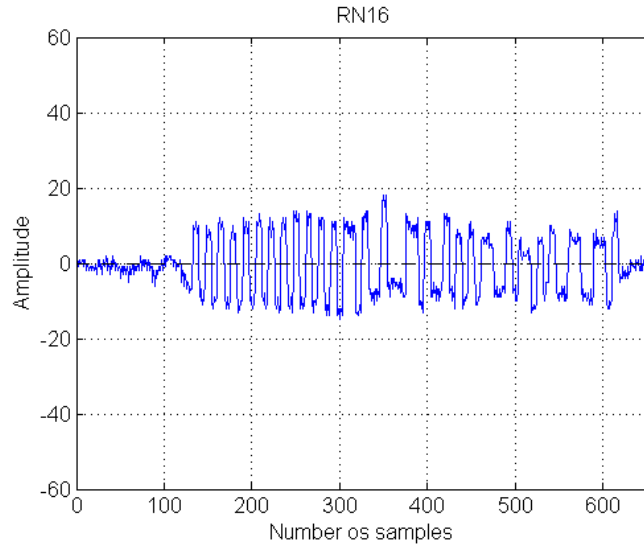


Fig. 8.18 RN16 signals at the different stages of the FIR filter chain implemented in Matlab. (a) Signal spectrum before FIR filter chain. (b) Signal spectrum after low-pass FIR filter to remove noise and decimator by 20 to reduce sampling rate. (c) Spectrum after high-pass FIR filter to remove DC component. (d) Time-domain signal before low-pass filter (bottom) and after high-pass filter (top). These results were obtained in Matlab while the ones in the next figure were obtained using the FPGA test bed.



(a)



(b)

Fig. 8.19 Filtered RN16 signal without DC component obtained in FPGA. (a) Frequency spectrum, b) Time-domain waveform centered at 0V.

8.6. Conclusions

Strong self-jammers can not only saturate the receiver front-end of passive readers, but also propagate the phase noise of the local oscillator into the receiver. This can degrade the sensitivity of the receiver and reduce the reading range and tag identification rate. For this reason, self-jamming cancellation schemes are necessary to enhance the isolation performance of bistatic and monostatic systems, thus preventing excessive Tx power to leak into the receiver.

Typical wireless and mobile systems operating in full-duplex mode require wideband cancellation, because they need to cancel out wideband modulated signals [15-17]. In passive RFID systems, though, bandwidth requirements are more relaxed since the signal to be suppressed is an unmodulated CW. Nevertheless, moderate bandwidth capability is desired in order to suppress not only the CW, but also the leaked LO phase noise [8]. Broadband suppression may also be desired in approaches that use non-conventional signals, such as the MS signals studied in this thesis, which are inherently of wide band.

In this chapter, we presented state-of-the-art self-jamming suppression techniques, including approaches commercially used in modern RFID reader ICs. We also investigated MS self-jamming cancellation and came to the conclusion that CW schemes can also be effective for MS signals [XIII]. We studied adaptive algorithms for changing wireless channels. In the future, these algorithms will be applied to the developed SDR reader.

The generation of large DC-offsets, which is a direct effect of self-jamming in DCR receivers, is challenging for the baseband stages, mainly the ADC. Hardware and software approaches were presented to deal with DC-offsets, namely enhancements to the basic high-pass filter circuit, which allows the suppression of not only the DC-offset, but also the transient behavior.

References

- [1] D. M. Dobkin, *The RF in RFID: Passive UHF in Practice*. Elsevier, Burlington, MA, 2008.
- [2] R. Langwieser, G. Lasser, C. Angerer, M. Rupp, and A. L. Scholtz, "A Modular UHF Reader Frontend for a Flexible RFID Testbed", in *Proceedings of the International EURASIP Workshop on RFID Technologies*, p.p.: 1-12, Budapest, July 2008.
- [3] US Patent US7,684,751 B2: Radio Frequency Identification Apparatus, System and Method Adapted for Self-Jammer Cancellation, Joshua Posamentier, Intel Corporation, Santa Clara, CA, Mar. 2010.
- [4] US Patent US8,013,715 B2: Cancelling Self-Jammer Signals in an RFID System, Scott Chiu, Mohammed Sajid and Issy Kipnis, Intel Corporation, Santa Clara, CA, Sep. 2011.
- [5] Iker Mayordomo, Josef Bernhard, "Implementation of an adaptive Leakage Cancellation Control for passive UHF RFID Readers," *IEEE International Conference on RFID*, pp. 121-127, April 2011, Orlando.
- [6] Deogracias P. Villame and Joel S. Marciano, Jr., "Carrier Suppression Locked Loop Mechanism for UHF RFID Readers", *IEEE RFID 2010*, p.p.: 141-145, Orlando, FL, April 2010
- [7] Bin You, Bo Yang, Xuan Wen, and Liangyu Qu, "Implementation of Low-Cost UHF RFID Reader Front-Ends with Carrier Leakage Suppression Circuit", *International Journal of Antennas and Propagation*, p.p.: 1-8, Volume 2013, Article ID 135203, October 2013.
- [8] G. Lasser, R. Langwieser, and A. Scholtz, "Broadband suppression properties of active leaking carrier cancellers," in *IEEE International Conference on RFID*, p.p.: 208-212, Orlando, USA, 2009.
- [9] Robert Langwieser, Gregor Lasser, Christoph Angerer, Michael Fischer, and Arpad L. Scholtz, "Active Carrier Compensation for a Multi-Antenna RFID Reader Frontend", *IEEE, MTT-S, International Microwave Symposium 2012*, p.p.:1532-1535, Anaheim – CA, May 2010
- [10] Thomas Brauner and Xiongwen Zhao, "A Novel Carrier Suppression Method for RFID", *IEEE MICROWAVE AND WIRELESS COMPONENTS LETTERS*, VOL. 19, NO. 3, p.p.: 128-130, MARCH 2009.
- [11] M. Koller et al, "Adaptive Carrier Suppression for UHF RFID using Digitally Tunable Capacitors", *EuMC*, p.p.: 943-946, Oct 2013, Nuremberg.
- [12] J Lee, j Choi, KH Lee, B Kim, M Jeong, Y Cho, H Yoo, K Yang, S Kim, SM Moon, JY Lee, S Park, W Kong, J Kim, TJ Lee, BE Kim, BK Ko. "A UHF mobile RFID reader IC with self-leakage canceller." *IEEE Radio Frequency Integrated Circuits RFIC Symposium*, Honolulu, June 2007 (IEEE,Piscataway, 2007), pp. 273–276
- [13] Inc. Impinj. Indy R2000 Reader Chip (IPJ-R2000). REV. 1.3 2012, Impinj, Inc., Seattle
- [14] Kaihui Lin, Yuanxun Ethan Wang, Cheng-Keng Pao, and Yi-Chi Shih, "A Ka-Band FMCW Radar Front-End With Adaptive Leakage Cancellation" *IEEE Transactions on Microwave Theory and Techniques*, VOL. 54, NO. 12, Dec. 2006
- [15] Mayank Jain et. al, "Practical, Real-time, Full Duplex Wireless", *MobiCom*, p.p.: 301-312, Nevada, Sept. 2011.
- [16] Mayank Jain, "Single Channel Full-Duplex Radios". Ph.D. Thesis, Stanford University, August 211. <http://purl.stanford.edu/zh047jt6489>
- [17] Dinesh Bharadia, Emily McMillin and Sachin Katti, "Full Duplex Radios", *SIGCOMM'13*, Vol. 43, issue 4, p.p.: 375-386, August 12–16, 2013, Hong Kong, China.
- [18] Pedro Cruz, Hugo Gomes and Nuno Carvalho (2010). Chapter: Receiver Front-End Architectures – Analysis and Evaluation, Book: *Advanced Microwave and Millimeter Wave Technologies Semiconductor Devices Circuits and Systems*, Moumita Mukherjee (Ed.), ISBN: 978-953-307-031-5, INTECH, Rijeka, Croatia, March 2012.
- [19] Behzad Razavi, "Design Considerations for Direct-Conversion Receivers", *IEEE Transactions on Circuits and Systems –II: Analog and Digital Signal Processing*, Vol. 44, No. 6, p.p.: 428-435, June 1997.
- [20] R. Svitek and S. Raman, "DC Offsets in Direct-Conversion Receivers: Characterization and Implications", *IEEE Microwave Magazine*, Vol.6, issue 3, pp.: 76-86, September 2005.
- [21] Atsumi Niwa, Shigetaka Takagi, Takahide Sato, Nobuo Fuji, "Novel DC Offset Cancellation in Direct Conversion Receivers", *IEEE 3rd International Symposium on Communications, Control and Signal Processing*, p.p.: 584-597, St Julians, March, 2008.
- [22] Yoshida, H. et Al, "A Software Defined Radio Receiver using the Direct Conversion Principle Implementation and Evaluation", *The 11th IEEE International Symposium on Personal, Indoor and Mobile Radio Communications*, 2000. PIMRC 2000. , Vol.2, p.p. 1044-1048, Sep 2000, London.

- [23] Mehrbod Mohajer, Abbas Mohammadi, Abdolali Abdipour, "A Software Defined Radio Direct Conversion Receiver", The European Conference on Wireless Technology, Paris, Oct. 2005, p.p. 423-426.
- [24] AMS RFID products: <http://www.ams.com>, online 12/02/2015
- [25] Impinj Indy UHF RFID reader chips: <http://www.impinj.com>, online 12/02/2015
- [26] Ettus Research: www.ettus.com, online 12/02/2015
- [27] L. Catarinucci, D. De Donno, et.al., "A cost-effective SDR platform for performance characterization of RFID tags," IEEE Transactions on Instrumentation and Measurement, vol. 1, no. 4, pp. 903-911, April 2012.
- [28] M. Buettner and D. Wetherall, "A software radio-based UHF RFID reader for PHY/MAC experimentation," IEEE International RFID Conference, pp.: 134-141, Orlando, April 2011.
- [29] Ales Povalac, "Spatial Identification Methods and Systems for RFID Tags", Ph.D. Thesis, Brno University of Technology, Brno 2012
- [30] H. Lehpamer, RFID Design Principles, Artech House, Norwood, 2008
- [31] EPC Class-1 Generation-2 UHF RFID, Protocol for Communications at 860 MHz – 960 MHz, Version 1.2.0
- [32] W. Wang, S. Lou, K. Chui, S. Rong, C. F. Lok, H. Zheng, H. T. Chan, S. W. Man, H. C. Luong, V. K. Lau, and C. Y. Tsui, "A Single-Chip UHF RFID Reader in 0.18- μ m CMOS", IEEE 2007 Custom Integrated Circuits Conference, p.p.: 111-114, Sept 2007, San Jose.
- [33] Quellan Inc. QHX220 narrowband noise canceller ic. http://www.quellan.com/products/qhx220_ic.php, online 16/02/2015.
- [34] Analog Devices, RF Vector Modulator, <http://www.analog.com/en/products/rf-microwave/variable-gain-amplifiers/all-vgas/ad8340.html#product-overview>, online 18-06-2015.
- [35] Gregor Lasser, Robert Langwieser, and Christoph F Mecklenbrauker, "Automatic leaking carrier canceller adjustment techniques", Series on RFID and near field communications in embedded systems, EURASIP Journal on Embedded Systems, May 2013, Springer International Publishing AG, doi:10.1186/1687-3963-2013-8
- [36] G Lasser, W Gartner, R Langwieser, CF Mecklenbrauker, "Fast algorithm for leaking carrier canceller adjustment", Fourth International EURASIP Workshop on RFID Technology. p.p.: 46-51, Torino, 27-28 September 2012
- [37] Ales Povala, "Experimental Front End for UHF RFID Reader", Elektrotechnik Journal for Electrical Engineering, Vol. 2, No. 1, p.p.:55-59, April 2011.

9. A BATTERY-LESS RFID REMOTE CONTROL SYSTEM

9.1. Introduction

The remote control is one of the most widespread convenience devices ever invented. It is used to wirelessly control a variety of devices, such as TVs, doors, game consoles and air-conditioning equipment. Conventionally, remote control systems are based on infrared (IR) technology and the controller unit requires batteries to operate. Such systems present, however, some drawbacks namely the need for direct line-of-sight, the cost associated to battery maintenance and the limited lifetime of batteries. Furthermore, disposable chemical batteries at the end of lifecycle generate toxic waste that take hundreds of years to decompose, representing a risk for the environment and for the public health. In Portugal, we estimate an average of more than 23 Millions of batteries being disposed every year [XV].

An approach to mitigate the battery problem in conventional IR-based devices consists of using an event driven implementation in which the system is always in deep sleep mode and is waken up only when the user presses a key. This can significantly reduce the power consumption, extend the battery lifetime and reduce the disposal of chemical batteries. Another approach is the use of rechargeable batteries. However, this is not cost-effective for low-end home devices. In this chapter, we propose an eco-friendly battery-free solution based on WPT and passive RFID.

The first wireless remote control invented by Eugene Polley in 1955 used a light beam to control a TV [1]. At that time, the RF approach was not a viable option due to basic technology limitations. Due to its cost-effectiveness and low implementation complexity, the IR technology became preferred and widespread in the past decades. However, as the RF/microwave industry has grown and the price of components have been considerably lowered, radio has become a valid option, and it is likely that, in the future, radio will replace IR technology. Due to the advantages of radio technology, the industry now provides some RF-based remote control solutions for home devices. In 2009, ZigBee Alliance and a consortium of consumer electronics manufactures have announced a new technology/standard, especially tailored for home automation, the RF4CE (RF for Consumer Electronics) [2]. Nevertheless, the traditional radio approach based on super-heterodyne architecture is still needing disposable batteries.

Energy harvesting from mechanical strain energy using piezoelectric effect [3][4] has been proposed for use in low-power wireless devices (e.g. keyless entry and battery-less home control). In [5], the energy to power up a battery-less remote device is harvested from mechanical energy generated by the user when pressing a piezoelectric harvesting button. Despite the limited energy generation capability of current piezoelectric devices, this approach was claimed to generate enough energy to power up a digital encoder and a radio transmitter for use in battery-less devices such as light switches. This chapter presents a proposal [XV][XVII] to eliminate the batteries by

using WPT and passive RFID concepts [6][7].

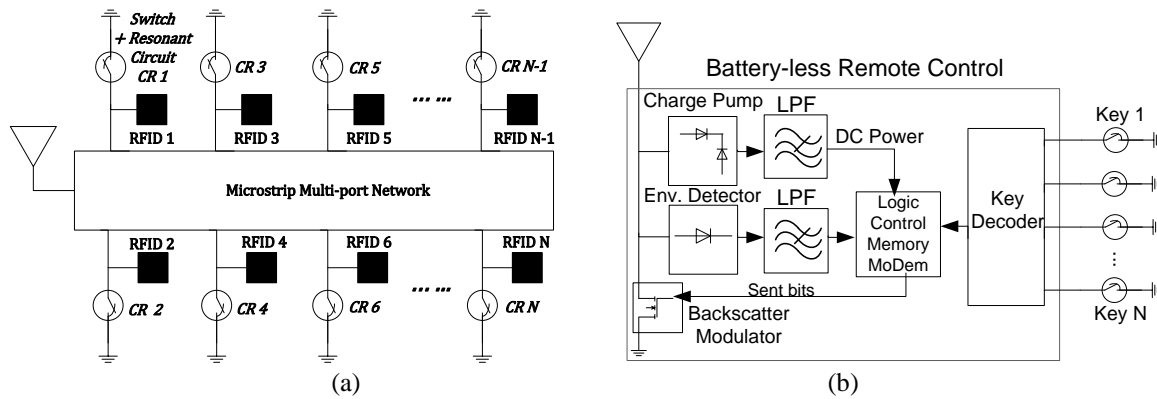


Fig. 9.1(a) Diagram of the proposed multi-RFID *ReC*. (b) alternative passive sensor-alike configuration.

9.2. The proposed system

The proposed Remote Control (*ReC*) is based on a multi-RFID approach in which each RFID chip is associated to a key as in Fig. 9.1(a). Alternatively, a passive sensor-alike configuration as in Fig. 9.1(b) can be used, in which a key decoder is used and a single RF front-end is shared by the keys. In order to read the transponders' ID and to identify the respective key, the Device to Control (*DeC*) incorporates an RFID reader. As an alternative, the RFID reader can be externally mounted on the *DeC* [refer to Fig. 9.9(a)]. This strategy guarantees compliance with already installed equipment by using an RFID-IR interface. A switch-controlled resonant circuit is used to activate each RFID chip [see Fig. 9.2(a)]. In order to interconnect the N passive RFID chips, a multi-port microstrip network [Fig. 9.2(b)] is proposed to guarantee that, by default all the chips are in idle mode, and once a key is pressed the respective transponder goes to active mode and is read by the reader to identify the pressed key. The inactive transponders do not interfere with the active one.

9.2.1. A multi-port switched network

First, a mechanism is required to allow the user to activate and deactivate the RFID chips. For this purpose, a resonant switch controlled LC circuit is parallel-connected to the matched chip. By default the switch is closed and the series circuit resonates at the operating frequency, short-circuiting the RFID chip. In this state the chip is unable to respond to the reader. Once the user presses a key, the respective switch opens and the series circuit no longer resonates. In this state, the reader is allowed to interrogate the chip. This activation/deactivation circuit is depicted in Fig. 9.2(a).

Additionally, a simple and low-cost multi-port network [Fig. 9.2(b)] is proposed to interconnect the N RFID chips and the respective N switch-controlled resonant circuits. This network must guarantee that only the active RFID chip is connected to the antenna (port Z_{IN}) while all the inactive chips do not interfere with the active one. Moreover, the structure should dynamically rearrange as the user presses different keys. Some similarities exist between the proposed multi-port network and traditional Single-Pole N-Throw (SPNT) switches [8-10]. This multi-port network could be considered as such a type of switch, connecting one of N RFID chips to a single antenna. However, while SPNT switches are electrically controlled (typically using PIN diodes), the proposed multi-port is mechanically controlled by the user through contact switches. Furthermore, in our implementation, the termination load of each port in inactive mode is tuned to the operating frequency by using a resonant circuit [see Fig. 9.2(b)]. The proposed network should meet the following requirements:

- Only the active port n ($Z_{i=n}$) should be routed to the antenna.
- All other ports do not interfere with port n and remain invisible to the antenna port.
- The insertion loss between the antenna port and the active port n is ideally 0 dB; the cross-talking between the antenna port and all inactive ports and the cross-talking between the active port and all other are ideally null.
- By default all ports are terminated with a short, $Z_{i \neq n} = 0$.
- The active port termination should be set to the characteristic impedance $Z_{i=n} = Z_0$.

Considering the lossless model of a microstrip transmission line, the input impedance looking into each branch i of the network of Fig. 9.2(b) is given by:

$$Z_i' = Z_0 \frac{Z_i + jZ_0 \tan(\beta_1 l_1)}{Z_0 + jZ_i \tan(\beta_1 l_1)} \quad (9.1)$$

where $i=1,2,\dots,n\dots N$, N is the total number of ports of the network, corresponding to the total number of keys of the *ReC*, Z_i is the load attached to each branch i , Z_0 is the characteristic impedance of the system, β_1 is the phase propagation constant and l_1 is the physical length of the line. Similarly, the impedance Z_A' can be obtained from Z_A as follows:

$$Z_A' = Z_0 \frac{Z_A + jZ_0 \tan(\beta_2 l_2)}{Z_0 + jZ_A \tan(\beta_2 l_2)} \quad (9.2)$$

If the central transmission line ($\beta_2 l_2$) phase-delays the signal by a multiple of half wavelengths, ($\beta_2 l_2 = k \cdot 180^\circ$), then $\tan(k\beta_2 l_2) = 0$ and consequently $Z_A' = Z_A$. The implication of this is that, if lossless lines are considered, then the central lines have no impact in the circuit. However, such lines allow

an increased freedom in the circuit layout design. Considering that $Z'_A = Z_A$, the input impedance of the circuit in Fig. 9.2(b) simplifies to a parallel impedance arrangement,

$$Z_{IN} = Z_1' // Z_2' // Z_3' // Z_4' = \left[\frac{1}{Z_1'} + \frac{1}{Z_2'} + \frac{1}{Z_3'} + \frac{1}{Z_4'} \right]^{-1} \quad (9.3)$$

and the input impedance of a general circuit of this kind (with N ports) is given by (9.4). The phase shift of each branch is set to be $\lambda/4$ plus a multiple of $\lambda/2$ (9.5).

$$Z_{IN} = \left[\sum_{i=1}^N \frac{1}{Z_i'} \right]^{-1} = \left[\sum_{i=1}^N \frac{Z_0 + jZ_i \tan(\beta_1 l_1)}{Z_0(Z_i + jZ_0 \tan(\beta_1 l_1))} \right]^{-1} \quad (9.4)$$

$$\beta_1 l_1 = 90^\circ + k \cdot 180^\circ \quad (9.5)$$

The impedance of each port of the network, Z_i , can assume two distinct impedance values corresponding to the active and inactive transponder states:

$$Z_i = \begin{cases} Z_n = Z_{TAG_MATCHED} = Z_0, & \text{if key } n \text{ is pressed} \\ 0\Omega, & \text{by default}^{12} \end{cases} \quad (9.6)$$

Considering a N -port network in which port n is active and matched to the system characteristic impedance ($Z_{i=n} = Z_{TAG_MATCHED} = Z_0$) and assuming that all other ports are short-circuited to ground ($Z_{i \neq n} = 0$) via the resonant circuits [see Fig. 9.2(a)], according to (9.1)-(9.6), the input impedance Z_{IN} and the impedance seen by the antenna are equal to the same value (9.7).

$$Z_{IN} = \left[\frac{Z_0 + jZ_1 \tan(90^\circ)}{Z_0(Z_1 + jZ_0 \tan(90^\circ))} + \frac{Z_0 + jZ_2 \tan(90^\circ)}{Z_0(Z_2 + jZ_0 \tan(90^\circ))} + \dots \right. \\ \left. \dots + \frac{Z_0 + jZ_n \tan(90^\circ)}{Z_0(Z_n + jZ_0 \tan(90^\circ))} + \dots + \frac{Z_0 + jZ_N \tan(90^\circ)}{Z_0(Z_N + jZ_0 \tan(90^\circ))} \right]^{-1} \quad (9.7)$$

$$= Z_n = Z_0$$

Previous results can be summarized as follows: if only one chip is activated and matched to Z_0 , while all other chips are short-circuited to ground, then only the matched active chip ($Z_n = Z_0$) is seen by the antenna.

¹² Ideally this should be a 0Ω impedance, in practice an approximate short-circuit is used.

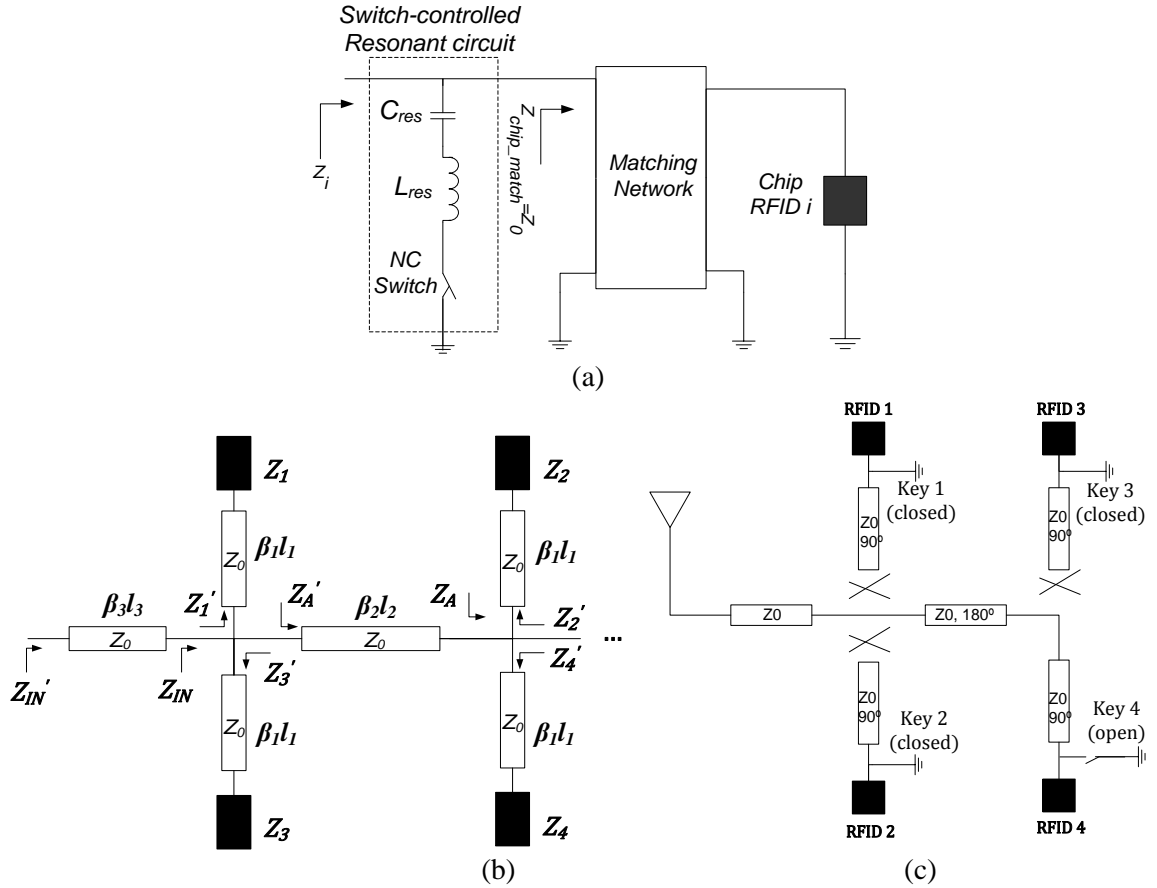


Fig. 9.2(a) Port termination composed of a switch-controlled series resonant circuit in parallel with a matched RFID chip. (b) Model of the multi-port microstrip network with $N+1$ ports. Port Z_{in} is the shared antenna port and ports Z_i are the N key ports. (c) Illustration of a 4-key ReC in which chip RFID4 is active and all other are inactive. The active chip is routed to the antenna port.

In order to better understand the dynamic routing mechanism involved in the ReC circuit, an illustrative example is presented in Fig. 9.2(c). Let's consider a 4-key ReC and assume the user has pressed the key number four, forcing the normally-closed switch to be open. Consequently, the impedance termination of branch four becomes equal to Z_0 (corresponding to the impedance of the matched chip RFID4). On the other hand, all other chips are in parallel with a short circuit, imposed by a resonant circuit at the operating frequency, so that the impedance seen by the deactivated branches is zero. These null impedances are transformed into open circuits by the 90° phase shifts imposed by the quarter wavelength lines. In this sense, the short-circuited chips are deactivated and do not interfere with the rest of the circuit as illustrated in Fig. 9.2(c), where the crosses represent infinite impedances that do not have impact in the parallel impedance association. Consider now a different scenario, where RFID1 or RFID2 is activated and RFID3 and RFID4 are deactivated. In this case, the infinite impedance (open circuit) appearing at the right crossover node would be transposed to the left crossover node by the central half wavelength line (180° phase shift). Again the infinite impedance would have no effect on the parallel association of impedances

and would not interfere with the rest of the circuit. This is in agreement with equation (9.2).

9.3. Simulation and measurement results

9.3.1. RFID chip and switch characterization and matching

EPCGlobal compliant NXP G2XN chips (manufacture ref. SL3S1002FTT) have been used in this work. In order to match the chip impedance, it is necessary to first know its Large Signal S-parameters. Details of UHF RFID chip measurements can be found in [11]. It is also important to characterize the RF behavior of the switches. The switch S-parameters model is extracted and imported into ADS simulations for further evaluation and design. In order to have accurate measurements both for the RFID chips and switches, first a calibration procedure is conducted. Since we are dealing with a non-insertable DUT (Device Under Test) and the reference plane must be exactly at the pins of the DUT, a commercial SOL (Short, Open and Thru) calibration kit is not suitable. For this reason, we have built a custom SOL calibration kit [see Fig. 9.3]. SMA connectors are used as the fixture for the DUT and for the calibration standards (mounted on the edge of the connectors). This allows the definition of a precise reference plane since both the calibration standards and the DUT are placed at the same physical location. Moreover, this will guarantee a straightforward characterization and specification of the standards in the Vector Network Analyzer (see reference [12]). To perform calibration and measurements, the calibration standards and DUT are mounted at the top of the SMA connectors [see Fig. 9.3]. The short standard is obtained by short-circuiting the inner SMA conductor to the outer conductor, the open standard is realized by an open-circuit SMA connector and the load standard is build up with a high quality 50 Ohms termination (manufacture ref. CHF1206CNT) on the top of an SMA connector.

The chip input impedance is depicted in Fig. 9.4. As can be observed, the non-linear impedance varies with the input power level. Thus, the matching circuit should consider the desired input power level, precisely the minimum input power level required to activate the chip. This information can be drawn from Fig. 9.4, in which the activation point is characterized by an accentuated fluctuation in the real part of the chip input impedance [13]. The knowledge of the unmatched activation point ($P_{unmatched} \approx -5dBm$) and respective reflection coefficient ($|\Gamma_{unmatched}|^2 = 0.86$) allows the calculation of the actual chip activation level according to (9.8), $P_{matched} \approx -13dBm$.

$$P_{matched} = P_{unmatched}(1 - |\Gamma_{unmatched}|^2) \quad (9.8)$$

$$f_c = \frac{1}{2\pi\sqrt{L_{res}C_{res}}} \quad (9.9)$$

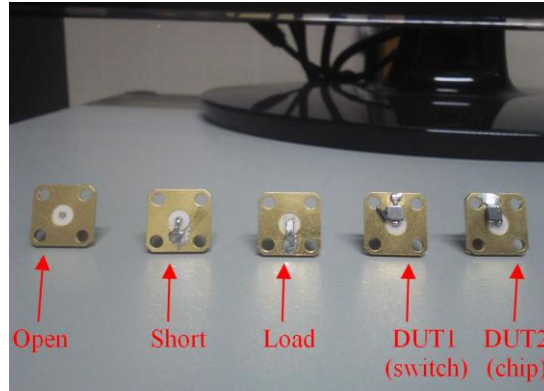


Fig. 9.3 Custom calibration standards and DUTs mounted on the SMA fixtures

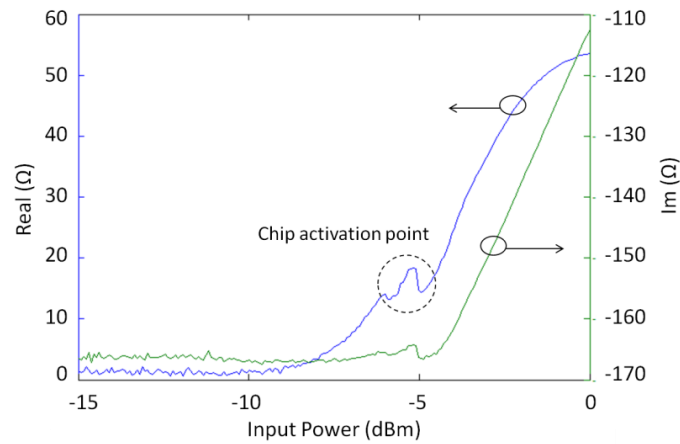


Fig. 9.4 Measured input impedance of the RFID chip. A simple L-matching circuit is used to match the chip to 50Ω .

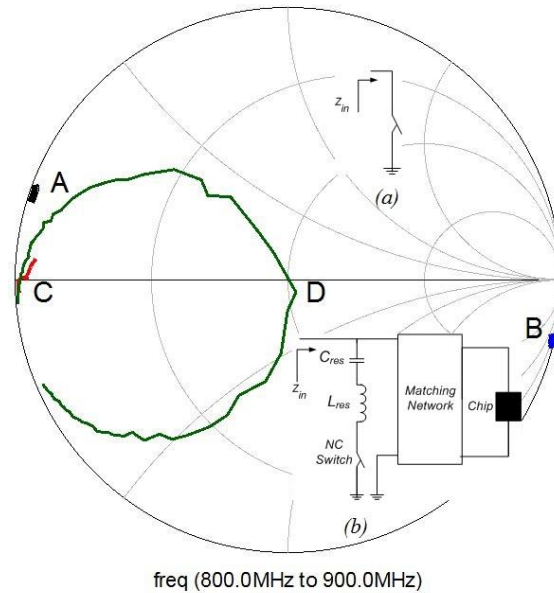


Fig. 9.5 Measurements of the stand-alone switch (points A and B), and measurements of the switch-controlled resonant circuit in parallel with the matched RFID chip. When the switch is closed the series circuit resonates at 866.6 MHz imposing an approximate short circuit (point C). When the switch is open the input impedance is approximately equal to the matched chip impedance (point D).

Figure 9.5 depicts the measured input impedance of the switch alone (point *A* and *B*) and complete port termination (points *C* and *D*). Point *A* corresponds to the default closed position in which the switch has a predominant inductive behavior and point *B* corresponds to the open position in which the switch behaves predominantly as a capacitor. In the default (closed) state of the switch, the series switch-controlled resonant circuit resonates at 866.6 MHz imposing a short circuit (point *C*). When the switch is open, the input impedance of the circuit approximates the matched chip impedance (point *D*), which means that the series switch has no significant impact. The series inductance (L_{res}) and capacitance C_{res} are inserted to achieve resonance according to (9.9). The port termination is formed by the switched resonant circuit in parallel with the matched RFID chip.

9.3.2. Multi-port simulation and measurement

First, a four-port network is simulated in ADS, prototyped and measured in order to validate and evaluate the proposed multi-port scheme. In order to reduce the overall circuit size, microstrip line meandering is used. An electromagnetic simulation is also carried out using Momentum electromagnetic simulator to access the inter-coupling between the meandered lines. Fig. 9.6(a) shows the fabricated four-port network. Return loss of the antenna port (P1), S_{11} , and of one of the key ports (P2), S_{22} , are measured and compared with simulations. Also, the insertion loss (S_{21}) between the antenna port and the probed key port is evaluated. Both the simulation and measurement scenarios consider that only one of the keys is pressed by the user. For this purpose, the active port is terminate with 50Ω both in simulations and measurements and the remaining ports are terminated with 0Ω by using a via-to-ground. This represents the ideal case in which the series circuit exhibit infinite impedance when the switch is open and zero impedance when the switch is closed. The obtained results are presented in Fig. 9.6(b). Simulated and measured return loss values agree well and indicate a good performance in the band of interest (return loss ($|S_{11}|$, $|S_{22}|$) better than 17 dB). The insertion loss ($|S_{21}|$) also achieves an acceptable value around 0.6 dB. In the second scenario, a multi-port with a larger number of ports is built [see Fig. 9.7(a)]. In this case the objective is to evaluate the performance of the network with respect the number of ports and distance between the antenna port and the active port. This allows to evaluate the performance degradation as the number of keys and the distance from the antenna port increases. The following quantities are measured: return loss of the antenna port (S_{11}) and the active port n (S_{nn}), insertion loss between the antenna port and the active port (S_{1n}), isolation between the active port and an adjacent inactive port ($S_{n,n+1}$) and isolation between the antenna and an inactive port adjacent to the active one ($S_{1,n+1}$). All these measurements are made as a function of the active port number or distance from the antenna (n). The evaluated circuit is depicted in Fig. 9.7(a). The upper branches are terminated with short-circuits simulating inactive ports, while the lower branches are terminated with switch-controlled resonant circuits, allowing the activation and deactivation of the

ports during the measurements. In addition, the lower branches are probed through SMA connectors. When not connected to the VNA, the active port n or the antenna port is terminated with a 50Ω load to keep the matching condition. Results are presented in Fig. 9.7 and Table 9.1.

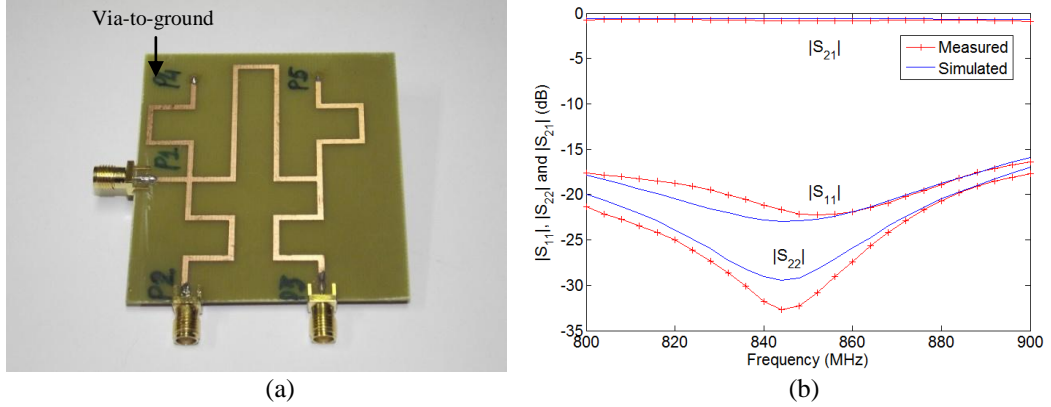


Fig. 9.6 (a) Four-port network in which the antenna port (P1) and one of the key ports (P2) are probed using the VSA in order to evaluate return loss and insertion loss performance. (b) Simulations (solid line) and measurement (crosses) of the four-port network.

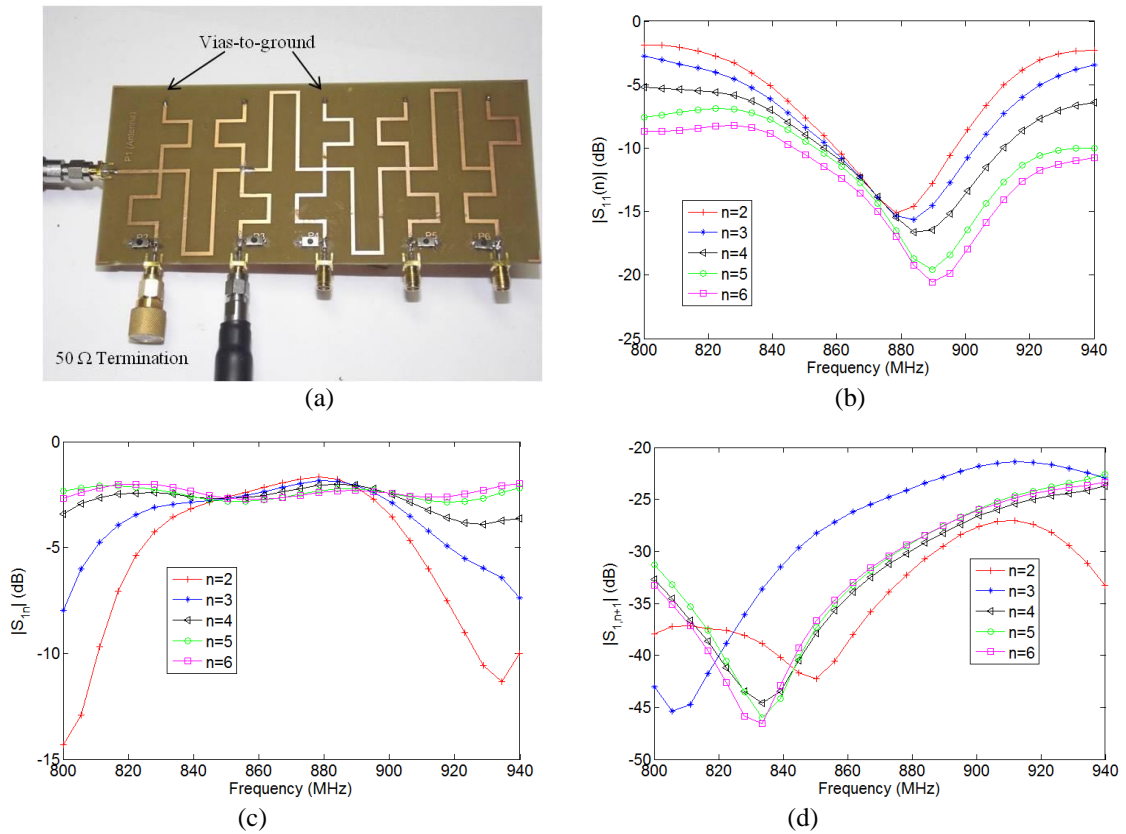


Fig. 9.7 (a) Evaluated multi-port network, fabricated in low-cost FR4 substrate in a 50Ω environment. (b) Measured return loss of the antenna port as a function of n (number of the active port). (c) Measured insertion loss between the antenna port and the active port. (d) Measured isolation between the antenna and an inactive port adjacent to the active one. The isolation between the active port and an adjacent inactive port, not shown here, presents similar values.

TABLE 9.1
MULTI-PORT PERFORMANCE AT 884 MHz DEPENDING ON THE ACTIVE PORT (N)

n	Antenna Return Loss $ S_{11} $ (dB)	Port n Return Loss $ S_{n,n} $ (dB)	Insertion Loss $ S_{1,n} $ (dB)	Isolation $ S_{1,n+1} $ (dB)	Isolation $ S_{n,n+1} $ (dB)
2	14.6	18.3	1.8	31.0	31.1
3	15.6	21.5	1.9	23.5	23.8
4	16.6	25.1	2.0	29.2	29.3
5	18.7	22.5	2.2	28.5	20.2
6	19.2	22.9	2.3	28.4	28.3

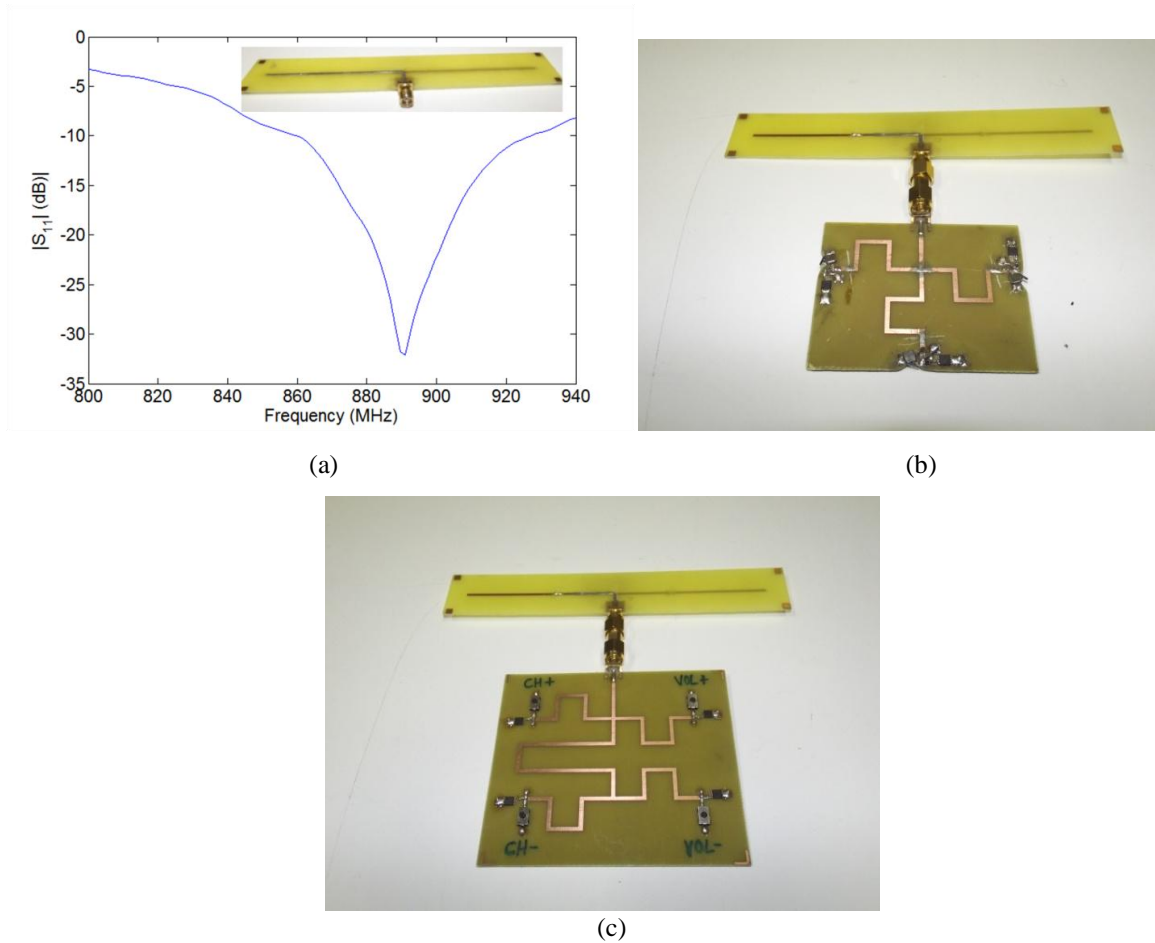


Fig. 9.8 (a) Simple dipole antenna fabricated in FR4 substrate and respective return loss at 50 Ω . (b) A three-key remote control prototype using a star configuration. (c) A four-key remote control prototype that implement the four basic TV control functions (CH +, CH –, Vol +, Vol –).

Table 9.1 summarizes the measured results of Fig. 9.7 for a single frequency (884 MHz). Although the central frequency is shifted away from the initial target frequency (866.6 MHz), the network presents a large bandwidth, maintaining good performance at 866.6 MHz. Good return loss values are achieved both at the antenna port as well as at the active port. Also, the insertion loss values are

acceptable. Compared to the previous measurement case (Fig. 9.6), the insertion loss performance is degraded because of the increase in the number of ports, which increases the circuit losses. In the multi-port circuit, as n increases, the insertion loss also increases. Therefore, there is a distance away from the antenna beyond which the performance is not satisfactory. Nevertheless, these values are quite acceptable considering the used substrate (FR4). An improved performance can be obtained with a better RF substrate. Also in terms of isolation, an acceptable performance is achieved.

The multi-port as well as the antenna are designed in a 50Ω environment. In order to keep the *ReC* design simple and very low-cost, a dipole antenna is used. The antenna is fabricated in an FR4 substrate, matched to 50Ω , and afterward it is integrated with the multi-port *ReC* circuit. The antenna return loss is depicted in Fig. 9.8(a), indicating a good performance at the band of interest. Alternatively to the dipole, a yagi-alike printed configuration similar to the one in [14] can be used to achieve higher gain while maintaining low size and complexity. Some *ReC* prototypes (including antenna) are depicted in Fig. 9.8(b) and Fig. 9.8(c).

9.3.3. Reading range measurements

Additional measurements have been conducted in an anechoic chamber in order to evaluate the reading range (Table 9.2), the impact of several blocking materials in the range (Table 9.3) and the dependence on the *DeC* antenna configuration and *ReC* orientation (Table 9.4). Using 5.5 dBi circularly-polarized antennas at the *DeC* transmitter and receiver, a maximum communication distance of 3.5 m has been achieved for a radiated power of 27 dBm. Table 9.3 shows that, cardboard, plastic and wood blockers are still allowing communication, while metal and the human body completely block the communication. On the other hand, all the tested materials inhibit a traditional IR remote control to communicate, which was expected since the blocking materials are opaque to the IR radiation. Table 9.4 presents the minimum transmitted power levels required to read the *ReC* using different transmitter/receiver antenna configurations.

TABLE 9.2
READING RANGE AS A FUNCTION OF TRANSMITTED POWER

P_t (dBm)	R (m)
17	1.05
18	1.22
19	1.39
20	1.90
21	2.24
22	2.43
23	2.53
24	2.61
25	2.98
26	3.22
27	3.50

TABLE 9.3
LINE-OF-SIGHT RELIABILITY TESTS

<i>Blocking Material</i>	<i>R (m), Proposed ReC ($P_t=17$ dBm)</i>	<i>R(m), IR Remote Control</i>
Cardboard	0.72	NC
Rigid plastic	0.76	NC
Metal	NC	NC
Wood	0.62	NC
Human body	NC	NC

TABLE 9.4
MINIMUM TRANSMITTED POWER REQUIRED TO READ THE *REC* AT 0.7M AWAY

Reader TX antenna	Reader RX antenna	Remote Control Dipole Antenna		
		Polarization on angle (θ)	P_{min} (dBm) Azimuth: $\phi=0^\circ$	P_{min} (dBm) Azimuth: $\phi=45^\circ$
A1	A1	0°	13.2	13.3
		45°	12.9	12.9
		90°	13.0	13.1
A1	A2	0°	13.3	13.3
		45°	13.2	13.2
		90°	13.3	13.1
A2	A1	0°	13.9	16.1
		45°	15.8	16.5
		90°	NC	NC
A2	A2	0°	13.9	18.3
		45°	15.7	18.3
		90°	NC	NC

A1 = High gain circularly-polarized patch antenna (5.5 dBi)

A2 = Low gain dipole antenna

NC = No Communication

9.4. Battery-free demonstration prototype

In this section a functional demonstration prototype of the battery-free system is described, including the developed RFID *ReC* device and the *DeC* (a TV). As a proof of concept the remote control system is integrated in a TV equipment and some control functionalities are implemented and tested. To do so, the four-key *ReC* prototype of Fig. 9.8(c) is used to implement channel up (CH +), channel down (CH -), volume up (Vol +) and volume down (Vol -) functionalities.

Concerning the communication between the proposed RFID *ReC* and the *DeC*, two options exist as illustrated in Fig. 9.1(a) and Fig. 9.9(a): the first case requires that an RFID reader front-end is embedded in the *DeC* during the manufacturing process. Such RFID front-end consists of a transmitter, which sends data (RFID commands) and wireless power to the *ReC* device, and a receiver responsible for receiving the backscattered data from the *ReC*. In this case, both the RFID transmitter and receiver are embedded in the *DeC* and a common control unit can be used. Alternatively, an interface unit can be externally mounted in the *DeC* [see Fig. 9.9(a)]. Such interface unit comprises an RFID reader and antennas and an RFID-to-infrared converter that acts as a bridge between the RFID reader and the *DeC*. In this case, the RFID reader has an independent control unit. In this scenario, there is no direct electrical contact between the RFID reader and *DeC*. Instead, the communication between the *ReC* and the *DeC* is made in two steps: the *ReC* communicates with the interface unit by RF backscattering (RFID) and the communication between the interface unit and the *DeC* is implemented using infrared. This is can useful to incorporate the proposed scheme into an already installed system that uses conventional infrared technology such an old TV.

A commercial RFID reader [15][16] is combined with a universal IR remote control to implement the aforementioned RFID-IR interface, which acts as a bridge between the RFID reader and the TV by receiving information from the reader via a digital I/O interface and sending this information to the TV via IR [refer to Fig. 9.9]. The used RFID reader can be controlled by a computer via an API (Application Programming Interface), allowing the implementation of custom applications. The used RFID reader provides a set of commands [16], namely to perform inventory of tags in the field, to read tags' ID and to access tags' memory. Such commands are accessible via TCP-IP interface by using a custom software application¹³. The RFID reader also provides digital I/O interfaces equally controlled by the software application. These I/O interfaces are used to interface with the universal IR remote control. The use of a universal remote control allows the prototype to adapt to several equipments.

Figure 9.11 depicts the flowchart of the developed demo application. First, the application sets the RFID reader to be continuously scanning its field searching for RFID tags. Once a tag is detected,

¹³ JAVA was used in this work to develop the demo application.

the application determines whether the read ID is valid or not. If it is a valid key ID, then the application activates the corresponding key in the universal IR remote control through the reader I/O interface. The universal IR remote control is placed in the proximity of the *DeC*, allowing line-of-sight IR communication between the RFID-IR interface and the TV.

Fig. 9.9(b) shows the complete transmitter/receiver setup including a TV, a commercial RFID reader and antennas, a computer running the demo application and a universal IR remote control. Figure 9.10 shows the aspect of the developed user interface. The application allows the configuration of the RFID reader (e.g. set output power level, start and stop field scanning) and the display of the tags' ID being read. Information about the control actions being performed is also displayed (CH-,CH+,VOL-, VOL+).

9.5. Conclusions

In this chapter, a battery-less remote control system based on a multi-RFID scheme has been proposed. A multi-port microstrip network has been fabricated and measured, and preliminary evaluation shows the possibility of extending the concept to a larger number of keys. A complete prototype of the battery-free remote control system has been implemented and tested. The system has been integrated in a TV and, as a proof of concept, four basic control functionalities have been successfully implemented (CH-,CH+,VOL- and VOL+). Although the prototype has been tested with a TV equipment, this scheme can be used in many other situations where the use of batteries is undesirable. The proposed multi-RFID scheme can also be applied to battery-less keyboards, multi-functionality cards or user-controlled cards.

Since the proposed approach is based on a commercially available low-cost technology compliant with EPCGlobal standard [17], the *ReC* unit can be manufactured at a very low-cost.

In this chapter, a backbone configuration with series chip activation mechanism is used. Appendix C presents several other configurations using series chip activation, parallel chip activation or a combination of both.

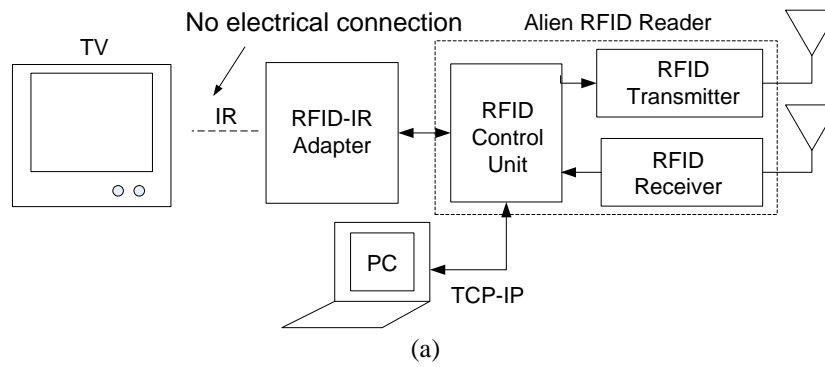


Fig. 9.9 (a) Diagram of the system using an external RFID-IR adapter to interact with the TV. (b) Demonstration prototype: 1 – RFID reader, 2 – reader antennas, 3 – external RFID-IR interface and universal IR remote control.

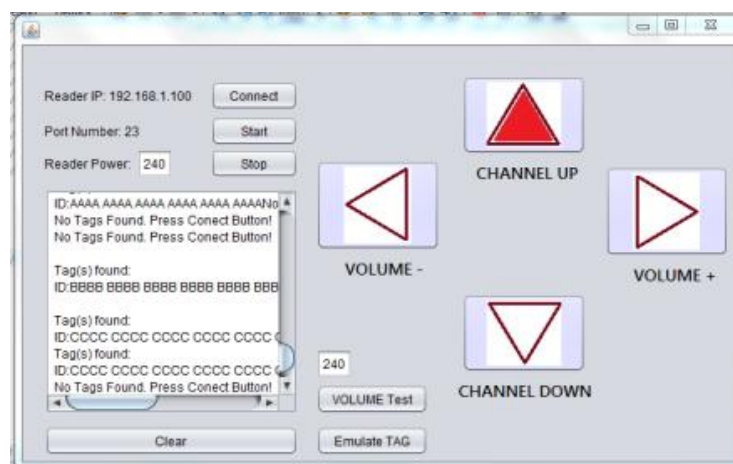


Fig. 9.10 Demo application software that controls the RFID reader. In this case the channel up icon is red indicating that the corresponding key is being pressed in the remote controller.

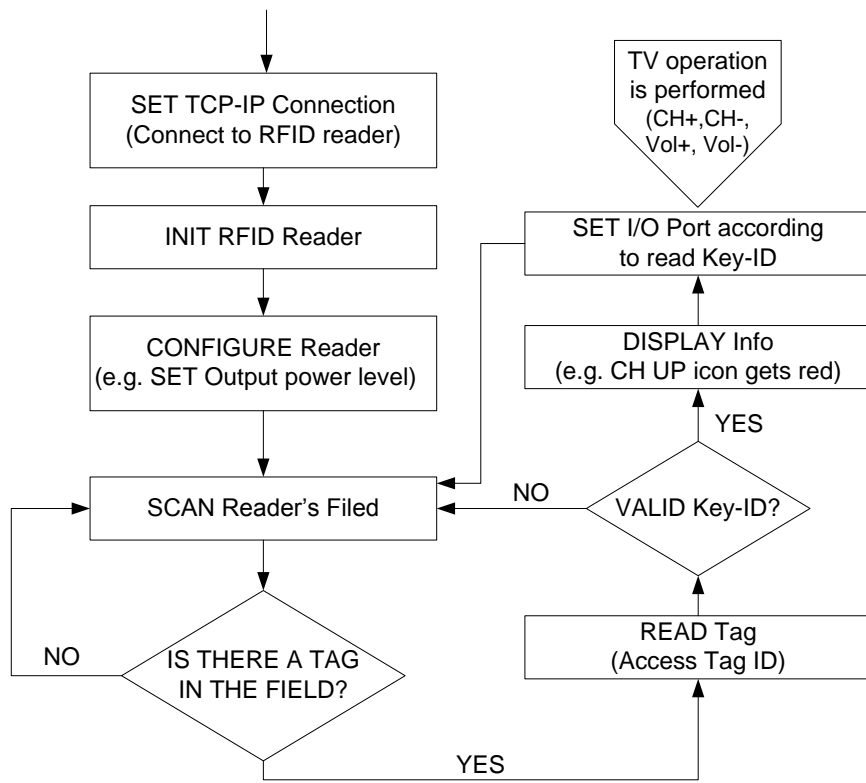


Fig. 9.11 Simplified flowchart of the developed JAVA application software.

References

- [1] IEEE Global History Network, Biography of Eugene J. Polley.
- [2] SU Dong-feng, CHEN Xiang-jian, LI Di, XU Zhi-jun and Cheng Zhi-feng, “*Research of New Wireless Sensor Network Protocol: ZigBee RF4CE*”, International Conference on Electrical and Control Engineering (ICECE), pp. 2921-2924, Wuhan, June 2010.
- [3] Action Nechibvute, Albert Chawanda, and Pearson Luhanga, “*Piezoelectric Energy Harvesting Devices: An Alternative Energy*”, Smart Materials Research, Vol. 2012, Article ID 853481, pp. 1-13, Mar. 2012.
- [4] P. Glynne-Jones, S. P. Beeby, and N. M. White, “*Toward a piezoelectric vibration-powered microgenerator*” IEE Proceedings Science, Measurement & Technology, vol. 148, pp. 68–72, Mar. 2001.
- [5] Paradiso, J.A. and Starner, T., “*Energy Scavenging for Mobile and Wireless Electronics,*” IEEE Pervasive Computing, Vol. 4, No. 1, pp. 18-27, Feb. 2005.
- [6] Finkenzeller, Klaus, *RFID Handbook*, 2nd Edition ed. Wiley, 2003.
- [7] Daniel M. Dobkin, *The RF in RFID: Passive UHF in Practice*, Burlington, MA, USA, Newnes, 2008.
- [8] J. Galejs, “*Multidiode switches*”, IRE Trans. Trans. Microwave Theory and Techniques, pp. 566-569, Sept. 1960.
- [9] J. F. White and K. E. Mortenson, “*Diode SPDT Switching at High Power with Octave Microwave Bandwidth,*” IEEE Trans. Microwave Theory and Techniques, pp. 30-36, Jan. 1968.
- [10] D. J. Kim et. al., “*Switched Microstrip Array Antenna for RFID Systems,*” Proc. 38th European Microwave Conf., pp. 1254-1257, Amsterdam, Oct 2008.
- [11] P. V. Nikitin, K. V. Seshagiri Rao, Rene Martinez, and Sander F. Lam, “*Sensitivity and Impedance Measurements of UHF RFID Chips*”, IEEE Trans. Microwave Theory and Techniques, Vol. 57, No. 5, May 2009.
- [12] Michael Hiebel, *Fundamental of Vector Network Analysis*, Rohde & Schwarz, 2007.
- [13] Rainer Kronberger, Alexander Geissler and Barbara Friedmann, “*New Methods to determine the Impedance of UHF RFID Chips*”, IEEE International Conference on RFID, Orlando, FL, April 2010.
- [14] P. V. Nikitin, K. V. Seshagiri Rao, “*Compact Yagi Antenna for Handheld UHF RFID Reader*”, Antennas and Propagation Society International Symposium (APSURSI), pp. 1-4, Toronto, July 2010.
- [15] Alien technology, Hardware Setup Guide ALR-8800, CA, USA, 2007.
- [16] Alien technology, Reader Interface Guide, CA, USA, 2007.
- [17] EPC Radio-Frequency Identity Protocols Class-1 Generation-2 UHF RFID, Protocol for Communications at 860 MHz – 960 MHz, Version 1.2.0, 2008.

10. CONCLUSIONS

Passive-backscatter radios such as passive RFID, RFID-enabled sensors and passive wireless sensors will certainly play an important role in the realization of the future IoT, and the supporting technologies such as wireless power transfer and energy harvesting will not be of less importance. Wireless power transfer has always been carried out by using a constant envelope CW signal, and the efficiency maximization has been achieved through circuit optimization. In contrast to this, this thesis explored a completely different approach, waveform optimization as an alternative to improve the efficiency.

In chapter 4, we demonstrated the effectiveness of non-CW signals, namely high PAPR MS signals, to improve the efficiency of energy harvesting circuits at low power levels. The obtained results have positively answered to the first question posed at the beginning of this thesis. This first validation was done in a cabled setup in which a signal generator was directly connected to rectifying circuits. The maximum efficiency gain obtained was limited both by waveform and circuit characteristics. Overall, the limiting parameters include the number of subcarriers, the frequency spacing between them, the MS bandwidth and PAPR, and the circuit input and output networks. A measured efficiency increase of up to 6 dB was obtained for a single diode detector under a 16-tone MS signal with 15 dB of PAPR. A charge pump circuit similar to those used in passive RFID transponders showed an efficiency improvement of 2.8 dB under a 8-tone MS signal excitation with 12 dB of PAPR.

In order to address the second challenge posed at the beginning of this thesis, two improved architectures using space power combining were proposed in chapter 5 to efficiently deliver high PAPR MS signals. The first architecture was based on multiple RF signal sources, externally synchronized to a common 10 MHz reference signal, to generate a high PAPR MS *E*-field in space. In this case, a gain of up to 1.8 dB was obtained for the same charge pump circuit used in chapter 4, under a perfectly synchronized 3-tone MS signal. The gain dropped to 0.6 dB when the subcarriers synchronization was lost. In the second case, a 4x1 mode-locked oscillator array working at 6 GHz band was used to illuminate an envelope detector circuit with a 4-tone MS signal, which provided an efficiency gain higher than 15 dB.

chapters 6 and 7 affirmatively answered to the third question of this thesis, by showing the ability of MS signals to improve the range of passive-backscatter systems. Simultaneous wireless power transfer and backscatter communications using MS signals was demonstrated and the concept was validated in a multipath faded channel. This was done first by equipping a commercial RFID reader with a MS front-end (chapter 6) and afterward by using a custom-designed SDR RFID reader (chapter 7). In chapter 6, by using a 9-tone MS signal, the reading range of the commercial RFID

reader was improved by 25% compared to the CW. In chapter 7, a passive transponder was interrogated with the built SDR RFID reader, and a gain of more than 3 dB compared to the CW was obtained for an optimal 9-tone MS signal (the transponder sensitivity was enhanced from 13 dB to 16 dB).

Chapter 8 addressed self-jamming and the consequent generation of DC-offsets, which is perhaps the second limiting factor of passive-backscatter RFID. Using a self-jamming cancellation scheme based on a simple coupler terminated with a reflective load in its traditionally isolated port, a Tx to Rx isolation of up to 50 dB was obtained for CW signals. The approach was also investigated for MS signals and proved to be effective, providing an isolation of up to 60 dB.

Finally, chapter 9 accomplished a major goal initially proposed, by providing a practical demonstration prototype of a battery-less system (a battery-less remote control system).

10.1. Concluding remarks

The coverage range of passive-backscatter systems has always been a central research concern and the efficiency of wireless power delivery has gained even more emphasis in today IoT context. Passive-backscatter RFID devices are evolving beyond mere identification to integrate new vital functionalities for IoT applications (e.g. sensing, intelligence, data logging, etc), which need also to be powered wirelessly. Therefore, the energy needs are also growing. Hopefully, in a near future, the combined research efforts in several fronts will enable the efficient realization of fully passive wireless sensor networks for IoT applications. Important topics include: low power semiconductor technologies; synergistic energy harvesting from multiple sources including electromagnetic, solar, thermal and vibration; improved backscatter schemes, such as QAM-backscatter, to improve the communication bandwidth and to significantly reduce the power consumption; efficient wireless power strategies to support longer operating ranges and expanded functionalities. It is our hope that the work presented in this thesis may give a small contribute toward these goals.

10.2. Main achievements in the scope of this thesis

- Twice finalist of the student paper competition of the IEEE – International Microwave Symposium (IMS 2011 and IMS 2016).
- ANACOM and URSI-Portugal 2011 Prize.
- IEEE MTT-S Graduate Fellowship Award 2013.
- Distinguished in the publication “Universidade de Aveiro, 40 Anos, 40 Inventores, 40 Empreendedores (University of Aveiro, 40 Years, 40 Inventors, 40 Entrepreneurs)”.

10.3. Future work

- Practical implementation of the adaptive self-jamming suppression scheme described in chapter 8, its integration in the developed SDR reader and its optimization for MS operation. So far, self-jamming suppression has been implemented using a load impedance tuner, and the optimal setting has been obtained by manual adjustments. An adaptive scheme/algorithm is necessary.
- Full implementation of the MS mode. Implementation of the presented MS demodulation methods within the reader.
- Integration of all the SDR RFID reader hardware in a single PCB board.
- Further investigation of MS multipath fading performance. In our experiments, relatively high-gain antennas were used, and a moderate reader-to-tag distance was considered in the lab environment. This may have benefited the MS fading performance. A more detailed study is necessary to investigate multipath fading of MS over longer distances, lower gain antennas and other wireless channels.
- In chapter 9, further work is needed to optimize the energy efficiency at the *DeC* side.
- More work is also required to optimize the *ReC*, namely in terms of size, number of keys and antenna performance.
- Behavioral models for RF-DC converter circuits are also a must. Improve the accuracy of the model presented in Appendix A to account for diode capacitive parasitic and ripple effects, broaden its reach to cover charge pumps and also validate it against simulations and measurements are also future objectives.
- Explore backscatter FDMA schemes for medium access and backscatter OFDM approaches for improved communication bandwidths. This cope well with the MS scheme studied in this work.

APPENDIX A – DERIVATION OF AN AC-DC TRANSFER FUNCTION FOR RECTIFIER CIRCUITS UNDER HIGH PAPR SIGNALS

The accurate simulation of multi-frequency or high PAPR signals with large spectral content may be difficult and very time-consuming. In this chapter, we attempt on the derivation of an analytical-numerical model to evaluate envelope detectors under high PAPR excitations in a fast and simple way, without requiring a specialized simulator. This model can be used to predict results such as the output DC voltage, output ripple, RF-DC conversion efficiency and efficiency gain of an envelope detector under high PAPR signals, given parameters as the input signal amplitude, duty cycle and frequency of the signal envelope, and output time constant of the output RC circuit. The following assumptions are made:

- 1) The diode capacitance effect is not considered in this derivation;
- 2) The sinusoid is approximated by a square wave with amplitude V_A and 50% duty cycle [see Fig. A.1(a)][1];
- 3) The output smoothing capacitor is assumed to be very large with respect to the RF frequency, such that there is no voltage drop between RF peaks at the output. Consequently:
- 4) in steady-state, $v_o(t)$ tends to a constant value V_{DC} ; the output capacitor current $i_c(t) = C \frac{\partial v_o(t)}{\partial t} = 0$; and the average current of the diode $\langle i_D(t) \rangle$ equals the output DC current I_o .

The high PAPR signal [Fig. A.1(b)] is obtained by shrinking the CW signal according to a duty cycle $D = T_{ON}/(T_{ON}+T_{OFF})$ such that its peak amplitude and envelope frequency become respectively $V_B = V_A/\sqrt{D}$ and $f_{env} = 1/(T_{ON}+T_{OFF})$.

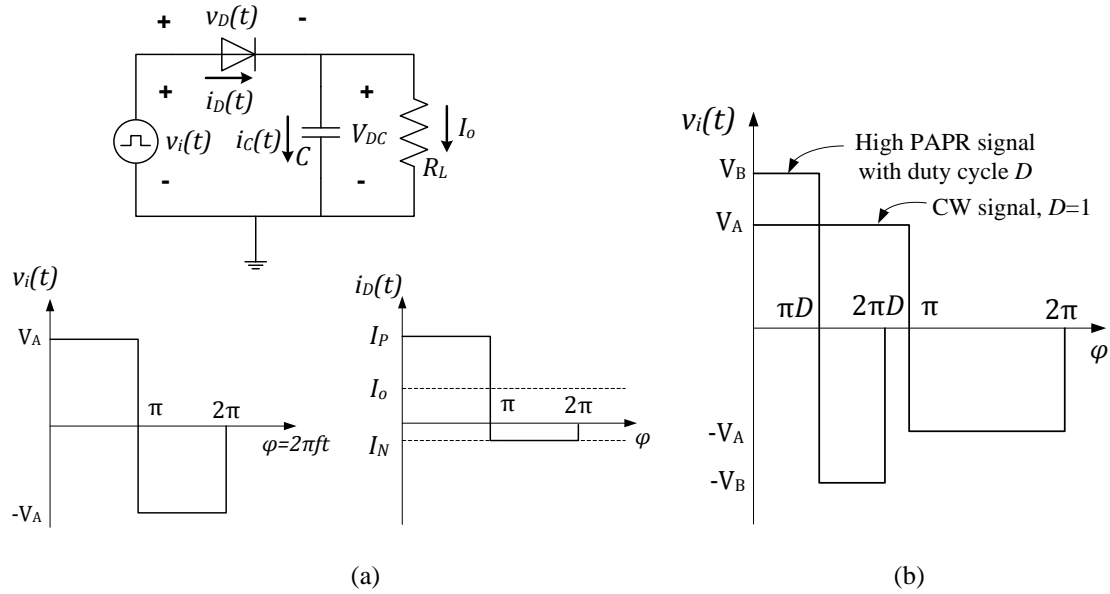


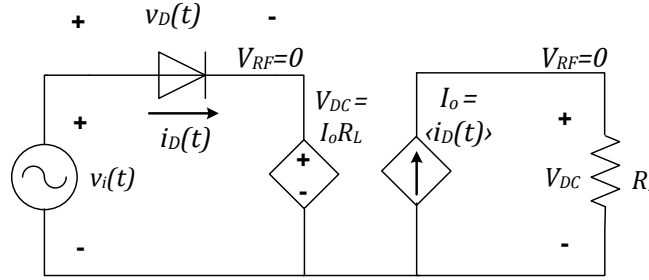
Fig. A.1 (a) CW excitation model. (b) High PAPR excitation model. Although the high PAPR signal is defined in the interval $0 - 2\pi D$, the integration period is 2π .

A. RF-DC model derivation

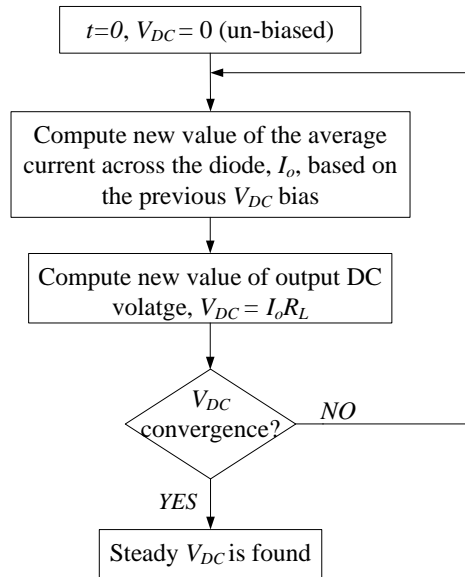
The proposed model of the RF-DC converter [Fig. A.2(a)] is based on equations (4.1)-(4.3), and encompasses a DC voltage source and a DC current source which are inter-dependent and account for the self-biasing mechanism in the diode as follows: at $t = 0^+$, right after applying the input signal, the output voltage V_{DC} is zero and the first (un-biased) iteration of the diode average current is computed; the average current, which is equal to I_o , will generate a DC voltage across the output load resistance; this DC value will now bias the diode and the next iteration of the (biased) diode average current can now be found; This process continues, and eventually, for a fixed amplitude of the input signal, the output DC voltage will converge to a steady-state value. The process ends when the relative error of the output DC voltage is found to be below a predefined value

$$(|V_{DC}^{n+1} - V_{DC}^n| = \sqrt{(V_{DC}^{n+1} - V_{DC}^n)^2} < \varepsilon),$$

where ε is a small positive number. As alluded in Fig. A.2(b), the presented model uses a double iterative loop, where the inner loop iterates to find the diode current using a Newton-Raphson method (described next) and considering a fixed DC output voltage, and outer loop iterates to find the steady-state value of the output DC voltage.



(a)



(b)

Fig. A.2 (a) RF-DC conversion model. Note that, according to the previous assumptions, the circuit output is assumed to be an RF ground. (b) Iterative process to find the output DC voltage for a given input signal amplitude. It iterates twice, to find the current through the diode and also the convergence of V_{DC} .

For each value of output DC voltage, the current through the diode is determined as follows. The input voltage and the voltage across the diode [Fig. A.1(a)] are given respectively by:

$$v_i(t) = \begin{cases} \frac{V_A}{\sqrt{D}}, 0 < \varphi < D\pi \\ -\frac{V_A}{\sqrt{D}}, \pi D < \varphi < 2\pi D \end{cases} \Rightarrow v_D(t) = \begin{cases} \frac{V_A}{\sqrt{D}} - V_{DC}, 0 < \varphi < \pi D \\ -\frac{V_A}{\sqrt{D}} - V_{DC}, \pi D < \varphi < 2\pi D \end{cases} \quad (\text{A.1})$$

where V_A is the amplitude of the CW signal and the duty cycle D determines the PAPR of the signal (for CW signal, $D = 1$). Considering equations (4.1)-(4.3) and (A.1), the diode current comes as follows:

$$i_D(t) = \begin{cases} I_P = I_S \left(e^{\frac{\frac{V_A}{\sqrt{D}} - V_{DC} - R_S I_P}{\eta V_t}} - 1 \right), 0 < \varphi < \pi D \\ I_N = I_S \left(e^{\frac{-\frac{V_A}{\sqrt{D}} - V_{DC} - R_S I_N}{\eta V_t}} - 1 \right) - I_{BV} e^{-\frac{\frac{V_A}{\sqrt{D}} - V_{DC} - R_S I_N + V_{br}}{V_t}}, \pi D < \varphi < 2\pi D \end{cases} \quad (\text{A.2})$$

Equations (A.2) are non-linear equations of the kind $x = a(e^{bx} - 1)$, $a, b \in \mathbb{R}$, which do not admit a closed-form analytical solution. Therefore, an iterative numerical method is required to find an approximate solution. The individual current components in the positive and negative cycles, I_P and I_N , can be determined separately. Approximating the first part of (A.2) is equivalent to find the root of a new function $\Psi(I_P, V_A)$:

$$\Psi(I_P, V_A) = I_S \left(e^{\frac{\frac{V_A}{\sqrt{D}} - V_{DC} - R_S I_P}{\eta V_t}} - 1 \right) - I_P = 0 \quad (\text{A.3})$$

The Newton-Raphson iterative method for non-linear equations [2] can be used to find an approximation for (A.3) and determine the positive diode current I_P . If the method converges, then, given an initial guess, a better approximation, I_P^{n+1} , can be obtained from a previous approximation, I_P^n , as follows:

$$I_P^{n+1} = I_P^n - \Psi(I_P^n, V_A) \left[\frac{\partial \Psi(I_P, V_A)}{\partial I_P} \Big|_{I_P = I_P^n} \right]^{-1} = I_P^n - \frac{I_S e^{\frac{\frac{V_A}{\sqrt{D}} - V_{DC} - R_S I_P^n}{\eta V_t}} - I_S - I_P^n}{-\frac{R_S}{\eta V_t} I_S e^{\frac{\frac{V_A}{\sqrt{D}} - V_{DC} - R_S I_P^n}{\eta V_t}} - 1}$$

(A.4)

The iterative process is terminated after $n+1$ iterations when a predefined error condition is satisfied,

$$|I_P^{n+1} - I_P^n| = \sqrt{(I_P^{n+1} - I_P^n)^2} < \varepsilon \quad (\text{A.5})$$

where ε is a small positive number that depends on the desired accuracy. The current in the negative cycle, I_N , can be computed similarly to (A.3)-(A.5). In this case, I_N [second part of equation (A.2)] is broken into two separate iterative problems and the results are then summed:

$$I_{N1}^{n+1} = I_N^n - \frac{I_S e^{\frac{-\frac{V_A}{\sqrt{D}} - V_{DC} - R_S I_N^n}{\eta V_t}} - I_S - I_N^n}{-\frac{R_S}{\eta V_t} I_S e^{\frac{-\frac{V_A}{\sqrt{D}} - V_{DC} - R_S I_N^n}{\eta V_t}} - 1} \quad (\text{A.6a})$$

$$I_{br}^{n+1} = I_{br}^n - \frac{-I_{BV} e^{\frac{-\frac{V_A}{\sqrt{D}} + V_{br} - V_{DC} - I_{br}^n R_S}{V_t}} - I_{br}^n}{-\frac{R_S}{V_t} I_{BV} e^{\frac{-\frac{V_A}{\sqrt{D}} + V_{br} - V_{DC} - I_{br}^n R_S}{V_t}} - 1} \quad (\text{A.6b})$$

$$I_N = I_{N1} + I_{br} \quad (\text{A.6c})$$

Finally, using the results obtained iteratively from (A.4) and (A.6), the total average current flowing through the diode, $\langle i_D(t) \rangle = I_o$, can be calculated in a single cycle of the input signal as:

$$\begin{aligned} I_o &= \langle i_D(t) \rangle = \frac{1}{2\pi} \int_0^{2\pi D} i_D(t) \partial \varphi \\ &= \frac{1}{2\pi} \int_0^{\pi D} I_P \partial \varphi + \frac{1}{2\pi} \int_{\pi D}^{2\pi D} I_N \partial \varphi = \frac{D}{2} (I_P + I_N) \\ &\Rightarrow V_{DC} = \langle i_D(t) \rangle R_L = \frac{D R_L}{2} (I_P + I_N) \end{aligned} \quad (\text{A.7})$$

The output DC power and the average input power are given respectively by:

$$P_{DC} = \frac{V_{DC}^2}{R_L} = \frac{D^2 R_L}{4} (I_P + I_N)^2$$

(A.8)

$$\begin{aligned}
P_{in} &= \frac{1}{2\pi} \int_0^{2\pi D} v_i(t) i_D(t) \partial\varphi \\
&= \frac{1}{2\pi} \int_0^{\pi D} V_A I_P \partial\varphi + \frac{1}{2\pi} \int_{\pi D}^{2\pi D} (-V_A I_N) \partial\varphi \\
&= \frac{D}{2} V_A (I_P - I_N)
\end{aligned}$$

(A.9)

By definition, the RF-DC efficiency comes as the ratio between the DC output power (P_{DC}) and the average input power (P_{in}):

$$\eta_{RF-DC} = \frac{P_{DC}}{P_{in}} = \frac{DR_L (I_P + I_N)^2}{2V_A (I_P - I_N)}$$

(A.10)

The efficiency gain can be obtained using the first part of equation (4.20), as the ratio between the efficiency under high PAPR signal and the efficiency under CW signal, and the PAPR can be defined as [V]:

$$PAPR(dB) = 10 \log_{10}\left(\frac{2}{D}\right)$$

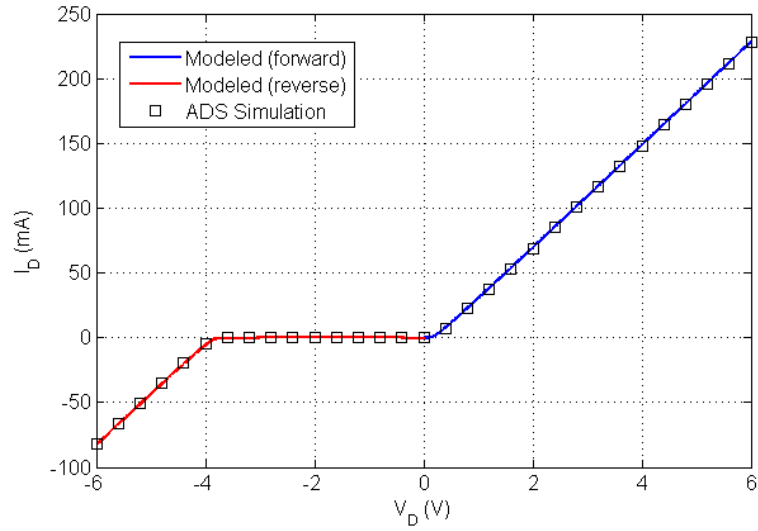
(A.11)

Note that $D = 1$ implies an always-on or CW input. It is also worth mentioning that, although the high PAPR pulse is only defined in the interval $0 - 2\pi D$ [see Fig. A.1(b)], the integration interval used in calculation of the average diode current and average input power (A.7-A9) is 2π . This is necessary to guarantee that the high PAPR pulse actually delivers a higher peak while maintaining a low average power.

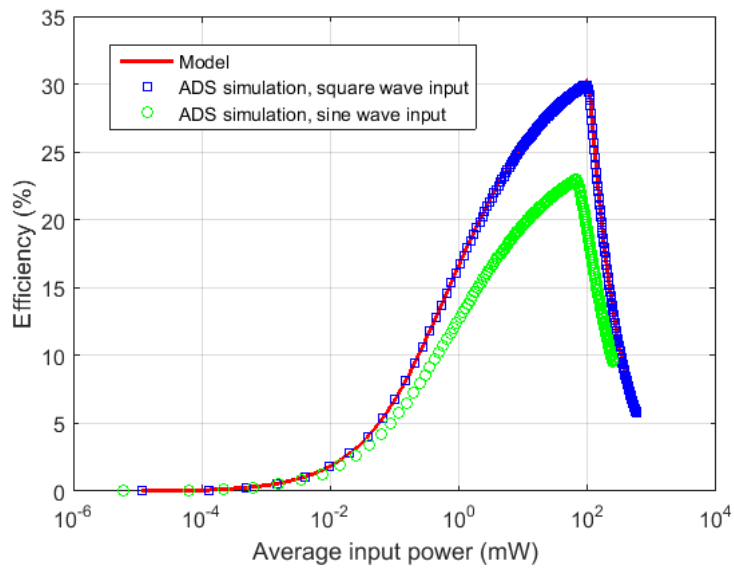
B. Preliminary model validation

Given diode parameters (Table below), input signal amplitude and duty cycle of the high PAPR signal envelope, the behavior of a single diode rectifier can be predicted. Figure A.2 plots the I-V curve given by the model, with $R_L = 0$, and the RF-DC conversion against ADS DC and ADS HB simulation results respectively, using the manufacture model. A good agreement is observed.

HSMS285x diode parameters	Symbol	Value
Saturation current	I_S	3 μ A
Series resistance	R_S	25 Ω
Zero-bias junction capacitance ¹⁴	C_{jo}	0.18 pF
Junction potential	V_j	0.35 V
Reverse breakdown voltage	V_{br}	3.8 V
Current at reverse breakdown	I_{BV}	0.3 mA
Thermal voltage	V_t	26 mV



(a)



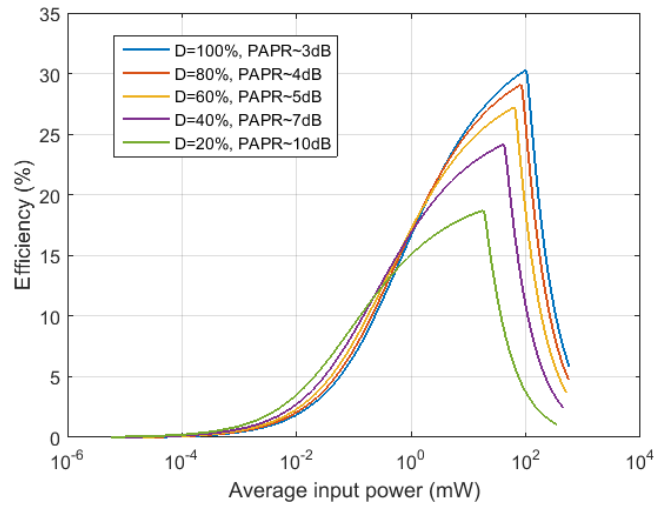
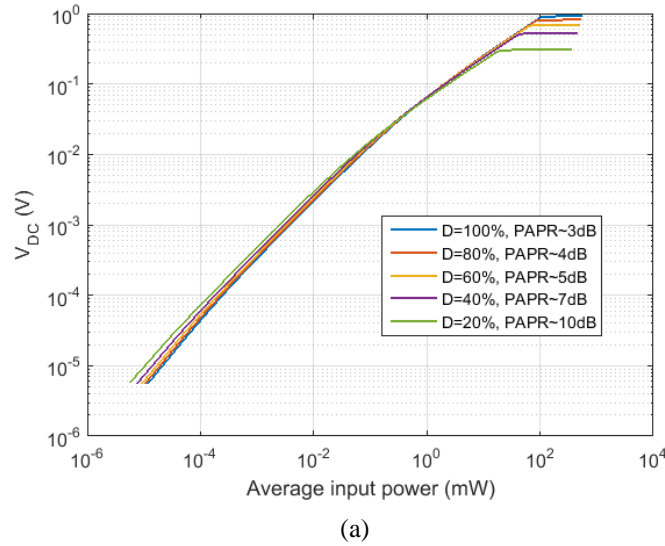
¹⁴ In the present derivation, the effect of the parasitic capacitance is neglected.

(b)

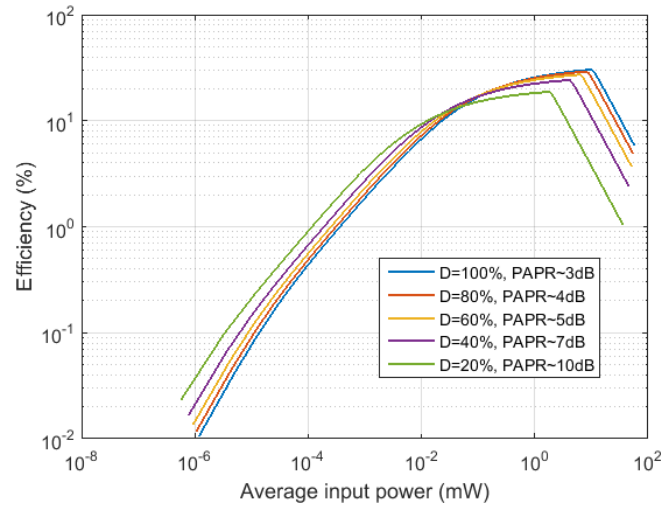
Fig. A.2 Model validation. (a) Diode I-V curve with $R_L = 0$, overlapped with ADS simulation results. (b) RF-DC conversion efficiency as predicted by the proposed model and by ADS HB simulations, with a square wave and sine wave input and a 25Ω DC load.

C. Output DC voltage, RF-DC efficiency and efficiency gain

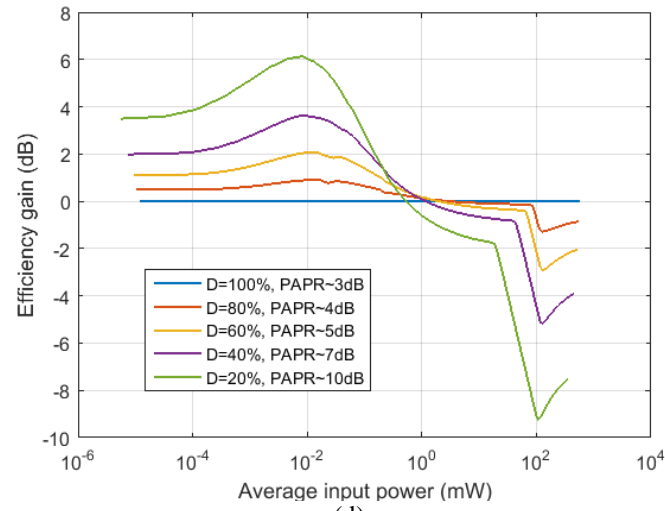
The output DC voltage, RF-DC conversion efficiency and efficiency gain as a function of the average input power level for different values of duty cycle D (and consequently different PAPR values) are depicted in Figures A.3. It is assumed a very large output capacitor value, which precludes any significant output ripple. In general, the preliminary model results are in agreement with [3]: as the PAPR increases, the RF-DC efficiency increases at lower power levels and degrades at higher power levels. The latter effect is due to an increased current voltage drop across the diode series resistance (caused by the higher peaks) and consequent resistive loss. Moreover, as the PAPR increases, the breakdown is reached earlier and the maximum efficiency is decreased.



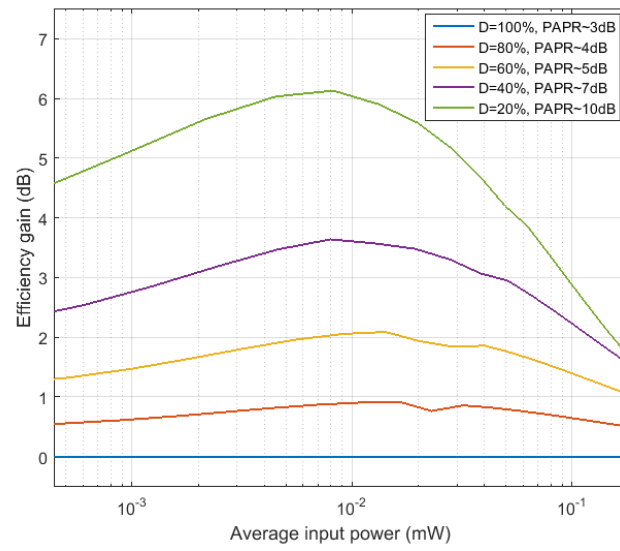
(b)



(c)



(d)



(e)

Fig. A.3 (a) Output DC voltage. (b) RF-DC conversion efficiency. (c) RF-DC conversion efficiency in log scale, where the benefit of high PAPR signal is visible at lower input power levels. (d) Efficiency gain. (e) Zoom on the efficiency gain. All the results are functions of the average input power and duty cycle.

D. Conclusions and future improvements

Although the proposed model is not yet fully validated and needs further improvements, it is a good starting point toward a more complete model. It is able to correctly replicate the DC I-V characteristic, account for the breakdown effect and describe general trends of output DC voltage, RF-DC conversion efficiency and efficiency gain with respect to input PAPR. Future improvements will cover the capacitive parasitic effect, the ripple effect and the input matching network.

- [1] Cardoso, A.J.; de Carli, L.G.; Galup-Montoro, C.; Schneider, M.C., "*Analysis of the Rectifier Circuit Valid Down to Its Low-Voltage Limit*," in *Circuits and Systems I: Regular Papers, IEEE Transactions on*, vol.59, no.1, pp.106-112, Jan. 2012.
- [2] Andrei Grebennikov, "RF and Microwave Transistor Oscillator Design", John Willey, & Sons, Ltd, 2007, England.
- [3] C. R. Valenta, "*Microwave-Energy Harvesting at 5.8GHz for Passive Devices*", Ph.D. Thesis, School of Electrical and Computer Engineering, Georgia Institute of Technology, August 2014.

APPENDIX B – PHYSICAL LAYER ASPECTS OF THE EPC GEN2 PROTOCOL

Reader-Transponder PIE Symbols

The R=>T link shall use PIE, shown in Figure 6.1. Tari is the reference time interval for interrogator-to-Tag signaling, and is the duration of a data-0. High values represent transmitted CW; low values represent attenuated CW. Pulse modulation depth, rise time, fall time, and PW shall be the same for a data-0 and a data-1. Interrogators shall use a fixed modulation depth, rise time, fall time, PW, Tari, data-0 length, and data-1 length for the duration of an inventory round.

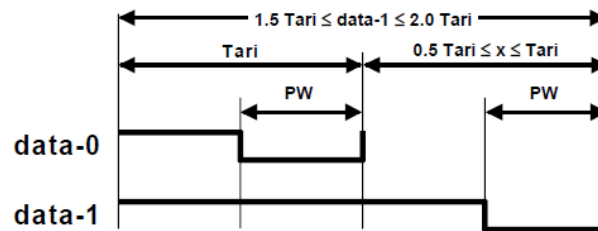


Figure 6.1: PIE symbols

Reader-Transponder Preamble and Frame-Sync

An Interrogator shall begin all R=>T signaling with either a preamble or a frame-sync, both of which are shown in Figure 6.4. A preamble shall precede a *Query* command and denotes the start of an inventory round. All other signaling shall begin with a frame-sync.

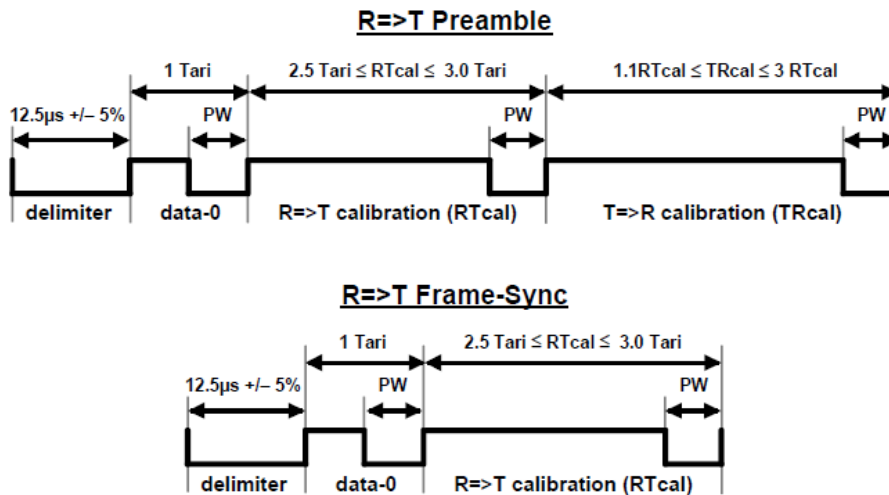


Figure 6.4: R=>T preamble and frame-sync

Transponder-Reader FM0 Symbols

Tags shall encode the backscattered data as either FM0 baseband or Miller modulation of a subcarrier at the data rate. The Interrogator specifies the encoding type.

Figure 6.8 shows basis functions and a state diagram for generating FM0 (bi-phase space) encoding. FM0 inverts the baseband phase at every symbol boundary; a data-0 has an additional mid-symbol phase inversion. The state diagram in Figure 6.8 maps a logical data sequence to the

FM0 basis functions that are transmitted. The state labels, S1–S4, indicate four possible FM0-encoded symbols, represented by the two phases of each of the FM0 basis functions. The state labels also represent the FM0 waveform that is transmitted upon entering the state. The labels on the state transitions indicate the logical values of the data sequence to be encoded. For example, a transition from state S2 to S3 is disallowed because the resulting transmission would not have a phase inversion on a symbol boundary.

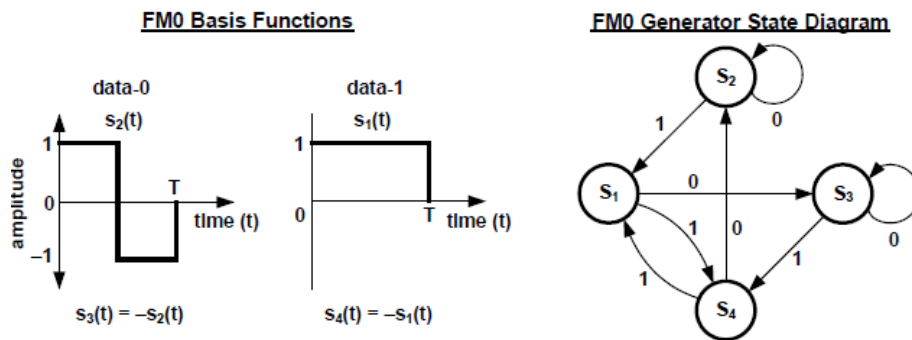


Figure 6.8: FM0 basis functions and generator state diagram

Transponder-Reader FM0 Preamble

T=>R FM0 signaling shall begin with one of the two preambles shown in Figure 6.11. The choice depends on the TRext value specified in the *Query* that initiated the inventory round. TRext chooses whether a Tag prepends the T=>R preamble with a pilot tone. The “v” shown in Figure 6.11 indicates an FM0 violation (i.e. a phase inversion should have occurred but did not).

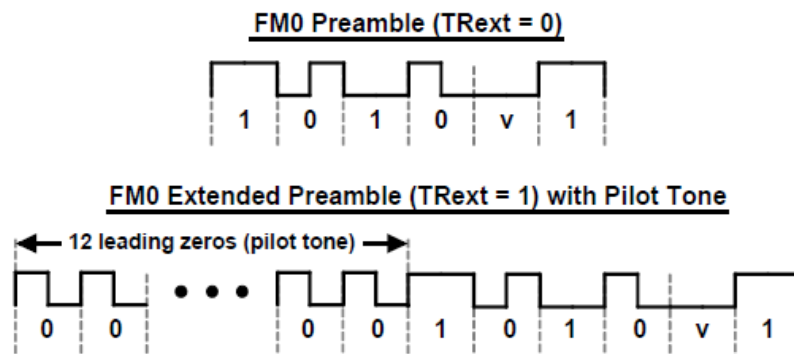


Figure 6.11: FM0 T=>R preamble

Example inventory and access of a single Tag

Figure E.1 shows the steps by which an Interrogator inventories and accesses a single Tag.

APPENDIX C –ALTERNATIVE CONFIGURATIONS FOR THE BATTERY-LESS REMOTE CONTROL

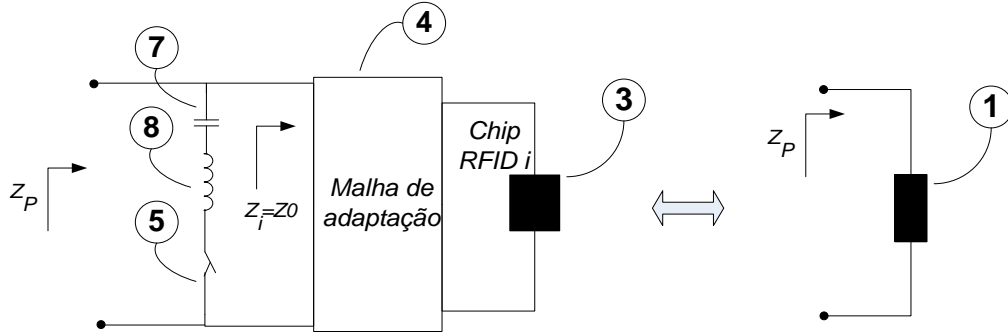


Fig. C.1 (a) Parallel chip activation mechanism

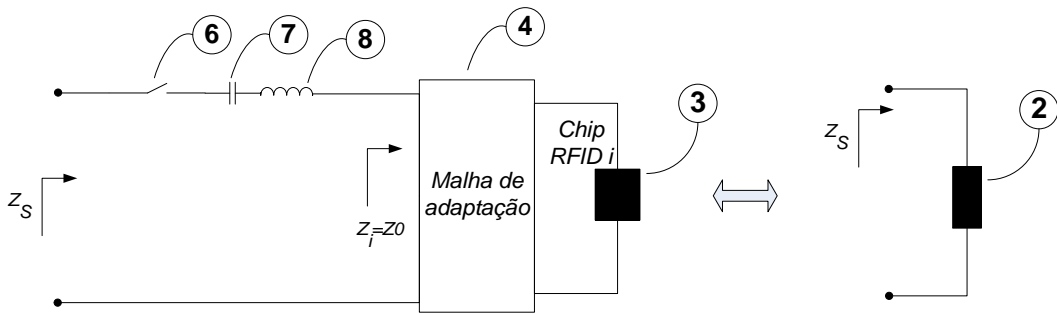


Fig. C.1 (b) Series chip activation mechanism.

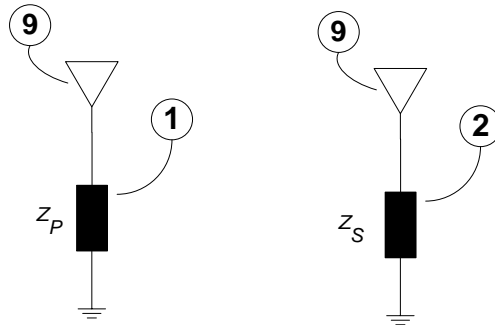


Fig. C.2 (a) Single-key remote control with parallel and series activation mechanisms respectively.

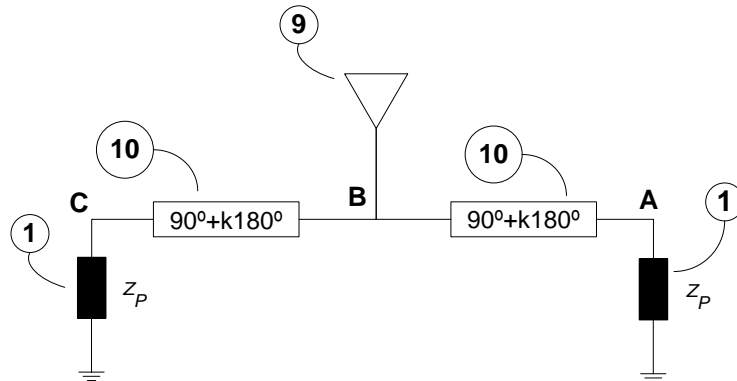


Fig. C.2 (b) Remote control with two keys using parallel activation mechanism.

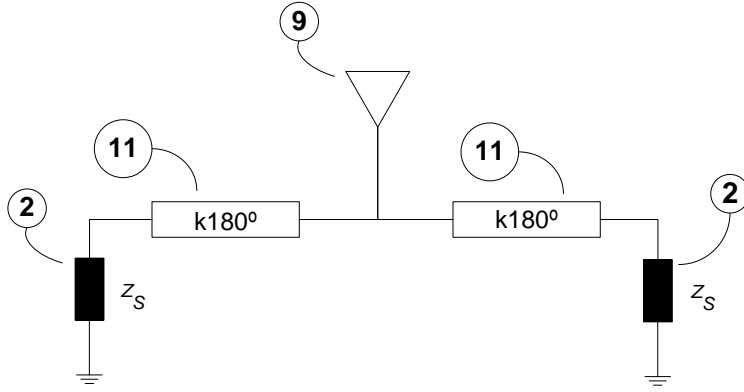


Fig. C.2 (c) Remote control with two keys using series activation mechanism.

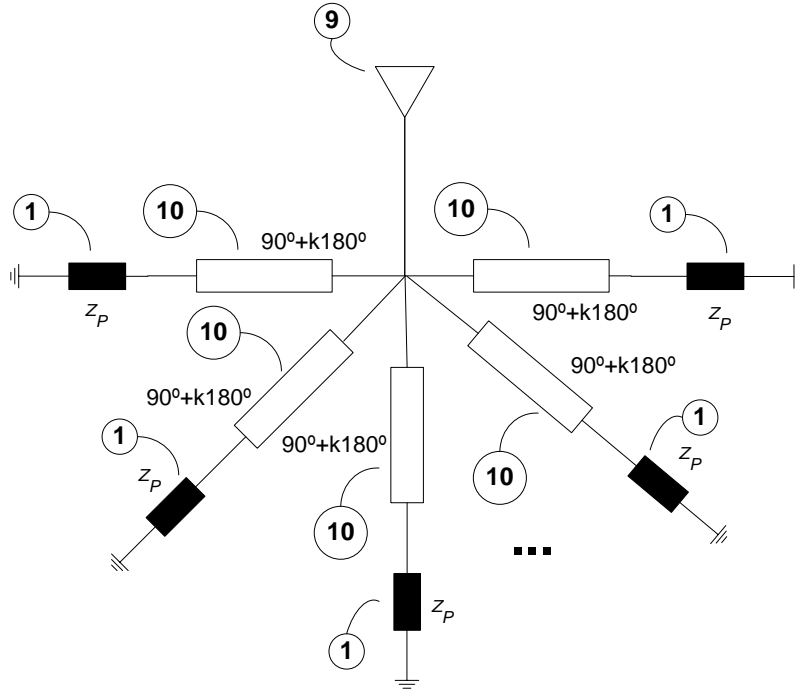


Fig. C.2 (d) N-key remote control in star configuration, using parallel activation mechanism.

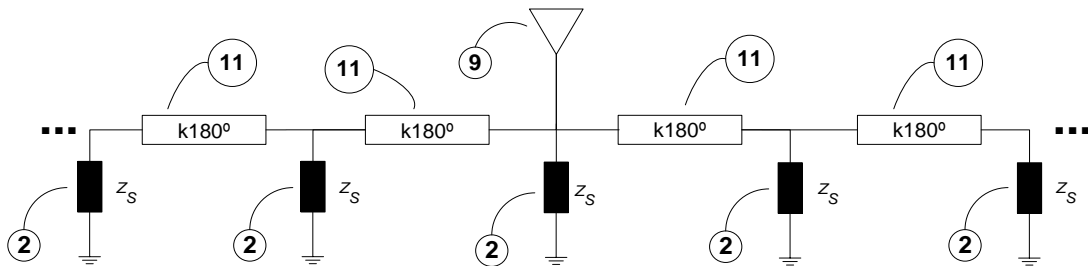


Fig. C.2 (e) N-key remote control in cascade configuration, using series activation mechanism.

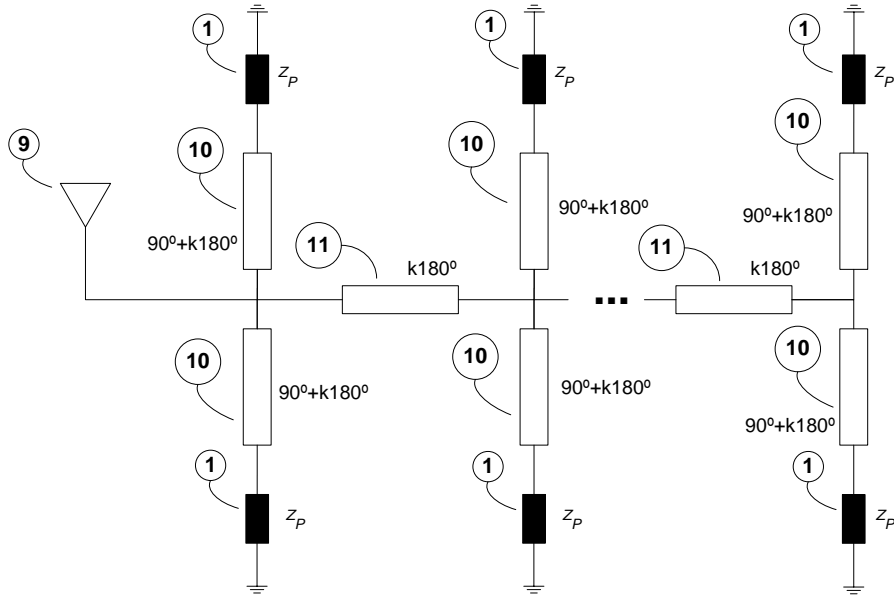


Fig. C.2 (f) N-key remote control in backbone configuration, using parallel activation mechanism.

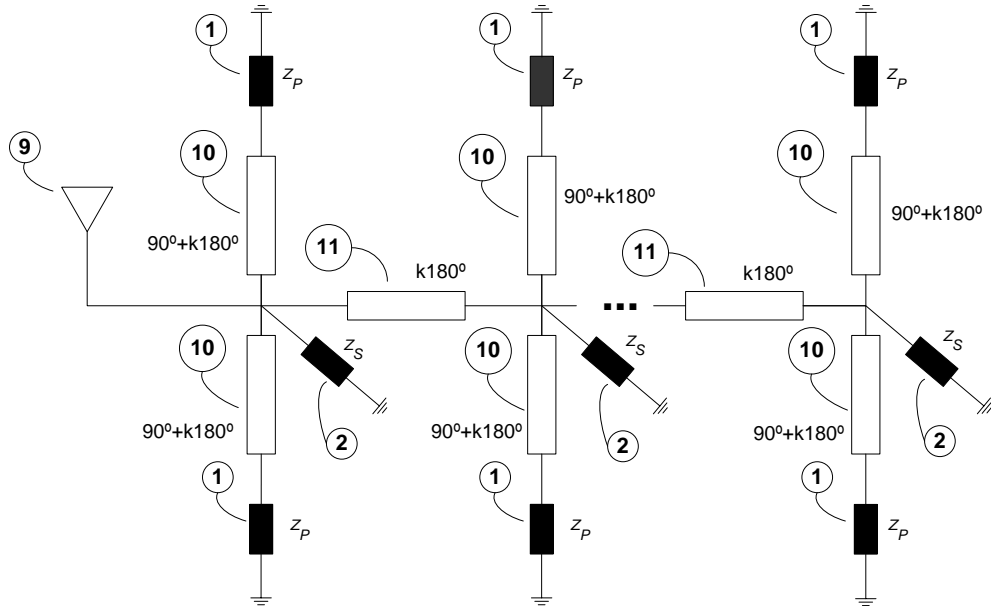


Fig. C.2 (g) N-key remote control with an hybrid configuration (backbone, cascade and star), using both parallel and series activation mechanisms.

